An investigation of low energy quasiparticle excitations via thermal transport measurements

by

William Henry Toews

A thesis
presented to the University of Waterloo
in fulfillment of the
thesis requirement for the degree of
Doctor of Philosophy
in
Physics

Waterloo, Ontario, Canada, 2017

Examining Committee Membership

The following served on the Examining Committee for this thesis. The decision of the Examining Committee is by majority vote.

External Examiner	Nigel Hussey Professor, Radboud University
Supervisor	Robert Hill Associate Professor, University of Waterloo
Internal Member	Anton Burkov Associate Professor, University of Waterloo
Internal-external Member	Adam Wei Tsen Assistant Professor, University of Waterloo
Other member(s)	Adrian Lupascu Associate Professor, University of Waterloo

This thesis consists of material all of which I authored or co-authored: see Statement of Contributions included in the thesis. This is a true copy of the thesis, including any required final revisions, as accepted by my examiners.

I understand that my thesis may be made electronically available to the public.

Statement of Contributions

The $Ho_2Ti_2O_7$ and $Dy_2Ti_2O_7$ samples were grown by Bruce Gaulin's group at McMaster University. I aligned the crystals, shaped them into rectangular prisms and prepared the thermometer leads at the University of Waterloo. The majority of the characterization of the two DTO samples via x-ray diffraction was conducted by Stefan Kycia and his graduate student Al Rahemtulla at the University of Guelph.

The unannealed $Yb_2Ti_2O_7$ sample was grown by Bruce Gaulin's group at McMaster University and the annealed sample was grown by Dharmalingam Prabhakaran at the University of Oxford. I aligned, shaped and prepared the samples for measurements at the University of Waterloo.

The SmB_6 samples were grown by Geetha Balakrishnan at the University of Warwick and the sample thermometer leads were prepared by Michael Sutherland's group at the University of Cambridge.

I performed and analysed all of the transport and magnetostriction measurements at the University of Waterloo.

Abstract

Thermal transport measurements can provide a unique perspective of the nature of a system by exploring the behaviour of the low energy excitations from the ground state. Delocalized quasiparticle excitations can affect the conductivity either by providing an additional channel of heat conduction, or by scattering the phonons. Thus, extensive thermal conductivity measurements have been conducted on a number of materials in order to examine their exotic ground state manifolds by probing the low lying excitations.

Thermal transport measurements of the classical spin ice materials $Ho_2Ti_2O_7$ (HTO) and $Dy_2Ti_2O_7$ (DTO) have revealed evidence for a non-negligible contribution to the conductivity from magnetic excitations in excess of the phonon conductivity. Hysteresis is observed below 360 mK upon cycling the field above 1.5 T for HTO, and 1 T for DTO, due to a first order phase transition from the Kagomé phase into a field induced long range ordered phase. Hysteresis can be induced at higher temperatures by increasing the field sweep rate, which is shown to cause spikes in the sample temperature resulting from out of equilibrium thermal runaway processes. The high field conductivity of HTO shows an enhancement in the conductivity until it saturates above ~ 4 T indicative of the suppression of spin-phonon scattering. On the other hand, the high field conductivity of DTO decreases to a constant value, suggesting a much weaker spin-phonon coupling in DTO compared to HTO. Thus, the field independent data at high field only accurately depicts the zero field phonon conductivity in DTO.

As in any real material, imperfection in the crystal lattice will always be present. The effect of disorder in the lattice has on the monopole excitations in the spin ice manifold is explored by considering two DTO samples with differing levels of disorder. The level of disorder in each sample is initially characterized via x-ray diffraction measurements as well as high temperature conductivity measurements which probes defect scattering of phonons. The magnetic channel of conductivity in the sample with less disorder follows an exponential temperature dependence with an activation energy comparable to the energy gap of a monopole excitation as intuitively expected for an activated quasiparticle excitation. The magnitude of the magnetic conductivity in the sample with a higher level of disorder is greater than the less disordered sample and also follows a power law temperature dependence. This indicates that the impurities tend to enhanced monopole density possibly by acting as nucleation sites. An analogy is made to the enhanced carrier concentration in a doped semiconductor.

The observation of a strong sample dependence of many physical properties in the quantum spin ice material $Yb_2Ti_2O_7$ (YbTO) has been proposed to be in part caused by disorder in the lattice from the floating zone growth technique. Thus, in order to examine the effect of this disorder on the magnetic excitations, thermal transport measurements were conducted on two separate YbTO samples; one sample was measured as grown, and the other sample was measured after annealing in oxygen. The annealed sample exhibits a sharp step-like drop in the conductivity at approximately $T_c \sim 200$ mK whereas the as grown sample shows a broad feature indicating a change in the power law of the temperature dependence. The field dependence of the conductivity above 200 mK reveals a substantial contribution from dispersive quantum monopoles which can be suppressed with the application of a small field. The monopole suppression rate increases monotonically as the temperature approaches T_c, consistent with ferromagnetic fluctuations indicative of the onset of a long range ordered ferromagnetic phase. This is corroborated by the disappearance of the monopole excitations below 200 mK.

Electrical resistivity and thermal conductivity measurements were conducted on three single crystals of the topological Kondo insulator, $\mathrm{SmB_6}$; two sample grown in an image furnace, and one grown via the flux method. The resistivity increases exponentially with decreasing temperature, reaching a saturation value below 4 K. This is due to an electrically insulating bulk with a gap of approximately 4 meV and topologically protected electrical surface states. The zero field thermal conductivity is well described by phonons in the boundary scattering limit. However, the floating zone grown samples show a field induced enhancement of the conductivity which is four orders of magnitude larger than what is expected from the electronic surface states via the Wiedemann-Franz law. Thus, this additional conductivity channel is from charge neutral excitations which are magnetic in nature. Furthermore, the temperature dependence of the magnetic conductivity is not described by magnons or spinon excitations. The flux grown sample does not exhibit the same field enhancement of the conductivity suggesting that variations in the sample composition can affect the magnitude of the charge and spin excitations gaps.

Acknowledgements

First and foremost, I owe my greatest gratitude to my supervisor, Robert Hill. Rob's genuine enthusiasm for his research and ability to think analytically has been a constant source of motivation and inspiration. His patience and guidance has provided the perfect environment for me to grow as an experimentalist. working with Rob has been a privilege and I am truly grateful for the opportunity.

Next I would like to thank my advisory committee members, Jan Kycia, Anton Burkov, Adam Wei Tsen and Richard Oakley. Whether it is Jan's unending supply of experimental expertise, Anton's understanding of a variety of exotic phenomena in condensed matter or the external perspective from Adam and Richard, their input has been invaluable throughout my education.

I also need to thank my collaborators and crystal growers who supplied the materials studied here. Hanna Dabkowska and Bruce Gaulin's group at McMaster University supplied us with all of the $Ho_2Ti_2O_7$ and $Dy_2Ti_2O_7$ samples as well as the unannealed $Yb_2Ti_2O_7$ sample. The annealed $Yb_2Ti_2O_7$ sample was grown and prepared by Dharmalingam Prabhakaran at the University of Oxford. The SmB_6 samples were all grown by Geetha Balakrishnan at the University of Warwick and the thermometer leads were prepared by Michael Sutherland's group at the University of Cambridge. Finally, the x-ray diffraction measurements of the two $Dy_2Ti_2O_7$ samples were conducted Stefan Kycia and his graduate student Al Rahemtulla at the University of Guelph. None of my research would have been possible without all the effort from each of these collaborators to provide us with these fascinating materials.

The members of Jan Kycia's group have been incredibly helpful throughout my entire course of study. David Pomaranski, Cliff Plesha and Jeff Mason have provided an endless supply of liquid helium, cappuccinos, and companionship; all of which are essential in a low temperature laboratory. It has been excellent working with the many undergraduate and graduate students who have made their way though the lab over the years, particularly my successor, Jennifer Reid.

Finally, I would like to thank my family. My parents and sisters have supported me throughout my entire educational career. Most of all, I need to thank my wife, Jennifer, for putting up with me through this whole process and for taking good care of the kids during the late nights in the lab. I could not have done it alone.

Dedication

For Joel and Claire.

Table of Contents

List of Tables

List of Figures

Chapter 1

Introduction

At temperatures approaching absolute zero, the thermal energy becomes comparable to the strength of the various interactions at play in the system. This can result in the realization of a variety of exotic states of matter. Such emergent phases include the highly degenerate spin ice ground state in the rare-earth pyrochlore family of materials or the topological Kondo insulating state observed in samarium hexaboride where electronic quasiparticles are topologically protected on the surface of the sample. Our understanding of the nature of these exotic phases is intimately entwined with our knowledge of the low energy excitations from the ground state. Thermal transport is an excellent probe of delocalized quasiparticles, and hence can reveal a great deal about the nature of the ground state. Complimentary electrical resistivity measurements can provide additional information about the excitations via the Wiedeman-Franz law (WFL) which is satisfied for electronic Landau quasiparticles. These unusual and novel systems provide a unique opportunity to explore a variety of exotic quasiparticles that do not exist in nature outside of these materials. The properties of these excitations may prove to be useful in future technological applications. The goal of this thesis is to utilize the versatility of thermal transport to explore exotic states of matter by examining the delocalized excitations.

The family of rare-earth titanates, $Re_2Ti_2O_7$ ($Re^{3+} = Ho^{3+}$, Dy^{3+}, Yb^{3+}), provide an excellent reference for studying frustrated magnetism in three dimensions. The rare-earth ions are located on a lattice of corner sharing tetrahedra with cubic symmetry. In the case of $Ho_2Ti_2O_7$ (HTO) and $Dy_2Ti_2O_7$ (DTO), the magnetic moments are nearly perfect Ising spins quantized along the local [111] direction (into or out-of each tetrahedron) due to the crystal electric fields [34, 35, 9]. The spin Hamiltonian consists of a antiferromagnetic nearest neighbour exchange interaction and a ferromagnetic long range dipolar interaction [5]. A 6-fold degenerate ground state per tetrahedron emerges such that two spins point into each tetrahedra and two spins point out of each tetrahedra. This arrangement is analogous to the locations of hydrogen ions with respect to the oxygen atoms in water ice, hence the "spin-ice" nomenclature. Excitations out of this ground state are theoretically described as magnetic monopole quasiparticles, which interact with a Coulomb potential. A single spin flip event breaks the 2-in-2-out ice rules, resulting in neighbouring tetrahedra with 3-in-1-out/1-in-3-out spin configurations which are defined to be a monopole/anti-monopole pair. Subsequent spin flips do not break the ice rules, and thus the monopole/anti-monopole pair can separate and traverse the crystal lattice.

Although HTO and DTO share many similarities, there are a number of key differences which affect how the spin system and the lattice interact. The field dependence of the thermal conductivity reveals that monopole-phonon scattering is a much larger effect in HTO than in DTO. We also show that disorder in the crystal lattice can greatly influence the behaviour of the monopole excitations and draw comparisons to doped semiconductors. In addition to probing the behaviour of monopole excitations, thermal transport measurements are also useful for detecting phase transitions. The field dependence of the conductivity in both HTO and DTO exhibits hysteresis below 360 mK corresponding with a first order phase transition. Thermal relaxation times are explored in regards to the dependence on field sweep rate and its effect on the observed hysteresis.

The rare-earth titanate $Yb_2Ti_2O_7$ (YbTO) is an excellent system to explore spin ice physics with the inclusion of quantum effects. Rather than the local [111] easy axis anisotropy of the spins as in HTO and DTO, the Yb^{3+} ions have an easy plane anisotropy perpendicular to the [111] direction [18]. Off diagonal terms in the spin Hamiltonian lead to quantum fluctuations which lower the monopole excitation energy. Although it has been shown that this Hamiltonian can support a quantum spin liquid phase at low temperature, the nature of the ground state is still debated due to conflicting reports finding either a short range correlated phase, or a first order ferromagnetic phase transition into a long range ordered phase [19, 36, 37, 38, 39, 40, 41]. There is clear evidence of a strong sample dependence on the anisotropic exchange coupling, which leads to differing ground states. Thermal transport measurements on YbTO samples as grown, and samples which have been annealed in oxygen provide insight into the effect disorder has on the quantum monopole excitations as well as the nature of the transition into the ground state. We find that the annealed sample shown a substantial contribution to the conductivity from monopole excitations above the transition temperature which is marked by a step-like drop in the conductivity. The field dependence of the conductivity shows considerable spin-phonon scattering which can be suppressed with the application of a large magnetic field.

Upon cooling SmB_6 below ~ 100 K, the localized f electrons from the Sm^{3+} ions hybridize with the conduction electrons, forming Kondo singlets. The screening of these local moments by the conduction electrons leads to a decrease in the electrical conductivity. However, the resistivity saturates below 3 K due to topologically protected electronic surface states [25, 26, 24]. Large de Haas-van Alphen oscillations have been observed in SmB_6 at low temperatures, however conflicting interpretations have been proposed [28, 29]. One group suggests that the quantum oscillations originate from the electronic surface states, which form a two dimensional Fermi surface on the surface of the sample [28]. Another group proposes that the oscillations are due to charge neutral excitations in the bulk, forming a large three dimensional Fermi surface in the bulk of the material [29]. Here, thermal transport measurements are used to probe the delocalized quasiparticles in the bulk. The thermal conductivity is enhanced with the application of a magnetic field surpassing the boundary limited phonon conductivity. This is clear evidence for an additional field-enhanced channel of conductivity. We also show that the field induced enhancement in the conductivity is several orders of magnitude larger than the contribution from the electronic surface states via the WFL.

1.1 Outline

This thesis is organized into three sections. Part I introduces the theoretical background and practical implementation of conducting thermal conductivity measurements at ultra low temperatures. Part II focuses on the rare-earth titanate family of materials, where field and sample dependent studies are presented for $Ho_2Ti_2O_7$ (HTO), $Dy_2Ti_2O_7$ (DTO) and $Yb_2Ti_2O_7$ (YbTO). Part III explores the thermal conductivity of the topological Kondo insulator SmB_6.

Part I - Experimental Details

Chapter 2 discusses the theory describing the various channels of thermal conduction in both metals and insulating materials. The device used to measure thermal transport is outlined in chapter 3. Finally, chapter 4 presents two systems used for achieving ultra low temperatures; a helium-4 pumped probe and a helium-3/helium-4 dilution fridge.

Part II - Rare-Earth Titanates

Chapter 5 introduces magnetism caused by the core electrons in a solid and introduces the concept of frustrated magnetism with the example of the spin ice materials. Chapter

6 explores the field dependence of the conductivity in the spin ice materials HTO and DTO. The effect of disorder on the monopole conductivity in the classical spin ice state is presented in chapter 7. Chapter 8 examines the temperature and field dependence of the conductivity in the quantum spin ice material YbTO for a sample as grown and a sample which has been annealed in oxygen.

Part III - Topological Kondo Insulators

Chapter 9 examines the interaction between conduction electrons and local magnetic moments. Several properties of the topological Kondo insulator SmB_6 are also discusses. Chapter 10 presents thermal conductivity and electrical resistivity measurements of three SmB_6 samples, two grown in an image furnace and one grown via the flux method.

Part I

Experimental Details

Chapter 2

Thermal Conductivity

The propagation of heat through a material is characterized by its thermal conductivity κ which is defined as the ratio of the heat flux density $\vec{q} \equiv \vec{Q}/A$ to the local temperature gradient $\vec{\nabla}T$ via Fourier's Law of Heat Conduction [42]:

$$\vec{q} = -\kappa\vec{\nabla}T \tag{2.1}$$

In general, the thermal conductivity is a rank two tensor allowing for directional anisotropies in the material as well as a possible transverse thermal gradient from the thermal Hall effect. However, in crystalline materials with a uniform heat current in one dimension, the thermal conductivity can be represented as a scalar quantity. Under these circumstances, Fourier's Law can be simplified as

$$\dot{Q} = -\kappa A\frac{\mathrm{d}T}{\mathrm{d}x} = -\kappa\Delta T\frac{A}{l} \tag{2.2}$$

where A is the cross-sectional area of the sample, l is the sample length and ΔT is the difference in temperature across the sample.

The heat transfer is mediated by electronic excitations (electrons), lattice vibrations (phonons), magnetic excitations (magnons, spinons, monopoles) etc. so that the total thermal conductivity is the sum of these components acting in parallel:

$$\kappa_{\mathrm{Total}} = \kappa_{\mathrm{e}} + \kappa_{\mathrm{ph}} + \kappa_{\mathrm{mag}} + ... \tag{2.3}$$

It is important to note that the separate contributions to the conductivity may affect one another via interactions between the different types of quasiparticles. For example, electron-phonon scattering will reduce both the electronic and lattice contributions to the conductivity.

Thermal transport is an excellent tool for measuring delocalized, low energy, quasiparticle excitations that are capable of carrying entropy. The temperature dependence as $T \to 0$ K can reveal a great deal about the nature of the delocalized quasiparticles; whether they are fermionic in nature, or if they are gapped excitations for example. Additionally, the ratio of the thermal conductivity to the electrical conductivity is an excellent test to see if a Fermi liquid state is established by verifying the Wiedemann-Franz law (WFL). In order to take advantage of the experimental power transport measurements can provide, an understanding of some of the more basic concepts of electronic charge and thermal transport and phonon thermal transport is essential. They will now be discussed under the framework set up by Drude, Sommerfeld and Debye.

2.1 Electronic Conduction in Metals

In 1900, Paul Drude developed a model to describe electronic and thermal conduction by applying the kinetic theory of gases to a gas of electrons. The validity of this model depends on two main assumptions of the system, however, it provides a satisfactory description of simple metals. The assumptions are as follows: in the absence of an external electromagnetic field, the conduction electrons travel in straight lines between collisions free from long range electron-electron and electron-ion interactions. This is referred to as the *independent electron approximation* and the *free electron approximation* respectively [42]. Furthermore, collisions will be treated as instantaneous events as in the kinetic theory of gases. These collisions will occur with a probability per unit time of τ^{-1} where τ is the relaxation time. Finally, Drude assumed that the system will attain thermal equilibrium only through these collisions. These assumptions can now be used to calculate the electrical resistivity.

The electrical conductivity σ is defined as the ratio of the electronic current density $\vec{j}$ to the electric field $\vec{E}$ at any given point in the metal so that

$$\vec{j} = \sigma \vec{E}. \tag{2.4}$$

Similar to the thermal conductivity, the electrical conductivity is also a second order tensor in general, but simplifies to a scalar quantity when the electric field is uniform and one-dimensional. The electrical resistivity ρ is then defined as the reciprocal of the conductivity so that $\rho = 1/\sigma$. A current $\vec{I}$ flowing through a wire can be described as n electrons with charge $-e$ travelling with an average velocity $\vec{v}$ through an area A such that $\vec{I} = -ne\vec{v}A$.

Therefore, the resulting current density is given by

$$\vec{j} = -ne\vec{v}. \tag{2.5}$$

In the absence of an electric field the net current density, and consequently the average electron velocity, equates to zero. This is due to the fact that the velocity of an electron immediately after a collision is completely random and thus averages to zero. So, a finite average electron velocity is a direct result of the force on the electron by an applied electric field which is equal to $-e\vec{E}$. Hence, the mean velocity of the electrons induced by the electric field over a time τ between collisions is given by

$$\vec{v}_{avg} = -\frac{e\vec{E}\tau}{m}. \tag{2.6}$$

Combining equations (2.4), (2.5) and (2.6) we arrive at the electrical conductivity as per the Drude model.

$$\vec{j} = \left(\frac{ne^2\tau}{m}\right)\vec{E}; \quad \sigma = \frac{ne^2\tau}{m} \tag{2.7}$$

We are able to use the Drude model to find this explicit form of the electrical conductivity because it does not depend on the energy distribution. Therefore, even though the Drude model is strictly classical and would thus use the Maxwell-Boltzmann distribution the conductivity is still valid. Furthermore, it was later shown by Lev Landau in 1957 that although electrons do in fact have considerable interactions, the Drude model is still valid since the interactions renormalize the mass of the electronic quasiparticles which then follow the independent electron approximation.

The purely classical Drude model, however, fails to accurately describe the temperature dependence of the resistivity in normal metals. According to the Drude model, the mean free path of the electrons between collisions is temperature independent, yet the average velocity is proportional to $\sqrt{T}$. Thus the relaxation time decreases as $\tau \propto 1/\sqrt{T}$ and therefore the resistivity would also be proportional the the square root of the temperature. In reality, well behaved metals approximately follow a linear temperature dependence from intermediate temperatures up to room temperature. This is due to thermal vibrations of the lattice through an electron-phonon interaction. On the other hand, as the temperature approaches absolute zero the electron mean free path is limited by impurities in the sample, resulting in a temperature independent relaxation time and therefore a saturation of the resistivity. This is referred to as the residual resistivity. It provides an excellent measure of the amount of disorder in metallic samples by comparing it to the room temperature value of the resistivity; a ratio known as the residual resistivity ratio (RRR). Figure 2.1

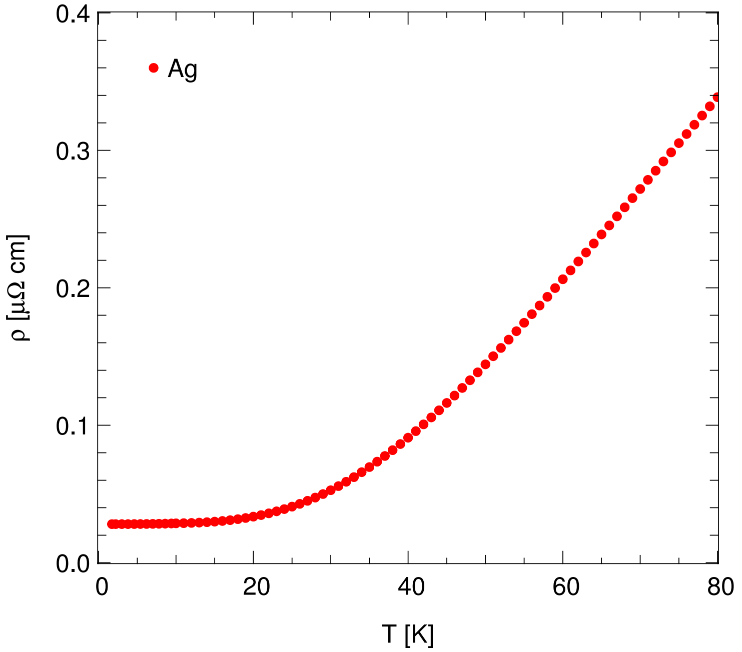

Figure 2.1: The temperature dependence of the resistivity is seen for silver from 40 mK to 80 K. The high temperature resistivity is linear in temperature, as saturates as $T \to 0$ as described in the main text.

shows the electrical resistivity of silver from 40 mK up to 80 K. Here we can see all the characteristics of a well behaved metal; a constant resistivity below 10 K, and a linear temperature dependence at higher temperatures. This sample has an RRR$\sim$ 72.5, however, in some ultra-pure metallic systems, the RRR can be as large as several thousand.

The Drude model can be modified by using Fermi-Dirac statistics as in the Sommerfeld theory of metals to derive the electronic specific heat and thermal conductivity of semi-classical metals. To determine the electronic thermal conductivity κ_e we start by calculating the electronic contribution to the specific heat from Fermi-Dirac statistics and take advantage of the following equation from kinetic theory which states:

$$\kappa_e = \frac{1}{3} c_v v_F^2 \tau \tag{2.8}$$

where c_v is the electronic specific heat, v_F is the Fermi velocity and τ is the electron scattering relaxation time. Since we are using Fermi-Dirac statistics, we will use the Fermi

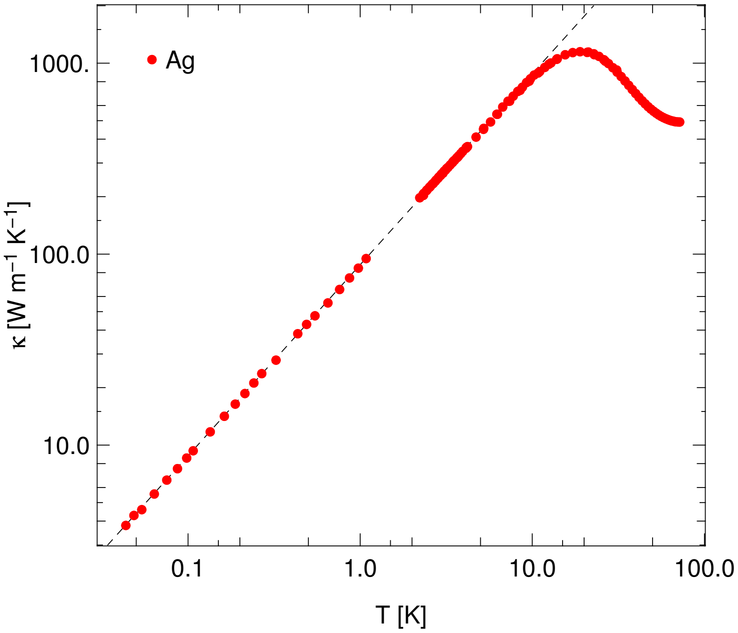

Figure 2.2: The thermal conductivity is plotted versus temperature for silver from 40 mK to 80 K. The dotted line is a linear fit to the low temperature data (below 10 K) clearly showing the expected linear electronic term. The conductivity displays a peak at 19 K followed by a reduction to a constant value at the highest temperature measured.

function to describe the electronic distribution which is defined as

$$f(\epsilon) = \frac{1}{e^{(\epsilon-\mu)/k_BT} + 1} \tag{2.9}$$

The Fermi function, $f(\epsilon)$, and the density of states, $g(\epsilon)$, can then be used to calculate the electronic specific heat by finding the total internal energy and recalling that $c_v = \left(\frac{\partial u}{\partial T}\right)_n$.

$$\begin{aligned} c_v &= \frac{\partial}{\partial T}\int\limits_0^\infty d\epsilon\ g(\epsilon)\epsilon f(\epsilon) \\ &= \frac{3}{2}\left(\frac{k_BT}{\epsilon_F}\right) nk_B \int\limits_{-\epsilon_F/k_BT}^{\infty} \frac{x^2e^x}{(e^x+1)^2}dx \\ &= \frac{\pi^2}{2}\left(\frac{k_BT}{\epsilon_F}\right) nk_B \qquad (\text{as } T \to 0) \end{aligned} \tag{2.10}$$

Here, $x \equiv (\epsilon - \epsilon_F)/k_B T$, and as $x \rightarrow \epsilon_F/k_B T$, $e^x \approx 0$ thus the lower limit on the integral can be replaced by $-\infty$ so that the integral can be easily evaluated to be $\pi^2/3$. Noting that the Fermi velocity $v_F = \left(\frac{\hbar}{m}\right) k_F$ and the Fermi energy $\epsilon_F = \frac{\hbar^2 k_F^2}{2m}$, we can now combine equations (2.8) and (2.10) to determine the electronic contribution to the thermal conductivity κ_e:

$$\kappa_e = \frac{\pi^2}{3}\frac{k_B^2 n\tau}{m}T. \tag{2.11}$$

This can alternatively be written in terms of k_F and the electron mean free path $l = v_F\tau$ such that

$$\kappa_e = \frac{1}{9}\frac{k_B^2 k_F^2 l}{\hbar}T \tag{2.12}$$

since the ground state of a system of N electrons in a volume V will occupy all of the single-electron states with wave-vector k less than the Fermi wave-vector k_F such that $n = k_F^3/3\pi^2$ where $n = N/V$ is the electron density [42]. This is because each single-electron state occupies a volume of $8\pi^3/V$ in k-space. So, the number of allowed k-states in the Fermi sphere is $(\frac{4}{3}\pi k_F^3)(V/8\pi^3)$. Thus, if there are N electrons (with spin-1/2) in a volume V, then we find that $N/V = k_F^3/3\pi^2$.

The important result here is that the electronic thermal conductivity follows a linear temperature dependence which originates from the electronic specific heat since the relaxation time is assumed to be temperature independent. This is in fact what is observed in metallic samples at low temperature. However at higher temperatures, electron-electron and electron-phonon interactions become more prevalent and modify the temperature dependence. This also occurs in strongly correlated materials.

2.1.1 Wiedemann-Franz Law

The ratio of the thermal conductivity (equation 2.11) and the electrical conductivity (equation 2.7) yield a constant value defined as the Lorenz number $L_o \equiv 2.44 \cdot 10^{-8}\ W\Omega/K^2$ [43]. This is the well known Wiedemann-Franz law (WFL) and is explicitly written as

$$\frac{\kappa_e}{\sigma T} = \frac{\pi^2}{3}\left(\frac{k_B}{e}\right)^2 \equiv L_o. \tag{2.13}$$

It is important to notice that this simple expression only holds when the scattering relaxation time, τ, is equivalent for both electrical and thermal conductivity. This occurs at low temperatures where the electron scattering is dominated by impurity scattering and at much higher temperatures where large angle, electron-phonon scattering affects the

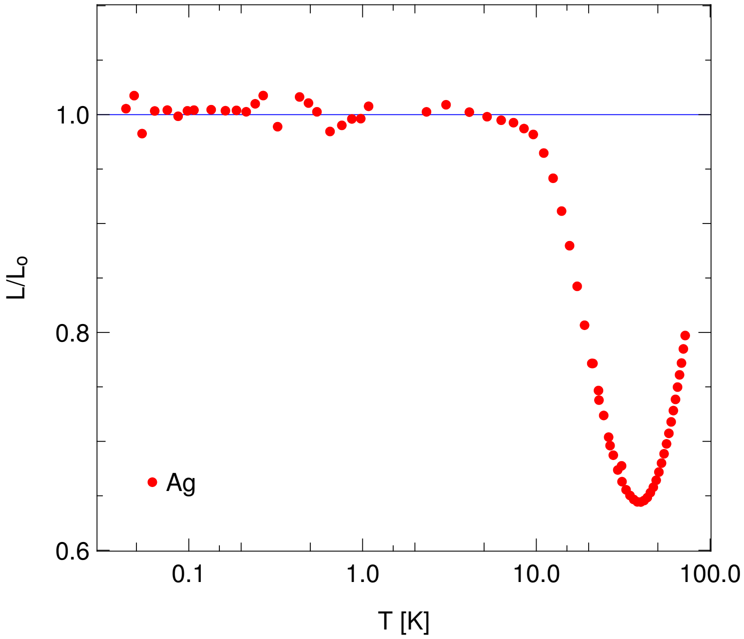

Figure 2.3: The Wiedemann-Franz ratio L/L_0 is plotted versus T for silver at temperatures from 40 mK to 80 K. It is evident that the Wiedemann-Franz law in satisfied to within 2% from 40 mK to 10 K. The scatter is due to random error in the data at low temperature. As the temperature is increased above 10 K, L/L_0 decreases to a minimum of ~ 0.65 occurring at 38 K. This is a result of an increase in electron-phonon scattering as described in the main text.

charge and thermal transport equally. At intermediate temperatures, the probability of inelastic, small angle scattering increases which greatly impedes the thermal transport, yet does not have as much of an effect on the charge transport. This causes a reduction in the Wiedemann-Franz ratio which is defined as $\frac{\kappa_e \rho}{L_o T} \equiv L/L_o$. It is possible to observe $L/L_o > 1$ if the phonon thermal conductivity becomes appreciable with respect to the electronic contribution. However, it is inappropriate to consider the WFL in this scenario since the WFL is only concerned with the electronic transport, not other channels of conductivity. Therefore, when examining the electronic conductivity, the Wiedemann-Franz ratio is usually less than, or equal to unity. In reality, the temperature dependence of the Wiedemann-Franz ratio can be quite complicated and difficult to predict *a priori*. However, we do expect the WFL to be satisfied both at low temperatures and at high temperatures ($T \gtrsim \Theta_\mathrm{D}$) [44].

This result is verified by measuring the electrical and thermal transport of a well behaved metal, silver in this case. The Wiedemann-Franz ratio, L/L_o, for a silver wire is plotted as a function of temperature in figure 2.3 for temperatures between 40 mK and 80 K. The WFL is clearly satisfied to within 2% from 40 mK to 10 K. Above this temperature L/L_o decreases dramatically, revealing that the WFL is not valid at intermediate temperatures. Above approximately 19 K, L/L_o begins to increase and approaches unity at the highest temperatures measured. This is expected since the probability of large angle electron-phonon scattering increases as the temperature increases, which affects the charge and thermal transport equally.

2.2 Phonon Thermal Conduction

2.2.1 Einstein solid

In 1907, Albert Einstein showed that lattice vibrations in a solid are quantized and well described as phonon quasiparticles. This allows us to determine the lattice specific heat, which in turn can be used to calculate the phonon thermal conductivity via kinetic theory. Einstein proposed that the ions in a solid act as independent oscillators in three dimensions all with frequency ω_E. The simple harmonic oscillator energy levels are specified by $E_n = \hbar\omega_\mathrm{E}\left(n + \frac{1}{2}\right)$. To find the total internal energy, and subsequently the specific heat, we first need the partition function, which is given by

$$Z = \sum_{n=0}^{\infty} e^{-\beta E_n} = e^{-\beta\hbar\omega_\mathrm{E}/2} \sum_{n=0}^{\infty} e^{\beta\hbar\omega_\mathrm{E} n} = \frac{e^{-\beta\hbar\omega_\mathrm{E}/2}}{1 - e^{-\beta\hbar\omega_\mathrm{E}}}. \tag{2.14}$$

There are $3N$ oscillators for a solid with N atoms, so the total internal energy U is

$$U = 3N\left(-\frac{\mathrm{d}\,\ln(Z)}{\mathrm{d}\beta}\right) = 3N\left(\frac{\hbar\omega_\mathrm{E}}{2} + \frac{\hbar\omega_\mathrm{E}}{e^{\beta\hbar\omega_\mathrm{E}} - 1}\right) \tag{2.15}$$

Finally, the specific heat is obtained by differentiating with respect to temperature such that

$$c_v = \left(\frac{\partial U}{\partial T}\right)_v = 3Nk_\mathrm{B}\left(\frac{\Theta_\mathrm{E}}{T}\right)^2 \frac{e^{\Theta_\mathrm{E}/T}}{\left(e^{\Theta_\mathrm{E}/T} - 1\right)^2} \tag{2.16}$$

where $\Theta_\mathrm{E} = \hbar\omega_\mathrm{E}/k_\mathrm{B}$ is defined as the Einstein temperature. In the high temperature limit, the Einstein solid model recovers the famous Dulong-Petit law where $c_v = 3Nk_\mathrm{B}$. However, the low temperature limit fails to accurately describe the T^3 temperature dependence experimentally observed. Thus, the Einstein model can be very useful at high temperatures, a different approach must be taken to accurately portray the low temperature behaviour.

2.2.2 Debye model

To more accurately depict the low temperature specific heat, and subsequently the thermal conductivity, we will follow the Debye model of lattice vibrations. Unlike Einstein's model of independent oscillators, the Debye model considered collective, coupled oscillations with $3N$ vibrational modes. At low temperature, low frequency acoustic modes dominate which have a linear dispersion relation $\omega = v_s k$. Additionally, Debye found that the phonon density of states, $g(\omega)$, is quadratic below a cut-off frequency $\omega_\mathrm{D} = (6\pi^2 N_o)^{1/3} v_s$, called the Debye frequency, and zero at higher frequencies. This is equivalent to assuming that the wave-vectors for each of the phonon modes lie in a sphere of radius $k_\mathrm{D} = \omega_\mathrm{D}/v_s$. So, if all three phonon branches have the same linear dispersion, we find that the density of states of the phonon modes is quadratic in frequency. The explicit form of the density of states in the Debye model is

$$g(\omega) = \begin{cases} 9N_o\omega^2/\omega_\mathrm{D}^3, & \omega < \omega_\mathrm{D} \\ 0, & \omega > \omega_\mathrm{D} \end{cases}$$

where N_o is the density of atoms and v_s is the speed of sound. Now in reality, the phonon dispersion is considerably more complex than a simple quadratic form. We will see below how this affects the Debye temperature below. The Debye temperature is a characteristic temperature scale of the lattice vibrations and is defined as $\Theta_\mathrm{D} = \hbar/k_\mathrm{B}\omega_\mathrm{D}$.

In order to calculate the phonon specific heat, Bose-Einstein statistics will be used since phonons are bosonic quasiparticles. The distribution function of interest is thus:

$$f(\epsilon) = \frac{1}{e^{(\epsilon-\mu)/k_B T} - 1}. \tag{2.17}$$

This is then used to calculate the phonon energy:

$$u = 9Nk_B T \left(\frac{T}{\Theta_D}\right)^3 \int\limits_0^{x_D} \frac{x^3}{e^x - 1} dx \tag{2.18}$$

where $x \equiv \hbar\omega/k_B T$ and $x_D \equiv \Theta_D/T$. We are concerned with the low temperature regime where $T/\Theta_D \ll 1$, so we can approximate $x_D \to \infty$ and the integral can be evaluated to be $\pi^4/15$. The phonon specific heat can now be easily obtained by taking the derivative with respect to temperature, yielding

$$c_{ph} = \frac{12}{5}\pi^4 N k_B \left(\frac{T}{\Theta_D}\right)^3. \tag{2.19}$$

This is the famous T^3 law for the low temperature phonon specific heat. Once again, using kinetic theory we can find the phonon thermal conductivity.

$$\kappa_{ph} = \frac{1}{3} c_{ph} v_s l \propto T^3 \tag{2.20}$$

This is a specific case of the phonon thermal conductivity where the phonon mean free path, l, is temperature independent, for example in the boundary scattering limit. However, the specific heat can be written more generally by taking the derivative of equation (2.18) without evaluating the integral, yielding

$$c(x)dx = \frac{3k_B}{2\pi^2 v_s^3} \left(\frac{k_B}{\hbar}\right)^3 T^3 \frac{x^4 e^x}{(e^x - 1)^2} dx. \tag{2.21}$$

Thus, we have an integro-equation for the thermal conductivity of the form

$$\kappa = \frac{1}{3} v_s \int l(x) c(x) dx. \tag{2.22}$$

which allows a frequency dependent mean free path, $l(x)$. This provides a very accurate method of fitting conductivity data for all temperature regimes. That said, it is often adequate to determine the various contributions to the thermal conductivity from each scattering mechanism and then add them via Matthiessen's rule, which will be discussed in section 2.2.3.

The Debye Temperature

Up until this point, we have assumed that the Debye temperature is a single-valued property of a given material. In reality, the Debye temperature can have a non-trivial temperature dependence (figure 2.4 (b)) due to a departure from the assumed quadratic frequency dependence of the density of states (figure 2.4 (a)). This tends to occur at higher temperatures where high frequency longitudinal phonon modes become important which can also be dependent on the coordination number of the lattice. However, at temperatures approaching absolute zero, where we will focus much of our attention, low frequency transverse modes dominate and the Debye model (with a constant Debye temperature) is a good approximation to reality. Therefore, the Debye T^3 relation for the phonon specific heat is an accurate representation at low temperature.

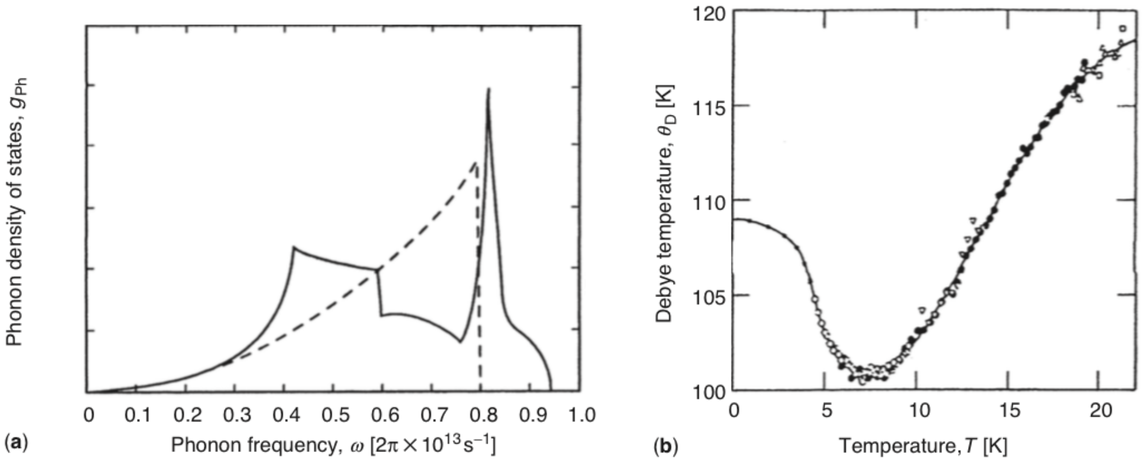

Figure 2.4: (a) The frequency dependence of the phonon density of states for aluminum measured at 300 K (solid line) and the Debye approximation with $\Theta_D = 382$ K (dashed line) are illustrated here. Although the Debye approximation does a fine job at approximating the low frequency data, it fails to describe the full density of states. (b) The temperature dependence of the Debye temperature of indium is seen here. The unfixed value of Θ_D is due to deviations from the quadratic density of states approximation.

2.2.3 Phonon Scattering Mechanisms

Now that we have a general form of the phonon thermal conductivity allowing the mean free path to have a frequency dependence, we can examine a variety of phonon scattering mechanisms which lead to a range of temperature dependencies in the thermal conductivity.

1. *Boundaries.* As the temperature approaches absolute zero, the low frequency, acoustic phonon modes dominate the phonon spectrum. In this case, the phonon wave lengths become long and local defects become ineffective at scattering the phonons. Thus, the phonon mean free path grows until it is eventually limited by the sample boundaries. The mean free path is independent of phonon frequency and temperature in this regime. In this case, the mean free path is equal to a geometric average of the sample width determined by $l = \sqrt{4A/\pi}$ where A is the cross-sectional area of the sample. This is determined by considering the diameter of a circle with the same area as the cross-sectional area of the sample. In light of this, equation (2.8) dictates

that the thermal conductivity due to sample boundary scattering will be given by

$$\kappa_{\mathrm{B}} = \frac{1}{3}\beta v_s \sqrt{\frac{4A}{\pi}} T^3 \tag{2.23}$$

where the phonon specific heat is $c_{ph} = \beta T^3$. A cubic temperature dependence of the conductivity is seen for other frequency independent mean free path scattering modes, for example, scattering off of grain boundaries where the mean free path is estimated to be the average grain size.

The validity of the assumption that scattering off the sample boundaries affects all phonons regardless of their frequency is in question when one considers the difference between diffuse and specular scattering. In fact, due to specular scattering of phonons off of the sample boundaries, the temperature dependence of the thermal conductivity can be slightly less than T^3, as seen in figure 2.5. This phenomena has been examined in depth in other insulating materials [45, 46, 1].

2. *Phonons: normal and Umklapp-processes.* Consider the interaction of two phonons with wave vectors $\vec{k}_1$ and $\vec{k}_2$ and frequencies ω_1 and ω_2 respectively such that they combine to result in a third phonon with wave vector $\vec{k}_3$ and frequency ω_3. Note that in these kind of three-phonon processes, energy must be conserved ($\hbar\omega_1 + \hbar\omega_2 = \hbar\omega_3$) and wave vector must also be conserved ($\vec{k}_1 + \vec{k}_2 = \vec{k}_3 + \vec{G}$) where $\vec{G}$ is a reciprocal lattice vector. Now, if $\vec{G} = \vec{0}$ then $\vec{k}_3$ lies in the first Brillouin zone (BZ) and the phonon momentum is conserved. This is known as a normal process (or N-process) and does not hinder the heat transport. If $\vec{k}_3$ falls outside of the first Brillouin zone then $\vec{G} \neq \vec{0}$ and thus changing the net direction of energy flow (see figure 2.6). This is known as Umklapp scattering (or U-processes) and does give rise to thermal resistance. For a U-process to occur, at least one of the phonons must have a frequency greater than half of the maximum allowed frequency, ie. $\omega_1 \geq \frac{1}{2}\omega_D = \frac{1}{2}k_B\Theta_D/\hbar$ which occurs with a probability of approximately $e^{-\alpha\Theta_D/T}$ at low temperatures ($T \ll \Theta_D$) where $\alpha \approx 0.5$. Similarly, the probability that the second phonon has a large enough wave vector to make $\vec{q}_3$ fall outside of the first Brillouin zone is usually assumed to proportional T^{-n} where $n \approx 3$. Thus the thermal conductivity will have the following temperature dependence:

$$\kappa_{\mathrm{U}} \propto e^{\alpha\Theta_{\mathrm{D}}/T}. \tag{2.24}$$

3. *Conduction electrons.* When phonons interact with conduction electrons in metals at low temperatures, the electrons will absorb or emit energy on the order of $k_{\mathrm{B}}T$ as a result of small angle scattering. This is enough energy to promote/demote an electron

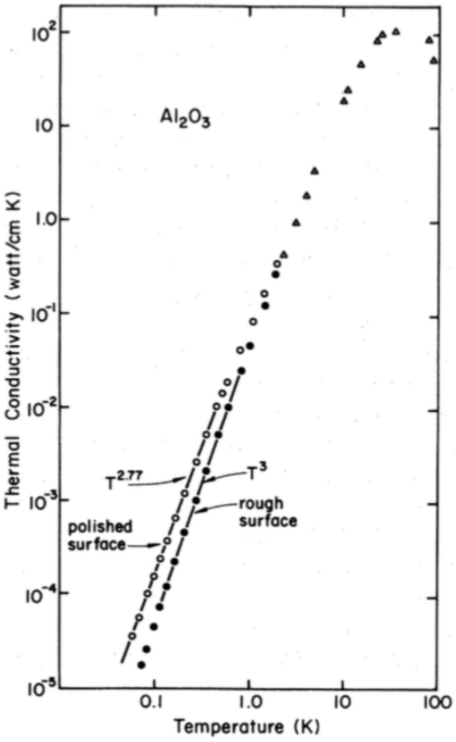

Figure 2.5: The temperature dependence of the thermal conductivity for Al_2O_3 is seen for two samples, one with a polished surface, and one with a surface that has been roughened. The polished surface allows for specular scattering of phonons, effectively lengthening the mean free path. This leads to a sub-T^3 temperature dependence. The sample with the roughened surface causes phonons to scatter in random directions at the boundaries. The expected T^3 temperature dependence is observed in this sample [1].

just above/below the Fermi-surface. That is, only electrons that lie within $k_{\mathrm{B}}T$ of the Fermi surface will be able to interact with the phonons. Hence, the number of electrons available for scattering at a given temperature will be proportional to T and therefore the phonon mean free path, l, will be proportional to T^{-1}. We have also seen that the phonon specific heat c_{ph} is proportional to T^3 (see equation (2.19)) thus using kinetic theory (equation (2.8)) we find that the conductivity is given by:

$$k_{\text{e-ph}} \propto T^2. \tag{2.25}$$

4. *Point defects and isotopes.* Defects in crystals that are on the atomic scale such

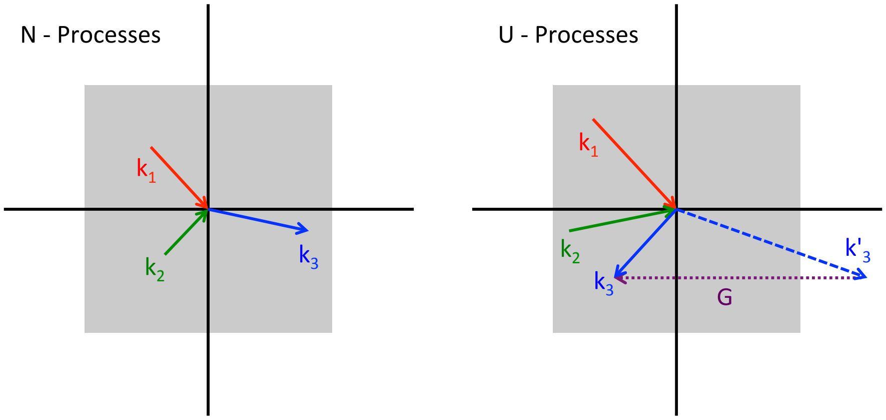

Figure 2.6: The figure on the left is an illustration of a normal process where the vector addition of two phonons with momentum $\vec{k}_1$, $\vec{k}_2$ sums to $\vec{k}_3$ which remains within the first Brillouin zone (grey square). Such a process does not affect the thermal conductivity of phonons since momentum is conserved. The figure on the right shows an Umklapp process. Here, $\vec{k}_3$ falls outside of the first Brillouin zone and thus must be translated back via a reciprocal lattice vector $\vec{G}$. Such a scattering event will invoke a thermal resistance in the lattice thermal conductivity.

as isotopes with different masses, impurities or a vacant lattice site will all appear as point defects in the crystal to the long wavelength phonons at low temperature. These defects will scatter phonons similar to Rayleigh scattering of photons such that they have a scattering probability proportional to q^4. The difference is that the phonon mean free path is ultimately limited by the sample dimensions. The scattering rate is thus proportional to T^4 which results in the thermal conductivity being proportional to T^{-1} since the phonon specific heat goes as T^3.

5. *Dislocations.* A dislocation is an extended three dimensional defect in a crystal lattice. The two main types of dislocations are edge dislocations and screw dislocations. An edge dislocation occurs when an extra partial atomic plane is inserted into the lattice. This causes a line of strain in the lattice parallel to the edge of the half plane of atoms. A screw dislocation can be thought of as a shift in the lattice sites between crystal planes resulting from a shear stress in the lattice. This again causes a line of strain in the lattice, however it is perpendicular to the stress caused by 'twisting' the lattice. In both cases, the scattering of phonons due to the induced strain field is analogous

to Rayleigh scattering off of a cylinder. The thermal conductivity can therefore be found to be proportional to T^2 [44].

6. *Stacking faults.* Similar to a dislocation, a stacking fault is a three dimensional defect where the periodic layers of atoms in a crystal are disturbed. Unlike a dislocation which has an endpoint within the sample, a stacking fault is a shift in the lattice sites extending across the entire sample. In this sense, a stacking fault can be thought of as a plane separating two halves of the crystal where the lattice sites are shifted relative to each other. When a phonon scatters from a stacking fault, the component of the momentum in the plane of the fault is conserved. That is, the phonons specularly reflect from the defect plane. It has been shown that the scattering rate of such a scattering process is quadratic in temperature and thus the conductivity is proportional to T [44, 47].

A brief reference table summarizing the conductivity temperature dependence for the various phonon scattering mechanisms is given in table 2.1. A more detailed discussion of phonon scattering mechanisms in both metals and non-metals, see "Low Temperature Solid State Physics" by H. M. Rosenberg [44].

Scattering Mechanism	$\kappa(T) \propto$
Sample boundaries	T^3
Umklapp processes	$e^{\alpha\Theta_D/T}$
Conduction electrons	T^2
Point defects	T^{-1}
Dislocations	T^2
Stacking faults	T^1

Table 2.1: Temperature dependence of the thermal conductivity for various phonon scattering mechanisms [44].

Matthiessen's Rule

When considering many sources of phonon scattering, it is often advantageous to examine the thermal resistance, $W \equiv 1/\kappa$, rather than thermal conductivity. The thermal resistances resulting from the various phonon scattering mechanisms can then be added analogous to electrical resistors in series. Thus, $W_{\text{Total}} = W_{\text{B}} + W_{\text{U}} + W_{\text{PD}} + ...$ Writing this in terms of thermal conductivity, using equation (2.8) we get Matthiessen's rule:

$$\frac{1}{\kappa_{\text{Total}}} = \sum_i \frac{1}{\kappa_i} = \frac{3}{c_{ph} v_s} \sum_i \frac{1}{l_i} \tag{2.26}$$

where l_i are the phonon mean free paths associated with boundary scattering, Umklapp processes etc. as discussed in section 2.2.3. The relevant κ_i are listed in table 2.1.

General behaviour at low temperatures: $T \to 0$ K

Recall that as the temperature approaches absolute zero the phonon mean free path increases and is eventually limited by the sample boundaries. This leads to a T^3 temperature dependence to the thermal conductivity, coming from the cubic temperature dependence of the specific heat. Thus, the low temperature conductivity of a metallic sample can be written as $\kappa = AT + BT^3$, where AT is the linear electronic term. An instructive way to plot the thermal conductivity of a metal is to plot κ/T versus T^2, which should be linear in a clean metallic system. When plotted in this manner, the electronic and phonon contributions can both be easily extracted by considering the $T = 0$ K intercept and the slope of the line respectively. Quite often when measuring a clean metallic samples at such a low temperatures, the electronic term dominates the conductivity, and it becomes very difficult to determine the lattice contribution. If we instead consider an electrically insulating system, then the cubic phonon temperature dependence becomes much easier to examine. The inclusion of disorder, which is present in any real system, tends to reduce the conductivity resulting is a sub-T^3 temperature dependence. The conductivity can then be fitted using Matthiessen's rule to estimate the scattering rates from the various scattering mechanisms.

General behaviour at intermediate temperatures: $T \sim \Theta_{\mathbf{D}}/20$

At temperatures comparable to the Debye temperature, phonon-phonon scattering becomes appreciable. Recall that the thermal resistivity due to Unklapp scattering is proportional to $e^{\alpha \Theta_{\text{D}}/T}$, which increases with temperature exponentially. Thus, the thermal conductivity will exhibit a peak at approximately $T \approx \Theta_{\text{D}}/20$ where the phonon mean free path transitions from being limited by the sample boundaries and other defects at low temperature to being dominated by Umklapp processes at temperatures closer to the Debye temperature [48, 49, 50]. This is true in general for insulating materials. The magnitude and shape of the peak conductivity is strongly dependent on disorder in the lattice. Imperfections in the crystal lattice, such as dislocations and stacking faults, increase the thermal resistance, suppressing the magnitude of the peak conductivity. Fitting the conductivity in this temperature range can provide an estimate of the relative amount of disorder between various samples.

Chapter 3

Measurement Details

3.1 Thermal Conductivity

As we have seen in chapter 2 the thermal conductivity, κ, is defined as the ratio of the applied heat to the temperature gradient across a sample. In practice the thermal gradient is established by affixing one end of the sample to thermal ground (the fridge) and the other to a metallic resistive heater. Passing a known current through the resistive heater produces a known amount of heat due to Ohmic heating ($Q = I^2R$). The thermal gradient is measured using two semiconducting resistors, whose resistance is strongly dependent on the temperature, positioned a distance l apart on the sample. The thermal conductivity can then be calculated via:

$$\kappa = -\frac{Q}{T_2 - T_1} \cdot g \tag{3.1}$$

where g is the geometric factor defined as the ratio of the length of the sample to its cross-sectional area.

Figure 3.1 shows a basic schematic of the one-heater-two-thermometer method used to measure thermal conductivity. In this arrangement, the electrical conductivity can be measured in parallel with the thermal conductivity using the thermal leads as voltage and current electrical contacts. The thermometers are uncalibrated semiconducting resistors and are thus calibrated *in situ* against the fridge temperature every temperature sweep. This technique is also done when performing field sweeps at constant temperature, which provides a magnetoresistive correction for the thermometers. At each temperature step, a calibration point is acquired while the heat is off allowing the thermometers to thermally equilibrate with the fridge. Another point is then recorded with the sample heater turned

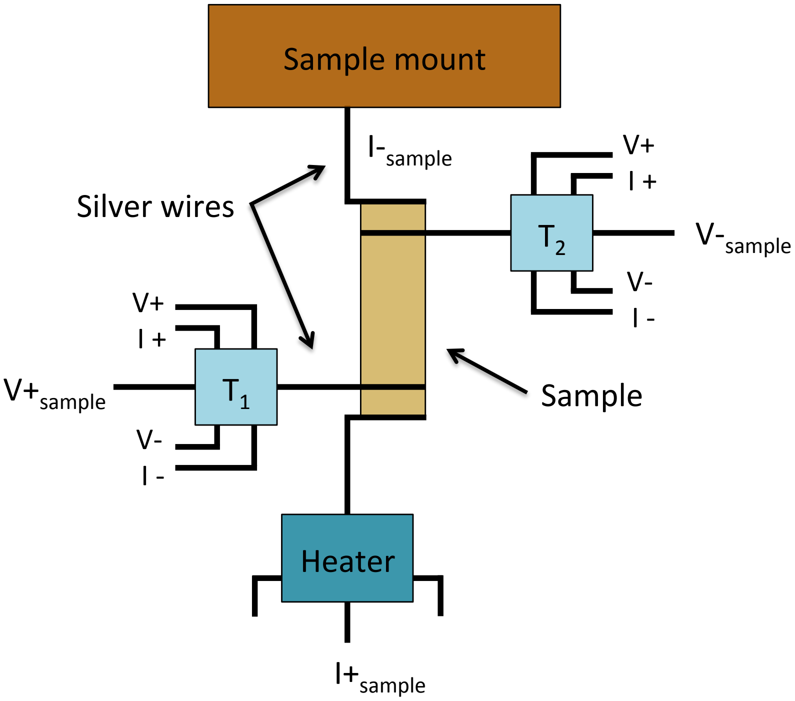

Figure 3.1: Schematic drawing of a thermal conductivity measurement.

on to measure the temperature gradient across the sample. The calibration curve is formed by fitting the heat off points using a Savitzky-Golay filter, which is typically a third order polynomial fit over a window of 15 to 20 points. The calibration curve can then be used to convert the resistance values measured when the heater is on to corresponding temperature values, which subsequently determine the thermal gradient.

3.1.1 Thermal Conductivity Device

So far, we have been concerned with the practical aspect of performing thermal conductivity measurements. In this section, we will explore the issues involved with physically implementing a thermal transport measurement. A thermal conductivity device is comprised of three main components: the thermometers and heater, the mount, and the wiring [51]. Each of these components are designed in such a manner as to maximize the signal-to-noise ratio and will now be discussed.

The Thermometers and Heater

Uncalibrated semiconducting resistors are used as the sample thermometers due to their highly temperature dependent resistance. It is important to choose resistors which have a high sensitivity in the temperature region of interest. So, 1 kΩ RuO_2 resistors are used for measurements below 1 K, and cernox resistors are used between 1 K and 100 K. In this section, we will focus on the sub 1 K regime. When constructing a thermometer, there are a few techniques which help ensure good thermal contact between the thermometer and the sample, improving the overall effectiveness of the thermometer. First, the substrate on which the RuO_2 is deposited is thinned down from 800 μm to approximately 300 μm. This reduces the heat capacity of the thermometer decreasing the time required for thermal equilibration. The most effective ways of making thermal contact to one of these thermometers is through the electrical leads. To do this, a 25 μm silver wire is coiled onto a 300 μm silver wire rod wrapped in a layer of 7 μm Kapton film (from DuPont). The rod is epoxied onto the backside of the substrate along with a 25 μm silver wire to make contact to the sample. The coiled silver wires are affixed to the gold contacts on the RuO_2 resistor using silver epoxy. Coiled PtW wires are soldered onto the opposite ends of the silver wire coils for electrical contact. An image of a completed thermometer is seen on the left in figure 3.2.

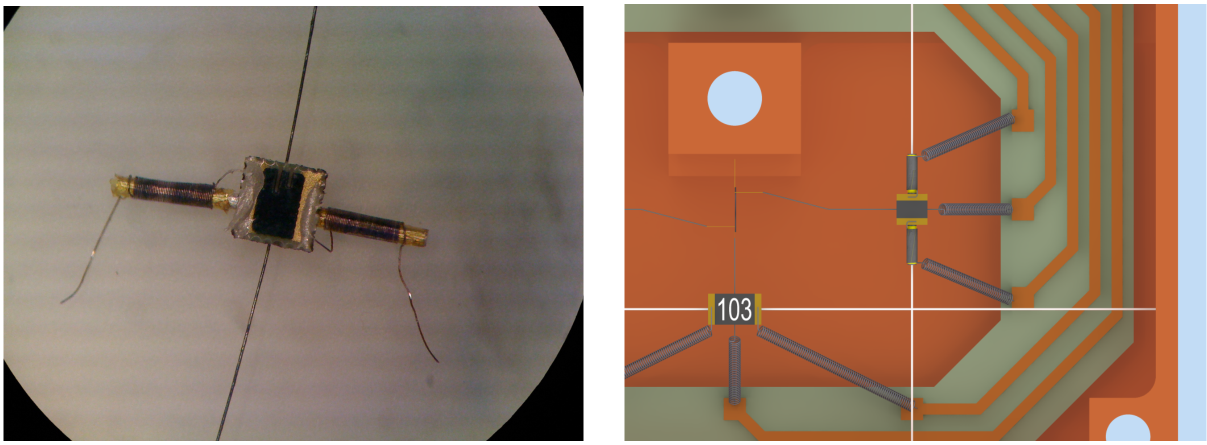

Figure 3.2: A digital image (left) of a thermometer prior to affixing PtW wires to the end of the Ag wires coiled around the Ag rod. A computer rendered image (right) of one of the sample thermometers and the sample heater mounted on nylon filaments in the copper box.

The Mount

The mount supports the sample, thermometers and heater needed to make a conductivity measurement. The entire thermal conductivity device used here is built into a copper box (figure 3.3) which acts as a miniature Faraday cage to locally shield the measurement from electromagnetic interference (EMI). The copper box construction also provides the much needed mechanical stability. The usefulness of a device is often closely related to its longevity. The two areas that must be addressed are the treatment of the 14 wires (4 wires for the hot thermometer, 4 wires for the cold thermometer, 2 wires for the heater and 4 wires for the sample resistance) needed to perform a thermal conductivity measurement and the protection of the delicately balanced thermometers, heater and sample.

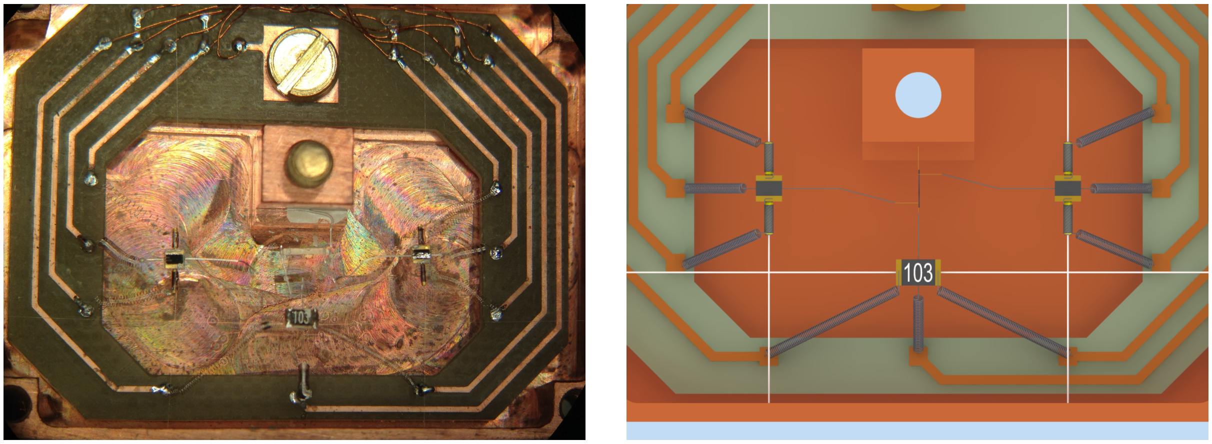

Figure 3.3: A digital image (left) and a computer rendered image (right) of the printed circuit board with both thermometers and heater mounted and soldered to the PCB.

The coils from the thermometers and the heater are soldered directly to a printed circuit board (PCB) which collects all the leads together at one end of the mount. A PCB is used because it is the most efficient and orderly method of handling the leads from the thermometers and heater while preventing any damage of the wires and conforming to the strict size constraints.

The Wiring

Proper handling of the wiring between the conductivity device and the resistance bridge at room temperature is essential for low noise measurements. Choosing appropriate cables and connectors will also improve signal quality as well as the mechanical stability. A ribbon cable (product code: A8-311 from Oxford Instruments) comprised of 12 twisted pairs is soldered to the PCB in the copper box device. Twisted pairs are used since they minimize noise caused by EMI. This is because the EMI induced in one wire is cancelled out by the equal and opposite EMI induced in its twisted pair. The ribbon cable is also affixed to the mount with a small amount of epoxy resulting in a sturdy joint between the two. The ribbon cable is a prime candidate for handling many small wires while maintaining mechanical stability since any strain on the cable is managed by the cotton ribbon and the wires are left unharmed. The other end of the ribbon cable is soldered into a micro-D connector (part number: MDM-25 SSB from ITT Cannon). A block of epoxy (STYCAST 2850FT Black from Emerson & Cumings) is then cast on the back of the micro-D connector to minimize the chance of breaking wires and to maximize the overall strength of the cable-connector junction. An image of the completed box and cable assembly is seen in figure 3.4.

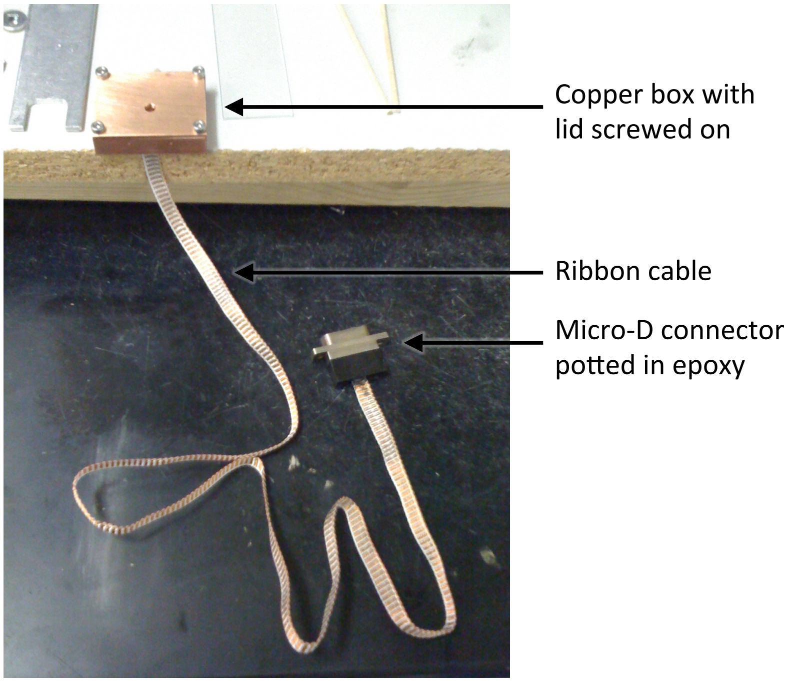

Figure 3.4: Completed thermal conductivity box with the lid screwed on and the 12 twisted pair ribbon cable stemming out the bottom terminating at the epoxied micro-D connector.

A well shielded, low voltage Fischer connector is used at the top of the fridge. The cable from the Fischer connector directly enters a ground isolating, RF shielded box (figure 3.5) where the signal is filtered using multiple low pass filters, removing any unwanted high frequency noise. This box is also used to separate the group of wires from both thermometers and the sample resistance measurement and outputs each to 5-pin bayonet connectors used by the LR-700 resistance bridge multiplexer. The current leads for the sample heater is also located on this box as a pair of BNC connectors. Since the shielded box is not electrically connected to the fridge, we can choose where to ground it in order to avoid ground loops. This provides excellent shielding from RF noise outside the cryostat.

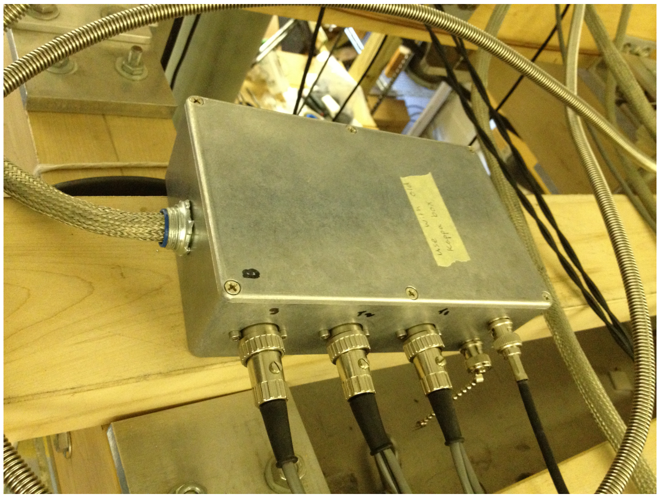

Figure 3.5: Shielded breakout box at the top of the dilution fridge routing the 24 wire cable through several low pass filters then on to three 5 pin bayonet connectors and 2 BNC connectors.

Proper grounding of the metallic braided sheath surrounding the cables is essential. The entire system must be grounded through a single point and branch out from there to avoid ground loops. Ground loops arise when two or more points in the system that should be at the same potential are not. This is often because they are grounded through two different paths (ie. through a water pipe and through the grounding rod in the bottom of the pit). This leads to a small current in the grounded sheath which is a major cause of noise and interference in the circuit. Improper grounding can be a serious problem when trying to achieve the lowest base temperature possible and thus should be addressed accordingly.

Computers are inherently electrically noisy machines. However, they are needed to run the experiment and to acquire data. Thus, it is necessary to electrically isolate the computer from the rest of the scientific equipment such as the resistance bridge used in measuring the sample thermometers. This is done via optical isolation. The electrical signal from resistance bridge is converted to an optical signal, which is transmitted through a fibre-optic cable and is then converted back to an electrical signal to be acquired by the computer. Essentially, optically isolating the computer from the measurement equipment will only allow the transmission of the desired signal between the two, isolating the noise associated with the computer.

3.1.2 Contact Resistance

One of the major challenges involved with performing thermal transport measurements at ultra low temperature is making good thermal contact between the sample and the heater, thermometers and sample mount. The contact resistance can often be assumed to be on the order of a few milli-Ohms for well behaved metallic samples, such as silver, where the thermal conductivity is dominated by electrons. This is because good thermal contact can be made by making good electrical contact to the sample since the dominant thermal transport mechanism is electronic. However, in insulators, or other samples where the surface is particularly susceptible to oxidization, making high quality thermal contacts becomes increasingly difficult since the heat is transferred through phonons which are scattered at interfaces. The ramifications involved with poor thermal contacts are discussed below.

For instructive purposes, we will consider a metallic sample ($\kappa \sim T$) in the limit of low contact resistance and in the case of an exaggerated thermal resistance at the sample boundaries due to the acoustic mismatch of phonons (Kapitza resistance) [52]. In this model, the boundary resistance is described by a T^{-3} temperature dependence [53]. A simplified schematic of such a thermal conductivity measurement is seen in figure 3.6. The blue line shows the normalized temperature along the length of the sample which has low contact resistance. The red line represents a sample with a large contact resistance. The magnitude of the contact resistance between the sample and the thermal ground (the fridge in this case) is estimated by the ratio of the difference between the cold thermometer (T_2) and the fridge temperature (T_o) to the temperature drop across the sample (ΔT). For an ideal system, this ratio should remain small, less than unity. Figure 3.7 (b) shows the contact resistance versus temperature for a sample with poor contacts.

There are two main complications that arise due to poor thermal contacts. First, when the contact resistance becomes comparable to the thermal resistance of the sample, the temperature drop between the heater and sample, or between the sample and the thermal ground becomes large. This reduces the thermal gradient across the sample relative to the average temperature, lowering the sensitivity of the measurement. A rule of thumb is to maintain $\Delta T/T_\mathrm{avg} \sim 10\%$, figure 3.7 (c) shows how this ratio is diminished at low temperature when the contact resistance is high. Second, attempting to enhance the relative

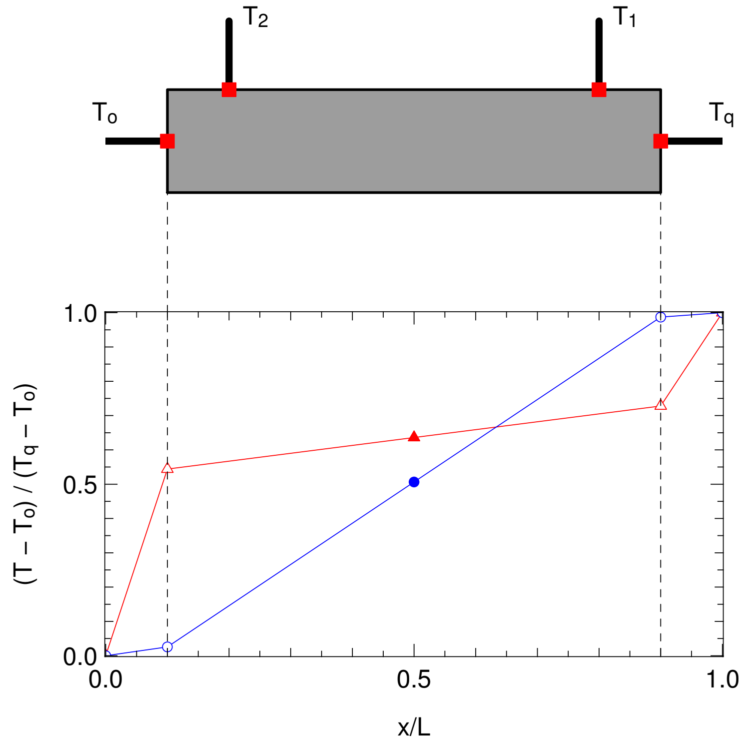

Figure 3.6: The temperature along the length of a sample with good thermal contacts (blue) and poor thermal contacts (red) to the heater and sample mount. The filled symbol is the average sample temperature.

temperature gradient across the sample by increasing the applied heat will simultaneously raise the average temperature of the sample, as illustrated by the solid symbols in figure 3.6. This effectively sets a minimum achievable temperature. Figure 3.7 (a) shows the average sample temperature versus the fridge temperature for a sample with poor contacts. Notice how T_{avg} plateaus at low temperature even though the fridge continues to cool. These two issues are often the limiting factors for ultra low temperature thermal transport measurements of many samples with poor contacts.

There are a number of methods to improve the thermal contacts. First, increasing the physical size of the contact will lower the contact resistance. However, doing this will certainly increase the uncertainty of the geometric factor of the sample (the length to cross sectional area ratio), which subsequently increases the systematic error in the magnitude of the measured conductivity. Additionally, this may not be possible for small samples, where the limited sample length imposes a hard limit on the size of the contacts. If the poor

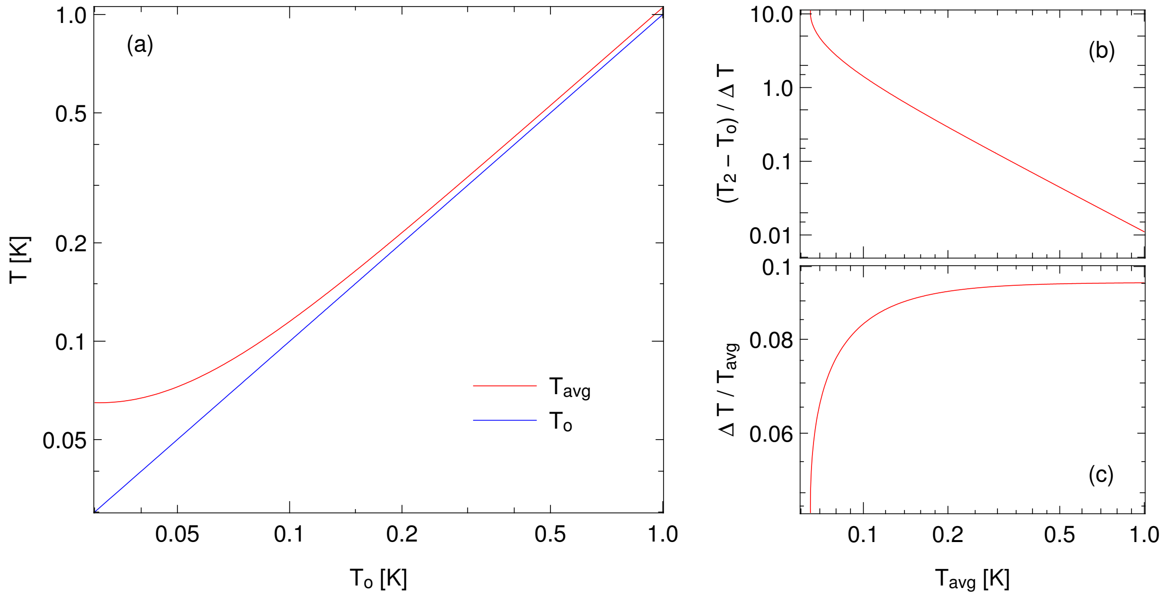

Figure 3.7: (a) Average sample temperature for a sample with poor thermal contact (red line) plotted versus the fridge temperature (blue line). (b) The contact resistance relative to the thermal resistance of the sample. (c) The normalized thermal gradient as a function of average sample temperature.

contact resistance is a result of an insulating oxide layer on the surface of a metallic sample, high quality contacts can be prepared by first etching the surface of the sample with ions, followed by depositing gold or platinum contacts directly onto the sample. The leads can then be spot welded to these contacts forming very low resistance contacts. Although this method produces high quality contacts, it is a non-trivial task and requires considerable effort. Thus, it is only utilized if necessary to accurately measure the thermal transport at ultra low temperatures. Finally, maximal thermal contact to the sample mount it achieved by affixing the end of the sample to a block of oxygen-free, high-conductivity copper using silver epoxy which increases contact area and provides mechanical robustness. The copper block is then mounted into the thermal conductivity device using silver paint. If the sample dimensions are on the order of 100 μm or less, then it becomes very difficult to epoxy onto a copper block. In this case, the sample is affixed to a 50 μm gold wire which is then attached directly to the conductivity mount using silver paint.

3.2 Magnetostriction

Magnetostriction describes the change in length of a sample as a function of field. The coefficient of magnetostriction (λ) is defined as the change in sample length (L) with temperature normalized by the zero field length so that

$$\lambda = \frac{1}{L_\mathrm{o}}\frac{\partial L}{\partial B}. \tag{3.2}$$

However, it is often useful to consider $\Delta L/L_o$ as a function of field, rather than the derivative, as it can reveal many details of the underlying spin system.

Magnetostriction is measured using a device called a dilatometer which measures minute changes in the length of a given sample. A dilatometer works on the principle that the capacitance (C) of a parallel plate capacitor is inversely proportional to the plate separation (d) via

$$d = \frac{\epsilon_o A}{C} \tag{3.3}$$

where A is the plate area and $\epsilon_o = 8.85 \cdot 10^{-12}$ F/m is the permittivity of free space. Essentially, a dilatometer is a parallel plate capacitor where one plate is fixed, and the other is affixed to the sample. As the sample expands or contracts co-linearly with the axis of the device, the capacitance changes accordingly. The capacitance can be measured to a precision of 10^{-7} nF via a high precision capacitance bridge (Andeen-Hagerling 2500A), corresponding to sub-angstrom changes in length! The following section covers a number of design features of the compact dilatometer used here.

3.2.1 Compact Dilatometer

As noted above, the dilatometer is little more than a parallel plate capacitor and thus is a fairly simple device [54]. There are three features that the dilatometer must have in order to be effective. First, the capacitor plates must be polished to have a mirror finish, second, the “floating” capacitor plate must be suspended by a leaf spring system and third, electrical isolation of both capacitor plates. To reduce the minimum plate separation, it is important that the plates be as flat as possible. Small irregularities in the surface of the capacitor plates can cause non-uniform electric fields which affect the capacitance measurement or even cause the plates to short when the plate separation is small. To avoid this, the plate surfaces are first machined to the highest achievable tolerance on a lathe, and then polished by hand using 1500 grit sand paper, followed by a polishing pad. This results in a mirror finish on the capacitor plates. Once the capacitor plates have been polished, they can be mounted in the device. A brass screw is inserted into a threaded hole on the back of the fixed plate with a couple of sapphire washers in place to electrically isolate it from the dilatometer shell. A sapphire rod is epoxied into a hole on the back of the floating plate. This rod is then inserted through two beryllium-copper leaf springs which allows for over 200 μm of linear motion of the floating plate. The force on the sample from the spring is approximately 0.6 N at a deflection of 80 μm. The sapphire rod is then in direct contact with the sample, so as the sample expands or contracts, the floating plate will move towards, or away form the fixed plate. Sapphire is used for two reasons. First it is insulating, which allows for both capacitor plates to be electrically isolated from each other and from the grounded body of the dilatometer. Second, since it is crystalline, its thermal expansion is highly reproducible, allowing for a simple subtraction of the cell effect. This is also explains the minimal use of epoxy along the measurement axis. Finally, the entire dilatometer assembly is held together by brass screws. The thermal expansion of brass is larger than that of copper, thus, as the temperature is lowered, the brass screws contract more than the copper device. This results in the screw holding the device firm at low temperatures. An image of the compact copper dilatometer can be seen in figure 3.8.

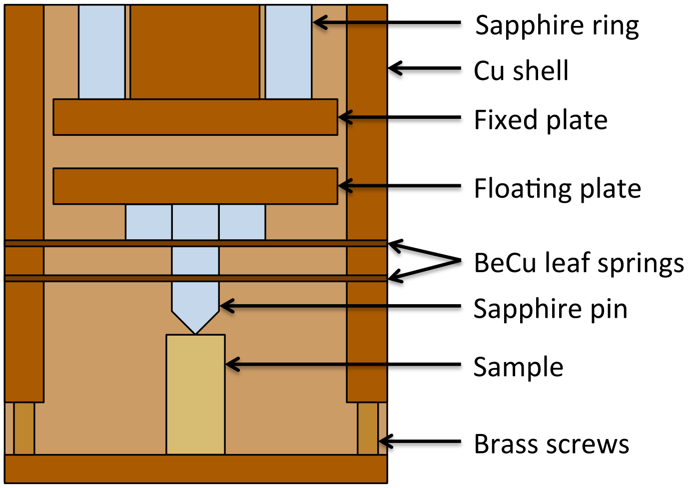

Figure 3.8: Schematic of a compact copper dilatometer.

The parallel plate capacitor equation from equation 3.3 is accurate when the plate separation is large. However, due to small misalignmnets when assembling the device, the plates may be slightly tilted with respect to one another. The parallel plate equation can be modified to account for the tilted plates via

$$d = \frac{\epsilon_o A}{C}\left(1 + \left(\frac{C}{C_{\max}}\right)^2\right) \tag{3.4}$$

where $C_{\max}$ is the maximum capacitance just before the plates short [55]. In the device used here, the maximum capacitance attainable before the plates short can be as high as 130 pF, which corresponds to a plate separation of 8 μm, since the effective surface area of the capacitor plates is 114 mm^2. Thus, the relative tilt in the capacitor plates can be approximated to be on the order of 8 μm.

Chapter 4

Cryogenic Techniques

4.1 Introduction

Our ability to observe and understand many phenomena in nature often relies on our ability to perform measurements at temperatures approaching absolute zero. High temperature thermal fluctuations can convolute the individual contributions to many thermodynamic quantities. Low temperature measurements allow us to reliably isolate each contribution, for example, the electronic and phononic channels of heat conduction. In addition to this, many exotic phases of matter occur at low temperatures due to weak interaction strengths, including the spin-ice state in rare-earth titanates, topological insulating states and superconducting states. Achieving these extremely low temperatures is a non-trivial task. There are many cryostats available to achieve varying base temperatures; each with their advantages and draw-backs. An early method of cooling consisted of merely submerging the system in a bath of a cryogenic liquid. A very well known example of this is from 1911 when Dutch physicist Kamerlingh Onnes discovered superconductivity in mercury at 4.2 K. He observed a vanishing resistivity in a mercury wire when submerged in liquid helium-4. A major drawback of this rudimentary technique is the base temperature is determined by the boiling temperature of the liquid, 4.2 K in the case of liquid helium-4. Other more sophisticated techniques such as the adiabatic demagnetization of a paramagnetic salt can achieve a much lower base temperature without the use of any cryogenic liquid, however these temperatures are only sustainable for a short time, on the order of hours. The two main cooling methods used in this thesis take advantage of some very clever techniques used to cool liquid helium (both pure ^{4}He and a ^{3}He-^{4}He mixture) well below its boiling point. The first method utilizes evaporative cooling of liquid helium-4 via a 1 K pot system (described below). The helium-4 pumped probe has a large temperature range from room temperature to 1 K and is relatively easy to use. In order to achieve even lower temperatures, we use a ^{3}He-^{4}He dilution fridge, which can theoretically be cooled to a few thousandths of a degree above absolute zero. Both of these techniques will now be discussed in detail.

4.2 Helium-4 Cryostat

4.2.1 Evaporative Cooling

Let us start by considering how to boil a volume of liquid water. One option would be to increase the temperature of the water until it reaches its boiling point under ambient pressure by adding heat via a kettle. Another method is to place the vessel of water in a vacuum chamber. When the external pressure above the liquid water is lowered below its vapour pressure, the liquid water will begin to vaporize. However, since the liquid-gas transition of water is a first order phase transition, there will be an associated latent heat of vaporization. Thus, without adding any additional thermal energy, the water will draw the heat required for vaporization out of the environment, lowering the overall temperature of the system. Now in this case, the water will eventually freeze into a solid below the triple point, but will continue to cool by sublimating vapour. We can take advantage of this evaporative cooling and the free expansion of gas to achieve low temperatures on the order of 1 K by pumping on a cryogenic liquid, liquid helium-4 for example.

4.2.2 1-K Pot

Pumping on the top of a bath of liquid helium-4 will certainly lower the temperature of the system below its boiling point at 4.2 K, reaching a temperature close to 1 K. As it turns out, this is not the most economical solution for lowering the temperature because about 40% of the liquid ^{4}He must be evaporated to cool from 4.2 K to 1.3 K due to the increasing heat capacity of ^{4}He at these temperatures. An alternative technique to pumping on the entire helium bath is to pump on a small volume of liquid in a vessel called a 1-K pot. The 1-K pot is continuously filled though an impedance connected to the main bath. This impedance is variable on our system since it is mediated by a finely tuned needle valve. This method had a number of advantages over pumping on the entire bath. One, the 1-K pot is much more effective at cooling the system through the use of metallic heat exchangers, whose heat capacity is much lower than liquid ^{4}He. Thus it requires much less evaporated liquid to lower the temperature to approximately 1 K. Two, the cooling power can be altered by varying the amount of liquid in the 1-K pot, allowing for a wide range of operational temperatures, ranging from 1 K to room temperature. This would be quite inefficient if the system was directly submerged in a bath of liquid helium. Three, this method can be run continuously, since the 1-K pot is only coupled to the main bath though an impedance, the main bath remains at atmospheric pressure and 4.2 K. This allows us to refill the helium bath without interrupting the experiment.

A similar technique can be implemented using liquid helium-3 which can reach temperatures approaching 200 mK. Running in continuous mode requires the system to be a closed loop. This means the pumped helium-3 vapour is recovered and re-liquified then fed back into the pumping chamber. These systems are considerably more expensive than a regular 1-K pot system since the helium-3 isotope is much less abundant than helium-4 and is proportionately reflected in the cost.

We will now examine the components that a 1-K pot system is comprised of.

4.2.3 1-K Pot Design

A helium-4 pumped probe, or 1-K pot, is a rather simple device. It consists of four main components: the vacuum can, the impedance, the vacuum pump and the 1-K pot vessel. These components can been seen in figure 4.1 which is a schematic illustration of a 1-K pot system. I will now briefly discus the four main components.

1. *Vacuum can.* The entire 1-K pot system is encapsulated in a vacuum. This is done for thermal isolation from the main bath, which is kept at 4.2 K, allowing for the temperature to be controlled at the desired set point. The vacuum seal on the can is conical, forming a metal on metal seal with a complementary conical taper on the bottom of the probe. A small amount of Dow Corning high vacuum grease is applied to the seal to help maintain a good vacuum. A leaky seal at low temperatures will result in a poor base temperature, as the helium in the vacuum will act as an exchange gas with the 4.2 K helium bath and the experimental system.

2. *The impedance.* The 1-K pot is filled with helium from the main bath through an impedance tube. This throttles the helium boil off as well as the cooling power by limiting the amount of helium allowed into the vessel. The impedance can be fixed if it is implemented by flowing the liquid through a fine capillary which is blocked

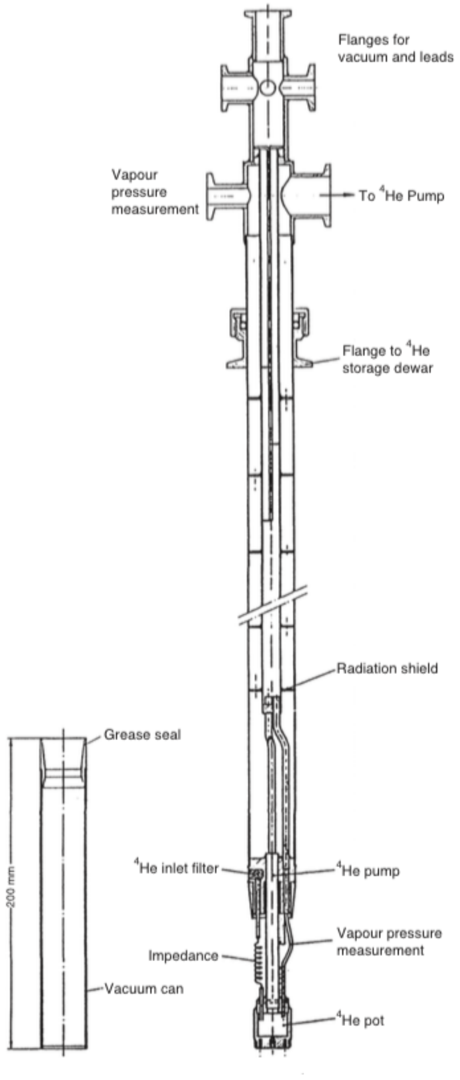

Figure 4.1: Schematic drawing of a 1-K pot system [56].

further by inserting a tight fitting wire into it. Impedance capillaries of this type are on the scale of tens of centimetres long, which need to be wound into coils to fit inside the vacuum can. The impedance can equally be set via a finely tuned needle valve, as in the case of our system. The impedance, Z is determined by the following relation

$$Z = \Delta P/\dot{V}\eta \tag{4.1}$$

where ΔP is the pressure differential across the impedance (from 1 bar in the bath to approximately 1 mbar in the 1-K pot), $\dot{V}$ is the flow rate and η is the viscosity. We can estimate the impedance required in order to run a 1-K pot system continuously (without flooding the 1-K pot or pumping it dry) with 5 mW of cooling power at 2 K by first considering latent heat of evaporation of helium-4 at 2 K. The latent heat of evaporation at 2 K is approximately 91 J/mol [56], thus a flow rate of $5.5 \cdot 10^{-5}$ mol/s is needed to achieve 5 mW of cooling. If the pressure is 1 mbar in the 1-K pot, and 1 bar at the pump, and the viscosity of helium-4 at 2 K is approximately $2.0 \cdot 10^{-11}$ bar/s [57, 58], then the required impedance to run continuously is on the order of $3.3 \cdot 10^{13}$ cm^{-3}. Since the impedance is so high, it is crucial that no contaminants enter the impedance at any time such as nitrogen, which solidifies at 63 K. To ensure that the impedance does not get blocked, it is essential to back flow helium gas through the capillary when cooling. This limits the possibility of nitrogen gas entering the capillary when initially cooling the probe. Additionally, the use of a filter at the impedance inlet made of fine copper powder will keep small pieces of frozen nitrogen in the bath from entering the capillary.

3. *Vacuum pump.* The 1-K pot is usually connected to a mid-size rotary pump capable of a throughput on the order of 10^{-4} mol/s. This flow rate is appropriate to sustain a good base temperature when the system is running continuously. The pump is connected to the top of the probe via a flexible bellows which is then connected to the 1-K pot through a central pumping line inside the probe. The vibrations from the pump can be dampened by pinning the bellows with a bag of lead shot.

4. *1-K pot vessel.* The 1-K pot is where the cooling power originates as it is where the evaporative cooling takes place. Its volume is usually on the order of 10 cm^3 and is located inside of the vacuum can. The cooling power of such a system is approximately 5 mW. The base temperature will be determined by balancing the heat load with the cooling power and is approximately 1 K, which is where the name is derived.

4.3 ^{3}He-^{4}He Dilution Refrigerator

4.3.1 ^{3}He-^{4}He Phase Separation

A ^{3}He-^{4}He dilution refrigerator is the most common system for achieving sustained temperatures below 300 mK. The mechanism of cooling in a dilution refrigerator is quite different from the helium-4 pumped probe described above. A 1-K pot system relies on the entropic change caused by mechanically driving a first order phase transition, whereas a dilution fridge depends on the difference in enthalpy between a helium-3 rich phase and a helium-3 dilute phase. A fascinating consequence of the dilution process is that the cooling power persists down to absolute zero due to the finite solubility of ^{3}He in ^{4}He. This non-vanishing cooling power allows for the realization of a sustained base temperature on the order of 10^{-3} K depending on the heat load and effectiveness of the heat exchangers.

Pure helium-4 becomes superfluid at 2.17 K. Pure helium-3, on the other hand, shows no sign of a phase transition in the temperature range of interest here. As a side note, it was later shown to also enter a superfluid phase at a much lower temperature of approximately 2.5 mK. Increasing the helium-3 concentration in a ^{3}He-^{4}He mixture lowers the superfluid transition temperature until a concentration of 67.5%, where the superfluid phase is fully suppressed at a maximum temperature of 0.87 K. Below this temperature, the Lambda line meets a forbidden region on the ^{3}He-^{4}He phase diagram (figure 4.2) where the mixture separates into a ^{3}He rich phase and a ^{3}He dilute phase. As the temperature approaches absolute zero the ^{3}He rich phase becomes pure but the ^{4}He rich phase will retain a constant ^{3}He concentration of 6.6% at saturated vapour pressure, even at 0 K! Taking advantage of this residual ^{3}He concentration in the ^{4}He rich phase is the key to achieving such low temperatures. Due to its lower density, the ^{3}He rich phase will float on top of the ^{3}He dilute phase. If we maintain the ^{3}He dilute phase at a temperature of approximately 0.7 K then the ^{3}He vapour pressure is about three orders of magnitude larger than that of the ^{4}He. Thus, pumping on this phase will draw ^{3}He atoms out of the dilute phase resulting in a less than 6.6% ^{3}He concentration, which is out of equilibrium. ^{3}He atoms from the rich phase will then cross the phase boundary into the dilute phase to maintain the 6.6% concentration. The act of crossing this phase boundary results in a positive enthalpy change which causes the system to cool. The ^{3}He vapour that is pumped away is then circulated and re-condensed into the ^{3}He rich phase.

We can approximate the cooling power at 30 mK by considering the heat of mixing, which is defined as

$$\dot{Q} = \dot{n}\left[H_{\mathrm{d}}(T) - H_{\mathrm{r}}(T)\right] \tag{4.2}$$

where $\dot{n}$ is molar flow rate of ^{3}He atoms from the rich phase to the dilute phase. Since the enthalpy is given by

$$H(T) - H(0) = \int_0^T C(T')\mathrm{d}T' \tag{4.3}$$

we require that the molar heat capacity, $C(T)$, of ^{3}He in the dilute phase be greater than in the rich phase for cooling to occur. The heat capacity of pure helium-3 has been measured

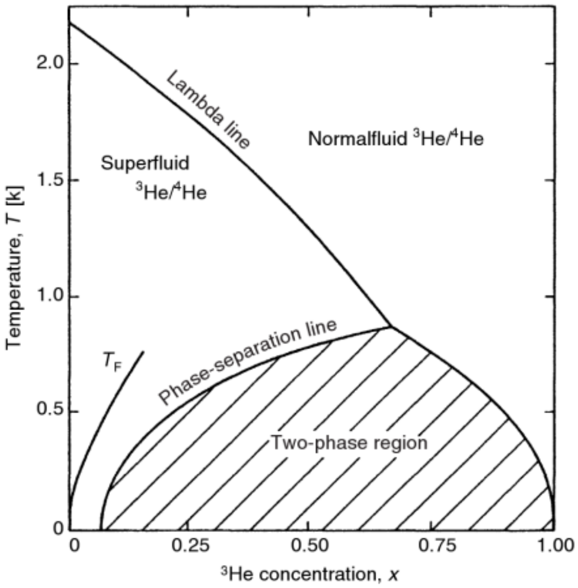

Figure 4.2: ^{3}He-^{4}He temperature versus ^{3}He concentration phase diagram [56].

to be $C_\mathrm{r} \simeq 22T$ J/mol(^{3}He) K below 40 mK [59, 60]. Thus, the enthalpy is calculated to be $H_\mathrm{r}(T) = H(0) + 11T^2$ J/mol. The specific heat of the helium-3 atoms in the 6.6% dilute phase can be approximated by assuming it behaves as a weakly interacting Fermi-liquid. This yields $C_\mathrm{d} \simeq 106T$ J/mol(^{3}He) K [61, 62, 56]. The chemical potentials of these two phases are required to be equal in thermodynamic equilibrium where $\mu = H - TS$. From this, we have

$$H_\mathrm{r} - TS_\mathrm{r} = H_\mathrm{d} - TS_\mathrm{d} \tag{4.4}$$

which is rearranged to yield $H_\mathrm{d} = H(0) + 95T^2$ J/mol. Therefore, the cooling power associated with helium-3 atoms crossing the phase boundary into the dilute phase at a rate of $\dot{n}$ is $\dot{Q} = 84\dot{n}T^2$ W. If we estimate the flow rate of helium-3 atoms to be $\dot{n} = 100$ μmol/s, then the cooling power at 30 mK is approximately 10 μW.

4.3.2 Dilution Refrigerator Design

Although the cooling mechanism of a dilution fridge may seem similar to a 1-K pot system in principle, its operation is considerably more involved. To learn how a dilution fridge works in practice, I will introduce the various components involved and the procedure to run a fridge. There are six main components in a dilution fridge: the mixing chamber, the still, the vacuum pumps, the cold traps, the 1-K pot and the heat exchangers. A schematic drawing of a dilution fridge is featured in figure 4.3.

1. *Mixing chamber.* The mixing chamber is where the helium-3 rich and dilute phase separation boundary resides and hence where helium-3 atoms cross the phase boundary into the helium-3 dilute phase in order to maintain the 6.6% concentration. Thus, the mixing chamber is where the cooling power originates and is therefore where your experiment must be well thermally anchored.

2. *Still.* After the ^{3}He-^{4}He mixture has phase separated at low temperatures, the ^{3}He rich phase will float on top of the ^{3}He dilute phase due to the lower density of the ^{3}He atoms. Since the phase separation boundary is located in the mixing chamber, a tube connects the bottom of the mixing chamber to the still. This allows the dilute phase to flow into the still, while remaining thermally isolated from the mixing chamber. The still is kept at about 0.7 K with the use of a small resistive heater. This promotes the circulation of the ^{3}He by increasing its vapour pressure to a value approximately 1000 times larger than for ^{4}He at this temperature. Removing ^{3}He atoms from the dilute phase in the still via a high throughput mechanical pump results in a concentration less than 6.6%. Helium-3 atoms from the ^{3}He rich phase then cross the phase boundary in the mixing chamber to maintain the appropriate concentration.

3. *Vacuum pumps.* The effectiveness of the dilution fridge to reach ultra low temperatures is partly limited by how quickly the ^{3}He can be circulated through the system. Thus, a powerful turbo pump, the roots pump, backed by a sealed rotary pump is needed to circulate the ^{3}He atoms. The 1-K pot also requires a rotary pump to cool to 1 K and will be discussed in more detail later.

4. *Cold traps.* The mixture circulation lines in a fridge can be quite small. The return line is particularly narrow as it includes a high impedance tube used to increase the incoming ^{3}He pressure which aids the condensation process. If any other gas, such as oxygen or nitrogen from the atmosphere, or hydrocarbons from the pump oil, were to contaminate the ^{3}He-^{4}He mix, it would freeze in these minuscule openings, eventually blocking the flow completely. Once this happens, the only hope to restart the circulation of the mix is to warm the fridge and pump out the contaminants. This is prevented by the use of two charcoal filters, which clean the mixture by freezing out the contaminants outside of the fridge allowing for easy disposal. One filter, or cold trap, is kept at the boiling point of nitrogen (77 K), and the other is much colder, at

the boiling temperature of helium-4 (4.2 K). The nitrogen cold trap condenses out any nitrogen or oxygen that might have leaked into the system from the atmosphere. The pump oil in the rotary pump can outgas small amounts of hydrocarbons which will be unaffected by the nitrogen cold trap. Thus the use of a helium cold trap is necessary to ensure that only a pure ^{3}He-^{4}He mixture will enter the fridge.

5. *1-K pot.* The purpose of the 1-K pot is to cool the returning ^{3}He to about 1 K, condensing it back into liquid. It is filled though from the main helium-4 bath in the dewar which contains the entire fridge. The 1-K pot is described in detail in the previous section.

6. *Heat exchangers.* Even though the returning ^{3}He is cooled to about 1 K from the 1-K pot, this is still often an order of magnitude hotter than the mixture in the mixing chamber. Thus it must be cooled further before re-entering the mixing chamber. An efficient method to do this is by transferring its heat to the ^{3}He dilute phase on its way to the still to be pumped away. All this takes place throughout several heat exchangers, both continuous and step heat exchangers.

4.3.3 Dewar and vibration reduction

The dilution refrigerator and experiment system is contained in a copper radiation shield which is primarily used to block thermal radiation. Essentially, it provides a thermal barrier at approximately 700 mK between the mixing chamber and the 4 K liquid helium-4 bath surrounding the inner vacuum chamber (IVC). The dewar is comprised of three main chambers: the inner helium bath, the nitrogen jacket, and the outer vacuum chamber. The best form of thermal insulation is to surround the system with a vacuum. This removes any convective heat transfer between the ultra cold experiment and the room temperature laboratory. The only remaining heat transfer mechanism is thermal radiation. Radiative thermal transfer follows the Stefan-Boltzmann law which states that the heat transfer per unit area (P/A) is proportional to the difference in the fourth power of the hot (T_h) and cold (T_c) temperatures such that

$$\frac{P}{A} = \mathrm{e}\sigma\left(T_\mathrm{h}^4 - T_\mathrm{c}^4\right) \tag{4.5}$$

where e is the emissivity of the black body (the inside of the dewar) and $\sigma = 5.67 \cdot 10^{-8}$ $\mathrm{W/m^2K^4}$ is the Stefan-Boltzmann constant. The thermal isolation of the helium bath from the room temperature of the lab is further improved by including a liquid nitrogen jacket.

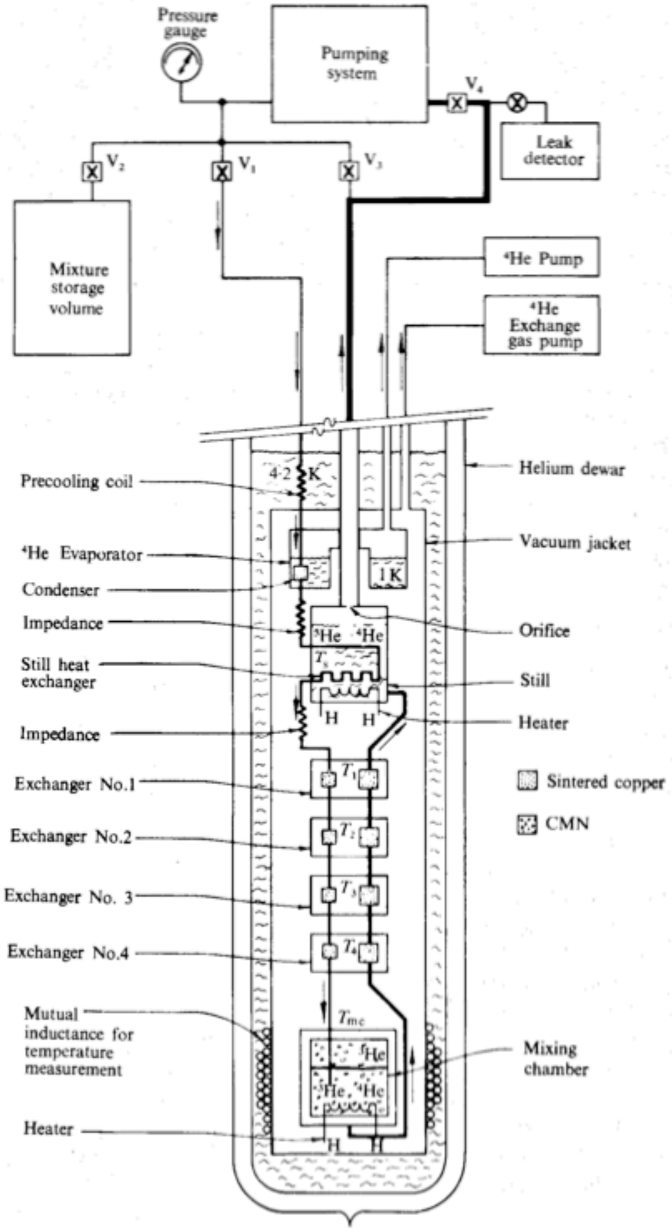

Figure 4.3: Schematic drawing of a Dilution fridge [56].

Thus, the thermal radiation seen by the helium bath is considerably less than what is produced by the outside of the dewar, which is at room temperature. This greatly reduces the helium consumption, extending the time between transfers. Finally, the outer vacuum chamber is lined with several layers of superinsulation; a thin plastic foil with a reflective aluminium coating yielding an emissivity of 0.06. Each layer has a progressively lower temperature from the outside to the dewar to the helium bath at the center of the dewar. Similar to the nitrogen jacket, the layers of superinsulation provide many thermal barriers which reduce the radiative heat transfer.

The helium bath has a number of uses in addition to being the primary method of cooling the fridge: the helium cold trap is submerged in the liquid in the bath, the 1-K pot is filled with the helium from the bath, and it also contains a large superconducting magnet. The magnet is a coil of superconducting wire allowing for large persistent currents to flow with no loss due to resistance. That is, once the magnet is energized, the resulting field will persist as long as the magnet remains superconducting at fields up to 14 T. Thus, experiments can be conducted at a wide range of temperatures and fields.

Vibration Reduction

Low temperature experiments are often extremely sensitive to vibrations. This is especially true in thermal conductivity experiments at high magnetic fields. As we have seen in the previous chapter, the electrical leads to the sample thermometers are coils of resistive wire to improve thermal isolation from the device mount. So, small vibrations in the device cause the coils to act as tiny pickup coils in the field, inducing random voltage noise in the resistance measurement. This is because the flux though the each coil fluctuates as they vibrate in the field. Faraday's Law states that the induced voltage (V_{ind}) in a coil is proportional to the change in magnetic flux (Φ) via

$$V_{\text{ind}} = -N\frac{\mathrm{d}\Phi}{\mathrm{d}t} \tag{4.6}$$

where N is the number of turns in the coil. Thus, removing all sources of vibrations from the system is necessary, especially when the magnetic field is on. This is achieved by suspending the dewar from large Canadian maple beams. The wooden beams are supported on either side by concrete pillars weighing 8000 pounds each. Vibration dampening rubber mats are embedded in the concrete. Multiple materials are used with different natural frequencies, suppressing the transmission of vibrations though each material. The concrete pillars were constructed on top of a large slab of concrete containing a 6 foot deep pit, into which the dewar can be lowered, allowing easy access to the fridge. This entire structure is isolated from the buildings foundation, separating it from the vibrations in the building. Space was left between the top of the pillars and the wooden beam for the addition of an air spring if so desired in the future as an additional vibration damping mechanism.

4.4 Thermometry

A thermometer is a device which has a measurable physical property that is strongly dependent on the temperature of the system. There are three characteristics a thermometer must possess for it to be practical. The physical property dependent on temperature must be reproducible, relatively straightforward to measure in a short amount of time and be of a reasonable size. In general, thermometers can be categorized into two classes, primary and secondary thermometers. In a primary thermometer, the theoretical understanding of the temperature dependence of the physical property must be well enough understood that the relationship can be derived from first principles. One example of a primary thermometer is a gas thermometer, where the pressure-temperature relationship is well understood by the ideal gas law or by the van der Waals equation of state for gases of interacting particles. Another primary thermometer that is more useful at low temperatures is a nuclear orientation thermometer where the angular anisotropy of the emission of gamma rays from a radioactive isotope is well understood by the Boltzmann population of the hyperfine energy levels. This method, however, requires acquiring data for extended periods of time to improve the count statistics which enhances the resolution of the thermometer. Thus, nuclear orientation thermometry is not the most practical method for determining the temperature. In fact, most primary thermometers are quite difficult to use. Thus they are primarily used to calibrate secondary thermometers; devices whose temperature dependence cannot be derived theoretically, however are much simpler to measure, and can be tailored to suit the needs of the current experiment. Hence, the use of secondary thermometers is much more common in low temperature laboratories. Perhaps the most utilized secondary thermometer in low temperature physics is the resistive thermometer. Resistive thermometry takes advantage of the band gap between the valence and conduction bands in a semiconductor which results in an exponential temperature dependence of the resistance at low temperature. In an ideal intrinsic semiconductor, the resistance follows a simple activated temperature dependence of the form

$$R(T) = \alpha \exp\left(\frac{\Delta E}{2k_{\mathrm{B}}T}\right) \tag{4.7}$$

where ΔE is the band gap. However, real materials may not follow this functional form over a large range of temperatures, as impurities will result in an extrinsic region at low temperatures. In this case, the resistance-temperature relationship takes a more pragmatic form rather than a temperature dependence based on a physical description. The resistance of many heavily doped semiconductors is well described by the following polynomial

$$\ln(R(T)) = \sum_{n=0}^{m} \alpha_n \left(\ln(T)\right)^n . \tag{4.8}$$

Figure 4.4 shows the resistance curves for a number of semiconducting materials which are often used in thermometry, revealing how complex the temperature dependence can be. This also illustrates how these materials can be engineered in such a way to maximize the sensitivity (defined as $\mathrm{d}R/\mathrm{d}T$) of a thermometer for a given temperature range. For example, a cernox thermometer (similar to the CX 1050 in figure 4.4) is used in the 1-K pot system where sensitivity is required between 1 K and 100 K. However, ruthenium oxide thermometers (RX 202A in figure 4.4) are used below 1 K on the dilution fridge.

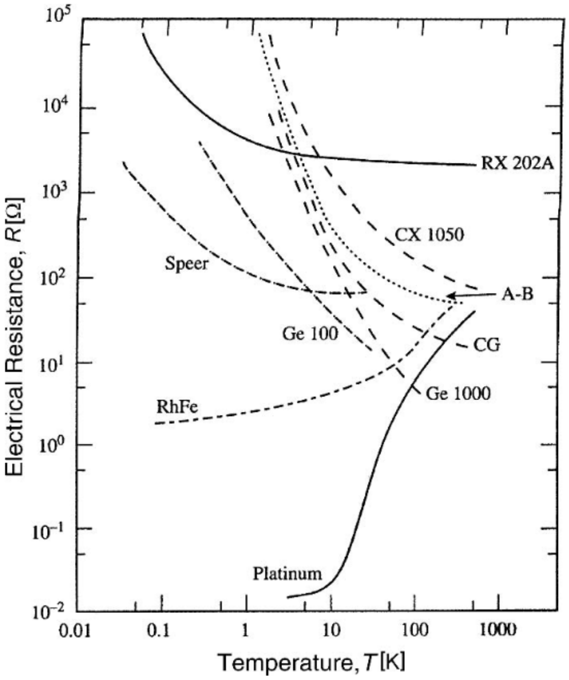

Figure 4.4: Resistance versus temperature for a variety of semiconducting materials which are often used in resistance thermometry [56].

Part II

Rare-Earth Titanates

Chapter 5

Dipolar Spin Ice

5.1 Magnetism of Localized Electrons

Magnetism and magnetic materials are ubiquitous, appearing in electric motors, computer hard drives and holding up photos on your refrigerator door. It is clear that there are many types of magnets, both intrinsic and induced. The magnetic materials examined in this thesis all exhibit some type of intrinsic magnetism either by the localized electrons located near the nucleus, or by the conduction electrons. This is unlike the magnetism caused by an electric current passing though a coil of wire, as in an electromagnet. In fact, the magnetism we are interested is entirely quantum mechanical, and the fundamentals are quite well understood. Although the basics are well understood, competing interactions and geometrical frustration can lead to new unusual and novel states with exotic excitations which still lack solid theoretical frameworks. The goal of this chapter is to provide sufficient theoretical background in order to understand the more complex subtleties in some very peculiar quantum states of matter, namely, the spin ice (SI) materials and a topological Kondo insulator (TKI).

5.1.1 The hydrogenic atom

We will start by considering the magnetism caused by the localized, core electrons of an atom. Perhaps the most logical place to start is the case of a single electron in a centralized potential, better known as the hydrogen atom. Here, we want to solve the eigenvalue equation

$$H\psi_i = \varepsilon_i \psi_i \tag{5.1}$$

where ε_i are the energy eigenvalues and ψ_i are the corresponding wavefunctions. The Hamiltonian, H, is given by

$$H = -\frac{\hbar^2}{2m_e}\nabla^2 - \frac{Ze^2}{4\pi\epsilon_o r}. \tag{5.2}$$

The first term in equation 5.2 is the kinetic energy where m_e is the mass of the electron. The second term is the potential energy from the Coulomb interaction between the electron with charge e and the nucleus of charge Ze separated by a distance r. This partial differential equation can be solved by separating the variables into a radial component $R(r)$ and an angular component $Y_l^{m_l}(\theta, \phi)$

$$\psi(r, \theta, \phi) = R(r) Y_l^{m_l}(\theta, \phi) \tag{5.3}$$

where $Y_l^{m_l}(\theta, \phi)$ are the spherical harmonics [63]. The radial part of the solution is given by

$$R(r) = V_n^l(Zr/na_o)\mathrm{e}^{Zr/na_o} \tag{5.4}$$

where V_n^l are the Laguerre polynomials and $a_o = 52.9$ pm is the Bohr radius. Here, $n = 1, 2, 3 \ldots$ is known as the principle quantum number, $l = 1, 2, 3, \ldots, (n-1)$ is the angular momentum quantum number and $m_l = 0, \pm 1, \pm 2, \ldots \pm l$ are the eigenvalues of the angular momentum operator $\hat{l}_z$ (when multiplied by $\hbar$). The fourth quantum number is the spin of the electron m_s which takes values of $m_s = \pm 1/2$ since electrons are spin-1/2 particles. Therefore each orbital $\psi_i(r, \theta, \phi)$ (determined by the three quantum numbers n, l, m_l) is able to contain at most two electrons since no two electrons in a state can have all four quantum numbers be identical (n, l, m_l, m_s). This is an explicit statement of the Pauli exclusion principle (PEP) and becomes important for atoms with more than one electron. However, the PEP alone does not determine to order of which orbitals are filled since a Coulomb interaction term between the electrons will modify the Hamiltonian given in equation 5.2. Table 5.1 indicates the order in which the orbitals fill with increasing number of electrons.

Hund's rules

Magnetic atoms will generally follow the $L-S$ coupling scheme [63], where the individual spin and orbital angular momenta sum to yield resulting quantum numbers via:

$$S = \sum s_i, \quad M_S = \sum m_{s_i}, \quad L = \sum l_i, \quad M_L = \sum m_{l_i}. \tag{5.5}$$

The spin-orbit coupling must be included to couple S and L to form the total angular momentum, J. A practical method for determining ground state term (written as ${}^{2S+1}X_J$)

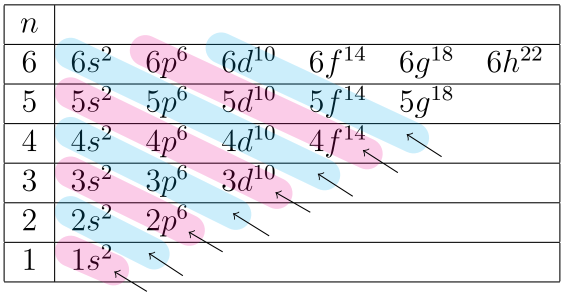

n						
6	$6s^2$	$6p^6$	$6d^{10}$	$6f^{14}$	$6g^{18}$	$6h^{22}$
5	$5s^2$	$5p^6$	$5d^{10}$	$5f^{14}$	$5g^{18}$	
4	$4s^2$	$4p^6$	$4d^{10}$	$4f^{14}$		
3	$3s^2$	$3p^6$	$3d^{10}$			
2	$2s^2$	$2p^6$				
1	$1s^2$					

Table 5.1: Electron orbital filling sequence. The shells are filled following the arrows along the highlighted lines from right to left starting with $n = 1$ (which is the lowest principle quantum number, and hence the lowest energy orbital).

for an atom with several electrons is to follow Hund's rules. Start by considering the partially filled shell of the electron configuration, then execute the following steps:

1. Maximize the spin, S, for the given electron configuration.
2. Maximize the angular momentum, L, consistent with S.
3. Couple S and L to obtain J such that (i) $J = L - S$ if the shell is less than half full, (ii) $J = L + S$ if the shell is more than half full, or (iii) $J = S,\ L = 0$ if the shell is exactly half full.

Now that we have a systematic method for determining the electronic ground state term for a multi-electron atom, we can now take a more rigorous look at the full Hamiltonian.

5.1.2 The multi-electron Hamiltonian

The full Hamiltonian for an ion on a crystal lattice is comprised of four terms: H_0, H_{SO}, H_{CF} and H_Z, which are the unperturbed, single atom Hamiltonian (including the electron-electron and electron-nucleus Coulomb interactions), spin-orbit coupling, crystal electric field, and Zeeman energy terms respectively. The full Hamiltonian is thus:

$$H = H_0 + H_{SO} + H_{CF} + H_Z. \tag{5.6}$$

Coulomb interaction

The single atom Hamiltonian has been covered in the previous section. It determines the total spin and angular momentum, S and L, as well as the order which the orbitals fill with increasing number of electrons. The explicit form H_0, including the full Coulomb interaction, takes is

$$H_0 = \sum_i \left[-(\hbar^2/2m_e)\nabla_i^2 - Ze^2/4\pi\epsilon_o r_i \right] + \sum_{i<j} e^2/4\pi\epsilon_o r_{ij}. \tag{5.7}$$

In reality, the interactions between the numerous electrons makes finding an analytical solution to this problem hopeless. Rather than considering each individual interaction between every pair of electrons, the interaction is instead approximated by examining single electrons in a modified potential which has been altered by the other electrons around the nucleus. This is known as the Hartree-Fock approximation [63, 42].

Spin-orbit coupling

We have already seen that the spin-orbit coupling is responsible for determining the ground state electronic configuration in addition to the total angular momentum J through Hund's rules. Evidently, this interaction is the cause of many interesting magnetic properties such as magnetostriction and anisotropic magnetoresistance. The spin-orbit coupling term is given by

$$H_{SO} = (\Lambda/\hbar^2)\hat{\boldsymbol{L}} \cdot \hat{\boldsymbol{S}} \tag{5.8}$$

where Λ is the multi-electron spin-orbit coupling strength. As in Hund's third rule, Λ is positive when the $3d$ or $4f$ shell is less than half full and negative when the shell is more than half full [63].

Single ion anisotropy: crystal fields

The single ion anisotropy is due to the interaction between the charge orbitals of the ion and the electrostatic field formed by the rest of the atoms in the crystal (the crystal field). The amount the energy levels are split by the crystal field is strongly dependent on the symmetry of the lattice and can be on the order of hundreds of Kelvin [44]. Hence, only the lowest energy doublet or singlet are usually occupied at low temperatures. Stevens showed that the crystal field interaction can be expressed in terms the angular moments operators, J_i, through the so-called Stevens operator equivalents, O_l^m [63, 64]. The most general form of the crystal field Hamiltonian can thus be written as:

$$H_{CF} = \sum_i \sum_{l,m} B_l^m O_l^m(J_i) \tag{5.9}$$

where B_l^m are the crystal field parameters which are determined through high resolution optical spectroscopy measurements. The Stevens operator equivalents are a convenient way to evaluate the matrix elements of the crystal field potential. A few common lower order operators are given in table 5.2. For more information on Stevens operator equivalents and the crystal field Hamiltonian see references [65, 66].

O_l^m	in $\lvert J, m\rangle$ basis
O_2^0	$3J_z^2 - J(J+1)$
O_2^2	$\frac{1}{2}(J_+^2 - J_-^2)$
O_4^0	$35J_z^4 - 30J(J+1)J_z^2 + 25J_z^2$ $- 6J(J+1) + 3J^2(J+1)^2$
O_4^4	$\frac{1}{2}(J_+^4 + J_-^4)$
O_6^6	$\frac{1}{2}(J_+^6 + J_-^6)$

Table 5.2: Select low-order Stevens operator equivalents [63].

In general, it can be quite difficult to predict the crystal field splitting of the energy levels. However, in some cases, we can take advantage of Kramers theorem to determine if the ground state will be a doublet. Kramers theorem states that in time-reversal symmetric systems with a half integer total spin (odd number of valence electrons), the ground state is at least two-fold degenerate. That is, the ground state is a collection of doublets called Kramers doublets. Consequently, ions of this type are known as Kramers ions. On the other hand, systems with integer spin (even number of valence electrons) will have a ground state of consisting of a collection of singlets and doublets which are determined by the crystal fields. These ions are known as non-Kramers ions.

Zeeman splitting

Whereas the Coulomb, spin-orbit and crystal field terms are all intrinsic to the material, the Zeeman term is extrinsic and caused by the application of an external magnetic field. The Zeeman Hamiltonian for a magnetic moment $\hat{\boldsymbol{m}}$ in a magnetic field $\boldsymbol{B}$ is given by

$$H_Z = -\hat{\boldsymbol{m}} \cdot \boldsymbol{B} = -\mu_B(\hat{\boldsymbol{L}} + 2\hat{\boldsymbol{S}}) \cdot \boldsymbol{B}. \tag{5.10}$$

The projected value of the moment along $\boldsymbol{J} = \boldsymbol{L} + \boldsymbol{S}$ can be written as $m = -g_J \mu_B \boldsymbol{J}$ where g_J is the Landé g-factor given by

$$g_J = \frac{3}{2} + \left[S(S+1) - L(L+1)\right]/2J(J+1). \tag{5.11}$$

Suppose the magnetic field is in the z-direction such that $\boldsymbol{B} = B\hat{z}$, then the Zeeman energy is $\varepsilon_Z = -m_z B = g_J \mu_B M_J B$ where M_J is the total magnetic quantum number [63].

5.2 Frustrated Magnetism

5.2.1 Ising Model

The previous section provides a reasonable, microscopic understanding of magnetism from electrons localized to the nucleus. We have seen that the ground state can be a doublet, or a collection of a singlet state and doublets depending on the number of electrons in the partially filled orbital via Kramer's Theorem. Furthermore, the crystal field created by several atoms arranged in a crystal lattice can split the degeneracy of the ground state for non-Kramers ions, isolating a particular doublet state. The crystal electric field (CEF) can also lead to an easy-plane or easy-axis anisotropy for the magnetic moments by stabilising certain orbitals. Let us consider the case where we have a well isolated ground state doublet with easy-axis anisotropy. This is the basis for the Ising model. In the Ising model, each site, i, on the lattice has a spin S_i taking the value of ± 1. The Ising Hamiltonian is then written as

$$H = -\sum_{\langle ij \rangle} J_{ij} S_i S_j. \tag{5.12}$$

Here, J_{ij} is the exchange energy between sites i and j on the lattice and is negative for an antiferromagnetic interaction (anti-aligned spins), and positive for a ferromagnetic interaction (aligned spins). The exchange interaction arises in insulating materials through the superexchange of electrons which involves the virtual exchange of two d-orbital electrons from neighbouring magnetic ions. In transition-metal oxide materials, the $3d - 3d$ overlap is small, and the exchange of electrons is mediated by the $2p$ orbitals of the oxygen ions, which hybridize with the $3d$ orbitals [63]. The strength of the interaction is on the order of $-2t^2/U$, where t is the $p - d$ transfer integral and U is the Coulomb interaction.

In this section, we will focus on the scenario with isotropic, nearest neighbour interactions. So, $J_{ij} = J$ when i and j are nearest neighbours, and $J_{ij} = 0$ otherwise. It is rather intuitive to find the lowest energy configuration of spins on a square lattice. However, as we shall see in the following section, different arrangements of spins can lead to more interesting, degenerate ground states.

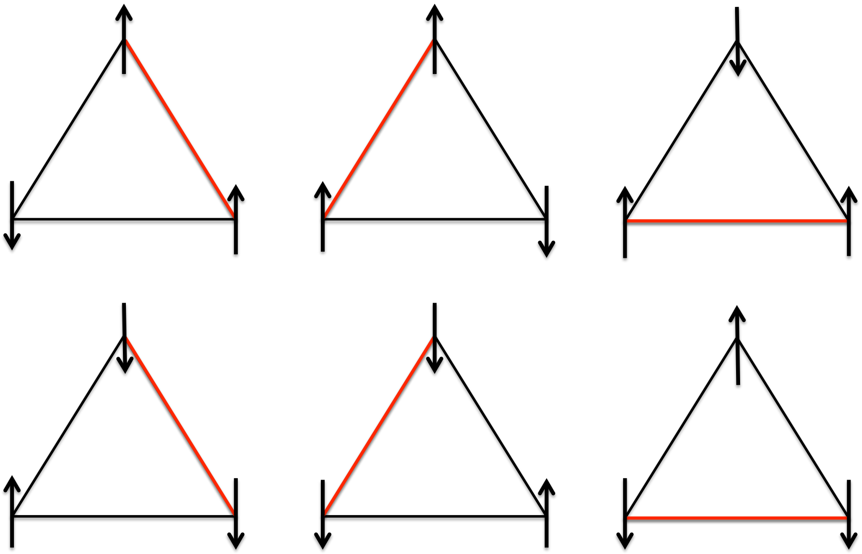

Figure 5.1: Six-fold degenerate ground state of Ising spins on a triangular lattice with an antiferromagnetic nearest neighbor interaction. The red line indicates the violated antiferromagnetic interaction.

5.2.2 Geometrical frustration

Let us start by examining a simple toy model of Ising spins on a two dimensional triangular lattice with nearest neighbour antiferromagnetic interactions. This was first investigated by Wannier and Houtappel close to 70 years ago [67, 68]. I will start by noting that it is trivial to find the ground state in the case of a ferromagnetic interaction ($J > 0$) since all the nearest neighbour exchange interactions are satisfied when all the spins are aligned, pointing up or down. The scenario with antiferromagnetic interactions is much more interesting. Figure 5.1 shows how the antiferromagnetic interaction can be satisfied between any two spins, but attempting to satisfy the interaction between either of the first two spins with the third spin will necessarily impose a violation of the remaining interaction as indicated by the red line. Minimizing the energy in the Hamiltonian thus results in a six-fold degenerate ground state with a residual entropy. This degeneracy does not exist for antiferromagnetic interactions on a square lattice since all the interactions are able to be satisfied simultaneously. This illustrates how the degeneracy is imposed by the geometry of the system coupled with a nearest neighbour antiferromagnetic interaction.

Pyrochlore lattice

A three-dimensional analogue of the triangular lattice is an array of corner sharing tetrahedra, commonly referred to as a pyrochlore lattice (figure 5.2). The 'pyrochlore' nomenclature is borrowed from another material with a corner sharing tetrahedral crystal lattice, $Na_2Nb_2O_6F$, which tends to burn green when ignited [64]. This three dimensional system was first studied in the context of a frustrated magnetic system in 1956 by Anderson [69]. He noticed that an Ising spin system with a nearest-neighbor exchange on the pyrochlore lattice also results in a residual entropy, similar to the triangular lattice. In fact, he recognized that this system shared many similarities to water ice. In water ice, the locations of the hydrogen ions follow the so-called Bernal-Fowler ice rules such that two ions are situated near (covalent bond) and two are situated far (hydrogen bond) from each oxygen atom. The oxygen atoms are arranged on a diamond lattice (dual lattice of the pyrochlore) [70]. Anderson mapped the ice rules to the spins on the vertices on each tetrahedra so that two spins were pointing up and two were pointing down along the global z-direction with six possible degenerate permutations. As in water ice, this degeneracy leads to a residual entropy which is very close to Pauling's zero-point entropy for water ice of $S_0 = (R/2)\ln(3/2)$ [71].

5.3 Rare-earth Titanates

The remainder of this chapter focuses on a class of pyrochlore materials with chemical formulas of the form $Re_2B_2O_7$ where Re^{3+} is a trivalent rare-earth metal and B^{4+} is a tetravalent transition metal. More specifically, we will consider materials where Re^{3+} is a magnetic ion (Dy^{3+}, Ho^{3+} and Yb^{3+}) and B^{4+} is nonmagnetic Ti^{4+}. This specific class of materials are known as the rare-earth titanates. A few rare-earth ions which are often found in these materials are listed in table 5.3 along with their electron configuration and ground state term [63, 42].

Each of these rare earth ions in $Re_2Ti_2O_7$ give rise to fascinating exotic magnetic phases at low temperature such as a possible spin liquid state in $Tb_2Ti_2O_7$ [72, 73, 74], an order-by-disorder state in $Er_2Ti_2O_7$ [75, 76], a classical spin ice phase in $Ho_2Ti_2O_7$ [35, 9] and

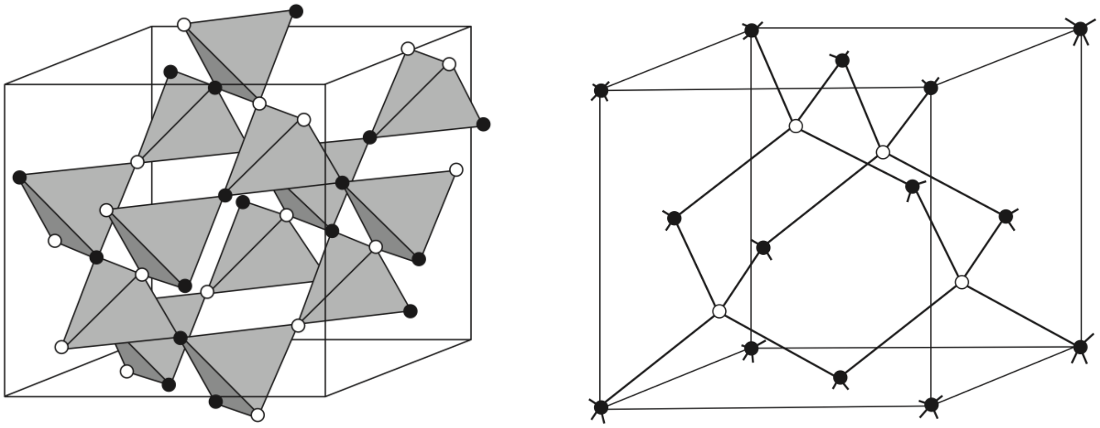

Figure 5.2: (a) Pyrochlore lattice. (b) Diamond lattice, dual lattice of the pyrochlore with sites at the centers of each tetrahedron [2].

Element	Electron configuration	Ground-state
Tb^{3+}	$4f^8$	$^7F_6$
Dy^{3+}	$4f^9$	$^6H_{15/2}$
Ho^{3+}	$4f^{10}$	$^5I_8$
Er^{3+}	$4f^{11}$	$^4I_{15/2}$
Yb^{3+}	$4f^{13}$	$^2F_{7/2}$

Table 5.3: Some rare-earth ions that are often found in the titanates of the form $Re_2Ti_2O_7$. The corresponding electron configuration and ground-state term are listed.

$Dy_2Ti_2O_7$ [34] and a quantum spin ice phase in $Yb_2Ti_2O_7$ [18]. This thesis is concerned with the classical and quantum spin ice materials. Previous theoretical and experimental results for $Ho_2Ti_2O_7$, $Dy_2Ti_2O_7$ and $Yb_2Ti_2O_7$ are summarized in the following sections.

5.4 Classical Spin Ice

The classical spin ice state has been realized in the rare-earth titanate materials $Ho_2Ti_2O_7$ (HTO) and $Dy_2Ti_2O_7$ (DTO) which have been studied in depth over the past 15 years. Here, the magnetic, trivalent rare-earth ions are located on the pyrochlore lattice and the tetravalent Ti ions are on a shifted pyrochlore sub-lattice. Recall that Ho^{3+} has a

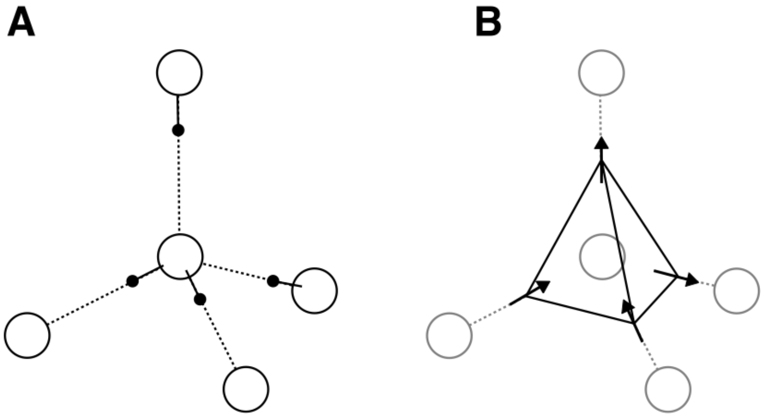

Figure 5.3: **(A)** A schematic view of the local proton arrangement in water ice. The oxygen ions (large open circles) are situated on the diamond lattice sites, that is, each oxygen ion is coordinated tetrahedrally with four other oxygen ions. Two protons (small black circles) are located near (covalent bonded) and two protons are located far (hydrogen bonded) from each oxygen ion. This is the so called Bernal-Fowler 'ice rules'. **(B)** A single tetrahedron from the pyrochlore lattice (centered on the diamond lattice) seen in HTO or DTO with magnetic moments (the arrows) located on the vertices which are aligned parallel to the local ⟨111⟩ direction. The direction which the spins point is analogous to the locations of the protons in water ice such that two spins are pointing in and two spins are pointing out of each tetrahedron. This illustrates the analogy between water ice and spin ice, hence the name 'spin-ice' [3].

ground state term of $^5I_8$ and hence is a non-Kramers ion, so the ground state could be a collection of doublets and singlets. In the case of HTO, the local crystal fields split the degenerate $|J, m_j\rangle$ states, isolating the $|J, m_j\rangle = |8, \pm 8\rangle$ doublet as the ground state. That is, the ground state doublet is accidental in HTO. To corroborate this, Jana and Gosh calculated the crystal field parameters in HTO and found that the splitting between the ground state doublet and the next excited state is ∼215 K [77]. This splitting was measured by Rosenkranz to be 236 K using neutron spectroscopy [78]. Conversely, Dy^{3+} has a ground state term of $^6H_{15/2}$ and is a Kramer's ion, thus Kramer's Theorem dictates that the ground state will be the $|J, m_j\rangle = |15/2, \pm 15/2\rangle$ doublet. This is confirmed by observing that the first excited state is ∼348 K above the ground state.

Early susceptibility measurements of HTO and DTO revealed that both of these ions have very large magnetic moments of approximately $\mu = 10\mu_B$ at low temperatures with a nearest neighbour antiferromagnetic exchange interaction. Furthermore, the susceptibility reveals that these large moments have an easy axis anisotropy with a local $\langle 111 \rangle$ quantization since $\chi_z/\chi_\perp \sim 350$ at 10 K for HTO and $\chi_z/\chi_\perp \sim 300$ for DTO. This ratio describes the anisotropy of the spins which align parallel to the local $\langle 111 \rangle$ direction rather than perpendicular to this direction. So we see that both HTO and DTO have large Ising spins situated on a pyrochlore lattice under the influence of nearest neighbour interactions, creating an excellent manifold for observing spin ice physics at low temperature.

In 2000, den Hertog and Gingras developed a dipolar spin ice model to describe the the low temperature spin ice state in the rare-earth titanates [4]. The Hamiltonian not only accounts for the antiferromagnetic exchange, $J < 0$, but also for the long range ferromagnetic dipolar interaction, $D > 0$, arising from the substantial magnetic moment and is given by

$$H = -J \sum_{(ij)} S_i^{\hat{z}_i} \cdot S_j^{\hat{z}_j} + D r_{nn}^3 \sum_{i>j} \frac{S_i^{\hat{z}_i} \cdot S_j^{\hat{z}_j}}{|\mathbf{r}_{ij}|^3} - \frac{3(S_i^{\hat{z}_i} \cdot \mathbf{r}_{ij})(S_j^{\hat{z}_j} \cdot \mathbf{r}_{ij})}{|\mathbf{r}_{ij}|^5}. \tag{5.13}$$

The local $\langle 111 \rangle$ quantization of the spins imposes a 109.4° tilt between the spins with respect to one another. Thus the nearest neighbour exchange energy is defined as $J_{\mathrm{nn}} = \cos(109.4^\circ)J = J/3$. The dipole interaction can be written as $D = (\mu_o/4\pi)g^2\mu^2/r_{\mathrm{nn}}^3$ and at nearest neighbour distance, $D_{\mathrm{nn}} = 5D/3$ [5]. This Hamiltonian can be simplified to an effective nearest neighbour exchange defined as $J_{\mathrm{eff}} \equiv J_{\mathrm{nn}} + D_{\mathrm{nn}}$ which retains the nearest neighbour spin ice physics. The nearest neighbour exchange coupling is $J_{\mathrm{nn}} \sim -1.24$ K for DTO and $J_{\mathrm{nn}} \sim -0.52$ K for HTO. The nearest neighbour dipole-dipole coupling is $D_{\mathrm{nn}} \sim 2.35$ K for both DTO and HTO. Thus, the effective exchange coupling is net ferromagnetic in both cases with $J_{\mathrm{eff}} \sim 1.1$ K for DTO and $J_{\mathrm{eff}} \sim 1.8$ K for HTO [5]. The Hamiltonian can then be written in the familiar form of the nearest neighbour Ising model:

$$H = -J_{\mathrm{eff}} \sum_{(ij)} S_i^{\hat{z}_i} \cdot S_j^{\hat{z}_j}. \tag{5.14}$$

The left panel in figure 5.4 shows a phase diagram of T/D_{nn} versus $J_{\mathrm{nn}}/D_{\mathrm{nn}}$ which was determined via Monte Carlo (MC) simulations using a standard single Ising spin flip Metropolis algorithm [4]. This result shows that the spin ice state is stabilized for ratios of $J_{\mathrm{nn}}/D_{\mathrm{nn}} \geq -0.91$. Since $J_{\mathrm{nn}}/D_{\mathrm{nn}} = -0.22$ for HTO and $J_{\mathrm{nn}}/D_{\mathrm{nn}} = -0.53$ for DTO, then this phase diagram indicates that both HTO and DTO enter spin ice states at low temperature.

Melko and Gingras introduced non-local dynamics into their spin ice simulation to impede the freezing of the spins by developing a loop algorithm which provides a method

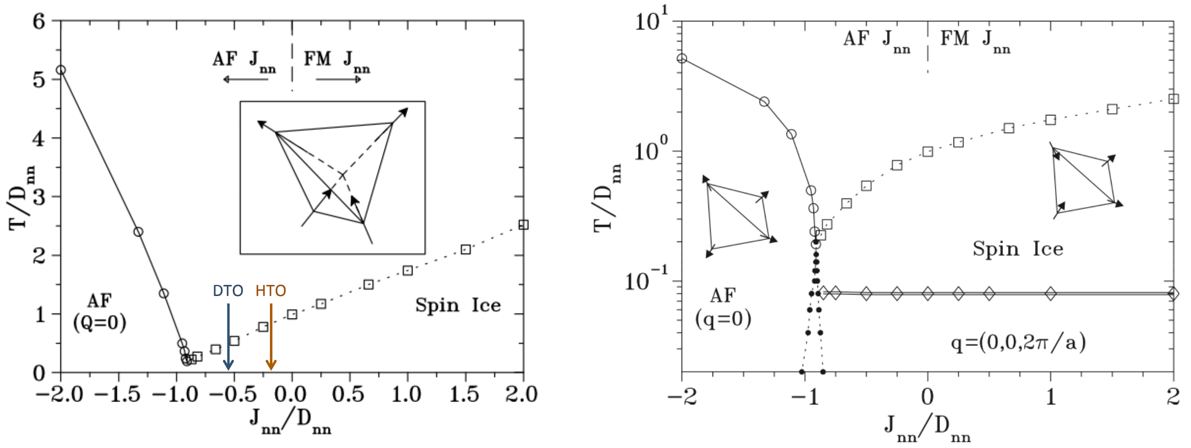

Figure 5.4: *Left:* T/D_{nn} versus J_{nn}/D_{nn} phase diagram produced by den Hertog and Gingras [4]. The arrows indicate the location of HTO and DTO in the phase diagram. *Right:* T/D_{nn} versus J_{nn}/D_{nn} phase diagram with ordered ground state from loop flip algorithm simulation [5].

to release the trapped entropy in the spin ice state [5]. This technique artificially speeds up the slow, low temperature dynamics by forcing loops of spins to flip, promoting the creation of a long range ordered state. Simulations reveal a long range ordered ground state with ordering vector $\mathbf{q} = (0, 0, 2\pi/a)$ (and the two other symmetrically equivalent wave-vectors) which satisfies the 2-in-2-out ice rules but recovers all of Pauling's entropy. The specific heat and the integrated entropy obtained from these simulations is seen in figure 5.5.

The specific heat displays a broad peak similar to experiments but there is a large peak indicative of a first order transition at about 180 mK. This causes the entropy to have a plateau at Pauling's entropy followed by a rapid drop to zero, indicating the recovery of all the $R\ln(2)$ entropy from the paramagnetic state. The resulting $T/D_{\rm nn}$ vs $J_{\rm nn}/D_{\rm nn}$ phase diagram is seen in the right panel of figure 5.4 which is similar to the den Hertog-Gingras phase diagram [4], however it includes the appearance of the low temperature ordered state occurring below 180 mK for all values of $J_{\rm nn}/D_{\rm nn} \geq -0.91$. Although each loop of spin flips may cause minimal change in the overall energy, there is an initial large energy barrier to overcome in order to access the other nearly degenerate ground states. That is, upon cooling the crystal, the spins freeze into a two-in-two-out state and spin flips become energetically unfavourable, leading to large energy barriers that separate the nearly degenerate ground states. Therefore it is very difficult to realize this ordered state

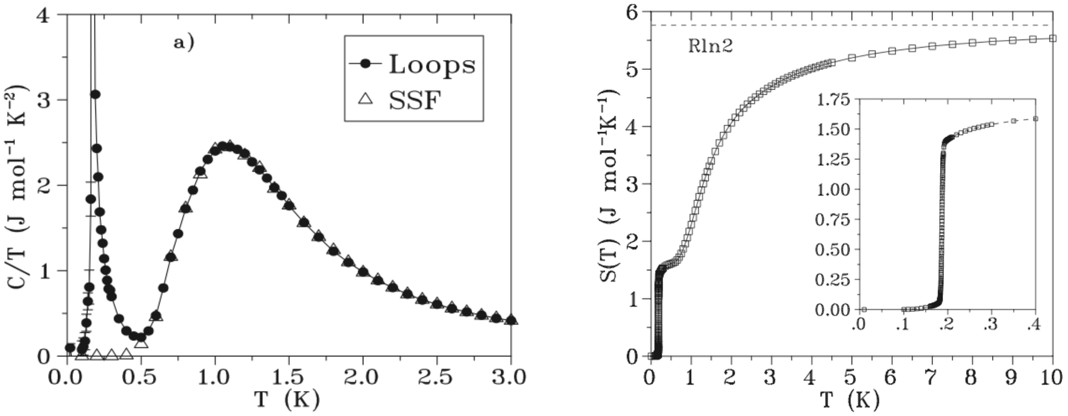

Figure 5.5: Monte Carlo simulations of specific heat (left) and entropy (right) for a spin ice system including a loop flip algorithm, illustrating the onset of an ordered state below 0.5 K [5].

experimentally.

Neutron scattering measurements have been conducted on both HTO and DTO in order to probe the spin dynamics over a wide range of temperatures as well as the onset of any potential spin correlations at low temperatures [35, 79, 80]. Harris *et al.* performed neutron scattering measurements on HTO at 20 K, 1.8 K and 0.35 K [35]. They observe several Bragg peaks, however there was no significant change to their intensities upon cooling from 300 K to 0.35 K indicating these peaks are nuclear in origin. Thus, there is no evidence of a magnetic phase transition. Broad scattering is observed below 1.8 K which is centred at the $(\frac{1}{2}\frac{1}{2}\frac{1}{2})$ point in the Brillouin zone, consistent with Monte Carlo simulations for the spin ice model [35]. Neutron scattering is much more challenging in DTO because natural dysprosium based materials have an affinity to absorb neutrons, resulting in a weak signal. Fennell *et al.* remedied this by growing a sample of DTO isotopically enriched with ^{162}Dy, reducing neutron absorption [79]. This made it possible to perform polarized neutron scattering measurements on DTO at 20 K, 1.3 K, 0.3 K and 0.05 K. These measurements allowed them to track the evolution of the diffuse scattering associated with the development of the spin ice correlations as well as the ability to separate spin flip and non-spin flip correlations by analysing the polarization. At 20 K, they see no scattering indicative of spin ice correlations, consistent with the high temperature paramagnetic state seen in susceptibility measurements [15]. Cooling the sample to 1.3 K shows strong diffuse scattering, taking the form of pinch points, similar to what is observed in HTO. Pinch point structures in neutron scattering develops when the static scattering function $S(\boldsymbol{Q})$

is singular in a single direction, and diffuse in all other directions. This behaviour is taken as a clear signature of spin ice correlations [80]. The scattering intensity at 0.05 K is not significantly different from the 0.3 K data. Nonetheless, neutron scattering measurements on both HTO and DTO yield strong evidence for the realization of the dipolar spin ice state at temperatures below approximately 1.3 K.

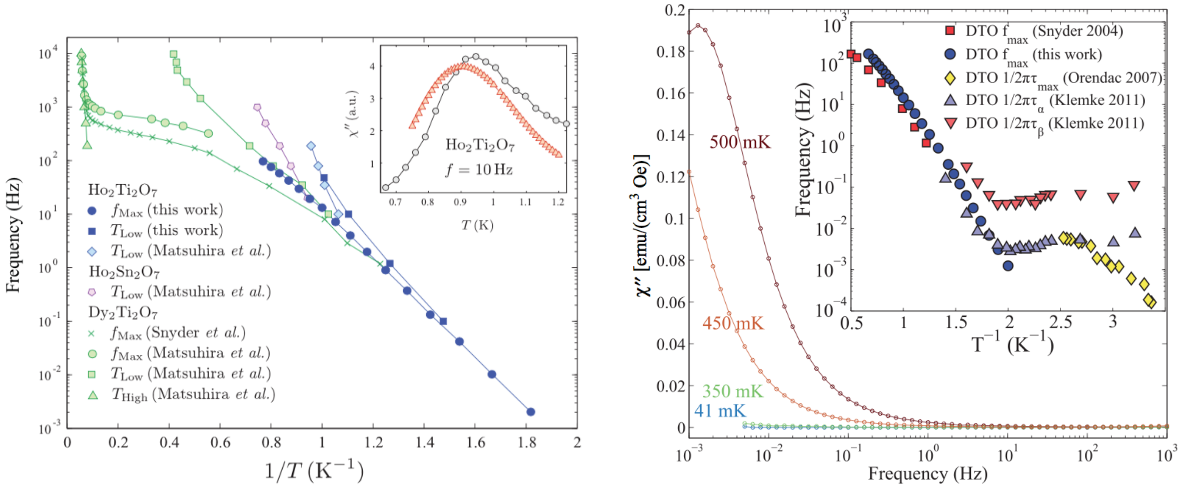

Figure 5.6: *Left:* AC susceptibility of HTO by Quilliam *et al.* showing the freezing behaviour in the spin-ice state [6]. A comparison of a variety of measured relaxation times [81, 82, 83, 6]. *Right:* AC susceptibility of DTO by Yaraskavitch *et al.* showing the freezing behaviour in the spin-ice state [7]. The inset shows a comparison of a variety of measured relaxation times [84, 85, 86, 7].

Similar to neutron scattering, preliminary ac-susceptibility measurements of both HTO and DTO also show no signs of long range magnetic ordering at low temperature. However, these measurements do reveal a slowing of the spin dynamics below ~ 2 K. Matsuhira *et al.* first discovered this unconventional freezing in polycrystalline samples of Ho$_2$Ti$_2$O$_7$ and Ho$_2$Sn$_2$O$_7$ when he noticed that the relaxation time was well described by a thermally activated Arrhenius behaviour with energy barriers of 27.5 K and 19.6 K respectively [83]. The magnetic relaxation time was measured in HTO down to ~ 550 mK by Quilliam *et al.* (seen in the left panel of figure 5.6) where they observe a single activation energy of 10.7 K $\sim 6J_{\text{eff}}$. Intuitively, this energy barrier makes sense since each spin has 6 nearest neighbours. Matsuhira *et al.* [82] and Snyder *et al.* [81] both performed similar measurements of the relaxation times in DTO. Matsuhira found that above 10 K, DTO displays a thermally activated behaviour with an activation energy of 220 K [82]. Below 10 K, the temperature dependence of the relaxation time flattens into a plateau until about 2 K, at which point there is a crossover to a second thermally activated behaviour with an energy barrier of approximately 9.8 K associated with a single relaxation mode as seen in the right panel of figure 5.6. It is interesting that this excitation energy is roughly equivalent to $9J_{\text{eff}}$ rather than the $6J_{\text{eff}}$ as observed in HTO. The origin of this discrepancy is unknown. There have been a number of other relaxation time measurements in DTO using the magneto caloric effect [85], thermal relaxation [86] and susceptibility [87] who all observe roughly the same activated behaviour from 2 K down to 0.55 K. Below this temperature, the relaxation becomes temperature independent, signifying a deviation from the Arrhenius-like behaviour. Yaraskavitch *et al.* [7] also measured the ac-susceptibility of DTO below 2 K, however, they do not observe the low temperature plateau in the relaxation time at the lowest temperatures (right panel of figure 5.6). Instead, the relaxation time follows the same Arrhenius behaviour below $\sim$ 2 K with an activation energy equal to $9J_{\text{eff}}$ down to half a kelvin. They argue that relaxation time measurements by Giblin [87] and Klemke [86] fall out of equilibrium below ~550 mK due to the exponentially long time constant which approaches 10^4 seconds below 450 mK indicating the freezing of spin dynamics. Yaraskavitch *et al.* suggest that the long relaxation time may be an indication of a spin-lattice decoupling in DTO [7, 8].

Early specific heat measurements of DTO by Ramirez *et al.* [34] revealed a broad peak in the magnetic specific heat centred at approximately 1.2 K, consistent with MC simulations in zero field above 0.5 K [5]. However, as the temperature is lowered below 0.5 K, the measured specific heat did not exhibit the peak at $\sim$ 180 mK which was seen in the MC simulations with the loop-flip algorithm (figure 5.5) [5] and hence, did not recover the full $R\ln(2)$ entropy of the high temperature paramagnetic state. Rather, Ramirez *et al.* found a residual entropy of $R/2\ln(3/2)$, equivalent to Pauling's entropy for water ice [34]. More recently, Pomaranski *et al.* [8] remeasured the specific heat of DTO below 1 K taking into account the extended relaxation times observed in susceptibility measurements [7], on the order of 10 000 seconds at 450 mK. In fact, they waited up 60 000 seconds at the lowest temperatures measured (340 mK) to ensure thermal equilibration between the spins and the lattice. Doing this, they find the relaxation time extracted from the specific heat measurements roughly follow the same Arrhenious temperature dependence as reported in susceptibility measurements by Yaraskavitch *et al.* [7]. They state that the extended relaxation times are consistent with a thermal decoupling of the magnetic and phonon contributions. In addition to this, they also observe the onset of a low temperature peak in the specific heat and a reduction in the residual entropy which falls below Pauling's value, similar to what is seen in the loop algorithm simulations by Melko *et al.* [5]. Pomaranski *et al.* are also able to recreate the previously reported specific heat data by truncating

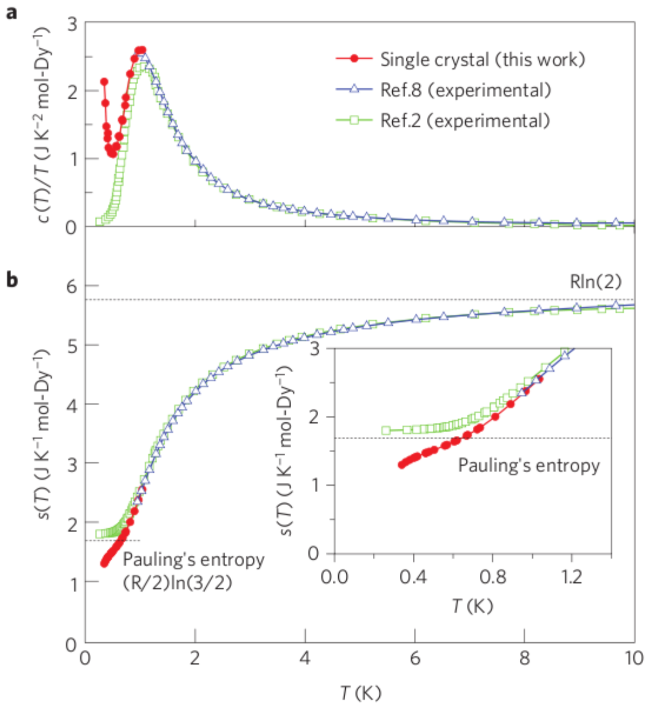

Figure 5.7: Temperature dependence of the specific heat (a) and residual entropy (b) of DTO measured by Pomaranski *et al.* with extended relaxations times reaching 60 000 seconds [8].

their relaxation time at 600 seconds, as in references [34, 88, 89]. This is a startling result, which suggests that many of the previous specific heat studies on DTO have been conducted out of thermal equilibrium. Clearly immense care must be taken to ensure the spins are properly equilibrated with the lattice.

The magnetic specific heat is much more convoluted in HTO since the Ho^{3+} ions carry a large nuclear heat capacity [9]. This reveals itself as a large Schottky peak in the specific heat just below 500 mK in addition to the broad peak at 2 K similar to the one seen in DTO [9]. This is illustrated in figure 5.8. The large nuclear contribution is estimated by calculating the maximum Schottky peak for Ho ($I = 7/2$) [90] in order to isolate the magnetic contribution. The magnetic specific heat shows a broad peak at 2 K, indicating the development of the spin ice correlations which is in good agreement with Monte Carlo simulations above approximately 700 mK [9]. The deviation of the measured magnetic specific heat from the MC simulation below 700 mK is attributed to the error that is

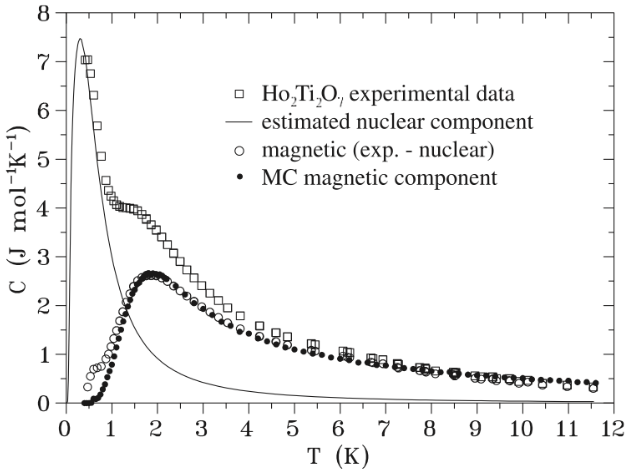

Figure 5.8: Specific heat of $Ho_2Ti_2O_7$ [9]. The data agrees with Monte Carlo simulations after subtracting off the Schottky peak.

incurred by approximating the nuclear contribution. Thus the heat capacity in this range cannot be reliably determined [9].

5.4.1 Magnetic monopoles

The search for a magnetic monopole started in 1931 when Dirac established that they were allowed under the quantum mechanical formalism such that their quantized magnetic charge was equal to $q = m\hbar c/e$ where m is an integer or half integer [91]. These monopoles were termed 'non-Abelian' monopoles whose gauge theory predicted huge masses on the order of tens of TeV. This is way outside of the range of current particle accelerators (LHC is presently operating at about 13 TeV [92]). Thus the direct search for free monopoles is currently futile.

Although free magnetic monopoles continue to elude high energy physicists, it appears that effective monopole quasiparticles may exist as fractionalized excitations within the spin ice framework. Ryzhkin [2] and Castelnovo *et al.* [10] separately proposed a fractionalized magnetic monopole quasi-particle as an excitation out of the spin ice ground state. A monopole anti-monopole defect pair is created upon a single spin flip resulting in a tetrahedron with 3 spins in, 1 spin out (monopole) and a tetrahedron with 1 spin in, and 3 spins out (anti-monopole). Ryzhkin compared these magnetic defects to ionic defects in water ice where an oxygen atom will have three hydrogen ions near, one far, and another oxygen atom with one hydrogen ion near and three far [2]. Figure 5.9 (a-d) illustrates how each individual spin can be considered as a dipole with a north (red ball) and a south pole (blue ball). So the 2-in-2-out state will have two positive charges and two negative charges in each tetrahedron and hence is charge neutral. Flipping a single dipole results in a pair of neighbouring tetrahedra with three positive charges in one and three negative charges in the other resulting in a net positive and negative charge respectively. The charge of this defect is quantified as $q_m = \pm 2\mu/a_d$ where μ is the magnitude of the magnetic moment and a_d is the diamond lattice constant (distance between the center of neighbouring tetrahedra). A fascinating consequence is that flipping subsequent spins thereby separating the monopole/anti-monopole defect pair, does not further violate the ice rules. So, the monopole/anti-monopole pair behave as free particles interacting with a Coulomb potential described by $-\mu_o q_m^2/(4\pi r)$. Separating the monopole/anti-monopole pair causes a trail of flipped spins known as a Dirac string. This is seen in figure 5.9 (e).

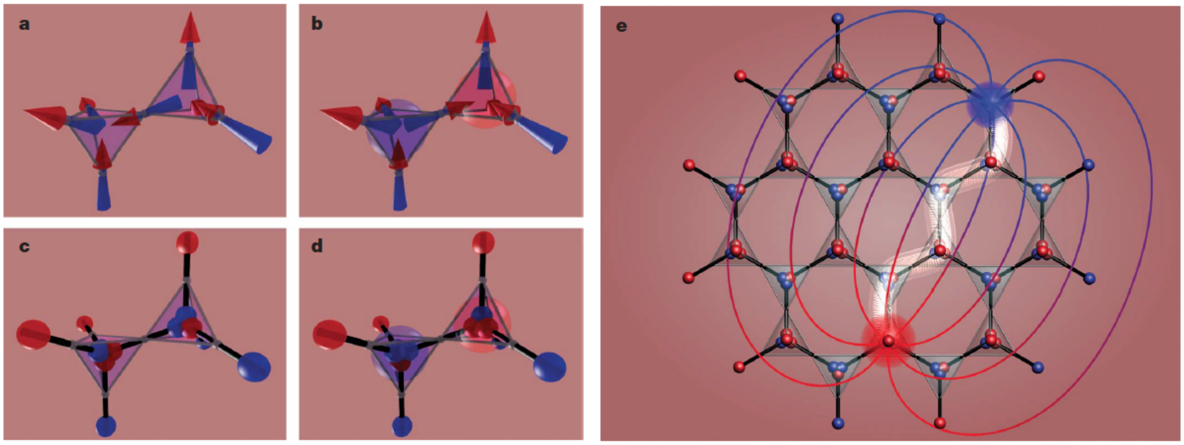

Figure 5.9: The dumbbell model illustrating the creation of a monopole anti-monopole pair. (a) Spin-ice ground state configuration with two spins pointing in and two spins pointing out of each tetrahedron. (b) A single spin flip causes one tetrahedron to have three spins in, one spin out and a neighbouring tetrahedron with one spin in, three spins out. (c,d) The arrows are replaced with dumbbells. (e) Subsequent spin flips separate the monopole anti-monopole pair which are connected by a Dirac string [10].

Castelnovo *et al.* described monopole dynamics in conjunction with experimentally observed thermodynamic properties by applying Debye-Hückel theory; a theory that describes a dilute Coulomb gas such as a dilute electrolyte solution [93]. Debye-Hückel theory describes an electrolyte by considering a discrete central reference ion surrounded by an atmosphere of charge made up of the other ions. It also assumes that the distribution of ions making up the charge atmosphere is not random, but rather the ions nearest to the reference ion are of opposite charge to the charge of the reference ion. Castelnovo *et al.* applied this theory to a dilute sea of monopoles in the Coulomb phase. This theory was then utilized to calculate the monopole density per tetrahedron, $\rho(T)$, given by:

$$\rho(T) = \frac{2e^{-\Delta_d/T}}{1 + 2e^{-\Delta_d/T}} \tag{5.15}$$

where Δ_d is the dressed creation cost of a single isolated monopole which can be calculated via:

$$\Delta_d = \Delta - \frac{1}{2}\frac{E_{nn}}{\frac{\xi_{Debye}}{a_d}} \tag{5.16}$$

Here, Δ is the unscreened value of the energy required to create an isolated monopole ($\Delta =$ 4.35 K for DTO, and 5.79 K for HTO) [93]. $E_{nn} = 3.06$ K is the magnitude of the Coulomb energy between a monopole pair at nearest neighbouring sites and $a_d = \sqrt{3/2}\ a = 4.34$ Å is the diamond lattice constant, which is the distance between the center of neighbouring tetrahedra. The screening length, ξ_{Debye}, is a function of monopole density, $\rho(T)$ and temperature, T and is written as:

$$\frac{\xi_{Debye}}{a_d} = \sqrt{\frac{2}{3\sqrt{3}\pi E_{nn}}}\sqrt{\frac{T}{\rho(T)}} \tag{5.17}$$

No analytic solution exists for this system of equations and therefore they must be solved self-consistently. Castelnovo used this theory to describe specific heat and susceptibility with moderate success [93]. Castelnovo mentions several methods which could improve this theory, such as including interactions between monopole pairs. He also states that Debye-Hückel theory is only applicable in the low monopole density limit which limits the usefulness of this theory to low temperatures.

Since the reports of Ryzhkin and Castelnovo *et al.* theoretically proposing the idea of magnetic monopoles in spin ice materials sparked a great deal of experimental activity searching for signatures of monopoles. Such experiments attempting to probe monopole dynamics include neutron scattering, muon spin resonance (μSR), adiabatic susceptibility and thermal conductivity measurements. Several numerical studies of monopole dynamics have also been pursued via Monte Carlo simulations. A brief overview of these methods will now be discussed.

Morris *et al.* utilized neutron scattering measurements to observe Dirac strings in DTO by applying a magnetic field in the [001] (symmetrically equivalent to [100]) [94].

A field in the [100] direction favours a single particular two-in-two-out arrangement of spins. Monopole/anti-monopole quasiparticle pairs are then thermally excited out of this ground state by flipping a single spin and are then free to separate creating Dirac strings. Recall that the act of separating a monopole/anti-monopole in the spin ice state creates a chain of flipped spins connecting the two defects. This chain of flipped spins represents an infinitely thin line of magnetic flux known as a Dirac string [10]. These Dirac strings reveal themselves as cones of scattering in the neutron scattering data which are reproduced in simulations [94]. They also measured the specific heat in DTO and found reasonable agreement with the Debye-Hückel theory of a dilute Coulomb gas below 1 K [93]. This is evidence for monopole-like excitations out of the spin ice ground state.

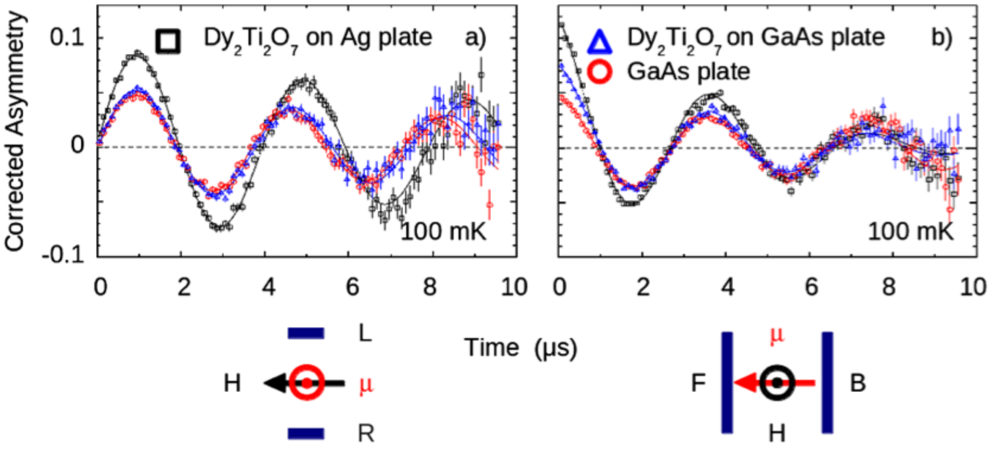

Figure 5.10: Muon spin precession of $Dy_2Ti_2O_7$ on a Ag mount and a GaAs mount as well a GaAs plate with no sample mounted measured by Dunsiger *et al.* [11]. This was used as evidence that the μSR measurements of DTO in Ref. [95] were not sensitive enough to detect monopole signatures, and they were merely measuring the sample holder.

Two separate groups used transverse field muon spin relaxation (μSR) to probe the local spin fluctuation rate in DTO in order to extract the magnetic charge of a monopole and the associated magnetic current [95, 11]. Bramwell *et al.* originally found that the muon precession decay rate corresponded to an effective elementary magnetic charge of $Q \sim 5\mu_B \mathring{A}^{-1}$ [95]. However, Dunsiger *et al.* refuted this report on account that transverse field μSR is unable to resolve the monopole excitations [11]. Monte Carlo simulations showed that the local field at the muon sites is on the order of 300 mT, which is much larger than the monopole signature, on the order of 1 mT [11]. This shows that transverse field μSR does not have the sensitivity required for detecting the monopole excitations in spin ice materials. Furthermore, Dunsiger *et al.* claimed that the exponential decay in the spin precession observed by Bramwell *et al.* was actually an artefact of the GaAs sample mount rather than from the monopole excitations. Thus, μSR measurements were conducted on DTO situated on both a GaAs mount and a Ag mount as well as a GaAs mount with no sample present (figure 5.10). This produced clear evidence that the muon precession seen in by Bramwell *et al.* [95] was largely due to the GaAs sample mount. However, careful μSR measurements in various configurations revealed persistent spin dynamics below 5 K, evidence for a low temperature thermally activated behaviour. Therefore, this technique neither proves or disproves the existence of monopole excitations, due to the fact that it does not possess the required resolution to accurately detect their local magnetic field.

The low temperature magnetic relaxation time in DTO was extracted by a.c. susceptibility measurements below 2 K [96] and by a boundary-free magnetization transport measurements of a toroidal sample below 3 K [97]. The toroidal geometry of the DTO sample removes any boundaries in the direction of the magnetization transport. Both of these studies yield similar results which show that the relaxation time for $T \gtrsim 1$ K is adequately described by the dipolar spin ice model (described by equation 5.13) or alternatively by Debye-Hückel theory for a dilute sea of monopole excitations. However, these models fail to accurately describe the ultra-slow spin dynamics observed below 1 K which follows a stretched exponential decay, rather than a simple Arrhenius temperature dependence. Revell *et al.* used Monte Carlo simulations to show that the rapidly diverging relaxation time can be caused by surface effects and a small level of Dy substitution on the Ti sub-lattice on the order of 0.3% [96]. This type of substitution is commonly referred to as stuffing, and is known to occur in the rare-earth titanates [98]. Nonetheless, this interpretation is consistent with the existence of monopole-like excitations. On the other hand, Kassner *et al.* suggests that the extended relaxation time observed in DTO at low temperature is an indication of a supercooled correlated spin liquid which is approaching a glass transition at $T_o = 240$ mK [97]. That is, if the temperature is lowered sufficiently faster than the magnetic relaxation time, then the system enters a meta-stable, supercooled state. Kassner *et al.* stress that this state does not constitute a classical spin glass since the spins are located on an ordered crystal lattice with identical spin Hamiltonians. Rather, the supercooled state is better described by the freezing of the spins in some microscopic configuration which could alternatively be described as the freezing of some configuration of monopoles. That said, they state that this result is inconsistent with the monopole dynamics predicted by the dipolar spin ice model.

Additional susceptibility measurements were conducted at temperatures above 2 K by Bovo *et al.* [12] to test the theory of Ryzhkin [2] which considers monopole transport in spin ice by drawing analogies to Jaccard's theory of proton defect motion in water ice [99].

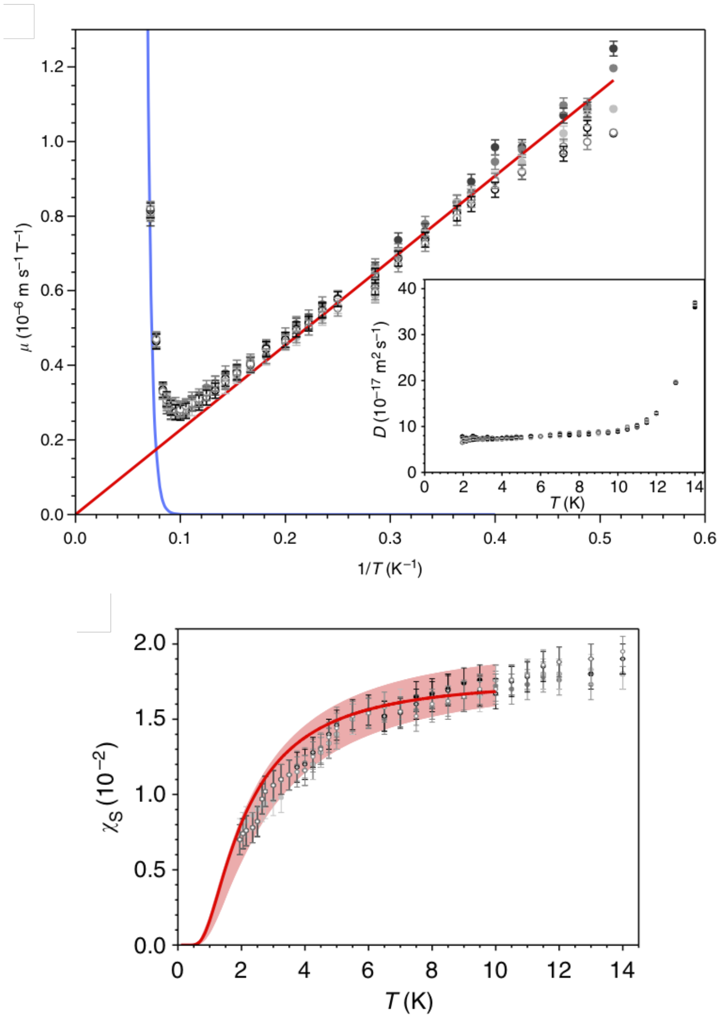

Figure 5.11: *Top:* Monopole mobility measured between 0 T and 38.5 mT plotted versus $1/T$. The blue line is the expected divergent behaviour of Orbach type spin flips above 10 K and the red line is proportional to $1/T$ consistent with the Nernst-Einstein equation [12]. The inset shows the temperature dependence of the diffusion constant D. *Bottom:* The temperature dependence of the adiabatic susceptibility χ_S of DTO follows the monopole density (solid red line) [12].

Bovo *et al.* modified Ryzhkin's expression for the frequency dependent susceptibility, $\chi(\omega)$, by including a finite adiabatic susceptibility such that

$$\frac{\chi(\omega) - \chi_{\mathrm{S}}}{\chi_{\mathrm{T}} - \chi_{\mathrm{S}}} = \frac{1}{1 + i\omega\tau}. \tag{5.18}$$

Here χ_{S} is the adiabatic susceptibility (the infinite frequency limit), χ_{T} is the isothermal susceptibility (the low frequency susceptibility), and τ is the relaxation time. This expression is identical to that of an ordinary paramagnet, however, in this case τ is a function of monopole parameters, rather than spin parameters. The relaxation time can be written as $\tau^{-1} = \mu_o u Q x / V_o \chi_{\mathrm{T}}$ where u is the monopole density, $Q = 4.266 \cdot 10^{-13}$ JT^{-1}m^{-1} is the monopole charge, x is the monopole density per diamond lattice site and $V_o = 1.29 \cdot 10^{-28}$ m^3 is the volume of each diamond lattice site. Here, $\chi_{\mathrm{T}}(T)$ can be measured directly and $x(T)$ is determined by fitting specific heat to the Debye-Hückel theory. With this information, they were able to examine the monopole mobility. Below 10 K they find that $u(T) \sim T^{-1}$, in agreement with the Nernst-Einstein equation for Brownian diffusion of magnetic monopoles [12]. From this, they find a temperature independent monopole hopping rate of $v_o = 2.43 \cdot 10^3$ s^{-1}, consistent with Ryzhkin's theory [2] and Jaubert's numerical results [100]. The Curie-like behaviour of the isothermal susceptibility, χ_{T}, is indicative of a purely spin system. Considering the susceptibility in the infinite frequency limit yields the adiabatic susceptibility, χ_{S}. Figure 5.11 shows the fascinating result that χ_{S} is directly proportional to the monopole density per tetrahedron. They interpret this as the observation of a frictionless oscillation of the monopole excitations analogous to plasma oscillations in an electrical plasma. Finally, they conclude that just as water ice can be thought of as a protonic semiconductor then spin ice can similarly be thought of as an intrinsic monopole semiconductor.

There is no obvious magnetic analogue to electrical conductivity measurements to probe a potential magnetic current in spin ice. This is in part due to the fact that the monopole excitations are confined to the diamond sub-lattice in the spin ice materials and hence there is no monopole source or drain like there is in electric circuits. Thus, perhaps the most effective method for observing monopole dynamics in the spin ice materials is through thermal transport measurements. The thermal gradient across the sample generates an increased monopole density at the hot end of the sample which then diffuses towards the cold end of the sample which has a lower density of excitations. There have been a number of recent thermal transport studies on both DTO and HTO yielding similar results, yet presenting varying interpretations concerning the role monopole excitations play in the behaviour of the conductivity [86, 14, 101, 102, 103, 104, 105, 13]. One interpretation is that monopole excitations contribute to the conductivity in addition to the phonons [14, 101, 103, 104, 105], while others claim that the magnetic excitations only affect the conductivity via acting as phonon scattering mechanisms [86, 102, 13].

Klemke *et al.* measured the thermal conductivity of DTO between 300 mK and 40 K in zero field and in field up to 1.5 T ∥ [110] [86]. The conductivity is modelled using the Debye-Callaway model and kinetic theory which states

$$\kappa(T) = \frac{16\pi^5}{15}\frac{k_B^4}{h^3 v_s}\frac{T^3}{\sum_\nu\left(\tau_\nu^{-1}\right)} \tag{5.19}$$

where τ_ν^{-1} are the scattering rates from the sample boundaries (v_s/d), dislocations ($A_D T^4$) and Umklapp processes ($A_U T^4 \exp\left(-\alpha\Theta_D/T\right)$). This adequately describes the zero field data in the temperature range above 10 K. However, below this temperature an additional magnetic scattering channel with scattering rate $1/\tau_\gamma$ is needed to fit the data. This is done because they fail to observe the usual T^3 temperature dependence of boundary limited phonons at low temperature. This magnetic scattering rate is shown to have an exponential form with an activation energy of 5.3 K, comparable to the creation energy of a monopole excitation. Therefore, they claim that monopole quasiparticles exist in the spin ice framework, however the monopoles only affect the thermal conductivity by acting as a phonon scattering mechanism.

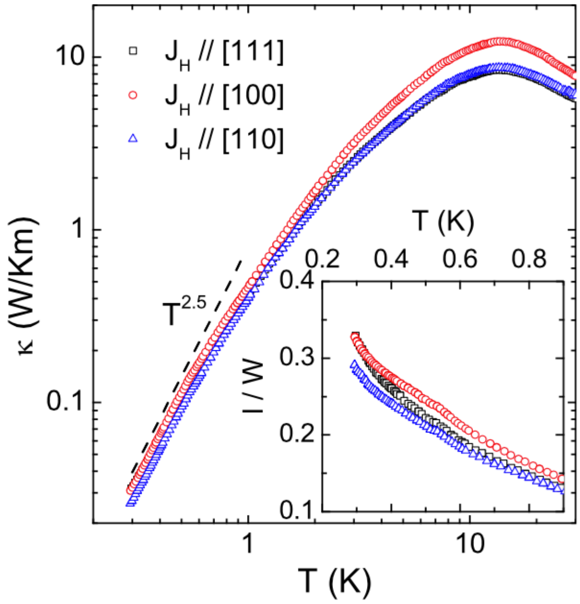

Figure 5.12: Thermal conductivity and phonon mean free path (inset) of DTO measured by Li *et al.* [13].

A few years later, a group from Hefei National Laboratory in China also reported thermal conductivity measurement of DTO between 300 mK and 100 K [102, 13]. They came to the same conclusion as Klemke *et al.* for two reasons. First, they plotted the phonon mean free path (l) of the zero field data by dividing out the phonon specific heat ($C_{\text{ph}} = \beta T^3$) and the sound velocity (v_{s}) from the conductivity according to kinetic theory such that $l = 3\kappa_{\text{ph}}/\beta T^3 v_{\text{s}}$. This reveals a mean free path that is only approximately 35% of the average sample width, meaning the phonons are far from the boundary scattering limits. They interpret this as a result of monopole-phonon scattering. Second, although they do observe a magnetic contribution to the conductivity by applying a magnetic field in the [100] direction, they show that it cannot be due to monopole excitations by using a kinetic theory for the monopoles similar to the kinetic theory for phonons. Using expressions for the monopole specific heat and mean free path, they deduce the monopole velocity would need to be on the order of $2 \cdot 10^4$ m/s to describe the observed magnetic conductivity. This value is unreasonably large considering monopoles have been shown to be dispersionless quasiparticles [23]. Therefore, they again suggest that monopole excitations may exist in spin ice materials, however they do not positively contribute to the conductivity.

Our group also attempted to describe the magnetic channel of conductivity using a kinetic theory approach [103]. We considered two scenarios, first, Kolland *et al.* estimated the monopole velocity by assuming an effective hopping bandwidth of ~ 1 K, yielding a velocity of ~ 20 m/s [14]. This leads to a monopole mean free path of about 1 μm, which is close to 3000 lattice spacings. If we rather consider a hopping frequency of $1.8 \cdot 10^3$ s^{-1} determined from relaxation experiments, we find a monopole velocity 10^6 times smaller than the first estimate and a mean free path on the order of meters which is many orders of magnitude larger than the sample. In general, kinetic theory is used to describe free particles which travel in ballistic trajectories and therefore is not applicable to monopole excitations which are confined to hopping on a diamond lattice in the spin ice materials. This leads us to the conclusion that monopole excitations require a more sophisticated theory to describe their dynamics.

Finally, a group from Köln, Germany have done extensive temperature and field dependent thermal conductivity measurements on both DTO and HTO [14, 101, 104, 105]. Their field dependent conductivity exhibits a low field suppression corresponding with an increase in the magnetization when the applied magnetic field is in the [001] direction (figure 5.13). As we will see in the following section, a [001] field affects the four spins at each vertex of the tetrahedra in the pyrochlore lattice equally. This induces a large Zeeman energy that selects one of the degenerate 2-in-2-out ground states. Thus, the [001] field effectively suppresses the formation of monopole excitations (3-in-1-out spin configurations). They interpret this finding as clear evidence that the monopole excitations do in fact contribute to the low temperature thermal conductivity. By assuming the data at 0.5

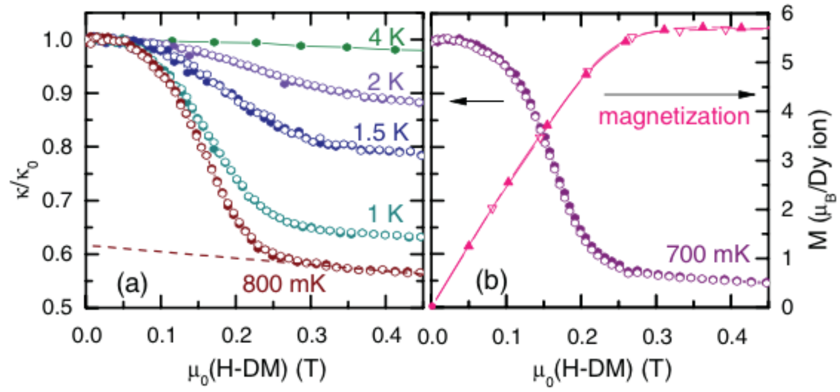

Figure 5.13: Field dependence of the thermal conductivity of DTO for $\mu_o H \parallel [001]$ measured by Kolland *et al.* [14].

T is purely due to phonons, they can estimate the magnetic contribution by considering the difference between the zero field data and the 0.5 T data. Figure 5.14 shows the monopole contribution to the thermal conductivity, revealing a peak at ~ 1 K, coinciding with the peak in the specific heat. The diffusion coefficient of the monopole excitations is defined as $D_{\mathrm{mag}} = \kappa_{\mathrm{mag}}/c_{\mathrm{mag}}$. Below 1 K, D_{mag} becomes large indicating a long monopole mean free path, consistent with a low density of monopole excitations.

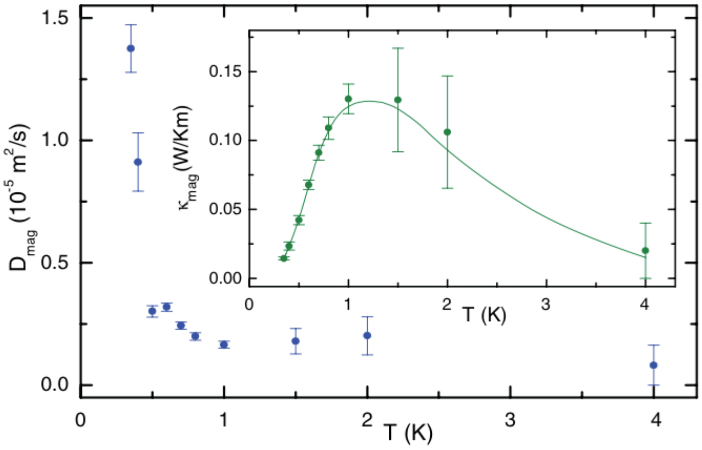

Figure 5.14: The diffusion coefficient of the monopole excitations defined as $D_{\mathrm{mag}} = \kappa_{\mathrm{mag}}/c_{\mathrm{mag}}$. *Inset:* The magnetic contribution to the thermal conductivity [14].

Therefore, there is clearly conflicting evidence for and against the realization of monopole quasiparticle excitations in the spin ice ground state. Additional experimental and theoretical input is required to help clarify this issue. Furthermore, if the excitations in the spin ice state can be described as monopole excitations, there is still a great deal to learn about how they interact with each other and with the lattice where they reside as well as how they behave in a magnetic field.

5.4.2 Spin ice in a magnetic field

The effect of an applied magnetic field on a spin ice material is highly anisotropic. The strength of the Zeeman energy of each Ising-like spin on the vertices of a single tetrahedron (labelled 1 through 4 in figure 5.15) will depend on the direction of the applied field since the easy axis of neighbouring spins are rotated by 109.5° with respect to each other. Thus, it is possible for an applied field along a specific crystallographic direction to polarize certain spins, while other spins remain dynamic. This results in rich field versus temperature phase diagrams. The effect of an external field applied along three cubic directions of high symmetries ([100], [110], [111]) of the pyrochlore lattice are considered below.

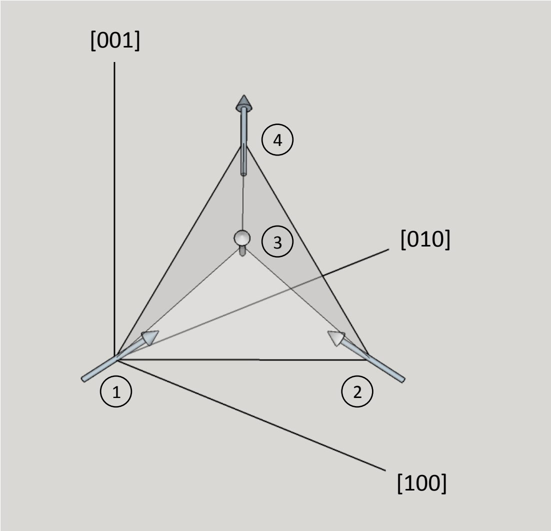

Figure 5.15: A single tetrahedron from the pyrochlore lattice found in spin ice materials. Each of the four spins (labelled one through four) are aligned with a line segment connecting the center of one triangular face to the opposite vertex.

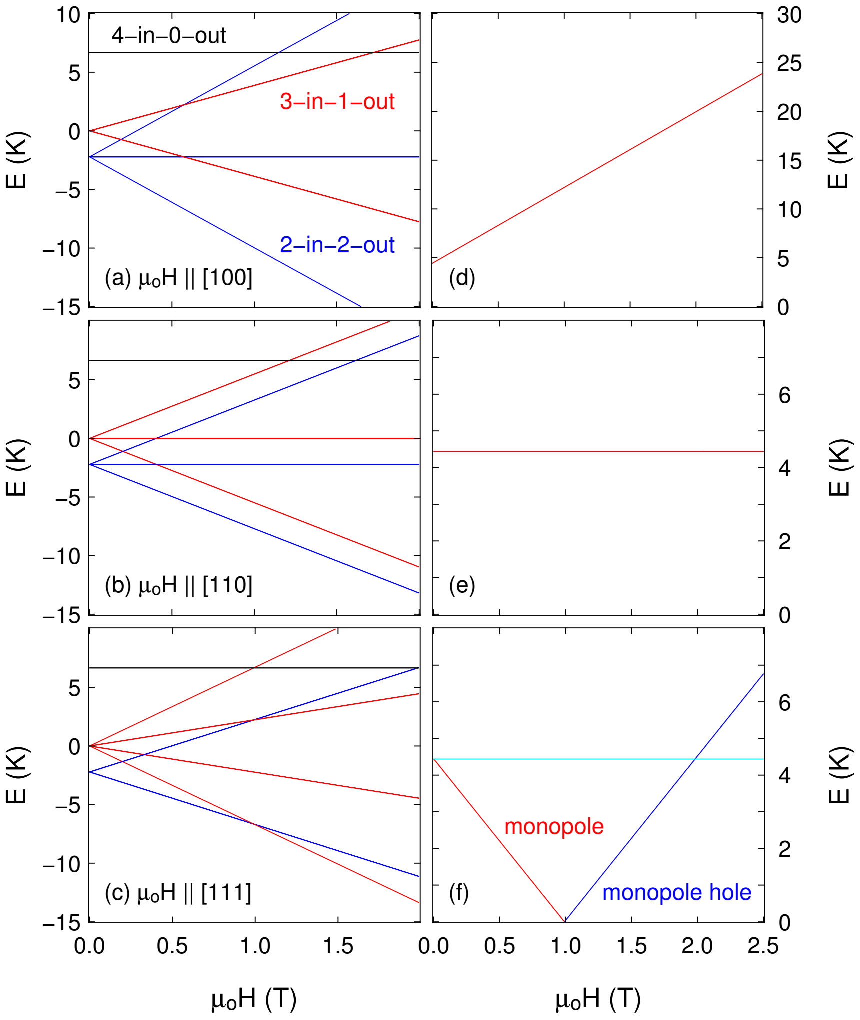

Figure 5.16: (a-c) The Zeeman energy splitting for each spin configuration (blue is 2-in-2-out, red in 3-in-1-out/1-in-3-out and black is 4-in-0-out/-o-in-4-out) for $Dy_2Ti_2O_7$ when $\mu_o H \parallel [100], [110], [111]$. (d-f) The single spin flip excitation energy. When the field is greater than ∼ 1 T in the [111] direction, the 1-in-3-out phase becomes the ground state and a spin flip results in neighbouring tetrahedra with the 2-in-2-out configuration (monopole holes).

$\mu_o \mathbf{H} \parallel$ [100]

The Zeeman energy caused by a [100] field is equivalent for all spins and is equal to $\frac{1}{\sqrt{3}} g_J J \mu_B \mu_o H$. This breaks the six-fold degeneracy of the spin ice manifold by lowering the energy of a single 2-in-2-out configuration (spins 1 and 4 point in, and spins 2 and 3 point out in figure 5.15) resulting in a long range ordered state [106]. Figure 5.16 (a) shows the splitting of the 2-in-2-out and the 3-in-1-out/1-in-3-out spin configurations as the field is increased. Figure 5.16 (d) shows how the excitation energy for a single spin flip increases linearly with field illustrating how a [100] field suppresses monopole excitations. When the field is large compared to the temperature of the system, the magnetization per Dy atom saturates at a value $M = \frac{1}{\sqrt{3}} g_{\mathrm{J}} J \approx 5.78 \mu_{\mathrm{B}}/\mathrm{Dy}$ since $g_{\mathrm{J}} J \approx 10 \mu_{\mathrm{B}}$ for Dy. This behaviour is experimentally observed (figure 5.17).

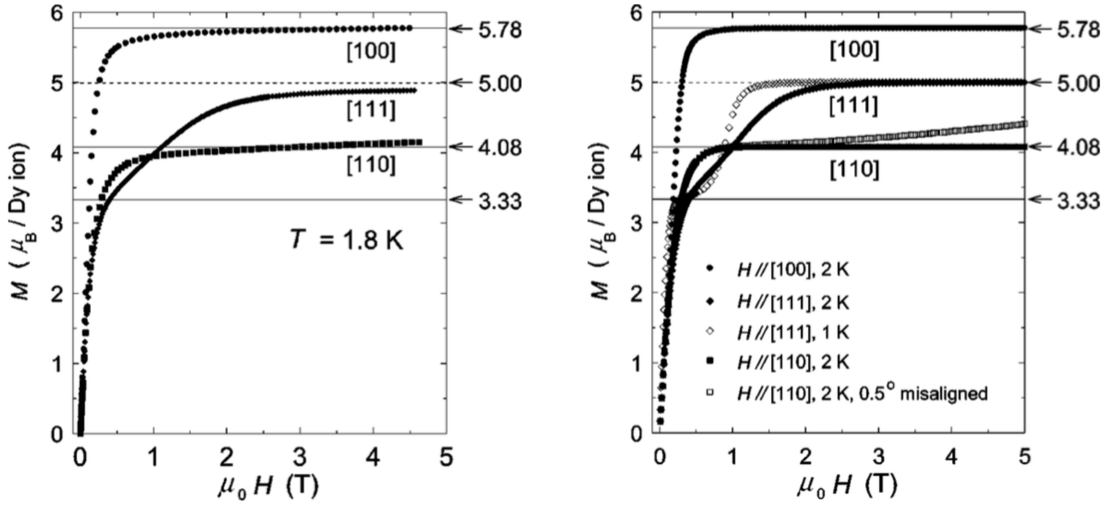

Figure 5.17: Measured (left) and simulated (right) magnetization curve of DTO with the field along [100], [110] and [111] [15].

$\mu_o \mathbf{H} \parallel$ [110]

Applying a field in the [110] direction affects the spins 1 and 2 equally causing a Zeeman energy of $\sqrt{\frac{2}{3}} g_{\mathrm{J}} J \mu_{\mathrm{B}} \mu_o H$. Spins 3 and 4, however, are perpendicular to the field direction and thus are completely unaffected by the magnetic field. This essentially decouples the spins into sets of perpendicular chains. The spins on the α chain (parallel to [110]) are polarized by the applied field whereas the β chain (parallel to $[1\bar{1}0]$) spins are free to fluctuate, maintaining the 2-in-2-out ice rules [106, 107]. The energy splitting of each spin configuration is seen in figure 5.16 (b), but what is interesting about this is that the spin flip excitation energy remains unaffected by the magnetic field due to the independent β

chains. Furthermore, due to two spins from each tetrahedra being perpendicular to the field direction, the magnetization for DTO only achieves a maximum value of $M = \frac{1}{\sqrt{6}} g_{\mathrm{J}} J \approx 4.08\mu_{\mathrm{B}}/\mathrm{Dy}$. Figure 5.17 shows that slightly tilting the sample towards the [100] direction with respect to the field direction leads to a small component of the β chain spins to align with the field, causing a high field increase in the magnetization.

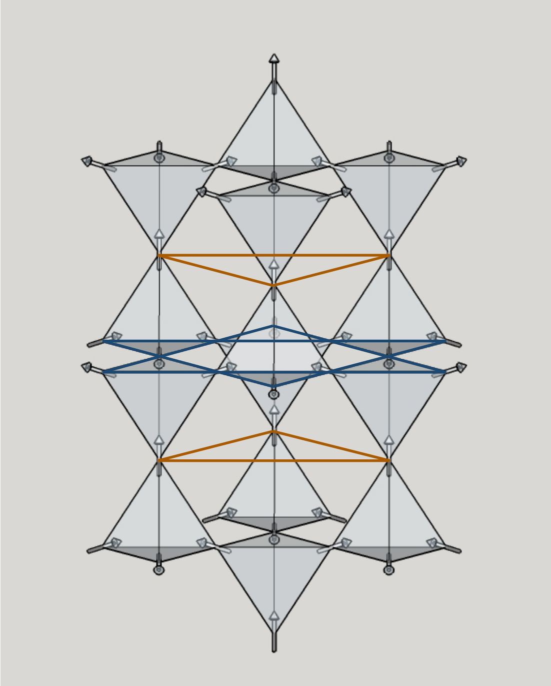

Figure 5.18: A pyrochlore lattice is comprised of alternating Kagomé (blue) and triangular (orange) layers stacked in the [111] direction.

$\mu_o\mathbf{H} \parallel$ [111]

The pyrochlore lattice can be thought of as alternating layers of Kagomé planes and triangular planes stacked in the [111] direction. This is illustrated in figure 5.18 as orange triangles and a blue Kagomé pattern. The local $\langle 111 \rangle$ quantization of the spins means that the spins on the triangular planes are parallel to the applied field in the global [111] direction whereas the spins on the Kagomé planes will have components both parallel and perpendicular to the field. The Zeeman energy for the triangular plane spins is equal to $g_{\mathrm{J}} J \mu_{\mathrm{B}} \mu_o H$, which is considerably larger than for the Kagomé plane spins, which have a

Zeeman energy of $\frac{1}{3}g_\mathrm{J}J\mu_\mathrm{B}\mu_oH$. This tends to promote the creating of monopole excitations by lowering the spin flip excitation energy. An additional fascinating consequence of the difference in energy scales is that at low temperatures, a single spin from each tetrahedron will align with the magnetic field leaving the other three spins free to arrange themselves according to the ice rules. This effectively reduces the dimensionality of the spin ice manifold to a set of decoupled two dimensional planes. This special case of the spin ice state is referred to as the "Kagomé ice" phase, since the dynamics, and hence the monopole excitations, are confined to the Kagomé planes [108, 109]. The Kagomé phase is observed in magnetization measurements of DTO as an intermediate plateau at $M = \frac{1}{6}g_\mathrm{J}J \approx 3.33\mu_\mathrm{B}/\mathrm{Dy}$ [110, 111, 80]. Increasing the field further results in a competition between the nearest neighbour interactions which satisfy the ice rules, and the Zeeman energy which prefers the alignment of the spins with the field. The energy cost of flipping a spin on the Kagomé plane, creating neighbouring tetrahedra in the 3-in-1-out/1-in-3-out configuration, can be estimated for DTO at $4J_\mathrm{eff} = 4.44$ K [5]. The Zeeman energy gain, on the other hand, is equal to $2E_\mathrm{Z}^\text{Kagomé} = 6.66\mu_\mathrm{B}\mu_oH$. Equating these two energies, we find that the Zeeman energy surpasses the exchange interaction when $\mu_oH = 1.0$ T. Above this field, all the spins align with the field forming a 3-in-1-out ordered phase. This can be visualized as alternating layers of monopoles and anti-monopoles. So, the ordered state can be equally referred to as a monopole crystal. In this state, flipping a spin results in neighbouring tetrahedra with a 2-in-2-out arrangement of spins, thus these excitations are effectively monopole holes [112]. The excitation energy for monopoles, and monopole holes as the field is increased is seen in figure 5.16 (f).

Thermal runaway processes

The slowing of spin dynamics in the spin ice state as $T \to 0$ K leads to unusual out-of-equilibrium scenarios when applying an external magnetic field experimentally. Below the spin 'freezing' temperature at ~ 600 mK, the spins are unable to track an increasing magnetic field, even for very slow field sweep rates resulting in the inability to follow the equilibrium magnetization curves. Slobinsky *et al.* examined this phenomena by studying the field dependent magnetization as a function of both temperature and field sweep rate along the [111] direction [16]. Figure 5.19 shows that at temperatures below 600 mK, the low field magnetization is initially much shallower than the equilibrium curve when the field is swept at a rate of 0.1 T/min. However, as the field is increased, the magnetization quickly jumps to a value greater than the equilibrium magnetization, followed by a flattening into an intermediate plateau before additional subsequent jumps until the saturation value is achieved. The inset in figure 5.19 shows the magnetization curves plotted versus internal

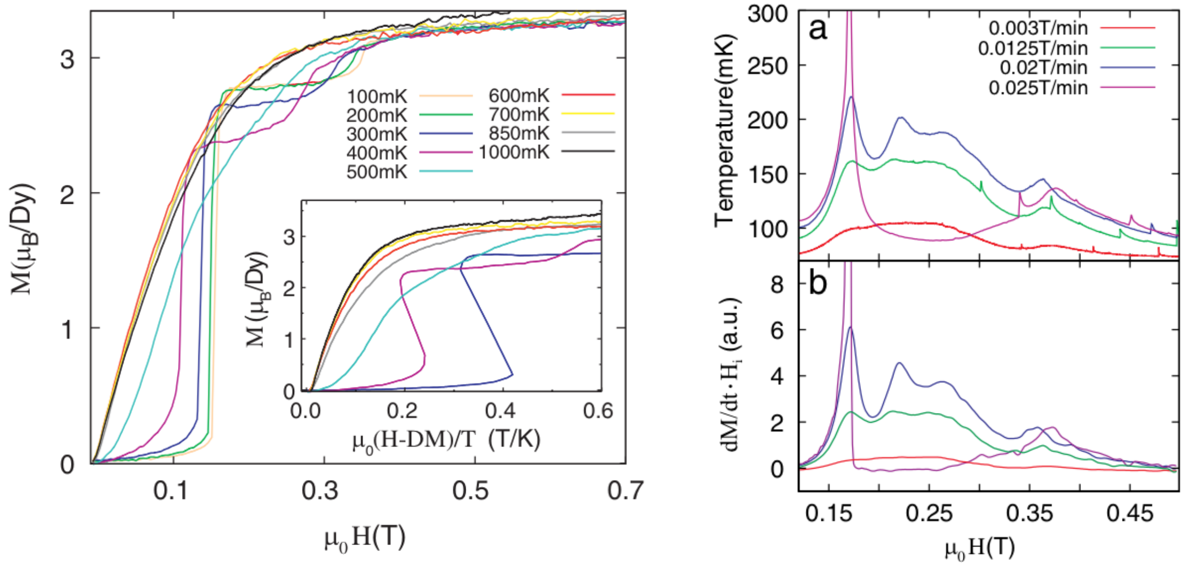

Figure 5.19: *Left:* The field dependence of the magnetization of $Dy_2Ti_2O_7$ between 100 mK and 1 K at a sweep rate of 0.1 T/min. Sharp jumps are seen in the magnetization for $T \lesssim 600$ mK [16]. *Right:* Local heating in the sample is observed as peaks in the temperature of the sample. The temperature spikes are correlated to the release of Zeeman energy which is proportional to HdM/dt.

magnetic field, revealing a negative slope in the magnetization. This suggests that the jumps in magnetization are triggered events, meaning once the critical field is reached, the spin flip processes do not stop even though the internal field is less than the critical field. Furthermore, the jumps in the magnetization are accompanied by sudden increases in the sample temperature as seen in the right side of figure 5.19. This is attributed to the so called 'thermal runaway process', where the field induced creation of a monopole/anti-monopole pair will release a certain amount of Zeeman energy into the system. This release of energy leads to a localized heating in the neighbourhood of the spin flip event, resulting in the creation of more monopole excitations. The rate at which the Zeeman energy is released is proportional to the field sweep rate so quicker sweep rates will cause larger temperature spikes. Additionally, the phonons are unable to effectively dissipate the heat due partly to a phonon bottleneck effect, and possibly due to the decoupling of the spins from the lattice which has been proposed to occur in DTO [7, 8]. Therefore, when conducting field dependent measurements of the spin ice materials at low temperature, it is very important to ramp the field as slow as possible to avoid large spikes in the sample temperature and to follow a quasi-static sweep procedure, allowing ample time for the phonons to dissipate any accumulated heat.

5.5 Quantum Spin Ice

5.5.1 From classical to quantum

The previous section considered a semi-classical system of Ising spins situated on a pyrochlore lattice with an effective ferromagnetic (FM) nearest neighbour interaction. Recall from equation 5.12 that the Hamiltonian of this classical spin ice system (CSI) can be written as

$$H_{\mathrm{CSI}} = -J_{\parallel} \sum_{\langle ij \rangle} S_i^z S_j^z. \tag{5.20}$$

where $J_{\parallel} > 0$ is the effective nearest neighbour exchange parameter [5]. The z superscript refers to the local $\langle 111 \rangle$ anisotropy of the spins, meaning that the spins point directly towards or away from the center of the tetrahedron. We have seen how this Hamiltonian supports a highly degenerate ground state referred to as the classical spin ice state which has a residual entropy equivalent to Pauling's estimate for water ice ($S_o = (Nk_{\mathrm{B}}/2)\ln(3/2)$). The 2-in-2-out spin ice correlations are observed in neutron scattering measurements as singularities in reciprocal space with a characteristic pinch-point structure around it [80]. Furthermore, spin flip excitations from the spin ice state can be thought of as emergent magnetic monopoles. Thus an effective theory of the low energy excitations in dipolar spin ice is that of a magnetic Coulomb gas in the grand canonical ensemble where the magnetic charges are confined to the diamond sub-lattice of the pyrochlore lattice.

The spins in a quantum spin ice (QSI) are no longer Ising-like as in the CSI case, rather they have an additional transverse component [18]. Hence, the spins are characterized by three orthogonal components, S_i^z, S_i^+, and S_i^-. In this case, additional terms are included in the Hamiltonian to account for the coupling between the different spin directions [18, 17, 22]. The explicit form of the full QSI Hamiltonian is

$$\begin{aligned} H_{\mathrm{QSI}} = \sum_{\langle ij \rangle} \{ & J_{zz} S_i^z S_j^z - J_{\pm}(S_i^+ S_j^- + S_i^- S_j^+) \\ & + J_{\pm\pm}(\gamma_{ij} S_i^+ S_j^+ + \gamma_{ij}^* S_i^- S_j^-) \\ & + J_{z\pm}\left[S_i^z(\zeta_{ij} S_j^+ + \zeta_{ij}^* S_j^-) + i \leftrightarrow j\right] \} \end{aligned} \tag{5.21}$$

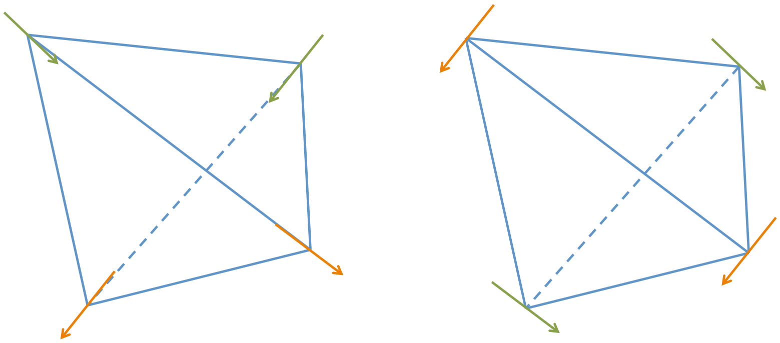

Figure 5.20: *Left:* The spins in a classical spin ice have an easy-axis anisotropy parallel to the local [111] direction. *Right:* The spins in a quantum spin ice have an easy-plane anisotropy perpendicular to the local [111] direction.

where $\gamma_{ij} = -\zeta_{ij}^*$ is a complex unimodular matrix defined in reference [18]. The first term in equation 5.21 is the usual CSI Hamiltonian defined in equation 5.20, which is responsible for the spin degeneracy at low temperature. The other three terms are the remaining nearest neighbour interactions allowed by symmetry [18, 113, 17, 114].

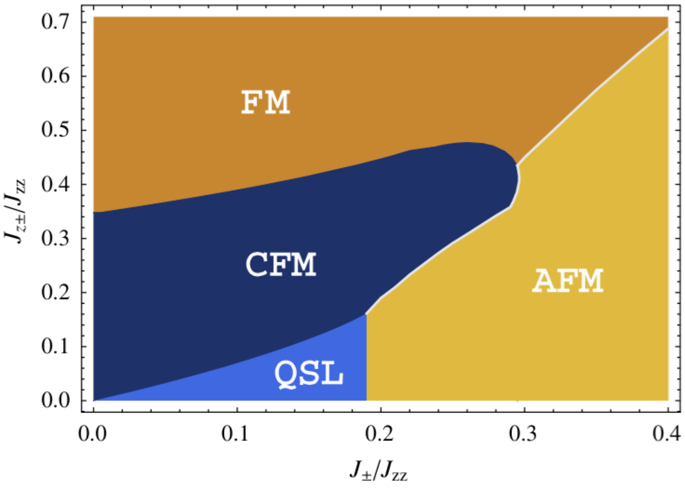

Figure 5.21: A phase diagram of $J_{z\pm}$ versus $J_\pm$ for the QSI model determined by a gauge mean field theory by Savary *et al.* [17].

A simplified version of this model has been studied theoretically which only considers the $J_\pm$ and J_{zz} interactions [115, 116]. These reports find that for a sufficiently small $J_\pm/J_{zz}$ ratio, the QSI model can support a quantum spin liquid (QSL) ground state which avoids magnetic ordering and remains dynamic at absolute zero. It has also been suggested that the addition of $J_z\pm$ may also help stabilize the QSL state for slightly larger values of $J_\pm$ as seen in figure 5.21 [17, 114]. The QSL state is essentially a quantum analogue of the Coulombic phase of the the CSI state. In other words, instead of the emergent magnetostatics and dispersionless magnetic monopole excitations in the classical spin ice, the quantum spin liquid state can harbour a complete electrodynamic field with emergent photon-like excitations with a linear dispersion in addition to quantum monopole quasiparticles as seen in figure 5.22 [113, 17, 114, 23].

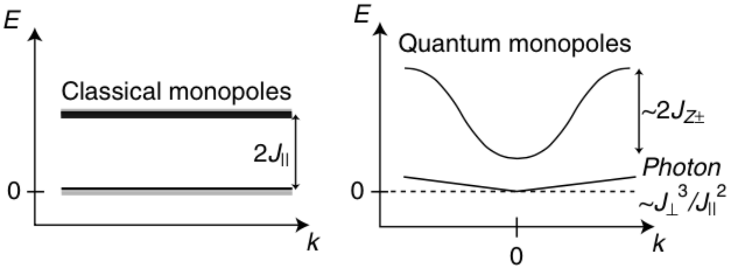

Figure 5.22: Structure of the dispersion for classical monopoles (left) and quantum monopoles and emergent photons (right) [23].

5.5.2 $Yb_2Ti_2O_7$

According to the previous section, a good place to start when searching for potential QSL candidates is with a material which exhibits the classical spin ice interactions yet is susceptible to significant quantum fluctuations which cause non-zero transverse terms in the Hamiltonian. Therefore the rare-earth pyrochlore materials are a sensible launching point for the realization of the QSL state. We will focus our attention on $Yb_2Ti_2O_7$ (YbTO) in this section as it possesses many qualities characteristic of a quantum spin ice [38, 18, 17].

The magnetic moment in YbTO is 1.3 μ_B, much smaller than the 10 μ_B moment in HTO and DTO [117]. Furthermore, the g-tensor components both parallel and perpendicular to the [111] direction have been calculated for YbTO reveal that $g_\parallel = 1.836$ cm^{-1} and $g_\perp = 4.282$ cm^{-1}, indicating an easy plane anisotropy perpendicular to the local [111] direction. To contrast this, the g-tensor values for HTO are $g_\parallel = 19.32$ cm^{-1} and $g_\perp = 0$

cm^{-1}, clearly demonstrating the [111] easy axis anisotropy (Ising like) [118]. Thus, YbTO can be described as an XY ferromagnet with a Curie-Weiss temperature of $\Theta_{\rm CW} \sim 0.5 - 0.75$ K obtained by fitting the susceptibility between 2.5 K and 10 K [117]. In addition to the easy plane anisotropy of the spin in YbTO, polarized neutron scattering measurements reveal pinch point features in the scattering intensity which are characteristic of spin ice correlations from dipolar interactions [41]. Therefore, YbTO exhibits all the attributes that are required to support a QSL state.

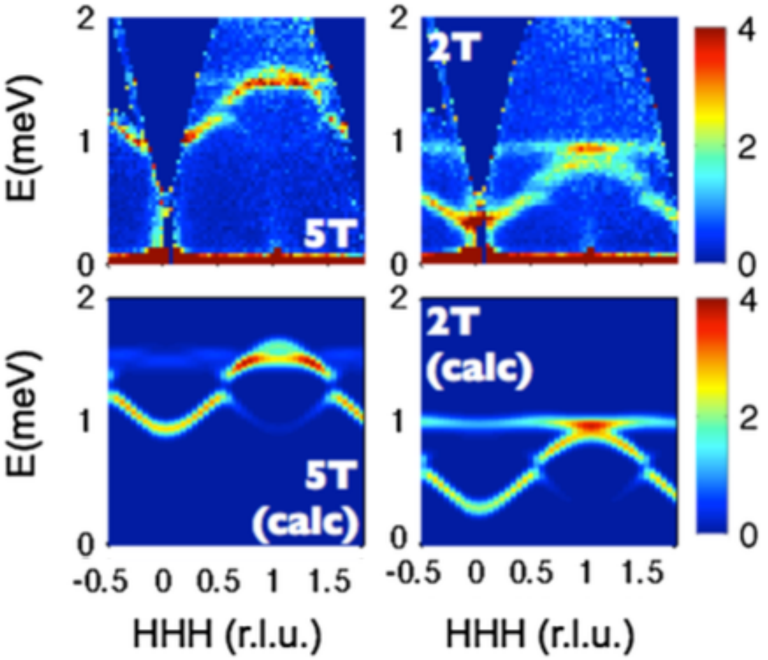

Figure 5.23: Inelastic neutron scattering intensity of YbTO in applied fields of 2 T and 5 T. The 5 T data was fitted using equation 5.21, and the resulting parameters successfully reproduced the 2 T data [18].

In 2011, Kate Ross *et al.* were successfully able to determine all of the parameters in the Hamiltonian [18]. This was achieved by using inelastic neutron scattering to probe the excitations in the field polarized paramagnetic state. The parameters they obtained from fitting their 5 T neutron scattering data to equation 5.21 are:

$$\begin{aligned} J_{zz} &= 0.17 \pm 0.04 \quad & J_{\pm} &= 0.05 \pm 0.01 \\ J_{\pm\pm} &= 0.05 \pm 0.01 \quad & J_{z\pm} &= -0.14 \pm 0.01 \end{aligned} \tag{5.22}$$

in meV. To show the success of this fit, they calculated the scattering intensity at 2 T revealing excellent agreement with their experimental results [18, 119]. This is illustrated in figure 5.23.

Considering the relative magnitudes of exchange parameters obtained from the fit, we find that $J_{\pm}/J_{zz} = 0.29$, and $|J_{z\pm}| \lesssim |J_{zz}|$. According to the phase diagram in figure 5.21, this would exclude YbTO from the QSL ground state. However, earlier inelastic neutron scattering experiments indicated low temperature two dimensional correlations which cross over into a regime of short range three dimensional correlations below ~ 240 mK [38]. That is, the ground state does not exhibit long range order below the transition at 240 mK. Therefore, it is possible that YbTO does magnetically order, but the order may have been suppressed in reference [18] due to lattice defects which may create domain walls, breaking up the order. The nature of the phase transition and the observed sample dependence in single crystals of YbTO is examined in the following two sections.

First order phase transition

In 1969, Blotë measured the specific heat of $Yb_2Ti_2O_7$ down to 50 mK. A broad mound was observed centred at approximately 3 K followed by a sharp peak at $T_c = 214$ mK, suggesting the onset of long range magnetic order. Close to fifty years later, there is still some debate about the true nature of the ground state. Hodges *et al.* have reported ^{170}Yb Mössbauer spectroscopy, μSR and neutron scattering measurements of YbTO [19]. The Mössbauer spectroscopy and μSR results reveal a suppression of spin fluctuations around T_c as seen in figure 5.24, however their neutron scattering data shows no signs of long range order [19]. A number of subsequent neutron scattering measurements have yielded similar results also showing no signs of long range order at low temperature [36, 37, 38, 39]. A more recent μSR measurement of both powder and single crystal samples of YbTO fails to exhibit the collapse in spin fluctuations at T_c which is consistent with the presence of quantum fluctuations [120].

Several other neutron scattering measurements have yielded contradicting reports to references [19, 36, 37, 38], stating that YbTO orders ferrimagnetically below T_c [40, 41]. Magnetization measurements have been conducted on both powder and single crystal samples of YbTO. The temperature dependence of the magnetization is seen in figure 5.25 revealing an irreversibility when zero-field-cooled or field-cooled below the transition temperature [20]. This is due to the formation of small domains when entering a ferromagnetic state. The fact that this field-cooled irreversibility occurs at 2 Oe indicates the barrier to overcome the domains is quite small. This could be a sign of strong spin fluctuations. Additionally, a small hysteresis loop opens with a width of 3 mK upon cooling and warming

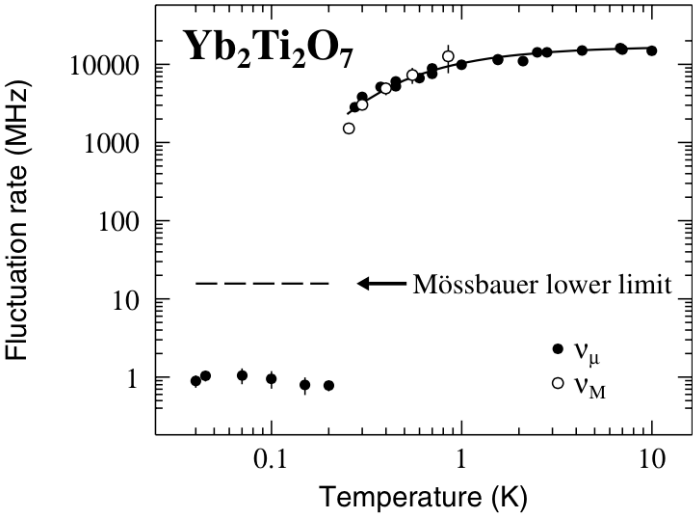

Figure 5.24: Mössbauer spectroscopy (ν_M) and μSR (ν_μ) measurements of YbTO reveal a collapse of the spin fluctuation rate at $T_c \sim 250$ mK [19].

through the transition temperature, indicating the first order nature of the transition. Both magnetization measurements and specific heat measurements performed in low magnetic fields $\lesssim 100$ mT have revealed an increase in the critical temperature, again suggesting the ferromagnetic nature of the phase transition [20, 22]. Therefore, these results suggest that the features at T_c indicate a first order phase transition into a ferromagnetically ordered state.

Sample dependence

The contradictory reports of the low temperature neutron scattering and μSR measurements seem to indicate a strong sample dependence in single crystals of YbTO. This sample dependence is extremely evident in the magnitude and locations of the peak in the specific heat. The specific heat feature in single crystals grown via the floating zone technique is quite broad and peaks around 150 mK, whereas the peak in sintered, powder samples is much more pronounced and occurs at higher temperatures between 250-265 mK as illustrated in figure 5.26 [121, 18, 120]. These incompatible results have lead to conflicting conclusions about the ground state of YbTO which has been described as being either a long-range ordered phase with ferromagnetic fluctuations [122], or a phase characterized by short-range correlated fluctuations [18]. Specifically, powder samples have shown a sharp

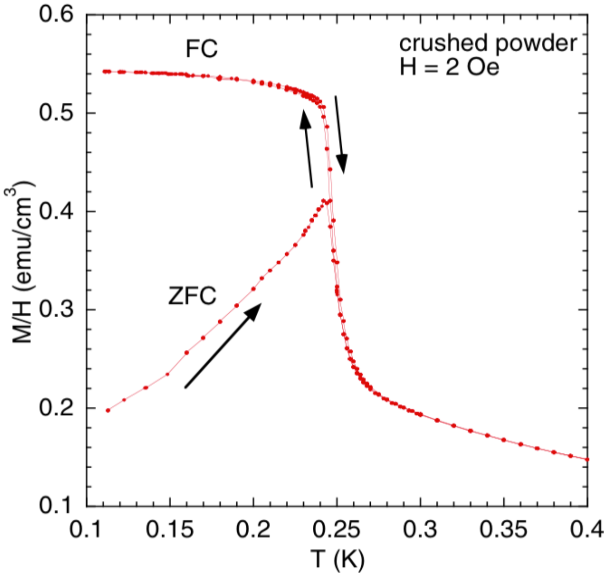

Figure 5.25: Field cooled and zero field cooled magnetization of YbTO [20]. A field cooled irreversibility is observed upon cooling below 250 mK.

first order drop in spin fluctuations at 250 mK, yet remain dynamic below this temperature, showing no signs of long range order [19, 123]. On the other hand, single crystals tend to exhibit a broad mound in the specific heat below 200 mK and can exhibit short range, three dimensional correlations [18]. However, other reports have shown single crystals of YbTO which exhibit a fairly sharp transition in the specific heat at approximately 200 mK and is accompanied by ferromagnetic order observed via neutron scattering below this temperature [40, 41]. The variation in the observed quantities may suggest that YbTO is in the vicinity of a quantum critical point separating a quantum magnetic Coulomb phase and an ferromagnetically ordered phase [41]. Therefore, there are clearly some issues with the reproducibility of the results arising from small irregularities in the crystal lattice. Thus, details of the sample quality must be well understood in order to determine the true ground state.

Ross *et al.* explored the differences in the physical properties of crushed single crystals grown via the floating zone technique and sintered stoichiometric powder samples by performing neutron scattering measurements. Although the starting materials were initially mixed in perfectly stoichiometric ratios [18], Rietveld refinements [124] of the neutron scattering data revealed a 2.3% substitution of Yb^{3+} on the Ti^{4+} lattice sites. This excess of

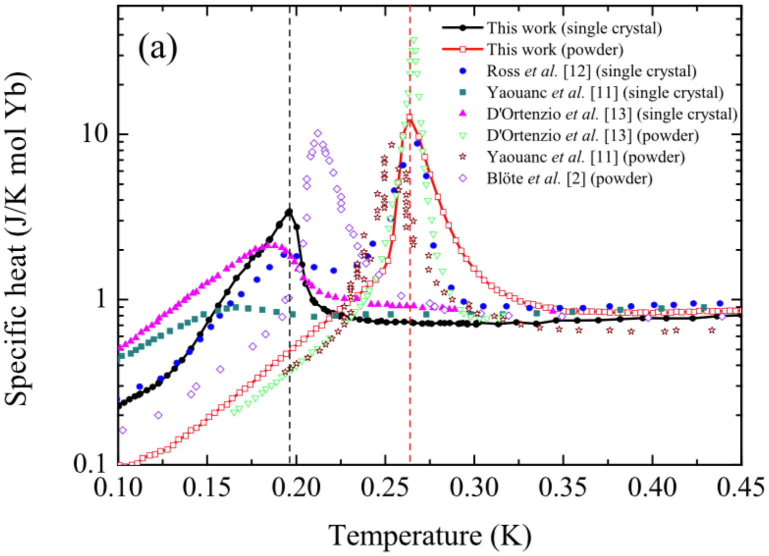

Figure 5.26: Temperature dependence of the specific heat for several powder samples and single crystals of $Yb_2Ti_2O_7$ [21]. The powder samples exhibit a sharp peak at approximately 265 mK, whereas the single crystals tend to exhibit a broad transition peak below approximately 200 mK.

magnetic moments on the titanium sub-lattice is referred to as stuffing. The randomly positioned stuffed magnetic ions provide additional nearest neighbour interactions with the Yb^{3+} ions in its vicinity, affecting the already frustrated exchange interactions. This could potentially lead to a spin glass state, which is consistent with the broad hump in the specific heat and reduced fluctuation time scales. Measurements of the lattice parameter also show an increased lattice constant for the stuffed sample due in part to the enlarged atomic radius of the Yb^{3+} ions. This was later confirmed by Baroudi *et al.* who performed detailed x-ray diffraction measurements on YbTO sample of known stuffing concentrations [125, 126]. Thus, the room temperature measurements of the lattice parameter can be a useful tool for determining the approximate stuffing concentration in YbTO samples.

An exploration of the zero field excitation spectrum in the ground state of YbTO has been conducted via neutron scattering and Monte Carlo simulations [22]. The exchange parameters resulting from this analysis revealed that the ground state of YbTO lies near a border between a splayed ferromagnetic (FM) phase and two antiferromagnetic (AFM) phases, ψ_2 and ψ_3, which are illustrated in figure 5.27 (c), (a) and (b) respectively. Figure 5.27 (d) shows the temperature versus J_2 exchange parameter phase diagram determined by Monte Carlo simulations using equation 5.21 [22]. The black line indicates a first order phase transition into the FM phase. The exchange coupling J_2 is a one dimensional measure of the anisotropic exchange in YbTO and is related to the parameters in the QSI Hamiltonian (equation 5.21) via $J_2 = 1/3(4J_{\pm\pm} - 4J_{\pm} + 4\sqrt{2}J_{z\pm} + J_{zz})$. The simulations find a range of J_2 parameters that accurately describes the neutron scattering data spanning from $J_2 = -0.34$ to -0.19 meV. Thus, the ground state of YbTO falls deep in the FM phase, or near the phase boundary with the ψ_3 antiferromagnetic phase. This result suggests that the proximity to the AFM phase is responsible for enhanced quantum fluctuations. It has also been suggested that the proximity to this phase boundary may explain the origin of the differing observed ground states due to varying exchange parameters caused by chemical pressure from disorder in the lattice [127]. This could also explain the variations in the shape and location of the peak observed in the specific heat, as well as the observation of two low temperature features in the specific heat [98].

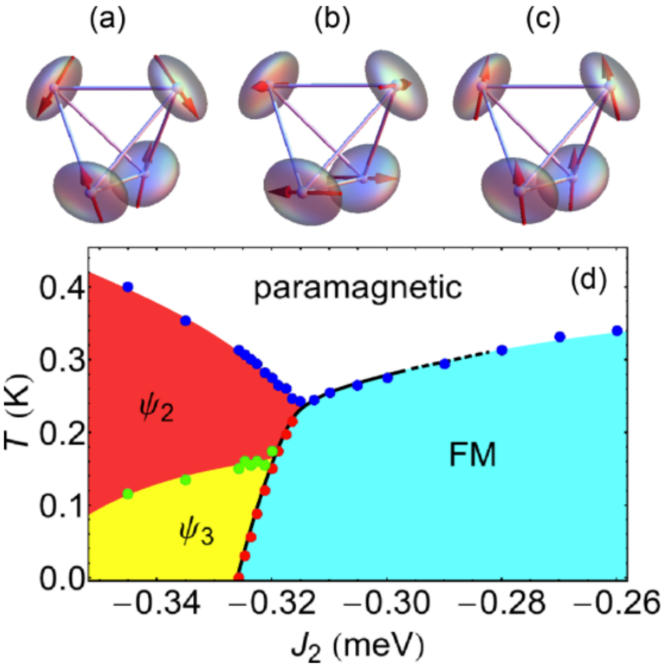

Figure 5.27: Spin configurations for the antiferromagnetic ψ_2 (a), ψ_3 (b) and splayed ferromagnetic (c) phases. The phase diagram of temperature versus an anisotropic exchange parameter J_2 at low temperature determined by equation 5.21. The black like indicates the range of J_2 values for which the transition in to the FM phase is first order [22].

Quantum monopole excitations

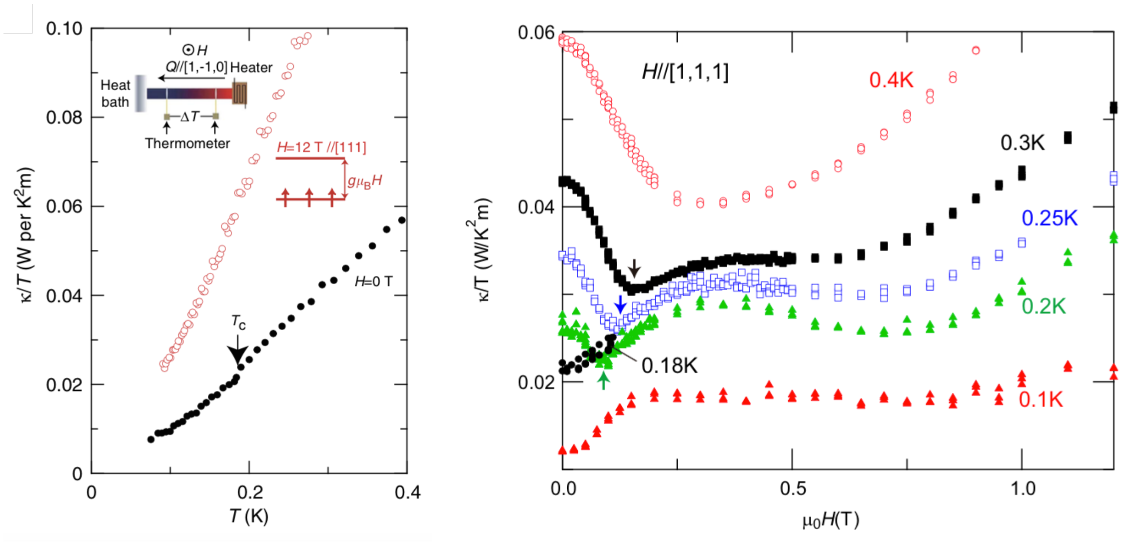

Figure 5.28: *Left:* Temperature dependence of the thermal conductivity of $Yb_2Ti_2O_7$. The kink in the zero field data just below 200 mK corresponds to the peak in the specific heat. *Right:* Field dependence of the thermal conductivity. The low field decrease disappears below 200 mK [23].

In the Coulombic ferromagnet (CFM) phase above the critical temperature, gapped excitations are observed in thermal transport measurements with an energy gap which is considerably suppressed compared to the semi-classical monopoles in the CSI state of HTO or DTO [13, 23]. These dispersive excitations are referred to as quantum monopoles. Field dependent thermal conductivity measurements in the CFM phase reveal a low field decrease in the conductivity. This is consistent with the suppression of heat carrying monopole excitations since a suppression of spin fluctuations can only increase the conductivity by reducing spin-phonon scattering [13, 23]. This decrease in conductivity remains quite substantial even at low temperatures, suggesting that the creation energy is much less than the excitation energy of classical monopoles whose density decreases exponentially with decreasing temperature. Thus, there is a considerable contribution to the thermal conductivity from itinerant quantum monopole excitations in the CFM phase. The high field regime shows an increase in the conductivity until a saturation value is achieved. Furthermore, the high field data scales with the Brillouin function. Thus, this behaviour is interpreted as a reduction of paramagnetic scattering of the phonons, which is suppressed by increasing the Zeeman energy with the large magnetic field. The field independent, saturated conductivity is entirely due to phonons in the absence of magnetic scattering. The zero field temperature dependence shows a kink at $T_c \sim 200$ mK corresponding to the first order phase transition into a ferromagnetic state. Additionally, the low field decrease in the conductivity disappears below this temperature indicating the complete suppression of the monopole excitations. However, the temperature dependence of the conductivity as $T \to 0$ K does not show the usual cubic behaviour of phonons in the boundary scattering limit, as expected for a magnetically ordered insulator. Rather, the conductivity follows a T^2 temperature dependence, indicating the presence of some amount of phonon scattering from spin fluctuations. That said, there is no evidence of the photon excitations predicted to exist in the QSL phase.

Chapter 6

Spin Ice: Field Dependence

6.1 Introduction

As we have seen in chapter 5, the rare-earth pyrochlore materials $Ho_2Ti_2O_7$ (HTO) and $Dy_2Ti_2O_7$ (DTO) have drawn a considerable amount of interest from condensed matter theorists and experimentalists alike due to the realization of a highly degenerate spin ice ground state. In the spin ice state, the Ising-like magnetic moments are governed by the so-called ice rules, such that each tetrahedron has a pair of spins pointing towards its center, and a pair of spins pointing away from the center. The elementary excitations from this degenerate state are theoretically described as fractionalized magnetic monopoles. A single spin flip event will create a monopole/anti-monopole pair, which is able to disassociate through subsequent spin flips [10]. The existence of monopole excitations in the spin ice state is still debated due to differing interpretation of the data [96, 97, 14, 101, 103, 102, 13]. However, there have been a number of thermal transport studies reporting the observation of a magnetic channel of conductivity [14, 101, 103]. Thermal conductivity is one of the most effective measurement techniques for probing delocalized excitations by examining their ability to transport heat, or scatter the phonons. Hence, thermal transport is an ideal technique for detecting the proposed monopole excitations.

The effect an external magnetic field has on the spin system is highly anisotropic [128, 111, 101]. The local [111] easy axis anisotropy of the magnetic moments can cause dissimilar Zeeman energy splitting for each spin depending on the direction of the applied field. As a result, the application of a magnetic field can lead to a dimensional reduction of the spin system. For example, applying a field in the [110] cubic direction will align chains of spins parallel to the field direction, while leaving one dimensional spin chains perpendicular to the field direction unaffected. On the other hand, applying a field in the [100] direction will have an equal effect on all the spins, resulting in a long range ordered phase. A modest field in the [111] direction will polarize the spins in the triangular planes of the pyrochlore lattice, resulting in decoupled, two dimensional Kagomé planes of spins [129]. This appears as an intermediate plateau in the magnetization [128, 130]. Unlike a [110] or [100] field which do not result in ice rule breaking arrangements of spins, a large [111] field leads to alternating planes of tetrahedra with 3-in-1-out and 1-in-3-out spin arrangements, also known as a monopole crystal [131]. A more detailed description of the anisotropic behaviour of spin ice in a magnetic field is found in chapter 5. In this chapter, we will focus our attention on the effect an applied field in the [111] direction has on monopole dynamics.

Field dependent magnetization measurements of DTO in the [111] direction have revealed hysteresis below $\sim$ 670 mK centred at 0 T and again below $\sim$ 370 mK centred around 1 T [110, 132, 133, 101]. The hysteresis below 670 mK and at low fields ($\lesssim$ 300 mT) is attributed to the freezing of the spins, however no ordering is observed due to the lack of magnetic Bragg peaks [130]. The high field hysteresis at 1 T for DTO for T $<$ 370 mK is the result of a first order transition from the Kagomé ice phase below 1 T and the magnetic saturation phase (3-in-1-out/1-in-3-out) [129]. Above 370 mK, this transition is no longer first order and is better described as a crossover transition with no hysteresis [134]. Thus, the first order phase line at approximately 1 T terminates at a critical end-point at 370 mK [110, 132, 133, 111]. Similar hysteresis is seen in the magnetization of HTO occurring at similar temperatures but centred around 0 T and 1.5 T respectively [130].

Recent thermal transport studies on both DTO and HTO have shown large hysteresis loops at temperature below $\sim$ 600 mK in a [111] field [14, 101, 102, 104]. This is attributed to the spins freezing, consistent with the low field hysteresis observed in magnetization measurements [130]. As discussed in chapter 5, this spin freezing is also associated with the observation of extended relaxations times at low temperatures [84], which can lead to out-of-equilibrium physics if not properly accounted for [8]. Furthermore, magnetization measurements have revealed that ramping the magnetic field at moderate sweep rates will also lead to out-of-equilibrium dynamics at low temperatures [84, 16, 135], hindering our ability to accurately observe the thermally equilibrated spin dynamics below 700 mK. Finally, it has been shown that the hysteresis loop in the conductivity previously observed at 600 mK can be suppressed if the system is allotted ample settling time [104], suggesting that the system is not fully equilibrated in this regime.

This chapter focuses on the effect field sweep rates and settling times have on the hysteresis observed in the thermal transport. Specifically, we investigate the hysteresis for $T > 360$ mK resulting from out-of-equilibrium dynamics caused by fast magnetic field sweep rates [84, 16, 135] as well as the hysteresis below 360 mK which is associated with the first order phase transition from the Kagomé ice phase into the field induced ordered phase as observed in magnetization measurements [128, 111, 130]. A phase diagram is then extracted from the field dependent conductivity data and is compared to previously reported B versus T phase diagrams for $B \parallel [111]$.

In addition to detecting phase transitions, thermal transport is also an excellent technique for probing the dynamics of delocalized quasiparticle excitations. Hence, thermal conductivity measurements were conducted on both DTO and HTO in a [111] field in order to probe the magnetic channel of conductivity by observing the suppression of magnetic excitations via increasing the Zeeman energy. This will also allow us to examine the spin-lattice coupling through monopole-phonon scattering. These thermal transport measurements in conjunction with complementary magnetistriction measurements allow us to perform a detailed comparison between HTO and DTO in order to illuminate the subtle differences between these two materials.

6.2 Experimental Details

Thermal conductivity and magnetostriction measurements have been made on HTO and DTO at temperatures from approximately 200 mK to 1.2 K, in applied magnetic fields up to 8 T along the [111] crystallographic direction using the standard one-heater-two-thermometer method as described in chapter 3. Magnetostriction measurements were also conducted on the samples for $B < 3$ T via a compact dilatometer. The diverging internal relaxation times observed in DTO at low temperatures [8] effectively sets a minimum temperature that is experimentally achievable. Hence, the lowest temperature data is taken at ~ 200 mK. The heat current for the conductivity measurements was applied along both the [111] direction (parallel to the field) and in the $[1\bar{1}0]$ direction (perpendicular to the field). All samples were grown using the floating-zone method and were oriented using the Laué back scattering technique to find the [111] and $[1\bar{1}0]$ directions. The samples were then prepared into rectangular prisms by first cutting thin slices via a diamond saw then by polishing the surfaces using 1500 grit sand paper. The sample dimensions are listed in table 6.1. The HTO and DTO (s1 from chapter 7) samples were all cut from the same respective parent crystal to ensure identical sample quality.

The samples were zero field cooled (ZFC) from above 1.5 K following a logarithmic cooling rate to allow the sample to thermally equilibrate and to avoid quenching the spins. The field sweeps were then conducted via a quasi-static sweep method. That is, the field swept to discrete field steps at a ramp rate between 4 mT/min and 15 mT/min depending on the set temperature. Once the desired field value is reached, it is held constant allowing the sample to relax in the new state. The settling time exceeds 10^5 seconds at the lowest temperatures. Following this protocol results in an effective sweep rate of 0.6 - 1.5 mT/min; slow enough to avoid thermal runaway processes which can affect the magnitude of the conductivity. This process is continued through all field values ramping the field up and back down, resulting in a spin polarized state. Implications of not allowing the system to properly thermalize are discussed below.

6.2.1 Demagnetization correction

Before we examine the conductivity and magnetostriction results, We will briefly discuss the demagnetization correction which determines the effective internal field in the sample B. The demagnetizing field is due to the magnetization of a magnetic material and has the effect of modifying the internal field in the sample. Recall that the magnetizing field H is related to the magnetic field B through $B = \mu_o(H + M)$. So, the internal magnetic field B is related to the applied field B_o and magnetization M via

$$B = B_o - \mu_o N M \tag{6.1}$$

where μ_o is the permeability of free space and N is the demagnetizing factor and is related to the geometry of the sample. In general, the demagnetizing factor is a 3×3 tensor with unit trace (ie. $N_x + N_y + N_z = 1$). For arbitrarily shaped samples, N_i can be very difficult to calculate. However, rectangular prism shaped samples can be approximated by ellipsoids, simplifying the calculation of N_i. This is because the demagnetizing field is uniform along the principle axes of ellipsoids, and thus the demagnetizing factor can be calculated along each of these directions. A special case of this is a cubic sample which is approximated by a sphere and hence will have $N_x = N_y = N_z = 1/3$. The general form for N_i is considerably more complicated and is derived by Aharoni [136]. A rule of thumb to minimize the demagnetization factor is to shape the sample into a thin needle with the long axis parallel to the field direction. To illustrate this, consider a rectangular prism sample of length a in the x direction, and length b in both the y and z direction. The demagnetization factor in the x direction, N_x, will approach 0 when $a/b \to \infty$, or when the sample is long and slender. This is then seen in figure 6.1.

The sample dimensions are listed in table 6.1 for all the classical spin ice samples studied in this thesis, including DTO s1 and DTO s2 which are studied in the following chapter. The error in the values of these dimensions is estimated to be no more than 10%. The

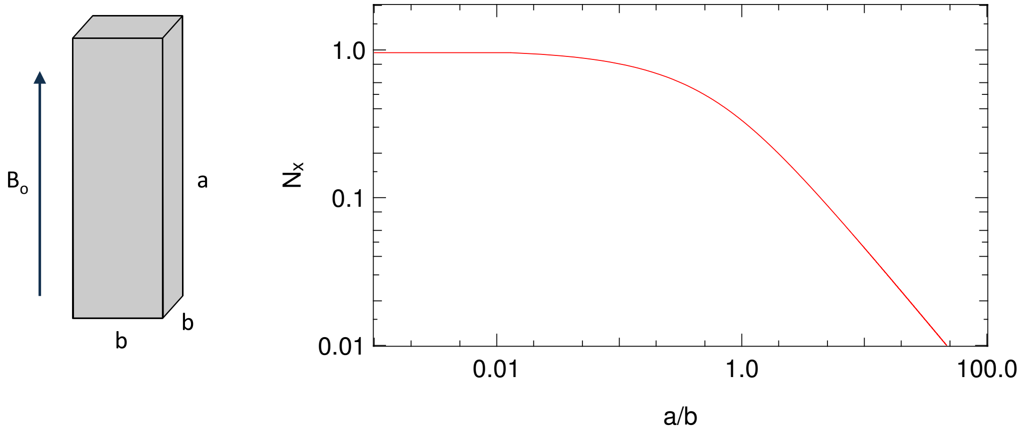

Figure 6.1: Demagnetization factor in the x direction for a rectangular prism shaped sample with dimension $a \times b \times b$.

Sample	Dimensions (mm)	Demagnetization factor N
HTO [111]	$2.0 \times 0.35 \times 0.34$	0.08
HTO [$1\bar{1}0$]	$0.30 \times 1.9 \times 0.25$	0.43
DTO s1 [111]	$0.70 \times 0.23 \times 0.20$	0.13
DTO s1 [$1\bar{1}0$]	$0.25 \times 0.56 \times 0.11$	0.28
DTO s2 [111]	$0.69 \times 0.38 \times 0.25$	0.18
DTO s2 [$1\bar{1}0$]	$0.97 \times 4.14 \times 0.49$	0.32

Table 6.1: Sample dimensions for all classical spin ice samples studied here. The first dimension is parallel to the [111] direction. The demagnetization factor in this direction is also listed.

demagnetization factors have also been calculated for each of these samples along the [111] direction of the sample, which is the first dimension listed for each sample.

6.2.2 Spin ice in a magnetic field

The issues that arise when measuring the spin ice materials in a sweeping magnetic field at low temperatures are explored in this section. The hysteresis observed in thermal transport measurements of DTO is examined in the context of out-of-equilibrium dynamics and thermal avalanche processes caused by rapid field sweep rates.

Thermal runaway processes

Similar to reference [16], local heating of the sample due to a continuously sweeping magnetic field is observed at low temperatures. Figure 6.2 shows the increase in the temperature of a HTO sample as a result of a continuous field sweep of 4 mT/min at 250 and 305 mK, and 15 mT/min at 365 and 483 mK. This is measured by recording one of the thermometers which is in good thermal contact with the sample, as the field is continually swept. It is clear that even slow sweep rates as low as 4 mT/min result in increased sample temperature. This will affect the magnitude of the thermal conductivity two fold. First, the non-constant temperature means the field sweep curves are no longer isotherms, but will be modified by the change in temperature. Second, as stated in reference [16], the peaks in sample temperature are related to a thermal runaway process, which is akin to an avalanche effect of flipping spins appearing as jumps in the magnetization to above the equilibrium value. Thus, the spin system will be out of equilibrium, affecting the magnetic contribution to the conductivity. This verifies the necessity for quasi-static field sweeps, which allows for the sample temperature to stabilize at each field step.

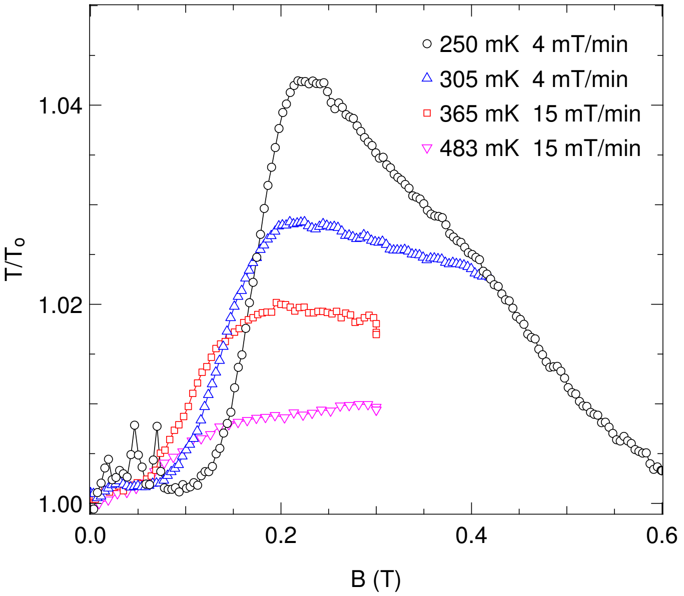

Figure 6.2: The change in sample temperature when ramping the field at 4 mT/min starting at 250 mK and 305 mK, as well as a rate of 15 mT/min starting at 365 mK and 483 mK.

Settling times and sweep rates

Previously reported field dependent thermal transport measurements of DTO and HTO have shown hysteresis loops at temperatures up to 600 mK [102, 14, 101, 104]. Although these reports follow a similar field sweep protocol to our own, their field sweep rate and settling time may not be sufficient to ensure thermal equilibrium is maintained. Fan *et al.* [102] state that they wait for the sample thermometers to stabilize, indicating the sample is approximately in thermal equilibrium. Kolland *et al.* [14, 101] and Scharffe *et al.* [104], on the other hand, use an effective sweep rate of approximately 10 mT/min. This sweep rate might result in local heating of the sample due to thermal runaway processes at low temperature [16, 135] and may also not provide an adequate settling time, especially in DTO which is known to have longer relaxation times than in HTO [107]. In this section, we show that the magnitude of the hysteresis below 360 mK is dependent on the length of settling time consistent with the behaviour of a first order phase transition [137]. Furthermore, we show that the hysteresis previously observed above 360 mK is reproducible by increasing the field sweep rate, suggesting it is due to out-of-equilibrium physics.

As stated above, the hysteresis observed in magnetization measurements below 360 mK centred at 1.5 T and 1.0 T in HTO and DTO respectively is due to the presence of a first order phase transition [111, 130, 101]. Hysteresis associated with crossing a first order phase boundary can be suppressed if the system is allowed to settle for an extended amount of time. This is a general characteristic of first order transitions [137]. Figure 6.3 (a, b) shows the thermal conductivity for an increasing (filled symbols) and decreasing (open symbols) field at 280 mK with a 20 mT/min sweep rate. Hysteresis is seen in panel (a) when the quasi-static step settling time is cut off at 30 min. When the settling time is extended to 150 min, then the hysteresis loop closes. Thus, the magnitude of the hysteresis loop is dependent on the settling time.

Figure 6.3 (c, d) shows the thermal conductivity for an increasing (filled symbols) and decreasing (open symbols) field at 455 mK with a 20 mT/min sweep rate (c) and 50 mT/min (d). This demonstrates that the high temperature hysteresis can be reproduced by increasing the field sweep rate to 50 mT/min. As discussed in chapter 5, it has been shown that a field sweep rate greater than 20 mT/min will cause thermal runaway processes in spin ice materials, resulting in a deviation from thermal equilibrium [16, 135]. That is, a large field sweep rate will cause a local increase in the sample temperature due to the release of entropy from flipping the spins, leading to out-of-equilibrium spin dynamics. This is explicitly shown in figure 6.2. The sudden increase is spin fluctuations when the sample temperature spikes will cause an increase in phonon scattering resulting in a decrease in total conductivity. This is evident in panels (c, d), no hysteresis is observed for a sweep rate

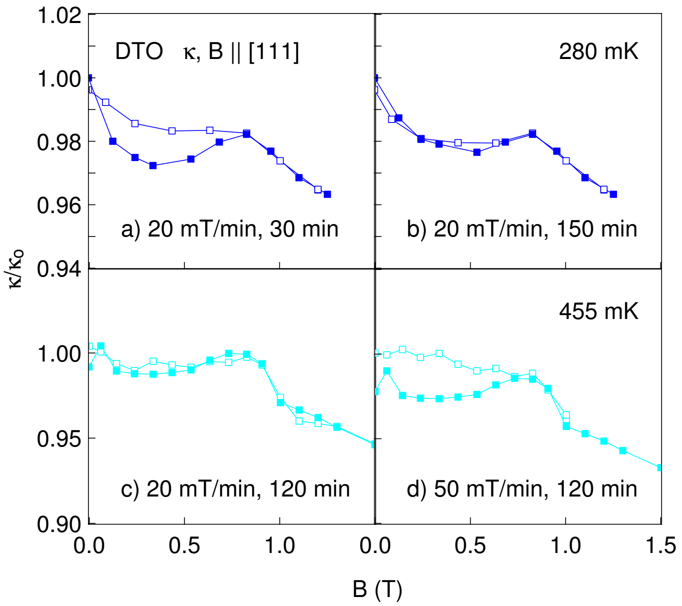

Figure 6.3: Field dependence of the thermal conductivity of DTO at 280 mK with a short settling time (a) and an extended settling time (b) showing the suppression of the hysteresis loop when the settling time is increased. Field dependence of the thermal conductivity at 455 mK with a slow sweep rate (c) and a more rapid field sweep rate (d) illustrating that hysteresis can be induced by ramping the field too quickly.

of 20 mT/min, whereas hysteresis is seen when the field is swept at a rate of 50 mT/min since the initial drop in conductivity is slightly larger. This could explain the appearance of hysteresis at temperatures above 360 mK reported in references [102, 14, 101, 104].

Now that we have a solid understanding of the effect a quick sweep rates and short settling times can have on transport measurements, we are able to ensure that our samples remain in thermal equilibrium throughout the measurement.

6.3 Results

6.3.1 Thermal transport

In this section, we will examine the behaviour of the thermal conductivity for both HTO and DTO when the heat current and magnetic field are applied in the [111] crystallographic direction. Recall from chapter 5 that a [111] field can lead to a two dimensional Kagomé ice state as well as a field induced ordered state at high field. Thermal conductivity is used here to probe the monopole dynamics in each of these phases.

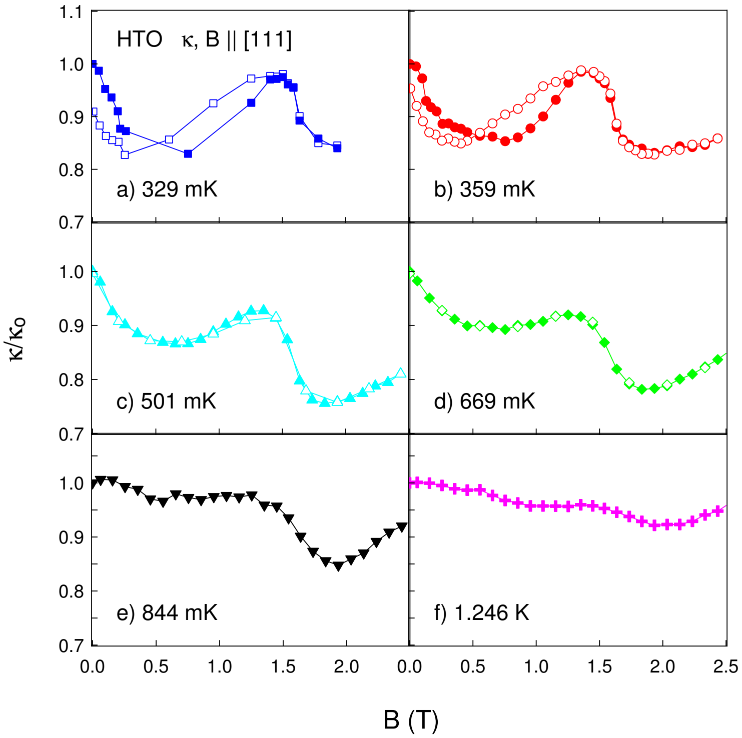

Figure 6.4: Normalized thermal conductivity isotherms of HTO with the heat current and applied field in the [111] direction at (a) 329 mK, (b) 359 mK, (c) 501 mK, (d) 669 mK (e) 844 mK and (f) 1.246 K. Closed symbols indicate an increasing magnetic field and open symbols indicate a decreasing field.

$Ho_2Ti_2O_7$

Figure 6.4 shows the [111] field dependence of the thermal conductivity plotted with the heat current in the [111] direction. Consider first the 329 mK data seen in panel (a). After zero field cooling the sample, the field is quasi-statically swept up (filled symbols). The conductivity decreases to a minimum value approximately 80 % of the zero field conductivity as the field is increased to ∼700 mT. As the field is increased further to 1.5 T, the conductivity is enhanced, nearly recovering the zero field value. Above 1.5 T there is a sharp drop in the conductivity. Figure 6.8 shows that the conductivity then increases until it enters a field independent regime above ~ 3.5 T. Sweeping the field back down to 0 T from above 1.5 T (open symbols) reveals clear hysteretic behaviour below 360 mK. The hysteresis is completely suppressed for $T \gtrsim 360$ mK (panels (c-f)). The initial low field decrease in the conductivity disappears by 844 mK and the sharp drop at 1.5 T becomes smeared out.

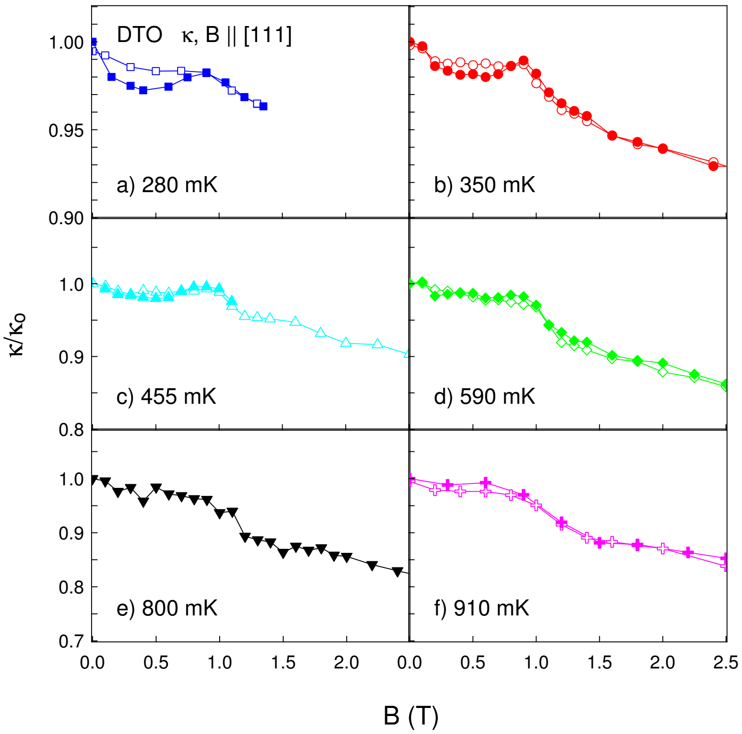

Figure 6.5: Normalized thermal conductivity isotherms of DTO with the heat current and applied field in the [111] direction at (a) 280 mK, (b) 350 mK, (c) 455 mK, (d) 590 mK (e) 800 mK and (f) 910 mK. Closed symbols indicate an increasing magnetic field and open symbols indicate a decreasing field.

$Dy_2Ti_2O_7$

The [111] field dependence of the thermal conductivity of DTO is seen in figure 6.5. The low field data shares many similarities to HTO; an initial decrease in the conductivity followed by a peak at approximately 1 T. Additionally, the isotherms for $T \leq 350$ mK show clear hysteresis upon cycling the field above 1 T. Similar to HTO, the hysteresis is suppressed for $T > 350$ mK. The field range and the shape of the hysteresis loop, however, differ from what is observed in HTO. The peak in the conductivity occurs at ~ 1 T in DTO rather than at ~ 1.5 T as in HTO. This is due to the different effective exchange parameters in these two materials. Equating the Zeeman energy of the spins in the Kagomé planes to the nearest neighbour exchange energy, we find that the transition into the ordered state will occur at 1.0 T for DTO ($J_{\text{eff}} = 1.1$ K) and 1.6 T for HTO ($J_{\text{eff}} = 1.8$ K), comparable with our observations. The low field drop in conductivity also becomes suppressed with increasing temperature, similar to HTO.

6.4 Discussion

6.4.1 Low field conductivity

The zero field conductivity is composed of magnetic and phonon channels of conductivity which are convoluted in HTO through strong monopole-phonon interactions [101, 103]. The behaviour of the thermal conductivity of HTO in a [111] field can be organized into four regions of decreasing (regions I and III) or increasing (regions II and IV) conductivity as seen in figure 6.6. When applying a field $\gtrsim 250$ mT in the [111] direction, the spins on the triangular planes begin to align with the magnetic field. This results in isolated Kagomé planes perpendicular to the field direction and is referred to as the Kagomé ice (KI) phase [80, 110, 111]. Monopole/anti-monopole pairs continue to be created in the KI state, however, they are confined to the Kagomé planes and should not significantly contribute to the conductivity in the [111] direction [101, 102]. The increased monopole density will however enhance the scattering of phonons, lowering the total thermal conductivity to a minimum at approximately 750 mT (region I). As the field is increased further the number of monopoles will continue to increase and will eventually start saturating the lattice. When this occurs, the monopoles become confined since the neighbouring tetrahedra will also contain monopole excitations, and double occupancy of a lattice site is energetically unfavourable (all spins pointing in or out). Thus the monopole-phonon scattering will decrease causing the conductivity to increase (region II). The conductivity reaches a peak at approximately 1.5 T, at which point the component of the spins in the Kagomé planes parallel to the field start to align with the field, resulting in a field induced 3-in-1-out/1-in-3-out ordered state. This can be thought of as alternating planes of monopoles and anti-monopoles stacked along the [111] direction as seen in figure 6.7. Spin flip excitations from this state create neighbouring tetrahedra with a 2-in-2-out spin configuration. These excitations are likened to monopole holes which behave similarly to monopole excitations in the spin ice vacuum [112]. Hence, it is possible for hole excitations to conduct heat similar to monopoles. However, recall from chapter 5 that the monopole hole activation energy scales with increasing field through the Zeeman energy and thus the number of hole excitations is reduced as the field is increased above 1.5 T, reaching a minimum at $\sim$ 1.8 T (region III). The behaviour of the conductivity of DTO mimics HTO in regions I, II and III, however the peak conductivity occurs at approximately 1 T. The difference in the field value of the peak conductivity is due to the difference in the effective exchange parameter. Recall from chapter 5 that the transition from the Kagomé ice phase to the ordered phase occurs when the Zeeman energy gained from aligning the spins with the field becomes greater than the energy cost of flipping a spin creating a tetrahedron with 3-in-1-out spin configuration. The Zeeman energy gain for aligning the spins with the field is $\sim 6.66\mu_B\mu_o H$ in both DTO and HTO since the magnetic moment is $\sim 10\ \mu_B$ in both materials [5]. The energy cost for creating neighbouring tetrahedra in the 3-in-1-out/1-in-3-out spin configuration is equal to $4J_{\text{eff}} = 4.44$ K for DTO and 7.2 K for HTO [5, 111]. Thus, the phase transition should occur at approximately 1.0 T for DTO and 1.6 T for HTO.

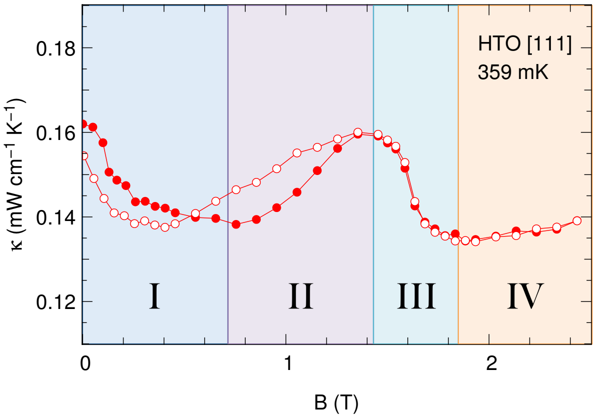

Figure 6.6: The thermal conductivity of HTO in a [111] field can be divided into four distinct regions. The conductivity decreases in regions I and III, and increases in regions II and IV (for HTO).

Figure 6.4 and figure 6.5 show that the magnitude of the initial decrease in conductivity in region I is considerably less in DTO than in HTO. If the spins are strongly coupled to the lattice in HTO, then monopole-phonon scattering in the Kagomé ice phase will have a much larger effect in HTO than in DTO where the spins are proposed to be thermally

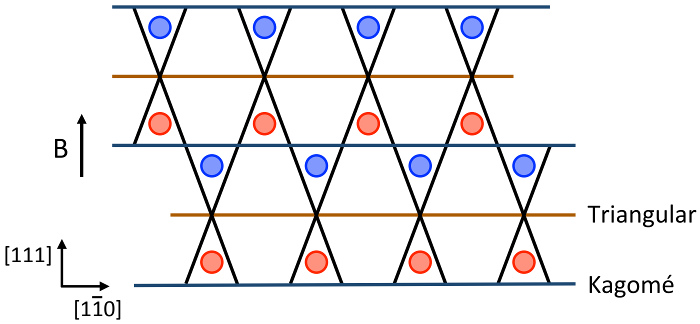

Figure 6.7: A two dimensional projection of the pyrochlore lattice in the field induced ordered monopole crystal phase [131]. The orange lines are the Kagomé planes and the blue lines are the triangular planes. The red (blue) circles indicate a tetrahedra with a 3-in-1-out (1-in-3-out) spin configuration.

decoupled from the lattice [8]. In this case, the effect of monopole-phonon scattering will be minimal in DTO.

It is interesting that the magnitude of the hysteresis loop in our DTO data is also much smaller than previously reported results [101, 102, 104, 105]. It has been shown that the internal thermal relaxation time in DTO is very slow at low temperature and will show signs of ordering below 360 mK if allowed to settle for extended periods of time [8]. Thus, our logarithmic cooling protocol could result in the system approaching this ordered phase, hence reducing the number of monopole excitations that are frozen into the system from higher temperatures [138]. Therefore, suppressing the monopole conductivity with a magnetic field will result in a smaller relative decrease in the total thermal conductivity. This is supported by the fact that the magnitude of the hysteresis loop is time dependent. Although the spins are relatively decoupled from the lattice, they will eventually thermalize with the lattice if provided an ample amount of time to settle, and the hysteresis loop will close. This was shown explicitly in section 6.2.2.

6.4.2 High field conductivity

The major distinction between these two materials is the behaviours of the thermal conductivity at high field (region IV). Figure 6.8 shows the [111] field dependence of the conductivity for HTO (left) and DTO (right) when the heat current is in the [1$\bar{1}$0] direction. Here, it is clear in HTO, that the conductivity increases to a constant value when the field is greater than approximately 3 T whereas in DTO, the conductivity decreases, reaching a constant value for fields greater than approximately 5 T. This rather stark difference in behaviour of the conductivity has implications in determining the phonon contribution to the conductivity at zero field. The lack of field dependence at high field suggests that the conductivity is entirely due to the lattice in this region since phonons, in the absence of magnetic scattering, should be insensitive to magnetic fields. Chapter 7 verifies that the 8 T data is indeed the phonon conductivity in DTO s1 since the temperature dependence is well described by phonons in the boundary scattering limit, with no free parameters. Now, in DTO, it is reasonable to assume that the high field data accurately describes the zero field phonon conductivity due to the minimal monopole-phonon scattering resulting from the spin-lattice coupling. On the other hand, although the high field data in HTO may be entirely due to phonons, it does not accurately depict the zero field phonon term. This is because monopole-phonon scattering in HTO will significantly reduce the low field phonon conductivity. Therefore, it does not appear feasible to accurately extract the zero field phonon conductivity in HTO. Details about the zero field phonon conductivity in DTO are discussed further in chapter 7.

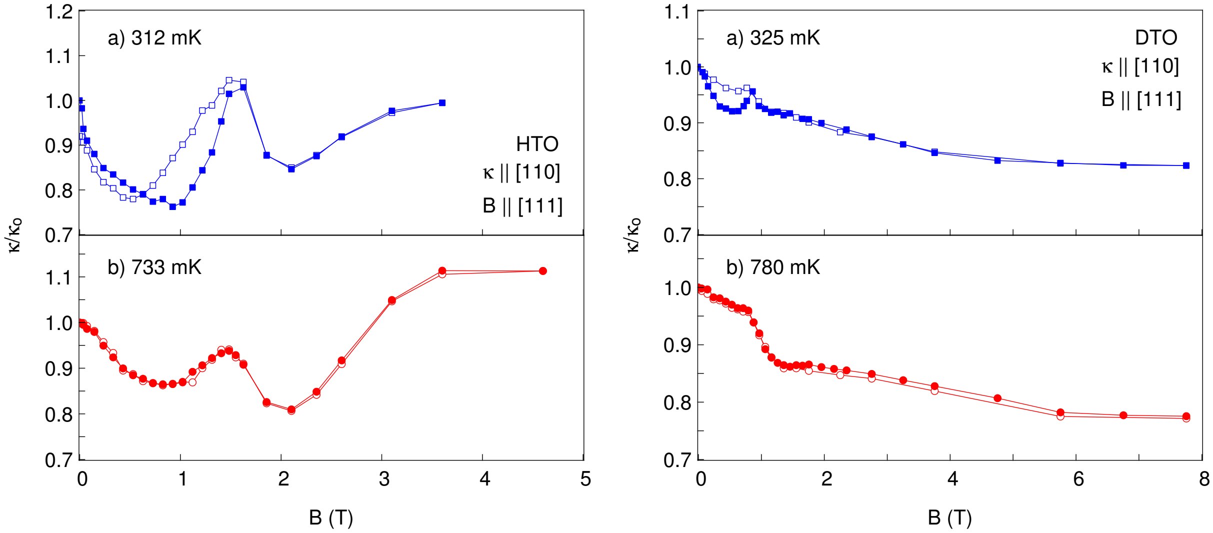

Figure 6.8: Field dependence of the thermal conductivity of HTO (left) and DTO (right) with the heat current in the $[1\bar{1}0]$ direction and the field in the [111] direction. Closed symbols indicate an ascending magnetic field and open symbols indicate a descending field.

The high field increase in the conductivity observed in HTO can be rationalized as paramagnetic scattering of the phonons. Figure 6.9 shows the thermal conductivity normalized by its high field saturated value κ_{sat} plotted versus $\mu_{\mathrm{B}}B/k_{\mathrm{B}}T$. The high field increase in conductivity scales well with the Brillouin function (red line) for spin 1/2 and $g_{\mathrm{J}} = 5/4$ (Landé g-factor for holmium). In general, the Brillouin function describes the magnetization of an ideal paramagnet. Thus, the increasing conductivity could be due to a reduction of spin-phonon scattering since spin fluctuations are suppressed as they align with the field. The absence of this behaviour in DTO is consistent with a reduced spin-lattice coupling compared to HTO. It is interesting to note that the high field behaviour of $Yb_2Ti_2O_7$ (YbTO), a quantum analogue to the classical spin ice materials, also scales with the Brillouin function [23]. The quantum spin ice material, YbTO, is discussed further in chapter 8.

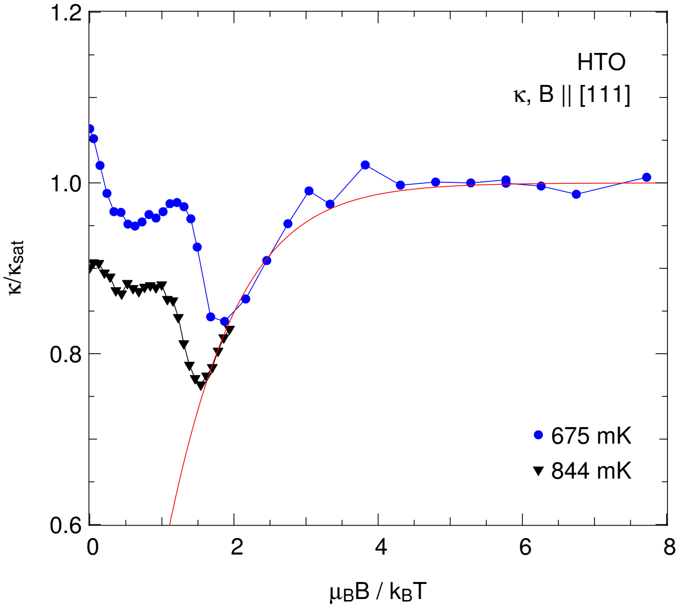

Figure 6.9: The thermal conductivity normalized by the high field saturated value is plotted versus $\mu_{\mathrm{B}}B/k_{\mathrm{B}}T$ for HTO at 675 mK and 844 mK. The high field increase in conductivity scales onto the Brillouin function (red line) for spin 1/2 and $g_{\mathrm{J}} = 5/4$.

6.4.3 Magnetostriction

Magnetostriction can be used to detect the critical fields at magnetic phase transitions by observing behavioural changes in the field dependence of $\Delta L/L_o$. Figure 6.10 shows

$\Delta L/L_o$ plotted versus magnetic field for HTO at 200, 450, 600 and 675 mK in the left panel and for DTO at 260, 350, 450 and 550 mK in the right panel.

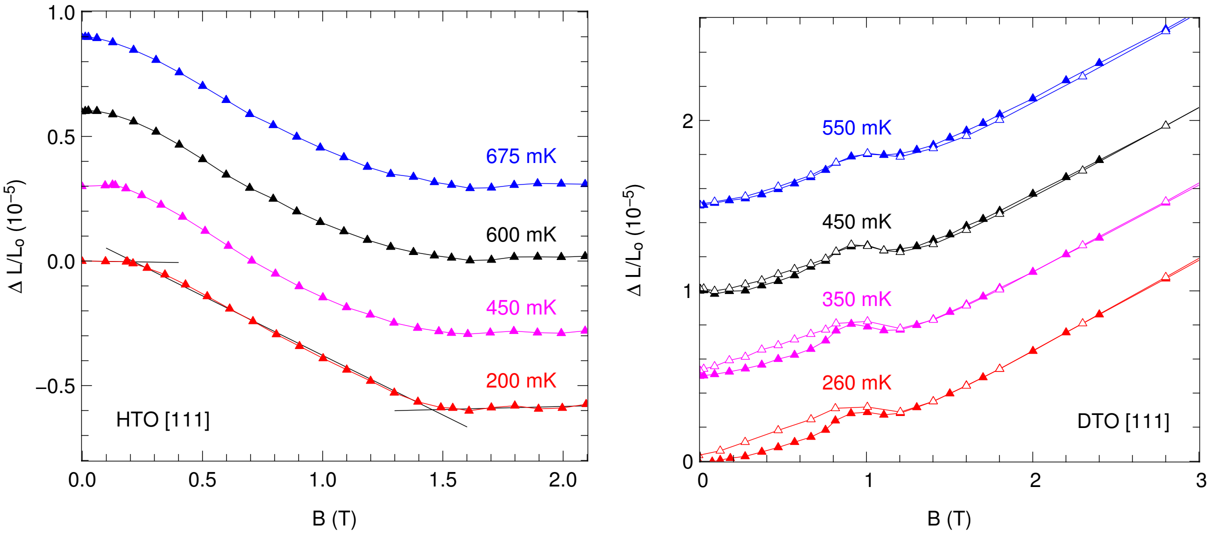

Figure 6.10: Magnetostriction of HTO (left) and DTO (right) along the [111] at temperatures ranging from 200 mK to 675 mK.

$Ho_2Ti_2O_7$

We will start by considering the HTO data. Three distinct behaviours can be seen in the lowest temperature data taken at 200 mK. There is a field independent region below ∼ 250 mT followed by a monotonic decrease in length until 1.48 T where the length becomes constant in field again. As the temperature is increased, the initial field independent region is suppressed to lower fields, vanishing above approximately 600 mK. Conversely, the onset of the high field region of constant sample length, remains unchanged for all temperatures measured.

A heuristic explanation of the HTO magnetostriction data is as follows. The initial horizontal behaviour is due to the low number of monopoles in the spin ice (SI) regime which are free to hop between tetrahedra with little interaction with the lattice and hence will not affect the sample length. As the system enters the Kagomé ice (KI) state, the spins in the triangular planes will align with the applied magnetic field, and the Kagomé planes start to saturate with alternating monopole and anti-monopole layers in the [111] direction. This causes these planes to be attracted to each other due to the Coulomb interaction between monopole excitations. However, since the monopoles are confined to the Kagomé planes they will reduce the distance between the planes to minimize their energy. This is detected as a decrease in the sample length. Increasing the applied field above 1.5 T results in full saturation of the Kagomé planes (in the 3-1-1-3 polarized state) and thus the attraction between the layers is at a maximal value and the sample will cease to compress further with an increasing field.

$Dy_2Ti_2O_7$

Let us now consider the DTO data. An increase in sample length is seen at low field which reaches a local maximum at approximately 1 T. Above 1 T, ΔL increases monotonically. Upon decreasing the field (open symbols), $\Delta L/L_o$ follows the increasing field data for $B > 1$ T. The decreasing field data shows a similar peak to the increasing field data at approximately 1 T, however $\Delta L/L_o$ does not decrease to the same value as the ascending field data for $B < 1$ T. Thus, hysteresis is observed in the magnetostriction upon cycling the field from 0 T to above 1 T and back to 0 T. This indicates that the peak in the data at 1 T marks a first order phase transition at low temperature. Furthermore, the hysteresis loop disappears for $T > 350$ mK, suggesting that the transition is no longer first order like, but a crossover. This is consistent with the thermal transport data.

To explain the high field monotonic increase in sample length, we will turn to a microscopic picture of the spins on the pyrochlore lattice. Recall that the pyrochlore lattice is comprised of triangular planes and Kagomé planes stacked in the [111] direction. The local [111] quantization of the spins (directly towards the centres of each tetrahedra) means that in the field-induced ordered phase, when $B > 1$ T, the spins on the triangular planes are fully aligned with the field, whereas the spins on the Kagomé planes are tilted at an angle of 109.4° with respect to the field. Therefore, each spin on the Kagomé planes will experience a torque equal to $\tau = (2\sqrt{2}/3)g_J J\mu_B\mu_o H$. This torque will slightly cant the spins towards the field, the act of which elongates the sample, resulting in a high field increase in $\Delta L/L_o$. This is consistent with the magnetostriction measured by Kolland *et al.* [101]. This behaviour is not observed in HTO for $B \leq 2$ T, however, it is possible that it occurs at higher magnetic fields, above our maximum field measured.

6.4.4 Phase diagram

The field dependent thermal conductivity and magnetostriction measurements allow us to construct field versus temperature phase diagrams for both HTO and DTO. In the

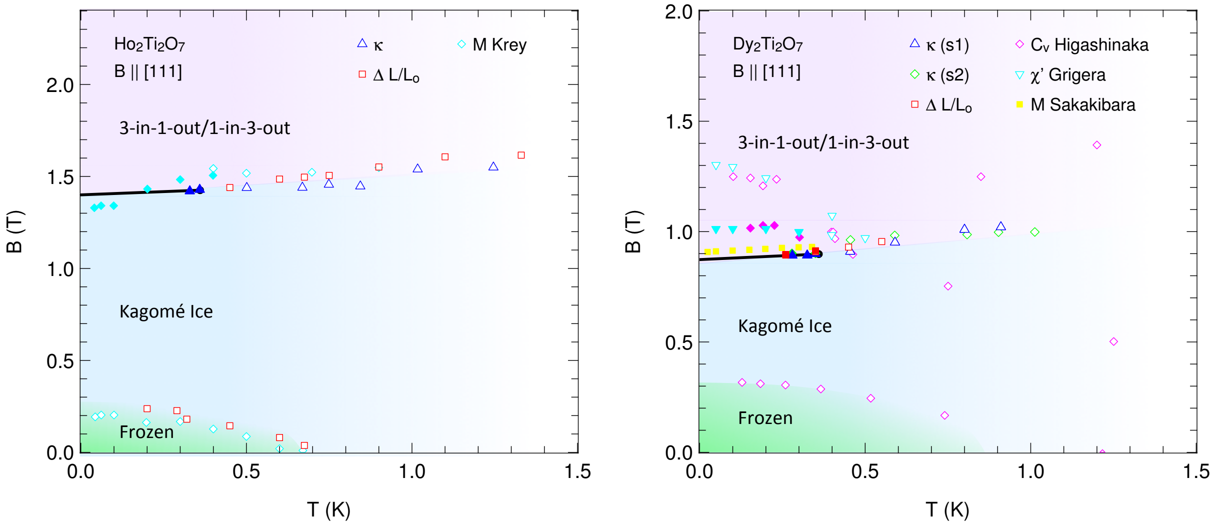

Figure 6.11: Field versus temperature phase diagram for HTO (left) and DTO (right) in a [111] field extracted from our conductivity and magnetostriction data. The phase lines extracted from magnetization measurements by Krey *et al.* [130] are included in the HTO phase diagram. Similarly, the phase lines from field dependent specific heat measurements by Higashinaka *et al.* [139], susceptibility measurements by Grigera *et al.* [140], and magnetization measurements by Sakakibara *et al.* [110] are included on the DTO phase diagram. The filled symbols indicate a first order phase transition. The black line is the slope of the first order phase line determined by the Clausius-Clapeyron equation.

thermal transport measurements, the critical field is defined at the position of the peak conductivity for both HTO and DTO. We have seen that the magnetostriction differs considerably between these materials, hence the definition of the critical field is defined in a different manner for each material. Figure 6.10 shows that the magnetostriction of HTO can be fitted with three line segments which describe the spin ice phase, Kagomé ice phase and ordered phase. The phase boundaries are thus defined as the point of intersection between the lines. The magnetostriction of DTO shows a peak at approximately 0.9 T, with hysteresis at temperature $\leq$ 350 mK. Thus, the critical field is defined as the location of the peak. The resulting field versus temperature phase diagrams are seen in figure 6.11. The phase lines determined by magnetization measurements of HTO by Krey *et al.* [130] are also featured on the HTO phase diagram and are in good agreement with our data. Additionally, the phase lines from field dependent specific heat measurements by Higashinaka *et al.* [139], susceptibility measurements by Grigera *et al.* [140], and magnetization measurements by Sakakibara *et al.* [110] are included on the DTO phase diagram. The phase boundaries extracted from the magnetization measurements agree well with our data. However, the first order phase lines extracted from the susceptibility and specific heat measurements are slightly higher in field and show an additional transition at approximately 1.3 T. An explanation for these effects is as follows. First, both Grigera and Higashinaka state that their samples are prepared such that the [111] direction is aligned with the longest axis of the sample which is parallel to the field. This minimizes the demagnetizing field and thus they do not apply a correction to their data to account for the demagnetizing field [139, 140]. This will cause the phase line to be situated at a slightly higher field. Second, it has recently been shown that if the sample is slightly rotated in the field so that the [111] direction is no longer aligned with the field, an intermediate polarization state can occur, leading to a second phase line at higher fields [141].

Finally, since the transition from the Kagomé ice phase to the 3-in-1-out/1-in-3-out ordered phase is first order for $T \lesssim 370$ mK, the Clausius-Clapeyron equation should hold such that

$$\frac{\mathrm{d}B_\mathrm{c}}{\mathrm{d}T} = -\frac{\Delta S}{\Delta M}. \tag{6.2}$$

Here, $\mathrm{d}B_\mathrm{c}/\mathrm{d}T$ is the slope of the critical first order phase line, ΔS and ΔM are the change in entropy and magnetization across the phase. Since the system is entering a spin polarized ordered state from a disordered Kagomé ice state, the change in entropy must be negative. Thus the slope of the critical phase line must necessarily be positive. We know the magnetization increases from 3.33 μ_B/(Ho/Dy) to 5.00 μ_B/(Ho/Dy) across the phase boundary, thus $\Delta M = 1.67$ μ_B/(Ho/Dy) [110, 132, 130]. Spin ice theory predicts a residual entropy in the Kagomé ice phase of 0.67 J/K mol (Ho/Dy) [142]. Thus $\Delta S = -0.67$ J/K mol (Ho/Dy) as the system enters the ordered phase. It is interesting to note that specific heat measurements of DTO in a [111] field reveal that the residual entropy in the Kagomé ice phase is approximately 0.65 J/K mol Dy, consistent with theory [111]. Therefore, according the Clausius-Clapeyron equation, we find that the slope of the critical phase line is approximately $\mathrm{d}B_\mathrm{c}/\mathrm{d}T \approx 0.07$ T/K. This is illustrated in figure 6.11 as a solid black line, which is in good agreement with our data.

6.5 Summary and Conclusions

Thermal transport measurements of HTO and DTO in the [111] direction have been used to examine the contribution to the conductivity from monopole excitations as well as their effect on the phonon conductivity through spin-phonon scattering. We have explicitly demonstrated the necessity of slow magnetic field sweep rates and long quasi-static settling times in order to maintain thermal equilibrium between the spin system and the lattice. That is, the hysteresis observed above 360 mK is likely due to out-of-equilibrium behaviour caused by a rapid magnetic field sweep rate. This is in contrast to the hysteresis below 360 mK which is a result of a first order phase transition from the Kagomé ice phase into the field induced-ordered phase consistent with magnetization measurements [128, 111, 130] and field dependent specific heat measurements [111].

Additionally, we have shown that the high field enhancement in the conductivity of HTO is possibly due to a reduction of phonon scattering from paramagnetic spins indicating a significant spin-lattice coupling. On the other hand, the high field behaviour of the conductivity of DTO exhibits a modest decrease, suggesting a decoupling of the spins from the lattice, consistent with other measurements [7, 8]. Thus, the high field data can be approximated to be the zero-field lattice contribution, allowing an accurate method for the extraction of the magnetic contribution to the conductivity.

Chapter 7

Spin Ice: Disorder Dependence

7.1 Introducton

It has been shown that the low energy excitations from the classical spin ice ground state of $Dy_2Ti_2O_7$ (DTO) can be theoretically described as fractionalized magnetic monopole quasiparticles. A monopole/anti-monopole pair of excitations are created by flipping a single spin in the 2-in-2-out ground state. Thus, the monopole quasiparticles are confined to hopping between the centres of each tetrahedra which constitute a diamond lattice. However, it is known that the rare-earth pyrochlore family of materials are susceptible to lattice defects arising from the floating zone growth technique. Samples of $Yb_2Ti_2O_7$, a sister compound to DTO, have been reported to have a 2.3% excess of Yb^{3+} ions on the Ti^{4+} sub-lattice, as grown [98]. This is commonly referred to as stuffing. Reports have also shown that stuffed Dy^{3+} ions in DTO can affect low temperature magnetic properties [96]. Excess Dy^{3+} ions will also cause a decrease in the oxygen content for the sample to remain charge neutral, resulting in a less than stoichiometric oxygen ratio in DTO. Oxygen deficiency has also been shown to affect both magnetic and optical properties of the rare-earth pyrochlores [143, 144, 145]. Therefore, it is necessary to understand the impact of disorder on the behaviour of the monopole excitations if there is to be any development of monopole physics for practical applications [95].

This chapter addresses the effect disorder has on the monopole conductivity by influencing either the monopole density or mobility. A combination of thermal conductivity and x-ray diffraction measurements have been conducted on two samples of DTO with different levels of disorder. This allows us to correlate the transport properties of the lattice and magnetic excitations at very low temperatures with the level of disorder in single crystal samples of DTO originating from the crystal growth procedure.

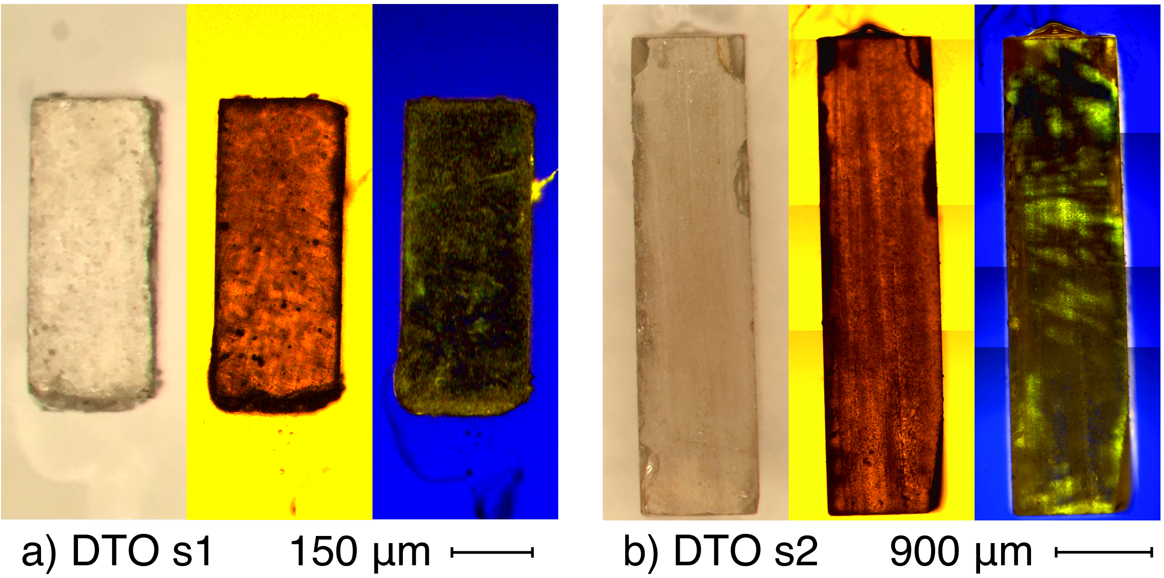

Figure 7.1: A regular photograph (left), a rear illuminated photograph (middle) and an image taken through a pair of crossed linearly polarized lenses (right) are seen for $Dy_2Ti_2O_7$ s1 (a) and s2 (b). Each type of image yields some information about the crystallinity of the sample.

7.2 Sample Characterization

Two separate DTO single crystals were grown via the optical floating zone image technique, sample 1 (s1) and sample 2 (s2). The growths were initially oriented using the Laué back scattering technique to find the [111] and $[1\bar{1}0]$ perpendicular crystallographic directions. Samples were then prepared from both crystals into thin rectangular prisms with dimensions listed in table 6.1 in the longitudinal orientation (longest axis along [111], second longest axis along $[1\bar{1}0]$) and in the transverse orientation (long axis along $[1\bar{1}0]$, short axis along [111]). This was done in order to measure the thermal transport both perpendicular to the Kagomé planes (parallel to [111]), and within the Kagomé planes (perpendicular to [111]) while in a [111] magnetic field.

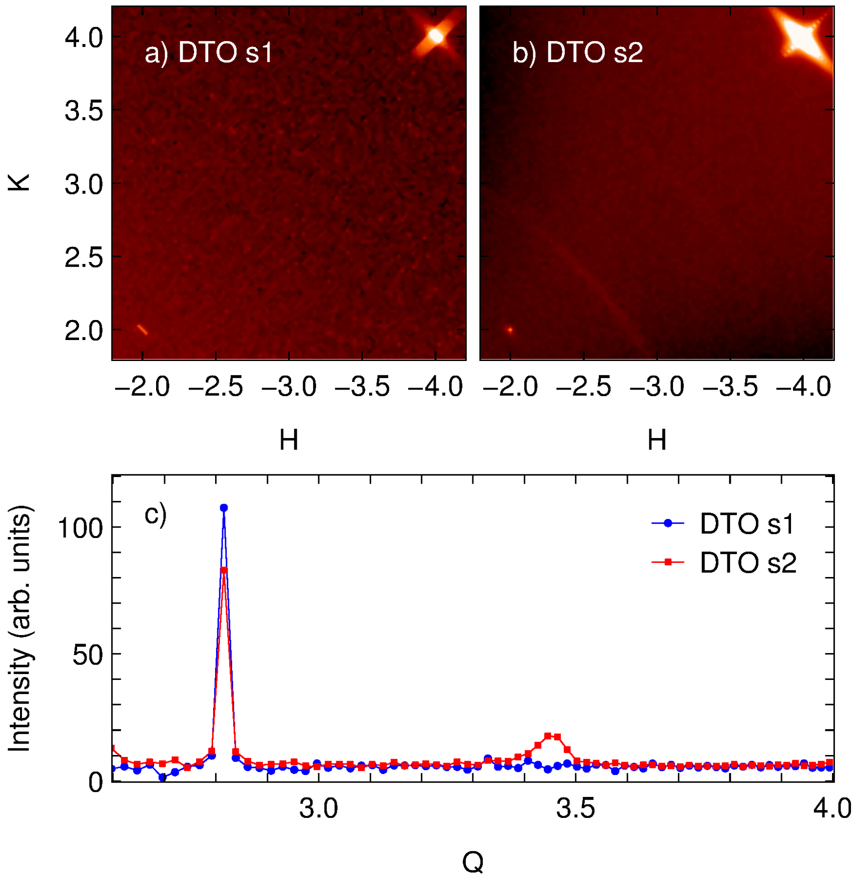

Figure 7.2: The (HK0) reciprocal space map of DTO is seen for s1 (a) and s2 (b). Panel (c) shows an intensity scan from the aforementioned reciprocal space maps where $Q = \sqrt{H^2 + K^2 + L^2}$. A (222) peak is clearly seen at $Q = 3.46$ in s2 which is not present in sample 1.

The transverse samples from both growths were initially characterized qualitatively by observing them with a variety of imaging techniques and then quantitatively via x-ray diffraction measurements. Figure 7.1 shows three images of samples from the two growths labelled s1 and s2. The first frame on the left in panels (a) and (b) is a regular photograph taken through a microscope showing that both samples are light beige in appearance. It has been shown that increased oxygen content in DTO can cause the colour of the sample to darken to an amber, or even a dark brown hue depending on the level of disorder [143, 144]. Thus, qualitatively it appears that both of the samples here do not have an abundance of excess oxygen in the lattice. The middle frame is a transmission light photograph showing no obvious signs of cracks, or fractures in the samples. It also illustrates that the samples are both fairly translucent. The final frame on the right of each panel is taken with the sample layered between cross-polarized lenses. Imaging optically anisotropic crystals between cross linearly polarized filters can survey the uniformity of the crystalline structure by revealing defects as variations in the colour and brightness of the imaged sample [146]. This is due to deviations in the birefringence caused by defects and stresses in the crystal lattice. Variations in the intensity of transmitted light through the crossed polarized lenses is observed in s2 (figure 7.1 (b)). However, s1 appears much more uniform in colour, indicating a more homogeneous lattice (figure 7.1 (a)). It is important to note, however, that s2 is approximately an order of magnitude larger in volume than s1. The smaller sample size reduces the possibility of having extended defects, such as stacking faults and grain boundaries which can be avoided when preparing the sample.

These imaging techniques are useful to acquire a preliminary qualitative assessment of macroscopic sample defects, however, they are incapable of detecting smaller scale impurities, such as dislocations and point defects. Hence, x-ray diffraction is utilized to probe these defects and to quantitatively assess the crystalline and structural characteristics of the DTO samples. Reciprocal space scans of both samples are are shown in Fig. 7.2. Strong single crystal peaks at $(\bar{2}20)$ and $(\bar{4}40)$ are seen in both samples, along with an absence of diffuse scattering indicating that there is not a significant amount of disorder in either sample. However, a weak ring of scattering is also observed in the scan of s2. This is more clearly identified in the intensity cut in figure 7.2 (c), which distinctly shows a sharp $(\bar{2}20)$ peak in both samples at Q = 2.83 and an additional (222) peak in s2 at Q = 3.46 whereas there is no observable peak in s1. This is indicative of a small polycrystalline component in s2, with all crystallites possessing the same lattice parameter.

The lattice parameter of both DTO samples was measured to a high degree of precision. The lattice constant is measured to be $a_o = 10.1274 \pm 0.0005$ Å for s1 and $a_o = 10.1329 \pm 0.0006$ Å for s2, which is 0.5% larger than s1. Baroudi et al. considered the relative change in the lattice parameter as a function of Ho^{3+} substituting for Ti^{4+}, x, in $Ho_{2+x}Ti_{2-x}O_7$ [125]. We assume a similar stuffing dependence of the lattice parameter for $Dy_{2+x}Ti_{2-x}O_7$ as for $Ho_{2+x}Ti_{2-x}O_7$ because DTO and HTO have a similar lattice spacing (∼10.13 Å , ∼10.10 Å respectively) and Dy^{3+} and Ho^{3+} have similar ionic radii (2.28 Å, 2.26 Å respectively) [147]. Therefore, an excess of either of these rare-earth ions on the Ti^{4+} sub-lattice could have a similar effect on the lattice parameter. Thus using the reported relationship, s2 has approximately a 2.5% excess of Dy^{3+} ions relative to s1. Therefore, x-ray diffraction analysis suggests that DTO s2 has higher levels of disorder than s1.

Having established a measurable variance in the level of disorder between the two

DTO samples, they provide an ideal system for observing the effect of this on monopole dynamics. Thermal transport measurements are initially utilized to examine the phonon conductivity at high temperatures, which additionally correlates with disorder levels and finally the magnetic conductivity at ultra-low temperatures.

7.3 Experimental Details

Thermal conductivity measurements were conducted on both of these single crystal growths via the standard 1-heater-2-thermometer method described in chapter 5 from $T = 100$ mK to 60 K quasistatically [51] using both a dilution fridge and a 1-K pot system to access the entire temperature range. The heat current was applied both parallel to the $[1\bar{1}0]$ direction and parallel to the [111] direction for each growth, along the long axis of the sample in either case. Measurements below 1 K were taken in zero field, as well as in field with $B \parallel [111]$ in all cases. The high temperature measurements were performed in zero field. The application of a magnetic field provides a reliable method for separating the magnetic and lattice contributions to the total conductivity. The RuO_2 sample thermometers are calibrated *in situ* as a function of magnetic field to account for magnetoresistive effects.

We ensure our samples are in good thermal equilibrium by waiting up to $1.5 \cdot 10^4$ seconds for each point at low temperatures and by slowly decreasing the temperature from 1 K to approximately 100 mK over the course of $2.6 \cdot 10^5$ seconds. We are confident in the measured value of the conductivity since the conductivity ceases to evolve in time after approximately 4 hours at the lowest temperatures measured. In addition to this, we can estimate the variation in conductivity if we consider the change in sample temperature from $1.5 \cdot 10^4$ seconds to $6.0 \cdot 10^4$ seconds at 340 mK reported in Pomaranski *et al.* [8]. This report reveals that at $T = 340$ mK, $\Delta T(t)/\Delta T(0)$ decreases by approximately 5% from $1.5 \cdot 10^4$ seconds to $6.0 \cdot 10^4$ seconds. This equates to a change in sample temperature less that 1 mK because $\Delta T(0) \approx 0.05 \cdot T$. Thus, if we assume the worst case scenario such that the hot thermometer is equilibrated and the cold thermometer decreases by 1 mK, then the conductivity drops by $\sim 5\%$. This is unlikely however, because both the hot and cold thermometers would be affected in the same manner and hence would relax at nearly the same rate. So the temperature gradient across the sample will remain constant for $t > 1.5 \cdot 10^4$ seconds and the only deviation in the conductivity will come from the average sample temperature, which would decrease by 0.3%. This is nearly at the resolution of our measurement. This small correction has no implications in the conclusions we draw from our analysis and would materialize as a systematic scaling of our data.

7.4 Results and Analysis

7.4.1 High temperature conductivity

The thermal conductivity for DTO s1 and s2 in both the $[1\bar{1}0]$ and [111] directions from 70 mK to approximately 50 K are seen in figures 7.3 and 7.4 respectively. All samples display a peak in the conductivity at approximately 13 K, as expected for insulating materials. Recall from chapter 2 that the peak height and shape is strongly dependent of disorder in the lattice, such that the maximum conductivity is suppressed with increased disorder. This is clearly seen in the data, where the maximum conductivity in s1 is approximately 3 times larger than in s2, indicating less disorder in s1. This is consistent with the increased levels of disorder in s2 determined by x-ray diffraction measurements. Furthermore, the conductivity of DTO measured by Kolland *et al.*[14], Klemke *et al.* [86] and Fan *et al.* [102] are featured in the top left panel. Here, we see that the peak conductivity in our s1 is approximately twice the peak conductivity in Kolland's data and 1.5 times larger than Klemke or Fan's data, suggesting that s1 is the highest quality sample so far studied from a thermal conductivity perspective.

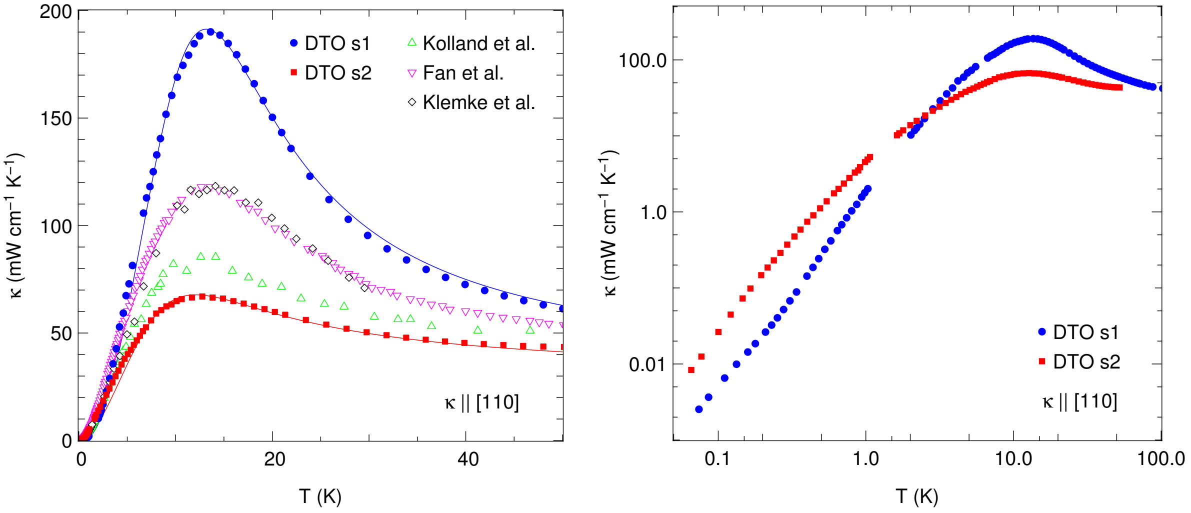

Figure 7.3: *Left:* The thermal conductivity in the $[1\bar{1}0]$ direction of $Dy_2Ti_2O_7$ s1 (blue circles) and s2 (red squares) is plotted versus temperature from 70 mK to 80 K. The DTO data from Kolland *et al.*, Fan *et al.* and Klemke *et al.* are also plotted on the same axis for comparative reasons [86, 102, 14]. *Right*: The same data plotted on a log-log scale clearly shows the low temperature enhancement of the conductivity in s2 over s1 below 2 K.

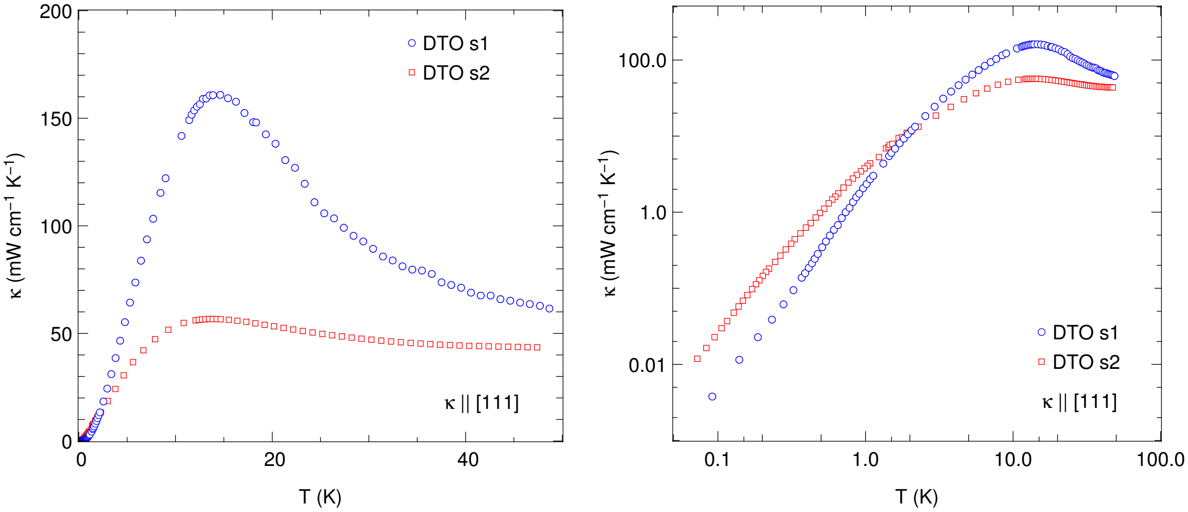

Figure 7.4: *Left:* The thermal conductivity in the [111] direction of $Dy_2Ti_2O_7$ s1 (open blue circles) and s2 (open red squares) is plotted versus temperature from 70 mK to 80 K. *Right*: The same data plotted on a log-log scale clearly shows the low temperature enhancement of the conductivity in s2 over s1 below 2 K.

The level of disorder in both s1 and s2 can be quantitatively assessed by fitting the high T phonon conductivity. We will focus on the $[1\bar{1}0]$ data in figure 7.3. Recall from chapter 2 that the total conductivity determined by kinetic theory and Matthiessen's rule is given by

$$\kappa_{\mathrm{ph}} = \frac{1}{3}\frac{c_{\mathrm{ph}} v_{\mathrm{s}}^2}{\sum_i \Gamma_i}, \tag{7.1}$$

where $c_{\mathrm{ph}} = 4.8 \cdot 10^{-4} T^3$ JK^{-1}mol^{-1} is the lattice specific heat [111], $v_{\mathrm{s}} = 3.2 \cdot 10^3$ m s^{-1} is the sound velocity for DTO [148] and Γ_i are the phonon scattering rates from the various scattering mechanisms. The boundary limited scattering rate can be calculated using the sound velocity and the average sample width, $d = \sqrt{4A/\pi}$, where A is the cross-sectional area of the sample via $\Gamma_{\mathrm{B}} = v_{\mathrm{s}}/d$. In this case, we consider impurity scattering from dislocations ($\Gamma_{\mathrm{D}} \sim T$) and stacking faults ($\Gamma_{\mathrm{SF}} \sim T^2$), where the coefficients are left as fitting parameters unique to each sample [48, 49]. Similarly, we need to include phonon-phonon scattering from Umklapp processes which has a functional form of $\Gamma_{\mathrm{U}} \sim T^3 e^{-\alpha\Theta_{\mathrm{D}}/T}$ in the modified Callaway model [149]. The fitting parameters for the Umklapp scattering term (the coefficient and α parameter) must remain constant between the two samples. This is because Umklapp scattering should be material specific, and hence not depend on impurity scattering. The parameters obtained from fitting the $[1\bar{1}0]$ data to equation

7.1 are listed in table 7.1. The magnitude of the dislocation scattering and stacking fault scattering in s2 is approximately twice as large as in s1. Again, this is consistent with the x-ray data and the qualitative observation of a suppressed conductivity peak in s2 over s1. It is important to note that we fit the high temperature data for $T > 6$ K because the spin ice correlations begin to develop below this temperature indicated by the onset of a broad peak in the specific heat [34] which will introduce additional magnetic scattering of the phonons and we are only interested in examining phonon-defect scattering in this analysis. We do not expect significant scattering from excited magnetic states above 6 K since the first excited state for the Dy^{3+} ions in DTO is on the order of 300 K [5, 150].

Sample	Γ_B (*const.*)	Γ_D (T)	Γ_SF (T^2)	Γ_U ($T^3 e^{-\alpha\Theta_\mathrm{D}/T}$)	α
s1 $[1\bar{1}0]$	$1.4 \cdot 10^7$	$1.8 \cdot 10^6$	$7.3 \cdot 10^5$	$6.7 \cdot 10^5$	0.059
s2 $[1\bar{1}0]$	$3.8 \cdot 10^6$	$4.2 \cdot 10^6$	$1.7 \cdot 10^6$	$6.7 \cdot 10^5$	0.059

Table 7.1: Phonon scattering rates for dislocations (Γ_D), stacking faults (Γ_SF) and Umklapp scattering (Γ_U) obtained from fitting the high temperature data in the $[1\bar{1}0]$ direction. The boundary scattering term (Γ_B) is calculated from the sample dimensions and sound velocity.

The right panels of figures 7.3 and 7.4 show the same data but on a logarithmic scale. This allows us to carefully track the magnitude of the thermal conductivity into the low temperature regime. As the temperature is lowered below 2 K, the conductivity of DTO s1 drops below that of s2. In general, increased levels of disorder leads to a suppression of the phonon conductivity by limiting the phonon mean free path [48, 151, 49, 50]. So, the observation of a larger conductivity below 2 K in s2, which has clearly been shown to have higher levels of disorder than s1, is quite surprising. The temperature at which the conductivity curves intersect is consistent with the onset of monopole excitations in the spin ice ground state in DTO. Thus, it would seem that the higher levels of disorder in s2 are in fact enhancing the monopole conductivity possibly by increasing the monopole mobility or by increasing the monopole density. This will be explored further in section 7.4.4.

In order to examine the effect of disorder on the magnetic channel of conductivity, we need to carefully separate the contributions from the lattice and magnetic excitations. This requires high precision thermal conductivity measurements below $T = 1$ K in zero field and at high magnetic fields. Conflicting methods have been proposed on how to procure the phonon conductivity in DTO [14, 101, 103, 105]. These methods are discussed in detail in section 7.4.2 followed by a thorough examination of the low temperature conductivity in section 7.4.3.

7.4.2 The zero field phonon conductivity

The lattice contribution to the thermal conductivity must be properly separated from the total conductivity in order to accurately examine the magnetic channel of conductivity. Conflicting reports on the method used to obtain the zero field phonon contribution in DTO and HTO has proven this to be a non-trivial task and therefore requires considerable attention [14, 101, 103, 105]. We initially consider the phonon conductivity separation method utilized by Kolland *et al.* and Scharffe *et al.* [101, 105] who use a [001] field to suppress magnetic excitations, eliminating the monopole conductivity. They observe a low field decrease in the field dependent conductivity followed by a plateau from approximately 0.5 T to 1.5 T where they claim the magnetization to be essentially saturated (see figure 7.5). The magnitude of this initial drop in the conductivity is assumed to be the magnetic contribution to the conductivity. That is, the conductivity at $\sim$ 1 T is deemed to be the lattice contribution at zero field. The conductivity has a step like decrease at higher fields, saturating by 3 T. They propose the feature at 3 T is due to a field dependent phonon conductivity induced by strain effects on the lattice due to a torque on the magnetic moments from the applied magnetic field. This is corroborated with the observation of an anisotropic magnetostriction on the order of $\Delta L/L \sim 5 \cdot 10^{-6}$ at 8 T. The observation of a small, temperature independent increase in the high field magnetization is attributed to the spins canting towards the applied field, consistent with the sample elongating in the same direction as the field. Furthermore, they measured the [001] field dependence of a sample which is diluted with non-magnetic yttrium, $\mathrm{DyYTi_2O_7}$. The low field drop in conductivity is mostly suppressed in the dilute sample. This is interpreted as a full suppression of spin ice physics, meaning $\mathrm{DyYTi_2O_7}$ is an accurate representation of the phonon conductivity in DTO. However, a similar high field feature is observed in the dilute system as in the pure DTO sample, supporting their theory that it is a field dependent phonon conductivity.

We will first consider the [001] magnetization. The magnetization has not reached a saturated value by 1.5 T, rather, it shows clear evolution from 5.2 μ_B/Dy at 0.5 T to 5.5 μ_B/Dy at 1.5 T. Recall that the saturation value of the magnetization in the [001] direction is expected to be $g_J J(1/\sqrt{3}) = 5.78\ \mu_\mathrm{B}/\mathrm{Dy}$ since the effective moment is $\mu = 10.0\mu_\mathrm{B}$. We see that the magnetization reaches this value at approximately 6 T, which is where the conductivity becomes field independent (seen in figure 7.5). Therefore, the spins are not fully polarized by 1.5 T and will still affect the phonon conductivity. A field of approximately 6 T is required to obtain the lattice conductivity in the absence of any magnetic contribution.

Kolland and Scharffe also consider an applied field in the [111] direction. In this case

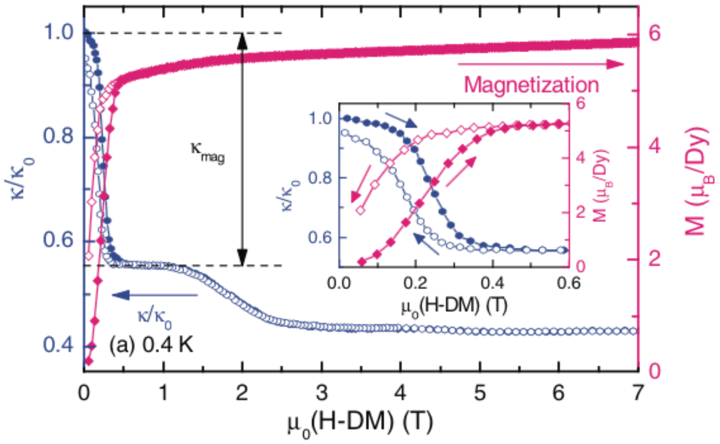

Figure 7.5: Magnetization and thermal transport of DTO in a [001] magnetic field at 400 mK as measured by Kolland *et al.* [14].

they attribute the lattice conductivity to the data at 1.5 T. Similar high field features are observed in the magnetostriction and magnetization as in the [001] case. Erfanifam *et al.* showed that the speed of sound increases by approximately $\Delta v_s/v_s \sim 4 \cdot 10^{-5}$ above μ_oH$\sim$6 T ∥ [111] due to a stiffening of the lattice [152]. If we assume that the specific heat is field independent [111], then we can estimate the change in conductivity resulting directly from the lattice distortion via kinetic theory, stating $\kappa = \frac{1}{3} c_{\mathrm{ph}} v_{\mathrm{s}} L$. This simple model shows that the change in conductivity directly due to the lattice distortions are on the order of 0.1%, three orders of magnitude lower than the observed decrease in conductivity which is approximately 50% of the zero field value. Thus, it is unlikely the field dependence of the conductivity above 1.5 T is directly due to distortions of the lattice caused by torque on the magnetic moments. Furthermore, it is also interesting to note that the thermal conductivity reported in reference [101] approaches the same value for magnetic fields greater than 6 T in both the [001] and [111] directions at the same temperature even though the magnetostriction in the [001] direction is three times larger than in the [111] direction. This is further evidence that the decrease in the conductivity at high fields is likely not caused by the magnetostriction of the sample.

We can also show that the data at 1.5 T does not accurately represent the lattice contribution by considering the excitations out of the magnetic ground state for different applied fields in the [111] direction. Recall from chapter 5 that spin flip excitations out of the 2-in-2-out, spin ice state are described as monopole/anti-monopole pairs (tetrahedra with 3-in-1-out/1-in-3-out spin configurations) [35, 153, 3, 5]. The excitation energy gap to create a monopole is approximately 4.4 K at 0 T. The Zeeman energy from an applied field in the [111] direction lowers this energy gap until B ≈ 1.0 T where the 3-in-1-out/1-in-3-out state becomes energetically favourable and the component of the spins in the [111] direction align with the applied field. This is commonly referred to as a monopole crystal [131]. Spin flip excitations out of this state will result in either neighbouring tetrahedra with an all-in/all-out arrangement of spins which has an energy gap of approximately 12 K, or alternatively neighbouring tetrahedra with a 2-in-2-out configuration (monopole holes) whose excitation energy is dependent on the field strength [112]. The excitation energy of a monopole hole out of the 3-in-1-out/1-in-3-out state will be approximately 4.4 K at 2 T which is equal to the monopole creation energy in zero field. Hence, at a given temperature, the density of monopoles at zero field may be comparable to the density of monopole holes at 2 T. Thus, the application of a magnetic field greater than 2 T is required to fully suppress the magnetic excitations in order to solely observe the lattice contribution to the conductivity.

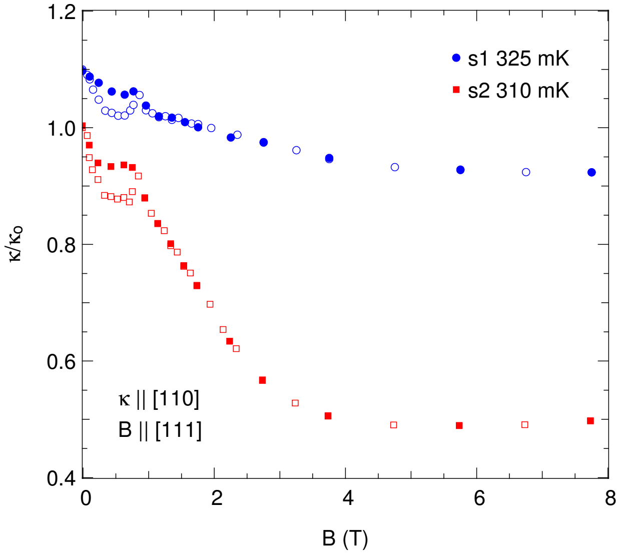

Figure 7.6: Magnetic field dependence of the thermal conductivity for s1 (blue circles) and s2 (red squares) with the field parallel to [111] and the heat current in the [1$\bar{1}$0] direction. Open symbols indicate ascending field and closed symbols are for a descending field.

The field dependence of the conductivity is featured in figure 7.6 for s1 and s2 in a [111] field. The drop in conductivity between 1 T and 4 T is much larger in s2 and in s1. This is consistent with the suppression of a large magnetic component to the conductivity in s2 from magnetic excitations. The conductivity becomes field independent at fields above $\gtrsim 4$

T for both samples. This field independent region provides a more accurate representation of the low field phonon conductivity. Furthermore, we will also see in section 7.4.3 that the 8 T data for DTO s1 is very well described by phonons in the boundary scattering limit, indicating that the conductivity is solely due to phonons. Finally, since the spin-lattice coupling has been proposed to be weak in DTO [8], the high field data should be a good approximation of the zero field phonon term. This is because of the absence of a significant spin-phonon scattering, which would reduce the conductivity from the boundary limited regime. Therefore, we will define the zero field phonon conductivity as the 8 T data here. For completeness, we will also consider the scenario where the 1.5 T data is the zero field phonon conductivity.

7.4.3 Low temperature conductivity

The low temperature thermal conductivity at 0 T and 8 T in the [111] direction for both samples is seen in figure 7.7 for the heat current in the $[1\bar{1}0]$ direction and in figure 7.8 for the heat current in the [111] direction. The conductivity in a 1.5 T field is also featured for the $[1\bar{1}0]$ samples in order to directly compare our data to the conductivity data reported by Kolland *et al.* [14, 101] and Scharffe *et al.* [105]. Let us start by considering the conductivity along the $[1\bar{1}0]$ direction in figure 7.7. The blue line in panel (a) is an extrapolation of the high temperature conductivity fit to $T < 1$ K. In this temperature range, the fit of the high temperature data is approximately equivalent to the calculated boundary limited phonon conductivity (the black line in panel (a)). First of all, it is clear that the 8 T data for s1 is very well described by boundary limited phonons, confirming the high quality of this sample. In fact, this is the first DTO sample studied where the boundary limited phonon conductivity is observed [14, 101, 105]. More importantly, however, is to note that the phonon conductivity in the boundary limited regime is the maximal phonon contribution. That is, any conductivity in excess to the boundary limited phonon conductivity must be from an additional channel of conductivity. Therefore, since the 8 T data is well described by boundary limited phonons, we can be confident that there is no additional magnetic conductivity or magnetic scattering of the phonons. On the other hand, the 1.5 T data is greater than the calculated phonon conductivity in the boundary scattering limit indicating residual magnetic excitations in addition to the lattice conductivity. Additionally, we have seen in figure 7.6 (and in chapter 6) that the conductivity for $B \gtrsim 5$ T is field independent since any magnetic excitations are suppressed by the large Zeeman energy. Therefore, we define the phonon conductivity to be the 8 T data ($\kappa_{\text{ph}} \equiv \kappa(8\text{ T})$). This is consistent with the conclusion drawn from the phonon conductivity discussion in section 7.4.2. Now considering s2 in figure 7.7 (b), the black line is again the calculated phonon conductivity in the boundary scattering limit for s2 and the red line is the extrapolation of the fit from the high temperature phonon conductivity peak seen in figure 7.3. It is clear that the measured 8 T conductivity is much less than the calculated boundary limited phonon conductivity. However, the extrapolation of the high temperature fit agrees reasonably well with the 8 T data, attesting that the high field conductivity is entirely due to phonons. The sub T^3 temperature dependence of the 8 T data in s2 indicates a higher level of disorder in this sample over s1, consistent with the high temperature conductivity, and the x-ray scattering results.

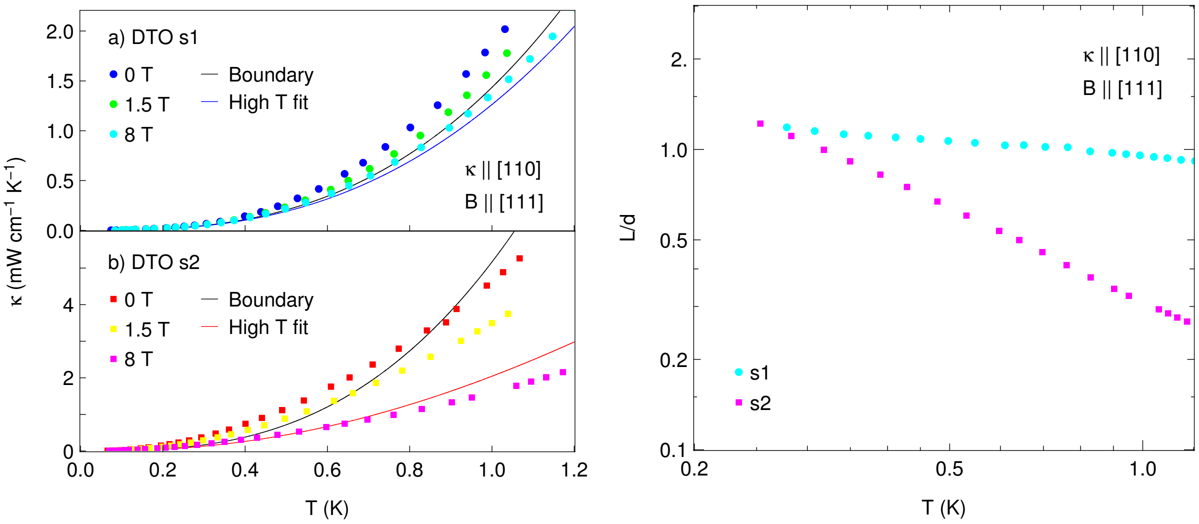

Figure 7.7: *Left:* Zero field, 1.5 T and 8 T thermal conductivity is plotted versus temperature for $Dy_2Ti_2O_7$ s1 (a) and s2 (b) for a $[1\bar{1}0]$ heat current. The black line is the calculated phonon conductivity in the boundary scattering regime for s1 in panel (a) and for s2 in panel (b). The blue and red lines are extrapolations of the high temperature fit of the conductivity peak for s1 and s2 respectively. *Right:* The phonon mean free path for the 8 T data normalized by the average sample dimension.

These results are mirrored in the conductivity data in the [111] direction in figure 7.8. Again, the 8 T data in s1 is very well described by the calculated boundary limited phonon conductivity (black line in panel (a)). Conversely, the 8 T data in s2 is not well described by the calculated phonon conductivity (black line in (b)). Rather, we find that in order to accurately model the 8 T data, we require phonon scattering from dislocations ($\Gamma_{\mathrm{D}} \sim T$) and point defects ($\Gamma_{\mathrm{PD}} \sim T^4$). This demonstrates the higher level of disorder in this sample. The impurity scattering rates obtained from this fit are seen in table 7.2 and are similar in magnitude to the fit results from the $[1\bar{1}0]$ high temperature fit.

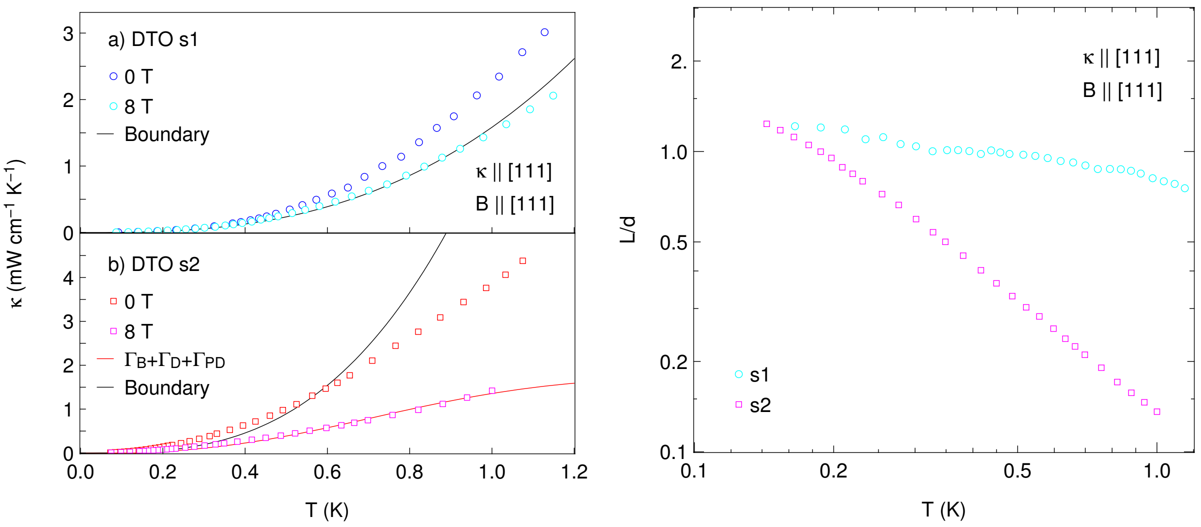

Figure 7.8: *Left:* Zero field and 8 T thermal conductivity is plotted versus temperature for $Dy_2Ti_2O_7$ s1 (a) and s2 (b) for a [111] heat current. The black line in (a) is the calculated phonon conductivity for s1 in the boundary scattering regime. The red line in (b) is a fit to the s2 data using kinetic theory and Matthiessen's rule (see main text) and the black line is the boundary limited phonon conductivity. *Right:* The phonon mean free path for the 8 T data normalized by the average sample dimension.

Sample	Γ_{B} (*const.*)	Γ_{D} (T)	Γ_{PD} (T^4)
s1 [111]	$1.35 \cdot 10^7$	/	/
s2 [111]	$3.00 \cdot 10^6$	$5.64 \cdot 10^6$	$7.18 \cdot 10^6$

Table 7.2: Phonon scattering rates for dislocations (Γ_{D}) and point defects (Γ_{PD}) obtained from fitting the low temperature temperature data in the [111] direction. The boundary scattering term (Γ_{B}) is calculated from the sample dimensions and sound velocity.

An alternative method of examining the level of impurity-phonon scattering is by considering the phonon mean free path, l_{ph}, as $T \to 0$ K. Kinetic theory is used to extract the phonon mean free path from the 8 T data via

$$l_{\mathrm{ph}} = 3\frac{\kappa_{\mathrm{ph}}}{c_{\mathrm{ph}} v_{\mathrm{s}}}. \tag{7.2}$$

The right panels in figure 7.7 and figure 7.8 shows the phonon mean free path in s1 and s2 in both crystallographic directions normalized by the average sample width. The phonon mean free path in DTO s1 is approximately equal to unity and nearly temperature independent, confirming the phonons are in the boundary scattering regime. As we have seen in chapter 2, specular scattering of phonons from the sample boundaries can cause the boundary limited conductivity to be slightly less than T^3 [45]. This effect can explain the small temperature dependence to L/d for s1. The mean free path in s2 is nearing unity at a lower temperature and has a much larger temperature dependence, as expected for samples with increased levels of disorder.

7.4.4 The magnetic contribution to the conductivity

The magnetic contribution to the thermal conductivity is estimated by considering the difference between the 0 T conductivity and the phonon conductivity ($\kappa_{\mathrm{mag}} \approx \kappa(0\ \mathrm{T}) - \kappa_{\mathrm{ph}}$). This analysis neglects a potential phonon-monopole scattering term which would convolute the lattice and magnetic channels of conductivity making it impossible to separate them in this manner. However, this approximation may be appropriate in DTO as it has been proposed that the spins decouple from the lattice at low temperatures [8] effectively resulting in two independent channels of conductivity. The magnetic conductivity is presented in figure 7.9 for DTO s1 and s2 when the heat current is in the $[1\bar{1}0]$ (left panel) and [111] (right panel) directions. As mentioned above, we define the lattice conductivity as the 8 T data. We also consider the magnetic conductivity in the $[1\bar{1}0]$ direction if the phonon conductivity is assumed to be the 1.5 T data as in references [14, 101, 105]. The DTO data from Kolland *et al.* is plotted on the same axes [14] for comparative reasons. Note that Kolland utilizes a 0.5 T field in the [001] direction to isolate κ_{ph}. It is evident that the magnetic conductivity in s2 is indeed greater than s1 for all measured temperatures regardless of the choice of the lattice conductivity or direction of heat flow. It is possible that the enhanced magnetic conductivity in s2 is a consequence of an increased monopole conductivity resulting from the higher level of disorder.

In support of these observations we note that recent studies of artificial spin-ice on a 2-dimensional Kagomé lattice have shown that randomly distributed magnetic impurities produce mobile magnetic monopoles in all regions of the sample [154, 155]. That is, the defects act as nucleation sites for monopoles by effectively lowing the activation energy. This result is consistent with our observation for the 3-dimensional pyrochlore lattice. Additionally, extended magnetic relaxation times observed in DTO have been shown to be due to small amounts of magnetic ion stuffing which tend to enhance the monopole density in the vicinity of the defects [96]. This is further evidence that impurities can cause an increase in monopole density at low temperatures which is consistent with our findings.

In addition to its magnitude, we can also investigate the temperature dependence of κ_{mag}. The solid lines are exponential fits to the s1 data. Here, the activated temperature

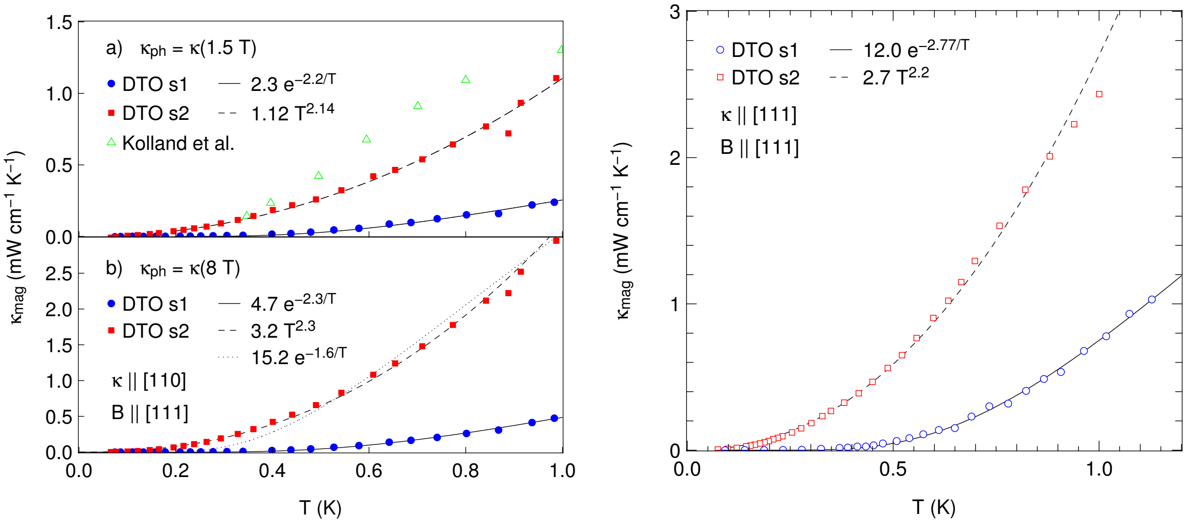

Figure 7.9: *Left:* The magnetic conductivity is plotted versus temperature for both s1 and s2 when the phonon conductivity is assumed to be the 1.5 T data (a) and the 8 T data (b) and the heat current is parallel to $[1\bar{1}0]$. The magnetic conductivity determined by Kolland *et al.* is also featured in panel (a) [101]. The solid line is an activated fit to the s1 data. The dashed line is a power law fit to the s2 data. The dotted line in panel (b) is an attempt to fit the s2 data with an exponential, which fails to describe the data as well as the power law fit. *Right:* The magnetic conductivity is plotted versus temperature for both s1 and s2 when the phonon conductivity is assumed to be the 8T data and the heat current and field are parallel to [111].

dependence does an excellent job at describing the data with an activation energy of approximately $2.2 - 2.8$ K. This is of the same order as the creation energy of a monopole excitation ($\Delta = 4.4$ K) [93]. The dashed lines in figure 7.9 are power law fits to the s2 data. We find that $\kappa_{\text{mag}} \sim T^{\eta}$ where $\eta = 2.1 - 2.3$ for s2 regardless of direction of heat flow. It is interesting to note that if we assume the phonon conductivity to be the 1.5 T data as in references [14, 101, 105], we come to the same qualitative result; that s1 is activated and s2 follows a power law temperature dependence. The dotted line in figure 7.9 panel (b) on the left is an attempt to fit κ_{mag} for s2 with an exponential functional form. It is clear that the curvature of the data is captured much better by the power law fit. Thus, s1 and s2 follow qualitatively different temperature dependences. Intuitively, an exponential temperature dependent thermal conductivity would be expected for activated quasi-particles such as magnetic monopoles, similar to electronic quasiparticles in fully gapped conventional superconductors [156]. This expectation is realized in s1, the sample with the lowest level of disorder measured here. On the other hand, the more disordered sample, s2, follows a power law temperature dependence. This could be a sign that the disorder in s2 is enhancing the monopole density at low temperatures. The power law temperature dependence is then a consequence of the Coulomb interaction between the monopole excitations.

An interesting comparison is with impurity states in semiconductors. Intrinsic charge carriers in a semiconductor are activated quasiparticles, much like monopole excitations in spin ice. Impurity doping can increase the carrier concentration which enhances the conductivity over a pure, undoped sample. In spin ice, impurities do not inherently introduce carriers into the system, but rather increases monopole density by possibly lowering the excitation energy in their vicinity essentially acting as nucleation sites.

7.5 Conclusion

In summary, thermal transport and x-ray diffraction measurements have been conducted on two separate samples of $Dy_2Ti_2O_7$ with varying levels of disorder. We have seen from the transport measurements that the monopole conductivity is strongly dependent on the level of disorder, which appears to affect both the monopole density and scattering rate. More specifically, the magnetic conductivity in the sample with less disorder exhibited an activated temperature dependence as expected for activated quasiparticle excitations. The magnetic conductivity in the sample with more disorder not only had a larger magnitude, but also followed a power law temperature dependence. This is possibly due to the stuffed magnetic Dy^{3+} ions acting as nucleation sites, effectively lowering the monopole creation energy in their vicinity, or by pinning monopole excitations upon cooling from higher temperatures. Therefore, it is feasible that the monopole conductivity can be tuned by controlling the level of disorder in the sample analogous to doping semiconductors.

Chapter 8

Quantum Spin Ice: $Yb_2Ti_2O_7$

8.1 Introduction

The quantum spin ice (QSI) Hamiltonian which describes the spin interactions in $Yb_2Ti_2O_7$ (YbTO) can theoretically support a quantum spin liquid (QSL) state at low temperature for a certain range of exchange parameters [17, 113]. That said, the true nature of the ground state in YbTO has eluded condensed matter physicists for years. Early μSR measurements have shown a suppression of spin fluctuations below $T_c \sim 240$ mK [19]. However, complementary neutron scattering measurements showed no signs of magnetic order below this temperature [19, 36, 37, 38, 39]. On the other hand, there have also been a number of neutron scattering measurements that do indicate ferromagnetic ordering below the critical temperature [40, 41]. Additionally, a strong sample dependence is observed in the behaviour of the low temperature specific heat. Samples prepared as a powder tend to exhibit a sharp peak at temperatures up to 265 mK whereas single crystals grown via the floating zone technique show a broad peak at much lower temperatures, or even multiple peaks [121, 18, 120]. These differing observations are in part due to known sample quality issues. It has been shown that single crystals grown via the floating zone technique can have an excess of Yb^{3+} ions on the Ti^{4+} sub lattice, known as stuffing [98]. In order to maintain charge neutrality, the oxygen stoichiometry is reduced such that the chemical formula is of the form $Yb_{2+x}Ti_{2-x}O_{7-x/2}$ [143]. Oxygen deficiency in these materials can affect the colour and transparency of the single crystals [143, 144]. Furthermore, the magnetization of $Dy_2Ti_2O_7$, a sister compound to YbTO, has been shown to depend on the oxygen content [143]. The oxygen concentration can be controlled during the growth process by altering the composition and pressure of the growth atmosphere or by annealing the single crystals in oxygen after they are formed which reduces the disorder associated with oxygen deficiency. Therefore, it is important to compare other physical properties of YbTO single crystals as grown, and after annealing in oxygen. This will help clarify the nature of the ground state.

Neutron scattering measurements above the critical temperature ($T_c \sim 180 - 265$ mK) reveal pinch point structure characteristic of spin ice correlations similar to the classical spin ice materials $Ho_2Ti_2O_7$ (HTO) and $Dy_2Ti_2O_7$ (DTO) [41, 80]. This indicates that YbTO is in a spin-ice like state above the critical temperature. The excitations from this phase can be described as quantum monopoles (QMP) and hence this phase is referred to as a magnetic Coulomb liquid phase [23]. The quantum monopoles are dispersive due to the off-diagonal $J_{z\pm}$ term in the Hamiltonian [23, 157]. This significantly suppresses the excitation energy of QMP quasiparticles ($\Delta \sim 2J_{zz} - |J_{z\pm}| \sim 2.3$ K) compared to the, dispersionless classical monopoles observed in HTO and DTO ($\Delta \sim 2J_{\text{eff}} \sim 4.3$ K) [23, 93]. Thermal conductivity measurements are a reliable probe for detecting such quasiparticles and may also reveal information about the spin dynamics in YbTO. Thermal conductivity measurements can also be used to detect phase transitions due to the existence of heat carrying quasiparticles in exotic phases, or by observing variations in the level of phonon scattering from excitations.

Previous thermal transport measurements have been conducted on single crystals of YbTO [13, 23]. Both studies report a quadratic temperature dependence of the thermal conductivity which is possibly due to phonon scattering from magnetic excitations. A kink-like anomaly is observed at approximately 200 mK which is related to the first order phase transition observed in the specific heat. The field dependence of the conductivity provides evidence for a contribution to the conductivity from magnetic monopole excitations for $T > 200$ mK which are suppressed with the application of a magnetic field. The low field conductivity for $T < 200$ mK is consistent with the suppression of phonon scattering from spin fluctuations in a ferromagnetic sate which is observed in magnetization measurements [20].

In this chapter, we present additional thermal transport measurements on two YbTO samples, one as grown, and one which has been annealed in oxygen to ensure correct oxygen stoichiometry. This is done to examine the effect oxygen disorder has on both the behaviour of the phase transition and the magnetic excitations in YbTO. A detailed study of the field dependence of the conductivity is also conducted. The field is swept quasi-statically with very fine field increments at temperatures near the phase transition in order to accurately observe the rapid suppression of the magnetic excitations with an applied field near T_c. Finally, the field dependent conductivity also allows us to form a field versus temperature phase diagram for YbTO with $B||[111]$.

8.2 Experimental Details

Thermal conductivity measurements were conducted on two single crystals of YbTO; one sample was measured as grown, and the other was annealed in oxygen. The conductivity was measured using the standard 1-heater-2-thermometer method described in chapter 3 from $T = 100$ mK to 50 K across two cryostats. The field dependence of the conductivity was measured in fields up to 8 T and temperatures up to 1 K with both the heat current and applied field in the [111] direction. The sample thermometers used to measure the thermal gradient were calibrated *in situ* to account for variations in the calibration between runs, and to accurately obtain the magnetoresistive correction for the resistive thermometers in field. To ensure the samples were thermally equilibrated at each temperature step, the system was allowed to settle for extended periods of time until the sample thermometers stabilised to a constant value. The magnet was zeroed before every field sweep to avoid remnant fields in the superconducting magnet, which can be on the order of a few milli-Tesla. This is done by ramping the field positive and then negative with a decreasing magnitude each sweep until the field reaches 0 T.

The annealed sample was obtained by initially preparing a polycrystalline sample using >99.99% pure Yb_2O_3 and TiO_2 via the standard solid state reaction technique. The resulting power was sintered at temperatures between 1200°C and 1300°C for 48 hours with intermittent regrinding to ensure a well mixed sinter. The sinter was then compressed into a 10 mm diameter rod approximately 140 mm long and sintered at 1250°C for 6 hours. Single crystals were grown in a four-mirror optical floating-zone furnace (Crystal System Inc.) in an argon environment with a growth rate of 1-2 mm/hour. The resulting crystals were oxygen deficient and hence are dark in colour. The oxygen stoichiometry was improved by annealing the as grown sample at 1200°C for 72 hours in a flowing oxygen atmosphere. This caused the single crystal to become transparent, a sign of stoichiometric oxygen content.

8.3 Results

8.3.1 Zero field temperature dependence

We will start by exploring the effects of annealing YbTO in oxygen has on the thermal transport. The left panel of figure 8.1 shows the thermal conductivity between 100 mK and 50 K for our as grown (red squares) and annealed (blue circles) YbTO samples. The thermal conductivity measured by Li *et al.* is plotted for comparative reasons (green triangles) [13]. Recall that for insulating materials, the conductivity peak is strongly dependent on disorder. In general, a peak appears in the lattice conductivity at approximately $\Theta_D/20$ where Umklapp scattering becomes the limiting factor of the phonon mean free path rather than the sample boundaries. However, increased levels of disorder will tend to suppress the magnitude of the peak, and can thus be used as a relative estimate of disorder in a series of samples. Therefore, our annealed sample appears to be the highest quality sample measured compared to our as grown sample, and the sample measured by Li *et al.* [13]. An interesting comparison can be made to the two $Dy_2Ti_2O_7$ (DTO) samples which are examined in depth in chapter 7. Recall that the high temperature peak conductivity was observed to be approximately 150 mW cm^{-1} K^{-1} in the DTO sample with the least amount of disorder (s1). This is nearly twice the magnitude of the annealed YbTO sample which peaks at approximately 80 mW cm^{-1} K^{-1}. Thus, although the annealed YbTO sample exhibits the largest peak conductivity amongst the YbTO samples measured, it is possible that some disorder exists in the lattice which scatter the phonons.

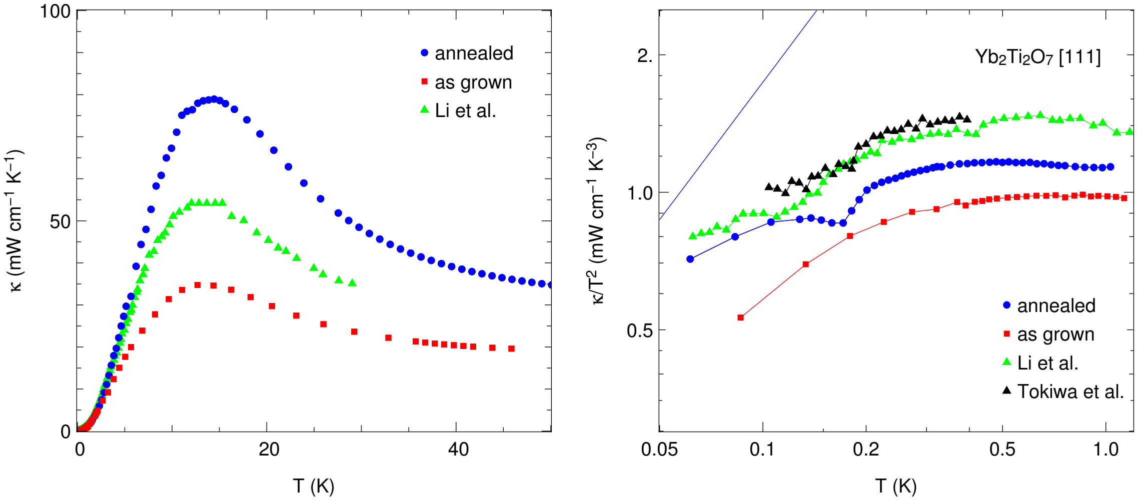

Figure 8.1: *Left:* High T conductivity for a YbTO sample as grown (red squares), and a sample annealed in an oxygen environment (blue circles). The high T conductivity measured by Li *et al.* [13] is also plotted on the same axes (green triangles). *Right:* Low temperature conductivity plotted as κ/T^2 versus T clearly shows a sharp transition in the annealed sample. This also illustrates the T^2 temperature dependence in both samples above 200 mK. The solid blue line is the calculated phonon conductivity in the boundary limited regime (see section 8.4.1). The low temperature thermal conductivity measured by Li *et al.* [13] (green triangles) and Tokiwa *et al.* [23] (black triangles) are plotted on the same axes for comparative reasons.

If we consider now the conductivity below 1 K (the right panel of figure 8.1), we see that both samples follow a T^2 above $T = 300$ mK. The reduction from the T^3 temperature dependence expected for boundary limited phonons (the solid blue line in figure 8.1 for the annealed sample) indicating the presence of significant phonon scattering in YbTO at zero field. As the temperature is lowered below $T_c \approx 180$ mK, the annealed sample exhibits a sharp step-like transition whereas the as-grown sample displays a gradual enhancement of the power law which is also seen in data measured by Li *et al.* [13]. Tokiwa *et al.* suggest that the step-like decrease in the conductivity at the transition temperature is evidence for the suppression of a magnetic channel of thermal conductivity [23]. The differing behaviour of the conductivity of each sample at the transition is qualitatively consistent with the different behaviours of the phase transition observed in specific heat measurements. Unannealed single crystals tend to have a broad feature in the specific heat between 150-180 mK, whereas powder samples, which are not ailed by oxygen vacancies, exhibit a sharp peak at temperatures up to 265 mK [98]. Magnetization measurements on both powder and single crystals of YbTO have revealed small hysteresis loops at the transition confirming the first order nature of the transition [20]. However, the width of the hysteresis loops is only 3 mK, which is less than the temperature step size used here. Hence, we are unable to resolve this hysteresis.

At temperatures below this transition region, both samples show an increase in the power law, approaching T^3 at the lowest temperatures measured. Excitations in the proposed QSL ground state are predicted to be emergent photon excitations with a linear dispersion. This would appear as a cubic term in the specific heat (similar to phonons). However, it is difficult to predict their effect on thermal transport either from scattering phonons or by conducting heat themselves. Furthermore, the characteristic photon energy scale is on the order of $J_\perp^3/J_\parallel^2 \sim 50$ mK [23], which is a factor of two lower than our minimum temperature. On the other hand, the increasing power law temperature dependence as $T \to 0$ K could be evidence of a suppression of phonon scattering from spin fluctuations, resulting in the phonon mean free path extending towards the sample boundaries. A detailed examination of the low temperature phonon conductivity is found in section 8.4.

8.3.2 Low field temperature dependence

The temperature dependence of the conductivity of the annealed sample is plotted as κ/T^2 versus T in figure 8.2 in applied fields up to 500 mT parallel to the [111] direction. We focus on the annealed sample here because a sharp transition is easily observed for all field values measured here as indicated by the arrows in figure 8.2. Each curve exhibits a similar T^2 temperature dependence at high temperatures ($T > T_c$) due to a combination

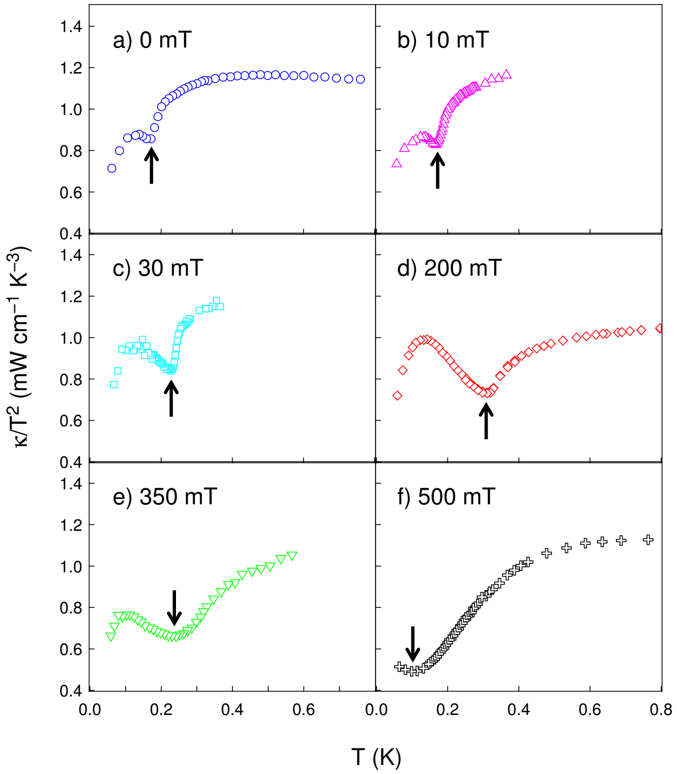

Figure 8.2: The thermal conductivity of the annealed sample in applied fields up to 500 mT in the [111] direction plotted as κ/T^2 versus T. The kink in the data (indicated by the black arrows) becomes smeared out by 200 mT and is nearly fully suppressed by 500 mT.

of phonon scattering from lattice defects as well as the existence of an additional magnetic channel of conductivity [13, 23]. The low field conductivity ($B \lesssim 200$ mT) reveals that the kink in the data shifts towards higher temperature as the field is increased reaching a maximum value of $T_c^{\max} \sim 315$ mK at 200 mT. A similar effect is observed in specific heat, magnetization and neutron scattering measurements, where small applied fields up to 100 mT shift the transition to higher temperatures [22, 20, 158]. The enhancement of the transition temperature with increasing field suggests the ground state is ferromagnetic in nature. A kink-like feature is still observed in the data at 200 mT, however it is much broader than the zero field conductivity, appearing as a minimum in κ/T^2 rather than a sharp step. As the field is increased further, the broadened transition shifts towards lower temperatures and is nearly fully suppressed by 500 mT.

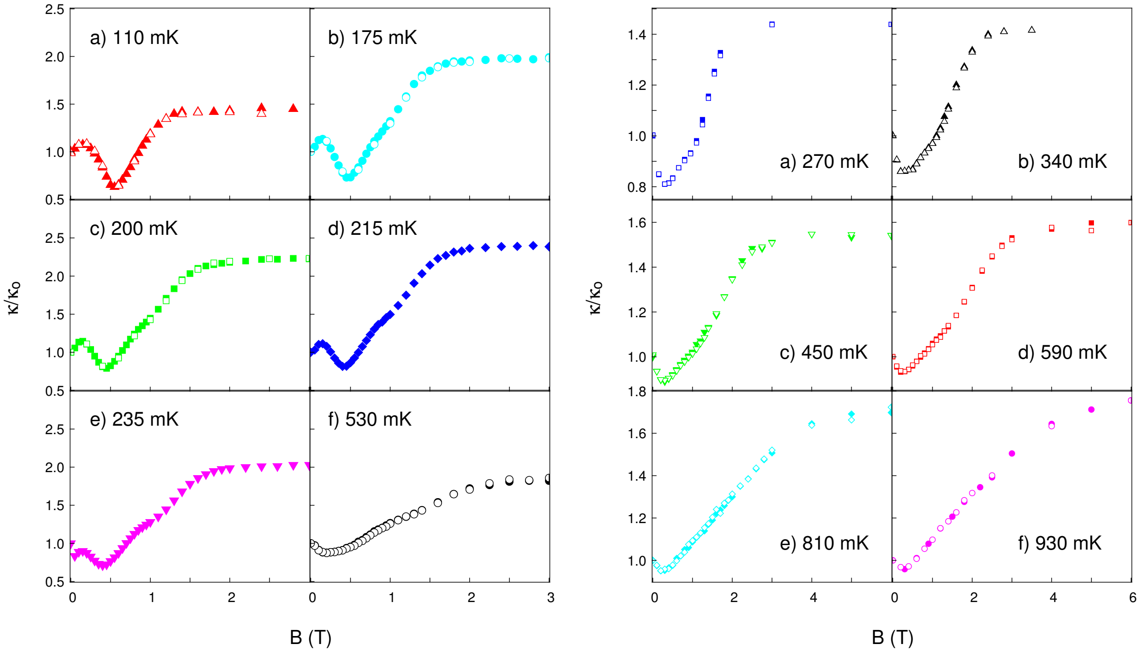

Figure 8.3: The field dependence of the thermal conductivity plotted as κ/κ_o versus B at constant temperatures from 110 mK to 530 mK for the annealed sample (left) and from 270 mK to 930 mK for the as grown sample (right). Filled (open) symbols indicate an increasing (decreasing) magnetic field.

8.3.3 Field dependence

The field dependent isotherms of the conductivity can be seen for the annealed sample and the as-grown sample in the left and right panels of figure 8.3, respectively. Both samples follow a similar field dependence for $T > T_c^{\max}$ which can be categorized into three regions as seen in figure 8.4. The low field regime (region I) is characterized by the initial decrease in the conductivity, the intermediate field regime (region II) shows an enhancement in the conductivity, and the high field regime (region III) is field independent. As the temperature approaches T_c, an additional mound of conductivity is observed in the data for the annealed sample which suppresses the initial decrease in the conductivity. The suppression of the initial decrease in the conductivity is examined in detail in section 8.4.2. This behaviour is not observed in the field dependence of the as-grown sample for all temperatures measured.

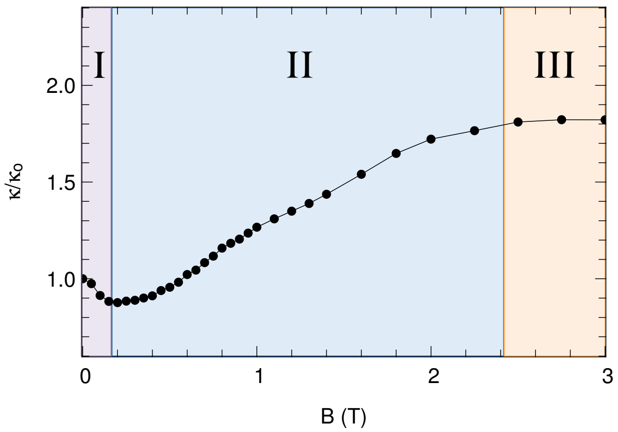

Figure 8.4: The field dependence of the thermal conductivity is divided into three regions for $T > T_c^{\mathrm{max}}$. The conductivity decreases in region I, increases in region II and is field independent in region III.

8.4 Discussion

8.4.1 High field limit

Phonon conductivity

Panels (a) and (b) in figure 8.5 show the field dependence of the conductivity for the annealed sample at 530 mK and the as-grown sample at 590 mK, respectively. The thermal conductivity is initially suppressed at low field (region I in figure 8.4), followed by an enhancement for $B \gtrsim 300$ mT (region II). Increasing the field further reveals that the conductivity saturates above 3 T (Region III), indicating the suppression of spin-phonon scattering. To first order, the contribution to the conductivity from the lattice should be field independent. Thus, we can ascribe the field independent data at high fields to be entirely due to phonons. The temperature dependence of the conductivity at 0 T and 8 T is seen in panel (c) for the annealed sample, and (d) for the as-grown sample. The solid lines are the calculated lattice contributions in the boundary scattering limit for each sample. The phonon conductivity was calculated via kinetic theory such that $\kappa = \frac{1}{3}c_{\mathrm{ph}}v_{\mathrm{s}}d$. Here $c_{\mathrm{ph}} = 0.5T^3$ J/mol K is the phonon specific heat [17] corresponding to a Debye temperature of $\Theta_{\mathrm{D}} = 157$ K. Thus, the sound velocity can be estimated to be $v_{\mathrm{s}} = 2.65 \cdot 10^5$ cm/s according to Debye theory. The average width d of the annealed and as-grown samples are approximately 300 μm, and 250 μm respectively. The 8 T data approaches the boundary limited value at the lowest temperatures, but it is clear there is some additional scattering at higher temperatures. This is illustrated in the right panel of figure 8.5 by plotting the phonon mean free path, l, normalized by the average sample width, d. The mean free path is determined using kinetic theory such that $l = 3\kappa/c_{\mathrm{ph}}v_{\mathrm{s}}$. The phonon mean free path in the annealed sample approaches the sample width at a higher temperature than the as-grown sample. This suggests a higher level of scattering in the unannealed sample, consistent with the different magnitudes of the high temperature conductivity peak seen in figure 8.1. This is further evidence for the existence of disorder scattering in both YbTO samples studied here.

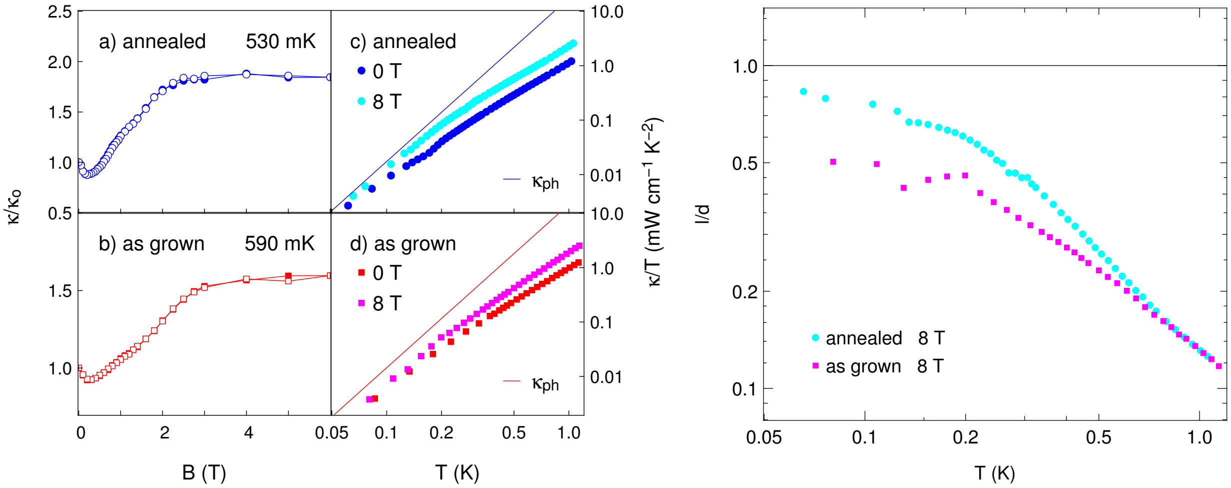

Figure 8.5: *Left:* Field dependence of the thermal conductivity of the annealed sample at 530 mK (a) and for the as-grown sample at 590 mK (b) shows that the high field conductivity is field independent. The temperature dependence of the thermal conductivity for the annealed (c) and as-grown (d) samples at 0 T and 8 T. The solid line is the calculated phonon conductivity in the boundary scattering regime. *Right:* The phonon mean free path of the 8 T data.

Spin-phonon scattering

As stated above, the increasing conductivity and saturation in regions II and III of figure 8.4 are consistent with a reduction of spin-phonon scattering due the increasing Zeeman energy as the field is increased. In general, suppressing phonon scattering from spin fluctuations by increasing the Zeeman energy can only result in an enhancement in the conductivity [23]. In order to examine the effect of the spin-phonon scattering in regions II and III, we plot the conductivity normalized by the high field saturated value ($\kappa_{\max}$) as a function of $\mu_B B/k_B T$ as seen in figure 8.6 for the annealed sample at 530 mK and the unannealed sample at 590 mK, 810 mK, 930 mK and 1.0 K. Plotting the data in this manner shows that the intermediate field range (region II) follows the Brillouin function for spin 1/2 and $g_J = 8/7$, the g factor for ytterbium. This suggests that the increasing conductivity in region II is due to the suppression of the scattering of phonons by paramagnetic spins. Additionally, the high field plateau corresponds to a full suppression of spin fluctuations where the system enters a field induced long range ordered state. Note that only the data at temperatures above $\sim$ 500 mK scale with the Brillouin function. The data at temperatures less than 500 mK follows a qualitatively similar field dependence, increasing conductivity with field which saturates at high field, however, it does not scale with the Brillouin function. The reason for this scaling only being appropriate above $\sim$ 500 mK is not understood. This effect has previously been demonstrated in YbTO by Tokiwa *et al.* at temperatures up to 5 K [23]. It is interesting to note that a similar high field scaling onto the Brillouin function is also observed in HTO (see chapter 6), implying that these two materials have a considerable spin-lattice coupling. This is in contrast to DTO where the spins and the lattice are decoupled and no such scaling is observed.

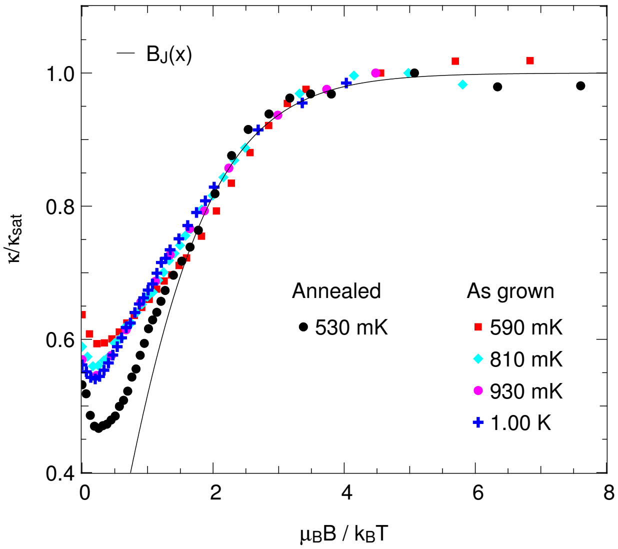

Figure 8.6: Field dependent conductivity of the annealed sample at 530 mK (black circles) and the unanealed sample at 590 mK (red squares), 810 mK (cyan diamonds), 930 mK (pink circles) and 1.0 K (blue crosses) plotted as $\kappa/\kappa_{\max}$ versus $\mu_B B/k_B T$. The high field conductivity scales onto the Brillouin function for spin 1/2 and $g_J = 8/7$, the g factor for Yb^{3+}.

Although we have shown that the high field data is entirely the phonon conductivity in the absence of any magnetic scattering, it is not an accurate representation of the zero field phonon conductivity. This is due to the large amount of spin-phonon scattering at low fields which will significantly reduce the phonon contribution to the total thermal conductivity. This makes a quantitative assessment of any potential magnetic channel of conductivity very difficult to obtain. Thus, the magnetic channel of conductivity is qualitatively assessed by examining the behaviour of the low field conductivity.

8.4.2 Low field limit

Magnetic excitations

Recall from figure 8.4 that the low field conductivity for $T > T_c^{\max}$ initially decreases in region I then increases in region II. This field dependent behaviour of the conductivity can arise in magnetic insulators due to the phonons being scattered from nearly paramagnetic spins which have a small energy gap between spin states [159, 160, 13]. A key feature of such a scenario is that the location of the conductivity minimum must shift towards higher fields as the temperature is increased [160, 13]. However, recall from figure 8.3 that the observed field value of the conductivity minimum decreases with increasing temperature, and hence, the initial decrease in the conductivity in region I cannot be described entirely by the paramagnetic scattering effect. Instead, Tokiwa *et al.* states that the low field suppression of the conductivity for $T > T_c^{\max}$ can be rationalized as the suppression of heat carrying monopole excitations in the Coulomb liquid phase due to the increasing Zeeman energy [23]. That is, at zero field, the conductivity is due to a combination of phonons and monopole excitations. Increasing the magnetic field suppresses the density of monopoles by increasing the Zeeman energy of the magnetic moments, which effectively increases the activation energy. Since the magnetic contribution to the thermal conductivity is proportional to the number of monopoles, a reduction in the monopole density will result in a suppression of the conductivity. Therefore, the low field suppression of the conductivity is taken as evidence for a significant contribution to the conductivity from monopoles at zero field for $T > T_c^{\max}$, consistent with previous conductivity measurements [13, 23]. Comparing the annealed to the unnanealed sample at 530 mK and 590 mK respectively in figure 8.3, we find that the value of the conductivity minimum is approximately 90% of the zero field value and occurs at 200 mT in both samples. This indicates that the magnetic contribution contributes equally in either sample suggesting that the oxygen content does not have a major impact on the behaviour or density of the magnetic excitations.

As the temperature approaches the critical temperature from above ($T \to T_c^+$), an

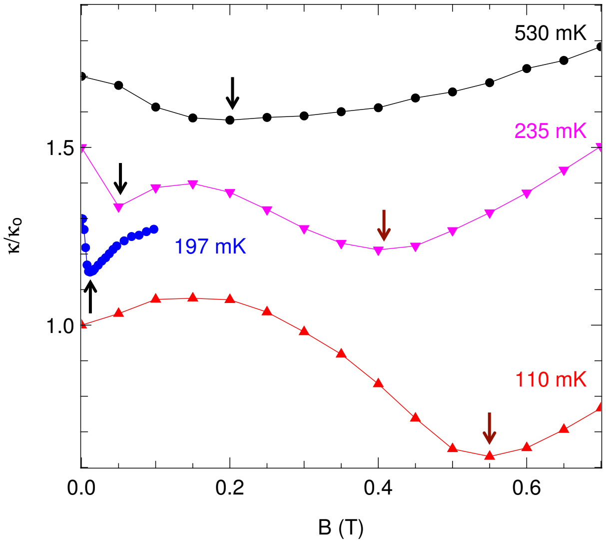

Figure 8.7: The field dependence of the thermal conductivity for the annealed sample for $B < 0.8$ T above T_c (530 mK), approaching T_c (235 mK) and below T_c (110 mK). The arrows indicate the position of the conductivity minima. The black arrows indicate the field value at which the low field conductivity is suppressed. the red arrows indicate the field value where the additional conductivity mound is suppressed.

additional conductivity peak is observed centred at approximately 150 mT in the annealed sample. This emergent conductivity mound is explicitly shown in figure 8.7 by examining the field dependence of the conductivity of the annealed sample at 530 mK, 235 mK, 197 mK and 110 mK up to 800 mT. The conductivity peak is observed in temperatures as high as 235 mK, which is greater than $T_c \approx 180$ mK in zero field. Additionally, the conductivity peak in the 235 mK or 197 mK data does not fully suppress the initial low field decrease, resulting in two minima in the data as indicated by the black and red arrows in figure 8.7. At temperatures below the critical temperature, the low field drop in the conductivity is fully suppressed, resulting in a single minimum in the data as seen in the 110 mK data. This low temperature field dependence is consistent with previously reported studies [13, 23]. It has been proposed that the low temperature ground state is ferromagnetically ordered with considerable ferromagnetic fluctuations [40, 41, 20, 22]. The suppression of these ferromagnetic fluctuations with an applied magnetic field is consistent with the observation of an immediate increase in the conductivity due to a reduction of phonon scattering from spin fluctuations [13]. Neutron scattering measurements corroborate this interpretation because of the observation of significant diffuse scattering in zero field which is weakened with the application of a magnetic field in the $[1\bar{1}0]$ direction [38]. However, as the diffuse scattering is reduced, well defined spin wave excitations appear [38, 13]. These spin waves scatter the phonons, resulting in a decrease in the conductivity [13]. Therefore, the observed conductivity peak is consistent with the onset of a ferromagnetically ordered state with ferromagnetic fluctuation and spin waves which affect the thermal conductivity by acting as phonon scattering mechanisms. As the field is increased further, the conductivity is enhanced due to a suppression of paramagnetic scattering of the phonons as described in section 8.4.1. This causes a minimum in the data pointed out by the red arrows in figure 8.7. The minima in these isotherms indicate phase transitions which allow us to generate a field versus temperature phase diagram for $B \parallel [111]$. This is found in section 8.4.3.

Conductivity suppression rate

We will now examine the low field decrease in conductivity for the annealed sample in the limit as $T \to T_c^+$. We have seen in figure 8.7 that the initial drop in conductivity disappears below T_c. At temperatures slightly above the critical temperature, the rate at which the conductivity decreases as the field is increased from zero becomes very quick. This is partly due to the observation of an additional mound of conductivity which is consistent with a ferromagnetically ordered phase. In order to resolve this rapid suppression of the conductivity, the field sweep steps must be very fine. Additionally, it is important to sweep the magnetic field through zero to observe symmetric behaviour for positive and negative field directions. This ensures that the data is not be skewed by a small remnant field in the superconducting magnet which can be on the order of a few millitesla. The left panel of figure 8.8 shows the field dependence of the conductivity well above the transition at 324 mK, just above the transition at 197 mK and below the transition at 110 mK for $B < 100$ mT. The field was swept in both the positive and negative directions to ensure the data is symmetric about 0 T. The 197 mK data shows a very rapid drop in conductivity reaching a minimum at 10 mT. Our ability to resolve the sharp drop in conductivity near T_c is by virtue of field steps of less than 2 mT. The field dependence of the conductivity is suppressed quadratically as $B \to 0$ T [23]. The quadratic suppression rate ensures that the conductivity is smooth when the field is ramped through zero. Plotting the data as κ versus B^2 allows us to examine the conductivity suppression rate. This is seen in the right panel of figure 8.8. Following the analysis established by Tokiwa *et al.* [23], we fit the low field conductivity as $\kappa(B) = \kappa_o - \alpha B^2$ where $\alpha > 0$. Since the magnetic conductivity is correlated to the number of excitations as described above, α is a measure of the monopole suppression rate.

Figure 8.9 shows the evolution of α as a function of temperature for our data (black

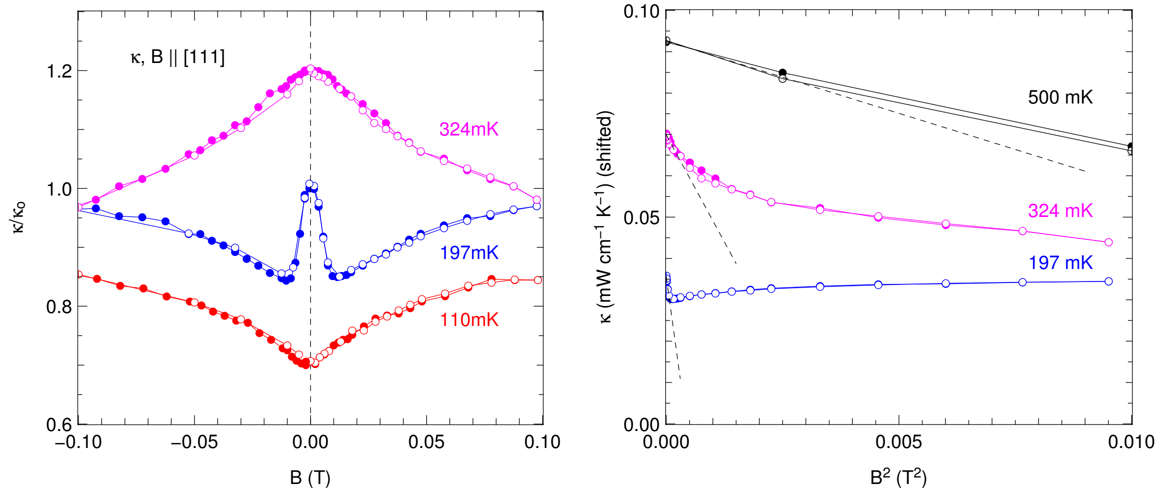

Figure 8.8: *Left:* The low field thermal conductivity of the annealed sample for $B < 100$ mT at 324 mK (pink), 197 mK (blue) and 110 mK (red). Closed symbols are for ascending field and open for descending. The 197 mK data shows a sharp drop in conductivity reaching a minimum by 10 mT. *Right:* The thermal conductivity (shifted for clarity) is plotted versus B^2. The dashed lines are linear fits to the data as $B \to 0$ T.

circles) and the data from Tokiwa *et al.* [23]. Tokiwa's data shows an increasing α with decreasing temperature until a peak is observed at $T_{\mathrm{max}} \sim 500$ mK. Below this temperature, they find that α decreases until T_c, where it is equal to zero. They suggest that the decrease in α below T_{max} is due to a reduction in the monopole density. The observation of a non-monotonic temperature dependence of α leads them to conclude that the suppression of the monopole excitations cannot be due to ferromagnetic fluctuations, which will certainly increase monotonically as $T \to T_c^+$ [23].

Contrary to Tokiwa *et al.*, our data shows that α continues to increase until $T_c \sim 180$ mK where is abruptly drops to zero. The monotonically increasing behaviour of α as the temperature is lowered means that we cannot rule out FM fluctuations as the origin of the low field reduction of $\kappa(B)$ as the system nears the first order FM transition. Furthermore, the data roughly follows a Curie-Weiss like temperature dependence (dashed blue line), consistent with the the Curie-Weiss behaviour observed in magnetization measurements suggesting the onset of a FM ground state in YbTO [20]. Finally, as we have seen above, a mound of conductivity appears at low fields for temperatures slightly above the critical temperature. This conductivity peak is associated with a ferromagnetically ordered state below T_c [13]. Our observations suggest that this ferromagnetically ordered phase extends

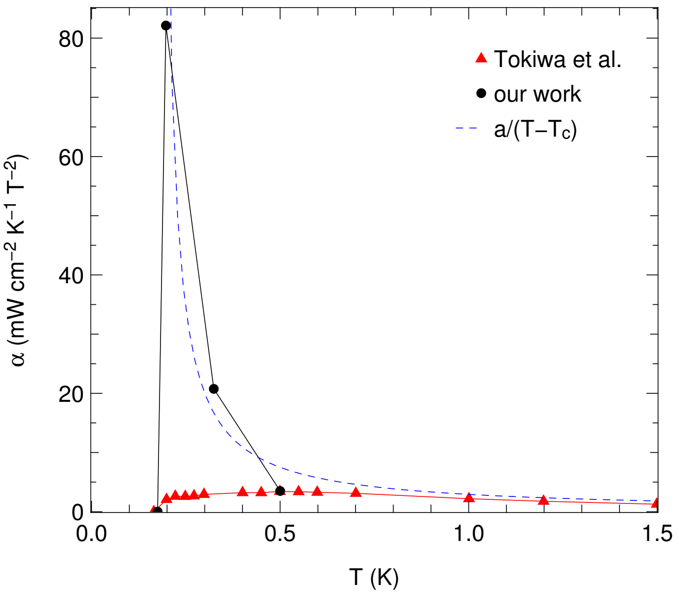

Figure 8.9: The temperature dependence of the monopole suppression rate α extracted from the low field conductivity. The suppression rate measured by Tokiwa *et al.* (red triangles) shows a peak at $T_{\text{max}} = 500$ mK, whereas our α increases monotonically until T_c. The blue dashed line is a Curie-Weiss temperature dependence with a Curie temperature of $T_c = 180$ mK (a is a scaling parameter).

to temperatures greater than the critical temperature in small applied fields. This is further evidence of the suppression of the monopole excitations by ferromagnetic fluctuations associated with the onset of this ordered phase.

We are unable to conduct this analysis on the as-grown sample for two main reasons. First, the size of the field steps in the field sweep data sets a limitation on our ability to resolve the low field behaviour in the as-grown sample. That is, we cannot accurately extract the α parameter from the low field data. Second, recall from figure 8.1 that there is no well defined critical temperature in the as-grown sample since there is no sharp feature in the temperature dependence of the conductivity as in the annealed sample. So, it is ill-posed to consider the conductivity suppression rate as $T \to T_c$ if there is no clear transition temperature. For these reasons, we have only considered the annealed sample for this analysis.

8.4.3 Phase diagram

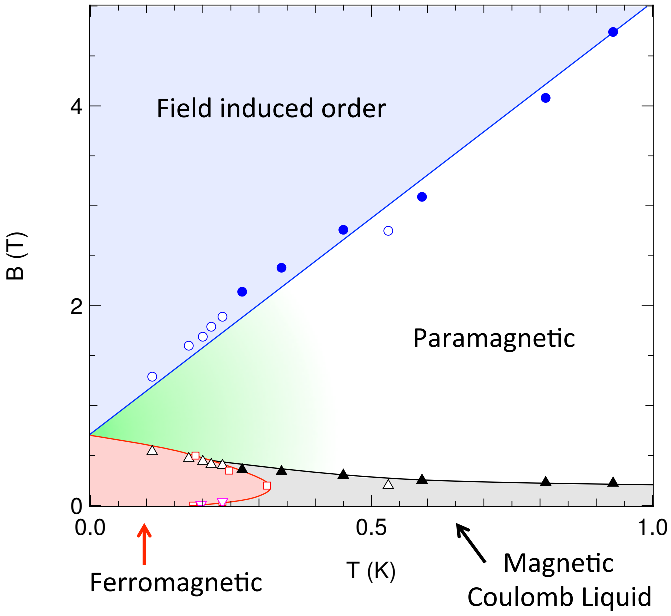

Figure 8.10: Field versus temperature phase diagram for YbTO for $B \parallel [111]$. The open symbols are extracted from the annealed sample data and the closed symbols from the as-grown sample. The green region indicates a potential quantum critical regime between the MCL phase and the field-induced ordered phase.

A field versus temperature phase diagram can be constructed from the thermal transport data by selecting the minima of the field dependent conductivity data, and the onset of the high field saturation regime. This allows us to determine the locations of the phase lines, however, knowledge of the various phases is supplemented with previous neutron scattering and magnetization measurements [40, 41, 20, 158]. The resulting phase diagram is seen in figure 8.10. In the QSL scenario, the MCL phase, which supports quantum monopole excitations, is separated from the classical field induced ordered state by a quantum critical point (QCP). Neutron scattering measurements reveal that a quantum critical point occurs at approximately $B_c \approx 0.5$ T parallel to the $[1\bar{1}0]$ direction [38, 18]. Our data suggest that a similar critical point may exist between the MCL phase and the field induced ordered phase for $B \sim 700$ mT parallel to the [111] direction (the green region in the phase diagram). Critical fluctuations in the vicinity of this proposed QCP could also potentially explain why the field dependence of the thermal conductivity does not scale with the Brillouin function for $T \lesssim 500$ mK. A field dependent study at temperatures below 100 mK would certainly help resolve this.

Finally, we will consider the low temperature ferromagnetic ground state. We find that the transition temperature initially increases with the application of a small magnetic field. As stated above, this is indicative of a ferromagnetic state and is consistent with a number of observed properties [22, 20, 158]. However, the transition temperature reaches a maximum value at approximately 200 mT, above this field, the transition temperature is suppressed. A similar effect has recently been reported in specific heat, magnetization and neutron scattering measurements, yielding a similar lobe-like shape of the phase diagram [158]. It is possible that the positive slope of the phase line for $B < 200$ mT is an indication of the suppression of the ferromagnetically ordered phase due to the proximity of YbTO to a QSL phase [158].

8.5 Conclusion

Temperature and field dependent thermal transport measurements have been conducted on a YbTO sample as-grown and a sample which has been annealed in oxygen. Our results reveal that the annealed sample has a lower level of defect scattering of phonons and also shows a sharp, step-like feature at the transition temperature $T_c \sim 180$ mK. The as-grown sample does not exhibit the same sharp transition, but rather a broad evolution of the power law temperature dependence of the conductivity. The field dependent study has shown that magnetic monopole excitations contribute a significant amount to the total thermal transport when $T > T_c$ for both the annealed and as-grown samples consistent with previously reported conductivity data [13, 23]. That is, although variances in the oxygen stoichiometry affect the phonon channel of conductivity and the behaviour of the low temperature transition, it appears that this does not play a major role in the behaviour of the magnetic excitations in YbTO. This is contrary to the considerable effect stuffed Dy^{3+} have on monopole excitations in $\mathrm{Dy_2Ti_2O_7}$ as seen in chapter 7. Contrary to Tokiwa *et al.* [23], we find that the suppression rate of the magnetic excitations exhibits a monotonic increase as $T \to T_c^+$, consistent with the presence of considerable ferromagnetic fluctuations associated with the onset of a FM first order phase transition. The field versus temperature phase diagram extracted from the conductivity data reveals a dome-like ferromagnetic phase below ~ 180 mK and 600 mT. This is consistent with recent magnetization, specific heat and neutron scattering measurements [158].

Part III

Topological Kondo Insulators

Chapter 9

Kondo Insulators

9.1 Magnetism of Conduction Electrons

The previous chapter was concerned with the magnetism generated by the core electrons localized on the ions in a solid. We have seen how this type of magnetism in conjunction with geometrical frustration can lead to some very interesting states with rather exotic elementary excitations. We now turn our attention to the magnetism brought about by delocalized electrons in metals and the interaction with magnetic ions. We will follow the theory laid out in Coey's book *Magnetism and Magnetic Materials* [63].

9.1.1 Exchange interactions in metals

Direct exchange

Unlike the insulating transition-metal oxides, where there is no direct $3d - 3d$ orbital overlap, the $3d$ orbitals in metals will overlap significantly. If the overlap is small but non-zero, the electron hopping between ions is described by the tight binding model with the Hamiltonian

$$H = \sum_{ij} t_{ij} c_i^\dagger c_j \tag{9.1}$$

where $c_i^\dagger$ and c_j are the electron creation and annihilation operators on sites i and j respectively. The bandwidth in the tight binding model with isotropic hopping ($t_{ij} = t$) is $W = 2Zt$ where Z is the number of nearest neighbours. The strength of the exchange interaction depends on bandwidth. As t becomes large, the exchange energy decreases and the electrons become delocalized regardless of their spin and the magnetic susceptibility is well described by Pauli paramagnetism as in a normal metal [63]. The sign of the direct exchange depends on the band occupancy; roughly half-filled bands have an antiferromagnetic exchange to satisfy the Pauli exclusion principle, and nearly empty or filled bands have a ferromagnetic exchange to minimize the Coulomb interaction.

$s-d$ model

If the ions in a metal have a magnetic moment, then the core spins $\mathbf{S}$ can couple to the conduction electrons with spin $\mathbf{s}$ resulting in a term in the Hamiltonian of the form

$$-J_{\mathrm{sd}}\Omega|\psi|^2\mathbf{S}\cdot\mathbf{s}. \tag{9.2}$$

Here, J_{sd} is the coupling strength, Ω is the volume of the d-orbital and $|\psi|^2$ is the conduction electron probability density [63]. This interaction can lead to uniform spin polarization of the conduction electrons either parallel or anti-parallel to the core spin. That is, long range ferromagnetic coupling between the conduction electrons regardless of the sign of J_{sd}. The $s-d$ model can also be applied to the rare earth ions, where the core electrons are $4f$ rather than $3d$ as in the transition metals. In this case the interaction takes the form $-J_{\mathrm{sf}}\mathbf{S}\cdot\mathbf{s}$. The $s-d$ model is used when examining the effect magnetic impurities have on conduction electrons in a metal as discussed below.

RKKY interaction

Consider now the effect of a magnetic impurity on the conduction electron spins in a metal. Ruderman, Kittel, Kasuya and Yosida showed that a magnetic impurity induces an oscillatory spin polarization of the conduction electrons which decreases as $1/r^3$. Thus, the effective coupling between two magnetic moments mediated by the conduction elections is given by

$$J_{\mathrm{eff}} \approx \frac{9\pi J_{\mathrm{sf}}^2\nu^2F(\xi)}{64\varepsilon_{\mathrm{F}}}. \tag{9.3}$$

Here ν is the number of conduction electrons per atom, ε_{F} is the Fermi energy and $F(\xi)$ is the RKKY function, defined as

$$F(\xi) = \left(sin(\xi) - \xi cos(\xi)\right)/\xi^4 \tag{9.4}$$

where $\xi = 2k_{\mathrm{F}}r$, k_{F} is the Fermi wave vector and r is distance from the impurity [63].

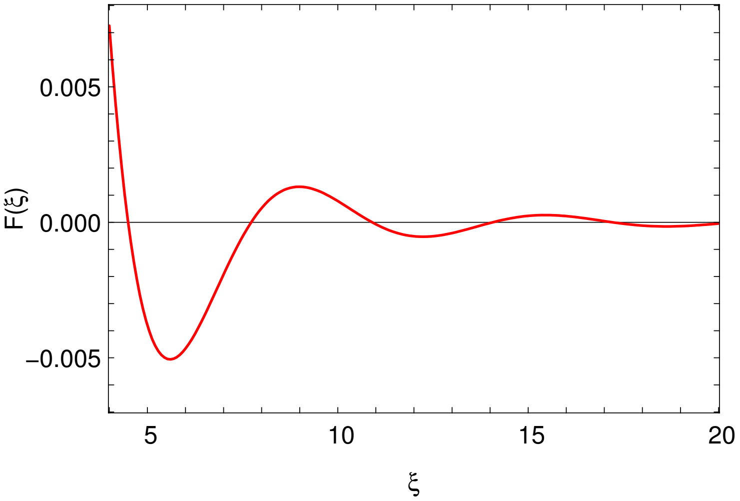

Figure 9.1: RKKY function $F(\xi)$ where $\xi = 2k_{\mathrm{F}}r$.

In the case of rare-earth magnetic ions, the spin S is only a good quantum number for gadolinium because the f shell is exactly half-filled. The rest of the rare-earth ions have the total angular momentum J as their quantum number which is determined according to Hund's rules. Therefore, S must be projected onto J to find the correct exchange coupling. We find that the effective RKKY exchange parameter is given by $J_{\mathrm{RKKY}} = GJ_{\mathrm{eff}}$ where $G = (g-1)^2J(J+1)$ is the de Gennes factor.

9.1.2 The Kondo effect

The full Hamiltonian describing magnetic impurities in a metal is given by

$$H = \sum_{ij} t_{ij}c_i^\dagger c_j - \sum_{kl} J_{\mathrm{sd}}\mathbf{S}_k \cdot \mathbf{s}_l \tag{9.5}$$

which is also known as the Kondo Hamiltonian. If J_{sd} is positive, the magnetic moment has the effect of creating an enhanced moment by polarizing the conduction electron spins in its vicinity. However, if J_{sd} is negative, the conduction electrons will anti-align with the moment, forming a nonmagnetic, Kondo singlet state. This is known as the Kondo effect. The Kondo effect can be observed in susceptibility measurements as a temperature independent region below a characteristic temperature, T_{K}, called the Kondo temperature. Above T_{K} the susceptibility follows the usual Curie-Weiss temperature dependence with a negative Θ_{P}. The Kondo effect is also observed in resistivity measurements as a shallow minimum at T_{K} resulting from the scattering of conduction electrons from the Kondo singlets. One good example of the Kondo effect is iron impurities in copper. The following section focuses on one of the earliest discovered examples of a Kondo insulator, $\mathrm{SmB_6}$.

9.2 Introduction to $\mathrm{SmB_6}$

The rare-earth hexaboride material $\mathrm{SmB_6}$ is a rather peculiar material where Sm ions on equivalent lattice sites have their $4f$ shells in either the $4f^6$ or $4f^5$ configuration in the ratio of 3:7 respectively [161]. A unit cell of the $\mathrm{SmB_6}$ lattice is seen in figure 9.2. First reported nearly half a century ago by Menth *et al.* of Bell Labs who observed no sign of magnetic ordering down to 350 mK and intrinsic semiconducting behaviour down to 3 K [162]. They proposed that the semiconducting behaviour was a result of thermally ionizing the Sm^{2+} ions ($4f^6$) producing Sm^{3+} ions ($4f^5$) and conduction electrons. A simple theoretical model was developed by Falicov and Kimball to describe this semiconductor-metal transition. Including an electron-hole interaction term in their model produces a qualitative fit to the resistivity data. This description, however, implies large valence fluctuations as a function of temperature which is not seen in a number of measurements in the following couple of years. Resistivity measurements showed that the large change in resistance below 65 K is not consistent with the change in carrier density which is on the order of a few percent of the number of samarium ions per cubic centimetre [161]. The change in the lattice parameter at low temperature is smaller than expected to account for the proposed change in valence from Sm^{3+} to Sm^{2+}, which have a larger ionic radius than the former. Finally, Mössbauer spectroscopy shows an absorption line peak between what is expected for divalent and trivalent Sm ions which is temperature independent between 1 K and 1000 K. All of these measurements demonstrate a lack of temperature dependence of the $4f^6$:$4f^5$ electronic configuration ratio in $\mathrm{SmB_6}$, invalidating the fluctuating valence model of Menth *et al.*

A better description of $\mathrm{SmB_6}$ is that of a Kondo Insulator (KI) which is described by the theoretical model outlined in section 9.1.2 [163, 164, 165]. In this scenario, the f electrons of the magnetic Sm^{3+} ions in the $4f^5$ electronic configuration hybridize with the $5d$ conduction bands forming Kondo singlets which screen the local moments. The hybridization causes a small band gap to open below the Kondo temperature $T_K \simeq 50$ K. This leads to insulating behaviour since the chemical potential falls somewhere in the middle of the energy gap, which suppresses the existence of electronic quasiparticles. Thus, the local moments from the Sm^{3+} ions are necessary for the Kondo effect to occur and the KI scenario is consistent with the observation of a temperature independent $4f^6$:$4f^5$

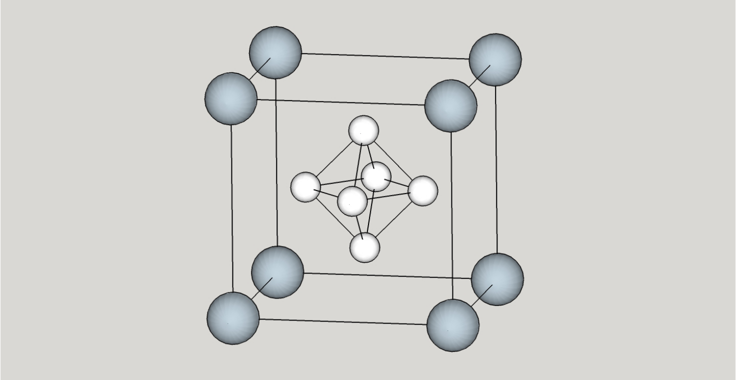

Figure 9.2: Boron octahedra (white spheres) are located at the centres of cubic samarium cages (grey spheres).

electronic configuration ratio in SmB_6.

The low temperature resistivity in SmB_6 exhibits a temperature independent plateau below approximately 5 K. This is a surprising result since the resistivity should diverge as the temperature approaches absolute zero in a fully gapped insulator. Initially, the saturation of the resistivity at low temperatures was ascribed to mid-gap impurity states [161]. Sluchanko *et al.* measured the ac-conductivity ($\sigma(v)$) of SmB_6 and found a step-like feature at $T = 5$ K, coinciding with the metallic-like behaviour of several other thermodynamic properties. They claimed this is an indication of the formation of a coherent electronic state brought about by an electronic phase transition causing the plateau in the resistivity [166, 167].

Another exotic explanation of the low T resistivity plateau was proposed by Dzero, Sun, Galitski and Coleman where they describe SmB_6 as a three-dimensional, topological Kondo insulator (TKI) [168]. Here, the hybridization of the f-electrons with the conduction electrons and strong spin-orbit coupling leads to a topologically nontrivial insulating state in the bulk with anomalous excitations on the surface [168]. This topologically nontrivial structure is a result of the symmetry of the hybridization amplitude which is determined by the symmetry of the Kramers doubles of the rare-earth ions (Sm^{3+} in this case). The reduced coordination of Sm^{3+} ions at the surface leads to a breakdown of the Kondo effect at the surface, effectively lowering the Kondo temperature by a factor of 10 [169]. That is, the screening of the localized f-electrons by the conduction electrons is either pushed to lower temperatures, or is never even fully realized due to a magnetic ordering on the surface. The absence of Kondo singlets on the surface leads to a significant increase in the number of conduction electrons at the surface [170].

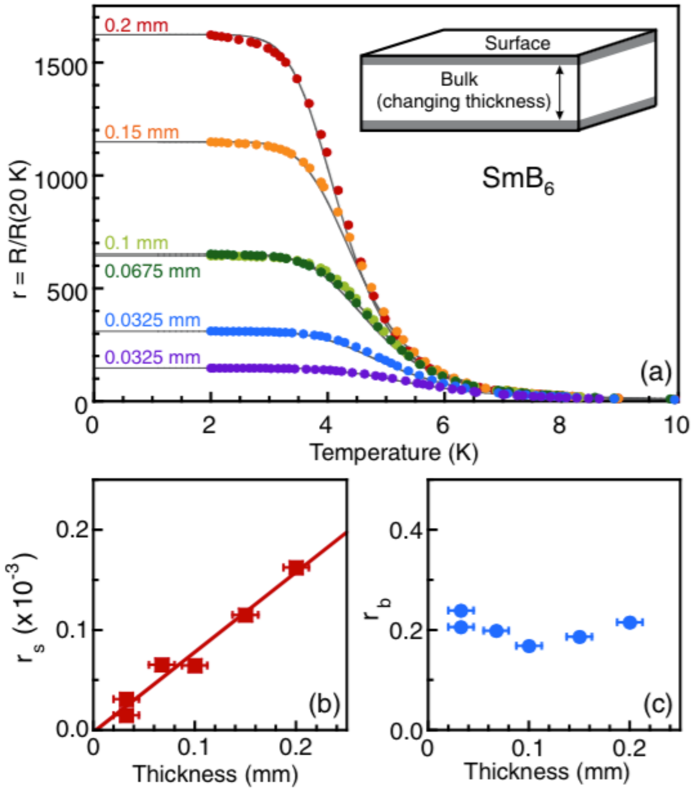

Figure 9.3: The thickness dependence of the resistivity ratio $r = R/R(20\ \mathrm{K})$ is modelled by the functional form $r(T)^{-1} = r_s^{-1} + \left[r_b e^{-\Delta/k_B T}\right]^{-1}$. The the thickness dependence of the surface contribution r_s and the bulk contribution r_b is seen in (b) and (c) respectively [24].

A number of very clever experiments have since verified that the low temperature resistivity plateau is in fact due to electrically conductive surface states theoretically predicted by Dzero *et al.* [168]. Johnpierre Paglione's group initially used point-contact spectroscopy to probe the temperature dependence of the electronic states. If the saturation of the resistivity was due to bulk, coherent in-gap states, you would expect an enhancement of the density of states (DOS) at the Fermi level which would appear as a peak in the point contact spectroscopy measurement at zero-bias. That is, the electronic structure would evolve for $T \lesssim 5$ K. However, they find that the DOS is temperature independent for all temperatures below 10 K, precluding the existence of in-gap states [171]. Thus, the temperature dependence of the resistivity must be a compilation of both the bulk channel and the surface channel. In order to separate the contribution from the bulk and the surface, Syers *et al.* considered several samples of varying thickness, ranging from 32.5 μm to 200 μm [24]. They developed a simple parallel channel conductance model for an activated bulk channel and a temperature independent surface channel. The total resistance normalized by the resistance at 20 K ($r(T) = R/R(20\text{ K})$) is thus given by

$$r(T)^{-1} = r_s^{-1} + \left[r_b e^{-\Delta/k_B T}\right]^{-1} \tag{9.6}$$

where $r_s \equiv R_s/R(20\text{ K})$ and $r_b \equiv R_b/R(20\text{ K})$ are the surface and bulk components respectively and are left as fitting parameters along with the excitation energy Δ. Their results are summarized in figure 9.3. The energy gap is found to be thickness independent and is equal to $\Delta = 3.3$ meV for all thicknesses, which is consistent with earlier transport measurements [167, 172, 162, 173, 174]. Furthermore, they find that r_b is independent of the sample thickness whereas r_s shows a clear linear dependence on thickness, with a negligible intercept. Relating the normalized values of r_b and r_s to the actual bulk and surface contributions to the conductance they found that the the linear dependence of r_s on the sample thickness corresponds to a decreasing relative contribution of the surface conductance to the bulk conductance. The zero intercept can thus be understood as zero conductance through the bulk, as expected for a sample with zero thickness. Therefore, this is clear evidence that the resistivity plateau is due to electrically conducting surface states in SmB_6.

Syers *et al.* also probe the surface conductance by applying a gate voltage to the surface by using a Corbino disk on the surface of the sample [24]. Similar to the sample thickness study, they employ a two channel conductivity model. Again, they find that the bulk channel has no dependence on the gate voltage whereas the surface channel is decreased with positive biasing. This verifies that the surface is responsible for the charge carriers in SmB_6. Furthermore, they found that the surface charge carriers are electron-like with a density of approximately 2×10^{14} cm^{-2} and a mobility of 133 cm^{2}V^{-1}s^{-1}, which is in good agreement with photoemission results [175, 27, 172, 176].

A number of other techniques corroborate the two dimensional nature of the charge carriers on the surface of an otherwise insulating bulk in SmB_6. Kim *et al.* measured the Hall effect as a function of sample thickness [25]. The Hall resistance, $R_{xy} \equiv V_{xy}/I$, stemming from the bulk is expected to be dependent on the sample thickness via $R_{xy}/B \propto 1/d$ while the Hall resistance from the surface should be independent of the sample thickness, d. Figure 9.4 (c, d) shows the Hall resistivity plotted versus the applied field. It is evident that the Hall effect is linear in the high temperature (20 K) and the low temperature (2 K) limit indicating single channel conductivity from either the bulk or the surface. The

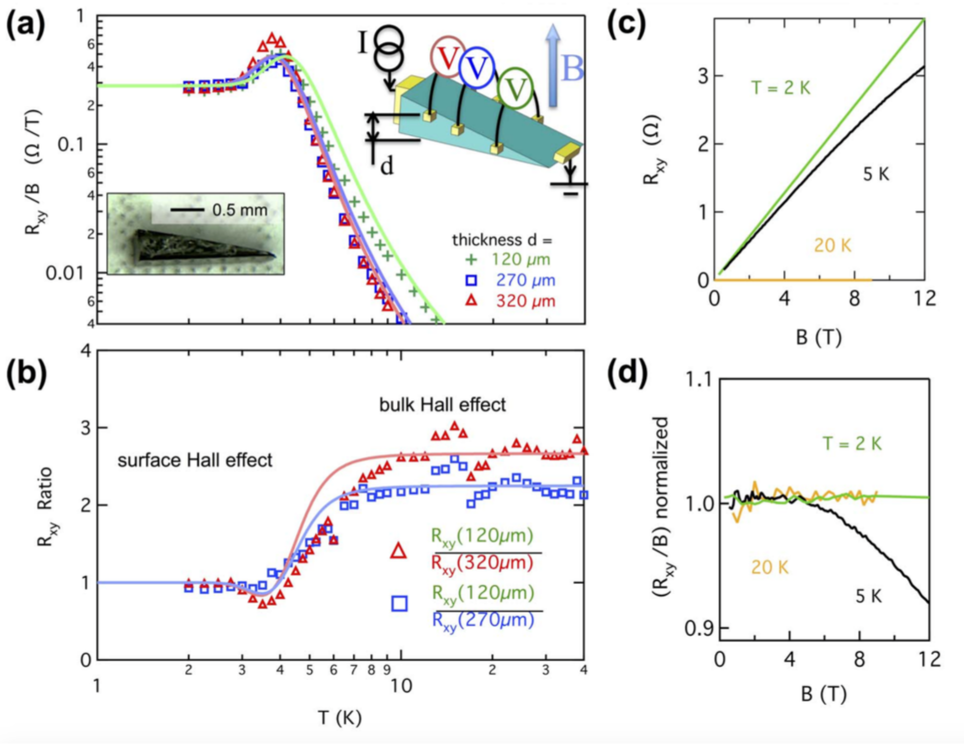

Figure 9.4: (a) Temperature dependence of the Hall resistance for different sample thicknesses. (b) Ratio of the Hall resistance for different width samples. The surface contribution at low temperature is independent of thickness, and the high temperature Hall resistance is proportional to the inverse of the sample width. (c, d) The field dependence of the Hall resistance at 2 K, 5 K and 20 K.[25].

data in the crossover region (5 K) is clearly not linear in field, signifying contributions from more than one channel. The ratio of the Hall resistances for different thicknesses is seen in figure 9.4 (b). The data in the low temperature limit shows no dependence on the sample thickness, as expected for surface dominated conductance. However, in the high temperature limit, the ratio of the Hall resistance displays the expected $1/d$ dependence on the sample thickness for bulk charge carriers. That is, $\frac{R_{xy}(120\mu\mathrm{m})}{R_{xy}(320\mu\mathrm{m})} = 2.67$ and $\frac{R_{xy}(120\mu\mathrm{m})}{R_{xy}(270\mu\mathrm{m})} = 2.25$, which is clearly observed in figure 9.4 (b). Thus, Kim *et al.* have clearly demonstrated that the low temperature conductivity is due to the surface. A key characteristic of the surface state excitations in a topological insulator is their protection against time-reversal invariant perturbations [177, 178, 179]. Thus, they explored the topological protection of these surface states by physically damaging the surface of their sample, a time-reversal invariant perturbation. They found that the low temperature Hall resistance remains unchanged after mechanically cutting and scratching their sample, providing good evidence for the topological nature of the surface excitations.

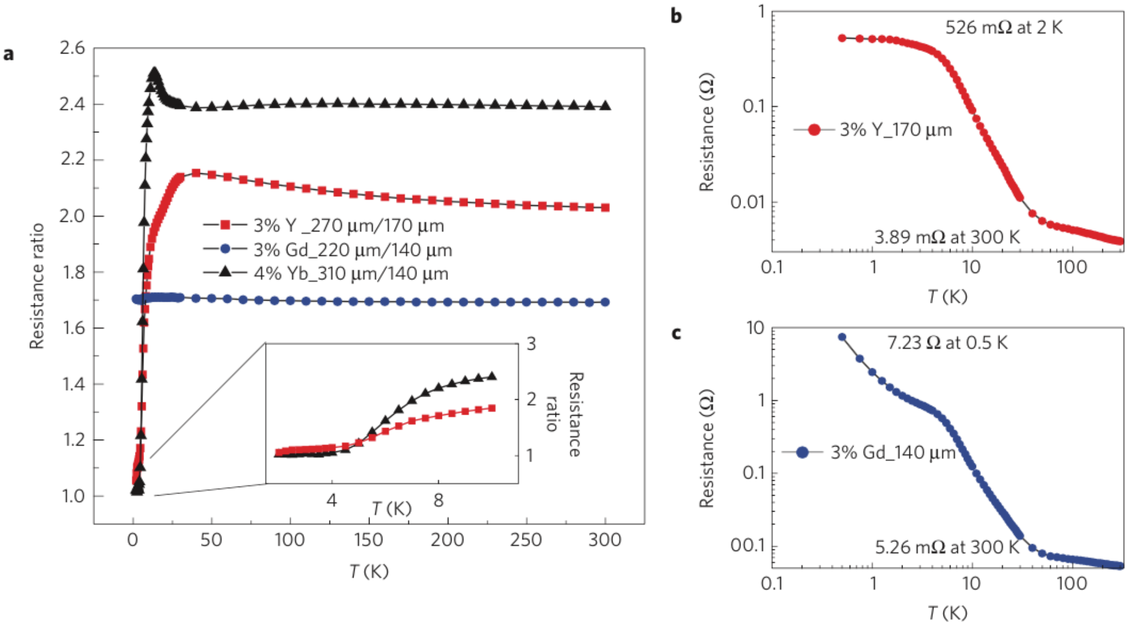

Figure 9.5: (a) Resistance ratio of SmB_6 samples of different widths with yttrium, ytterbium and gadolinium. (b) The resistance plateau persists with non-magnetic yttrium impurities. (c) Magnetic gadolinium impurities suppresses the electronic surface states, resulting in the absence of the resistivity plateau [26].

Shortly after they measured the surface Hall effect, Kim *et al.* went on to investigate the topological protection of the surface states by introducing magnetic and non-magnetic dopants and examining the temperature dependence of the resistivity [26]. Figure 9.5 (a) shows the thickness resistance ratio of SmB_6 with non-magnetic 3% Y, 4% Yb and magnetic 3% Gd substitutions of the Sm ions. Notice that divalent Yb ions have no magnetic moment in SmB_6. The high temperature data in all three cases exhibits the usual thickness dependence for electrical conductivity in a bulk conductor determined from Ohm's law. However, as the temperature is lowered below $\sim$ 5 K, the resistance ratios for the Y and Yb doped samples approach unity, indicating a thickness independent resistivity resulting from the conductive surface states. On the other hand, the Gd doped sample follows the same geometrical ratio over the entire temperature range. That is, the time-reversal symmetry breaking, magnetic ion substitutions suppresses the topological surface states, leaving the bulk as the only channel for electrical conduction. Figure 9.5 (b) and (c) show the temperature dependence of the resistivity for the Y doped sample and the Gd doped sample respectively. The Y doped sample shows the same resistivity saturation behaviour below 5 K as the undoped $\mathrm{SmB_6}$ case. The resistivity in the Gd doped sample continues to increase at low temperature, indicating a small gap insulating state with no sign of conduction from surface states. Therefore, there is a good deal of evidence suggesting that the surface states in $\mathrm{SmB_6}$ are indeed topologically protected under time-reversal invariant perturbations which strengthens the claim that $\mathrm{SmB_6}$ is a topological Kondo insulator.

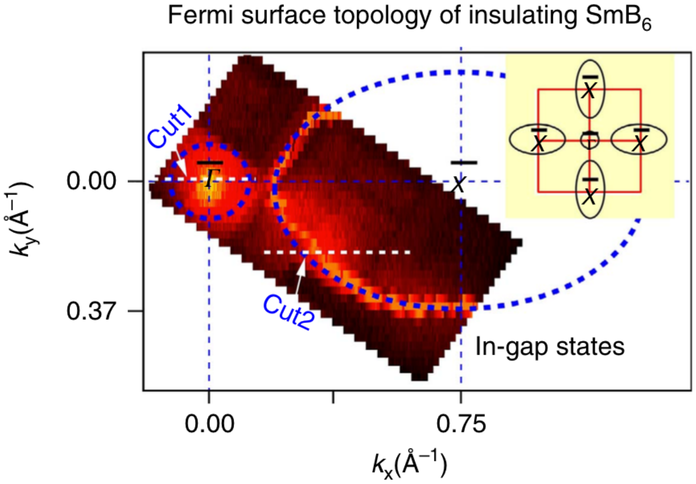

Figure 9.6: ARPES measurement of $\mathrm{SmB_6}$ at 6 K in a window of ±4 meV of the Fermi energy [27].

Angle-resolved photoemission spectroscopy (ARPES) measurements provide a direct probe of the distribution of electronic excitations in momentum space. Electrons near the surface of the sample are excited by absorbing incident x-rays and the angle at which they escape depends on their momentum. Thus ARPES measurements can be used to map the electronic band structure near the surface of the material. There have been several ARPES measurements conducted on $\mathrm{SmB_6}$ samples [175, 27, 172, 176]. Each of these studies come to the same general conclusion; the $5d$ bulk electronic band hybridizes with the f electrons, opening a gap of about $\Delta_B \sim 20$ meV below approximately 100 K. As the temperature is lowered below this temperature range, an in-gap state is observed around the $\bar{X}$ point with an energy gap of 4 meV. Below $\sim$ 6 K, low lying metallic states are observed near the Fermi level around $\bar{X}$ and $\bar{\Gamma}$. The emission intensity of these states show negligible dependence in the k_z direction, indicating they are two dimensional, and likely originate on the surface of the sample [175]. These results are consistent with the possibility that SmB_6 is a topological Kondo insulator.

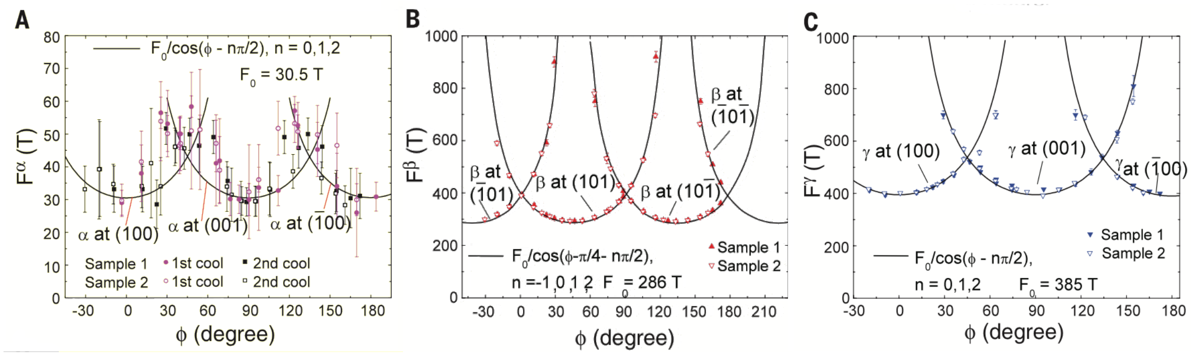

Figure 9.7: The angle dependence of the quantum oscillation frequencies is fitted with a two dimensional Fermi-surface originating from the conductive surface layer [28].

The realization of topologically protected, conductive surface states in SmB_6 is a fantastic discovery in itself. That said, possibly the most interesting result is the observation of de Haas-van Alphen (dHvA) quantum oscillations at low temperature [28, 29]. Quantum oscillations are a typical characteristic of a well behaved Fermi-liquid, thus it is surprising to clearly observe dHvA oscillations in a system which has been shown to be a bulk insulator. Quantum oscillation measurements can yield a great deal of information about both the Fermi-surface (FS) and the quasiparticle excitations. The cross sectional area of Fermi-surface, S, is related to the dominant frequencies of the quantum oscillations, F via

$$F = \frac{\hbar}{2\pi e} S. \tag{9.7}$$

Additionally, the effective mass and scattering rate of the quasiparticle excitations can be determined from the oscillation amplitude via the Lifshitz-Kosevich formula which states that

$$A \propto B^{1/2} \left| \frac{\partial^2 S}{\partial k^2} \right|^{-1/2} R_T R_D \tag{9.8}$$

where A is the oscillation amplitude, B is the magnetic field, $|\frac{\partial^2 S}{\partial k^2}|$ is the FS curvature, $R_T = \frac{\alpha m^* T/B}{\sinh(\alpha m^* T/B)}$ is the temperature damping factor and $R_D = \exp(-\alpha T_D m^*/B)$ is the

Dingle damping factor from defect scattering and $\alpha = 2\pi^2 k_\mathrm{B} m_e/eh = 14.69$ T/K [180]. The effective mass is given by m^*, and the scattering rate, τ, is related to the Dingle temperature $T_D = \hbar/2\pi k_\mathrm{B}\tau$.

Two separate groups observed dHvA oscillations in torque magnetometry measurements of $\mathrm{SmB_6}$. However, they arrived at conflicting interpretations [28, 29]. The first group was from the University of Michigan under the supervision of Lu Li [28] and the other was from Cambridge University supervised by Suchitra Sebastian [29]. Li's group performed torque magnetometry measurements on a number of $\mathrm{SmB_6}$ samples which were grown in an Al flux [28]. They observed large oscillations periodic in $1/\mu_o H$ appearing in the magnetic torque above 5 T followed by faster oscillations for $\mu_o H > 10$ T for $T = 300$ mK. Fourier transforming the oscillations revealed peaks at 35 T, 300 T and 450 T corresponding to three pockets of the Fermi-surface. These oscillations correspond to a Fermi-surface which only occupies a few percent of the first Brillouin zone. Additionally, they found that the electrons on each of these Fermi-surface pockets have an effective mass of $m^* \sim 0.1 - 0.2m_e$ and a mean free path of approximately $20 - 50$ nm, two orders of magnitude larger than the lattice spacing (~ 0.4 nm). The low effective mass of the electronic quasi-particles is unexpected since theories on topological Kondo insulators predict a heavy effective mass on the order of $m^* \sim 10 - 100m_e$ due to strong correlations [181]. Oscillations from heavier excitations may exist, but might only be observable at lower temperatures and higher magnetic fields due to the temperature damping of the oscillation amplitude. Finally, Li *et al.* found that the temperature dependence of the frequency peak amplitudes follow the Lifshitz-Kosevich formula (equation 9.8) at all temperatures, as expected for a normal metal.

The most significant conclusion from this study is the observation of a $1/cos(\phi)$ angle dependence of the oscillation frequencies for a half rotation of the sample ($\phi = 0°$ to $180°$) which is expected for a two dimensional Fermi-surface. As the sample is rotated in the field, the electron oscillations around the Fermi-surface will follow larger orbits and eventually will diverge. This is not the case for a three dimensional FS since the oscillations will always have an upper bound. Figure 9.7 shows the oscillation amplitudes from the Fourier transformation as a function of rotation angle for each of the three observed FS pockets (α, β, γ). The solid lines are fits to inverse sinusoidal function of the form $F(\phi) = F_o/cos(\phi - \phi_o)$. There are four branches of the inverse sinusoidal function because of the four-fold crystalline symmetry of the cubic lattice. They claim that it is possible that the α band could be caused by an extremely elongated 3D ellipsoidal FS, however a cleaner sample would be required to resolve this issue to reduce the Dingle damping factor. Nonetheless, this result is consistent with a two dimensional FS originating from the conductive surface states.

If the QO are indeed due to the electrically conductive excitations on the surface of the sample then it is reasonable to expect to observe Shubikov-de Haas (SdH) oscillations in the resistivity at high fields. Li *et al.* attempted to measure this effect using both the standard 4-wire measurement technique and a Corbino-disk geometry, used for probing charge conductivity on the surface of the sample. Fourier transforming their data failed to reveal any oscillations in the field dependent resistivity in applied fields up to 45 T in either geometry. Wolgast *et al.* [182] find a carrier density of $2.5 \cdot 10^{13}$ cm^{-2} and mobility of 122 cm^{2}V^{-1} s^{-1} for the surface states on the (011) surface, comparable to previously reported values [25]. They claim that SdH oscillations may not be detectable at fields below $\sim$ 81 T due to the low carrier mobility [182]. However, the lack of SdH oscillations could also be an indication that the QO are arising from charge neutral excitations, rather than the charged excitation from the surface. This exotic picture has been proposed by Baskaran and described in more detail below [183].

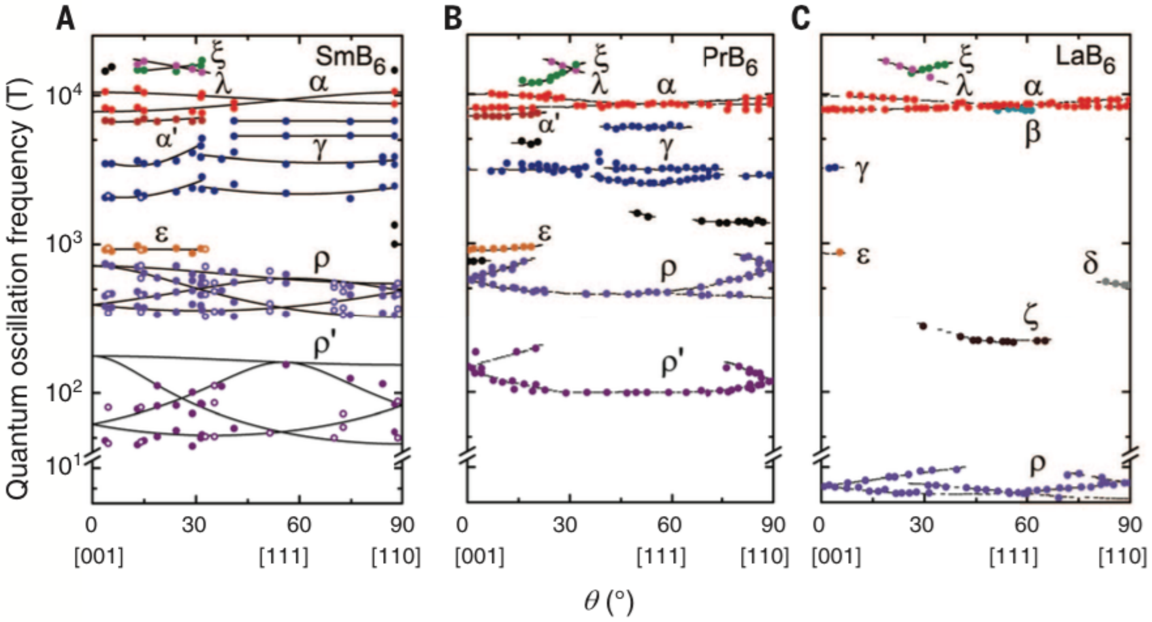

Figure 9.8: The high frequency angle dependence of the quantum oscillations in SmB$_6$ is well described by a three dimensional, bulk Fermi surface [29].

Shortly after Li's report was published, Sebastian's group released another report studying dHvA oscillations via torque magnetometry measurements on several single crystals of SmB$_6$ which were grown via the floating zone method [29]. Sebastian *et al.* measured the torque magnetization in fields up to 40 T at 0.4 K and up to 35 T at 0.03 K. They find large oscillations in the magnetization on top of a quadratic background which are periodic in $1/\mu_o H$, indicating well defined Landau quantization. Oscillations were observed at low frequencies between 50 T and 500 T comparable to Li *et al.*. However, Sebastian *et al.* also observed clear oscillations at high frequencies up to 15 000 T. These high frequencies correspond to Fermi-surface sheets approximately half the volume of the Brillouin zone and quasi-particle mean free path on the order of a few micrometers. The angular dependence of the QO frequencies in SmB_6 is comparable to other metallic rare-earth hexaborides suggesting similar Fermi-surfaces. Figure 9.8 (b) and (c) show the angular dependence for the antiferromagnet PrB_6, and metallic LaB_6 respectively. All three materials show similar high frequency α bands typical of a large, prolate spheroid FS. This is expected behaviour from band structure calculations for the metallic ground states of PrB_6 and LaB_6 with residual resistivities on the order of 1 $\mu\Omega$ cm. However, it is highly unusual in the non-magnetic, Kondo-insulator SmB_6 with a residual resistivity approximately six orders of magnitude larger than the other two materials. These high frequency oscillations require long electronic mean free paths, on the order of several microns. It is difficult to explain this long mean free path in the context of the electronic surface states because the conductive surface layer may only be a few unit cells thick, so the high frequencies would only appear at specific angles where the cyclotron orbits lay completely within the surface layer. Additionally, the angular dependence of the oscillations is independent of sample geometry preparation, exhibiting the same features for platelet like samples with the large plane perpendicular to the [110] or the [100] directions. Thus, Sebastian's results indicate a large, three dimensional Fermi-surface arising from bulk excitations, contrary to the two dimensional FS reported by Li [28].

Tan *et al.* state that it is unlikely that the quantum oscillations are arising from isolated metallic pockets in the bulk of SmB_6 since the cyclotron orbits would need to be at least 1 μm in diameter to account for the long mean free path, yet not affect the electrical transport. More than ten high quality single crystal samples have been measured, all of which display similar high frequency oscillations in the magnetization. Additionally, the large three dimensional Fermi-surfaces corresponding to the high frequency quantum oscillations would correspond to sizeable electronic density of states. This is consistent with the low temperature specific heat, which reveals a large linear term of $\gamma \approx 2 - 7$ mJ/K^{2}mol corresponding to a metallic-like density of states [30, 184, 185, 29]. Gabáni *et al.* estimate the lattice contribution to the specific heat by considering the specific heat of non-magnetic hexaborides [30]. This showed that the phonon contribution is small in comparison to the electronic contribution below approximately 5 K. To be more precise, the phonon specific heat is calculated to be $3.7 \cdot 10^{-2}$ mJ/K^{4}mol using a Debye temperature

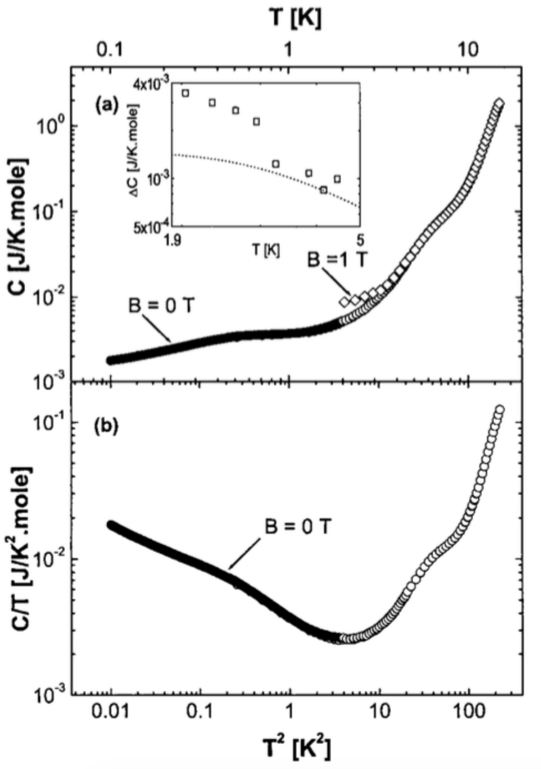

Figure 9.9: Low temperature specific heat of SmB_6 reveals a large enhancement of the linear term below 4 K [30].

of 373 K, which was obtained from low temperature measurements of the elastic constant [186, 187]. This is approximately 100 times smaller than the electronic specific heat at 1 K. It is interesting to note that the specific heat measured by Gabáni in figure 9.9 (a) shows an enhancement in a 1 T magnetic field. They state that this additional specific heat can only be partly explained by a nuclear contribution from the ^{11}B atoms and is unlikely to be caused by magnetic impurities, thus must be intrinsic in nature [30].

A rather intriguing observation is that the amplitude of the quantum oscillations follow the standard Lifshitz-Kosevich (LK) formula (equation 9.8) at high temperature typical of a metallic system with a low effective mass. However, as the temperature is lowered below 1 K, the amplitude does not saturate but rather increases, deviating considerably from the LK form [29]. This is in contrast to Li *et al.* whose QO amplitudes for each frequency range followed the LK formula at all temperatures [28]. The observation of a deviation from the LK scaling below 1 K by Sebastian *et al.* is a surprising result since the

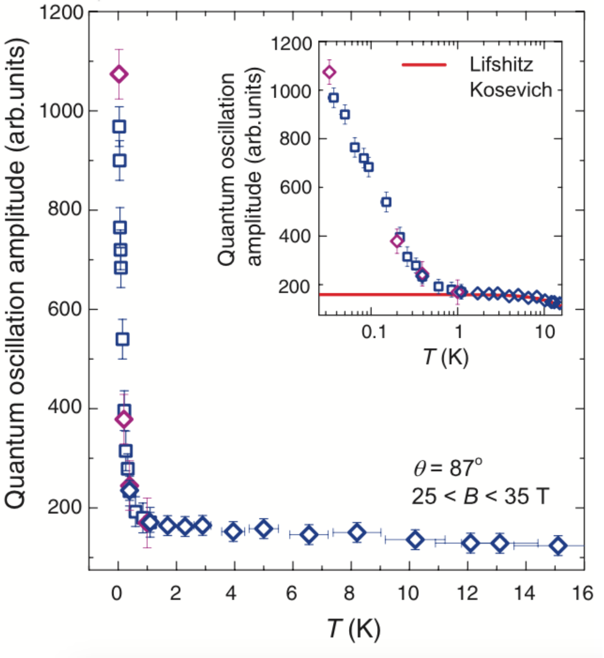

Figure 9.10: Temperature dependence of the quantum oscillation amplitude of the dominant 330 T frequency between $B = 25$ to 35 T [29]. The inset illustrates the large deviation from the standard Lifshitz-Kosevich form.

LK form has been successful to describe many strongly interacting systems [188, 189, 190]. It should be noted, however, that deviations from LK behaviour can arise in the case of unconventional quasiparticles as in reference [191].

Theoretical models have been proposed attempting to explain the origin of the QO in SmB_6 arising from either the two dimensional electronic surface states, or from three dimensional excitations in the bulk. Erten, Ghaemi and Coleman suggest that the quantum oscillations are due to the topologically protected surface states orbiting the two dimension Fermi surface centred at the X point of the Brillouin zone [170]. A suppression of the Kondo effect at the surface of the sample causes a decoupling of the magnetic moments from the conduction electrons, leading to electronic quasiparticles with a low effective mass and a large two dimensional Fermi surface, consistent with ARPES experiments. They suggest that the sizeable linear term in the specific heat could be due to inhomogeneous metallic pockets within the sample. The idea of the quantum oscillations arising from charge neutral excitations in the bulk is dismissed in their report on account that the energy accumulated by the quasiparticle from the increasing magnetic field is correlated to the electric field via

Faraday's Law. So, due to the gauge invariance of the electric field ($\mathbf{E} = -\nabla\phi - \partial\mathbf{A}/\partial t$), the quasiparticles must couple to the gradient of the electric potential ($\nabla\phi$) or to the electric field induced by the changing magnetic field ($\partial\mathbf{A}/\partial t$). This implies that the quasiparticles must have a non-zero charge and thus will be electrically conducting. On the other hand, Ganapathy Baskaran suggests that the quantum oscillations in SmB_6 are in fact due to charge neutral Majorana fermions in the bulk; labelling SmB_6 a bulk scalar Majorana Fermi Liquid (MFL) with finite gaps for charge and spin excitations [183]. Using a theory developed by Coleman, Miranda and Tsvelik [192], he shows that although the excitations are neutral, they respond to an external magnetic field and exhibit Landau diamagnetism, leading to quantum oscillations.

Therefore, there is clearly a great deal still to be learned about the low temperature behaviour of SmB_6. The origin of the dHvA oscillations in magnetization measurements remains unknown due to contradicting interpretations. Furthermore, the lack of SdH oscillations in charge transport raises further questions about the nature of the excitations giving rise to this unconventional Fermi surface. Thermal transport measurements can be utilized to observe the delocalized excitations in SmB_6 and will aid in determining their 2D or 3D nature as well as if they are charged quasiparticles when paired with complementary electrical resistivity measurements. In the following chapter, we present extensive thermal and charge transport measurements on multiple single crystals of SmB_6 which have been prepared either via the flux growth method, or using the floating zone growth technique. This will undoubtedly help address many of these open questions.

Chapter 10

Samarium Hexaboride

10.1 Introduction

SmB_6 is the first example of a topological Kondo insulator. It was first reported by Menth *et al.* in 1969 who found that SmB_6 showed no signs of magnetic ordering down to 350 mK, and that the temperature dependence of the resistivity resembled that of an intrinsic semiconductor. The resistivity exhibited a temperature independent plateau below 5 K which was initially attributed to in-gap impurity states [161]. It wasn't until 2010 that Dzero *et al.* proposed that SmB_6 was not an ordinary semiconductor, but an exotic topological state of matter known as a topological Kondo insulator (TKI) [168]. A fascinating consequence of this state is the emergence of topologically protected electronic surface states. It has been experimentally shown that the low temperature saturation of the resistivity is a result of these surface states [25, 26, 24]. Perhaps the most surprising result is the observation of large, high frequency quantum oscillations (QO) in magnetic torque measurements [28, 29]. Two separate groups have measured this phenomena with differing interpretations. Li *et al.* claim that the QO originate from the electronic surface states and thus can be described by a two dimensional Fermi surface [28]. Tan *et al.* on the other hand observe QO at much higher frequencies, and are thus well described by a three dimensional, bulk Fermi surface from exotic, electrically neutral bulk excitations [29]. Additional measurement techniques are certainly necessary to resolve these contrasting results.

Thermal transport is an excellent technique for measuring delocalized quasiparticle excitations. Therefore, thermal conductivity and electrical resistivity measurements are utilized here to probe the nature of the delocalized excitations in SmB_6. These measurements provide additional insight into the origin of these quantum oscillations. Furthermore, conductivity measurements were made on multiple samples which were prepared via the flux growth method as well as the floating zone technique since it has been shown that growth technique can effect the electronic properties in SmB_6 [164].

10.2 Experimental Details

Thermal transport measurements at temperatures approaching absolute zero allow us to probe delocalized, low energy excitations in the bulk. Using this technique in conjunction with electrical resistivity measurements will help address the different interpretations of the observed quantum oscillations by determining if the oscillations are from the electrically conductive surface states or charge-neutral excitations in the bulk. Therefore, thermal conductivity of three SmB_6 samples was measured from 100 mK to 50 K and in fields up to 12 T (for $T < 1$ K).

A number of technical challenges needed to be overcome in order to successfully probe the thermal transport of these materials. The foremost obstacle leading to the largest systematic error is from the immense contact resistance when compared to the thermal resistance of the sample, especially at low temperature. This is partly due to the electrically insulating nature of SmB_6. In metallic systems, the thermal transport is dominated by the electronic contribution, thus the quality of the thermal contact to the sample is related to the electrical contact. However, in insulating materials the heat is transported via phonons which scatter at material interfaces. Thus, it is difficult to make good thermal contact to insulating materials. As discussed in chapter 2, a large contact resistance introduces two main issues that need to be addressed. One, it introduces very long external relaxation times at low temperatures which is apparent by observing how long it takes the sample thermometers to equilibrate. Figure 10.1 shows the relaxation of both sample thermometers as a function of time at 120 mK (left) and 600 mK (right). The thermometers, and hence the sample, require 6000 seconds to equilibrate at 120 mK, whereas they only require 300 seconds to equilibrate at 600 mK. These relaxation times are extended further in large magnetic fields due to a greatly enhanced heat capacity at low temperatures which is partly due to the nuclear moments of the $^{11}\mathrm{B}$ atoms [30]. If the thermometers are not given enough time to properly settle, a lower resistance will be assigned to the sample thermometer at the set temperature of the fridge in the calibration curve. This means that the sample is actually warmer than what is recorded. The lowest temperature points in the calibration curve cannot be trusted when this occurs and are thus omitted. This essentially imposes a minimum achievable temperature. Two, the thermal gradient across the sample relative to the temperature drop across the cold contact will be minuscule. Usually, we like a relative thermal gradient of about 5 - 10 %, but in these samples we are only able to achieve 0.5 - 1%. These two effects in conjunction lead to a noisy data set that is very sensitive to errors in the calibration curve. The effect of this error is examined in detail in section 10.3.3 of this chapter. For more details about the difficulties associated with large contact resistances can be found in chapter 2.

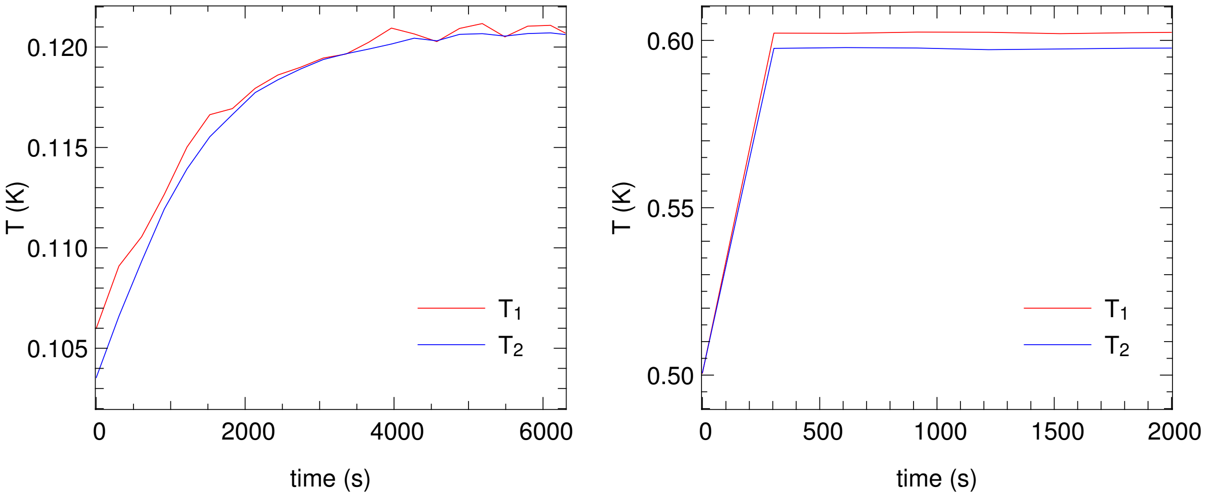

Figure 10.1: *Left:* Sample thermometers relaxing to 120 mK from 105 mK. *Right:* Sample thermometers relaxing to 500 mK from 600 mK.

The three ways to combat this issue are as follows. First of all, the entire thermal conductivity device is encapsulated in a copper box (see chapter 2 for more details). The use of this bespoke device minimizes both electromagnetic (EM) and thermal noise from the surrounding environment. Small heat spikes induced in the sample will cause a significant change in the sample temperature because of the large thermal resistance to the thermal ground which impedes the flow of heat to ground. So, minimizing the EM noise will help eliminate these heat pulses. Secondly, averaging each sample thermometer for an extended amount of time will statistically reduce random noise in the data. In fact, the standard deviation is reduced by a factor of $\sqrt{n}$ when averaging n points. Therefore, each point takes several hours to acquire at the lowest temperatures. Finally and most importantly, is the immense care our collaborator, Michael Sutherland and his graduate students at Cambridge University, put into preparing excellent low resistance contacts on the samples. The surface of the samples were etched to remove any oxide layer. Then four 25 μm Ag wired were spot welded to the surface (two current and two voltage leads) and were subsequently coated in conducting Ag paint for enhanced mechanical robustness. These low resistance contacts are the key to accurately measuring the thermal transport at low temperatures.

10.2.1 Sample Details

Two samples (FZ1 and FZ2) were grown via the floating zone technique in a xenon-arc lamp image furnace. These samples were prepared using 99.9% pure starting materials [193]. Laué x-ray diffraction reveals these samples are high quality single crystals with no sign of secondary crystallographic phases. Chemical analysis confirms that the presence of rare-earth ions other than Sm is less than 0.01%. Furthermore, scanning electron microscopy show a uniform Sm:B ratio across the sample with a standard deviation of 1% [29]. Strain in the samples caused by cutting them to size was relieved by electroplating them in weak acid. The third sample (FG1) was grown in Al flux [194]. A commercially prepared SmB_6 powder (99.9% pure from Alfa Aesar) was mixed with Al shot (99.9% pure from Sigma Aldrich) in a ratio of 0.2% : 99.8% respectively and placed in an alumina crucible [195]. Crystals were grown in an argon environment by heating the mixture to 1450°C for 4 hours then cooling to 650°C at a rate of 4°C/h followed by rapidly cooling to room temperature. Single crystal platelets of SmB_6 were then obtained by dissolving the flux in HCl. Each of the samples measured here are from the same batches of samples which displayed large quantum oscillations in high magnetic fields. A summary of the physical properties of all three samples is found in table 10.1.

Sample	Growth technique	l/A (cm^{-1})	IRRR
FZ1	Floating zone	98.3	$4.38 \cdot 10^4$
FZ2	Floating zone	193.9	$4.71 \cdot 10^4$
FG1	Flux grown	45.6	$14.2 \cdot 10^4$

Table 10.1: Growth technique, geometric factor (ratio of length l to cross-sectional area A) and IRRR for SmB_6 FZ1, FZ2 and FG1.

The inverse residual resistivity ratio (IRRR) is defined here as $\rho(0.5\text{ K})/\rho(300\text{ K})$. The IRRR has been used as a preliminary estimate of the level of disorder in the sample [29], much the same way as the RRR determines the disorder level in metallic samples [196]. However, in metallic systems the residual resistivity originates from impurity scattering of the electrons such that samples with higher levels of disorder will have a larger residual resistivity compared to a cleaner sample (see chapter 2). In high quality SmB_6 samples, the low temperature electrical conductivity is due to the topologically protected surface states since the bulk is electrically insulating [25, 26, 24]. The effect of disorder on the

IRRR in $\mathrm{SmB_6}$ has been studied via radiation damage [197] and by chemical substitution and off stoichiometry [198, 199, 26]. Unlike the RRR in metallic systems, the inclusion of impurities in $\mathrm{SmB_6}$ can either increase or decrease the IRRR depending on the impurity ion's valence and its magnetic moment [198, 199, 26]. Thus, the IRRR may not be the most reliable method of characterizing the sample quality on its own. Nonetheless, the IRRR for the samples measured here is included in table 10.1 for completeness.

10.3 Results

10.3.1 Resistivity

Figure 10.2 shows the temperature dependence of the resistivity for FZ1, FZ2 and FG1 (left panel). The qualitative behaviour of the resistivity is similar for all three samples; low room temperature resistance characteristic of a metallic sample, followed by a five orders of magnitude increase in the resistance as the temperature is lowered. The low temperature behaviour is however quite different from sample to sample. The resistivities of the floating zone grown samples, FZ1 and FZ2, saturate at 8.4 Ωcm and 8.5 Ωcm respectively below ~ 4 K. This is consistent with previously reported resistivity measurements [25, 26, 24]. The saturation of the resistivity is due to topologically protected electronic surface states which short-circuit the insulating bulk. The resistivity can be described using a two channel conductivity model as in references [174, 24]. Since the two channels of electrical conductivity are running in parallel, it is necessary to sum the individual conductivity channels. The electrical conductivity is defined as the inverse of the resistivity such that $G(T) = 1/\rho(T)$. The surface conductivity is constant in temperature ($G_\mathrm{S} = \rho_\mathrm{S}^{-1}$), and the bulk conductivity follows an activated temperature dependence with a gap Δ ($G_\mathrm{B} = \rho_\mathrm{B}^{-1} e^{-\Delta/k_\mathrm{B}T}$). Thus the total resistivity is given by

$$\rho(T) = \left(\rho_\mathrm{S}^{-1} + \rho_\mathrm{B}^{-1} e^{-\Delta/k_\mathrm{B}T}\right)^{-1} . \tag{10.1}$$

The resistivities of FZ1 and FZ2 are fitted to this model in figure 10.2 (a) and (b) respectively, and the resulting fit parameters are in listed in table 10.2. The bulk energy gap in both floating zone grown samples is approximately 4.2 meV, which is consistent with previously reported values [167, 172, 162, 173, 174, 24].

The resistivity of the flux grown sample, FG1, shows the onset of saturation below 3 K, however, the resistivity begins to increases further as the temperature is lowered below 1 K. A similar suppression of the low temperature resistivity plateau is observed when doped

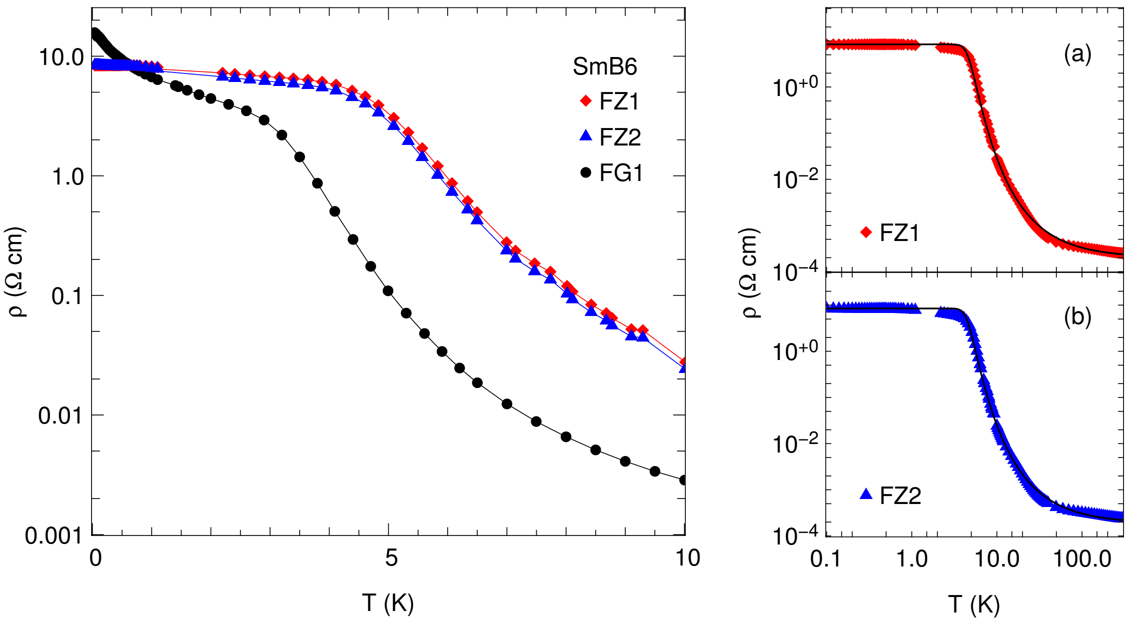

Figure 10.2: *Left:* The temperature dependence of the resistivity for FZ1 (red diamonds), FZ2 (blue triangles) and FG1 (black circles). *Right:* The temperature dependence of the resistivity for FZ1 (a) and FZ2 (b) is fitted using the two channel model from equation 10.1.

Sample	ρ_S (Ωcm)	ρ_B (mΩcm)	Δ (meV)
FZ1	8.4	0.20	4.28
FZ2	8.5	0.19	4.22

Table 10.2: The resulting fit parameters from fitting the resistivity data of FZ1 and FZ2 to the two channel conductivity.

with magnetic impurities [26, 198]. The magnetic impurities break time reversal symmetry on the surface of the sample which suppresses the electronic surface states causing the system to behave as a small gap insulator. It is possible that FG1 has a small concentration of magnetic impurities which are causing an increase in the low temperature resistivity.

The field dependence of the resistivity of FZ1 and FZ2 is seen in figure 10.3. The floating zone grown samples follow the sample qualitative behaviour. The resistivity is field independent for $B \lesssim 7$ T, and then shows a negative magnetoresistance. This is consistent with previously reported resistivity data [29, 182]. The inset of figure 10.3

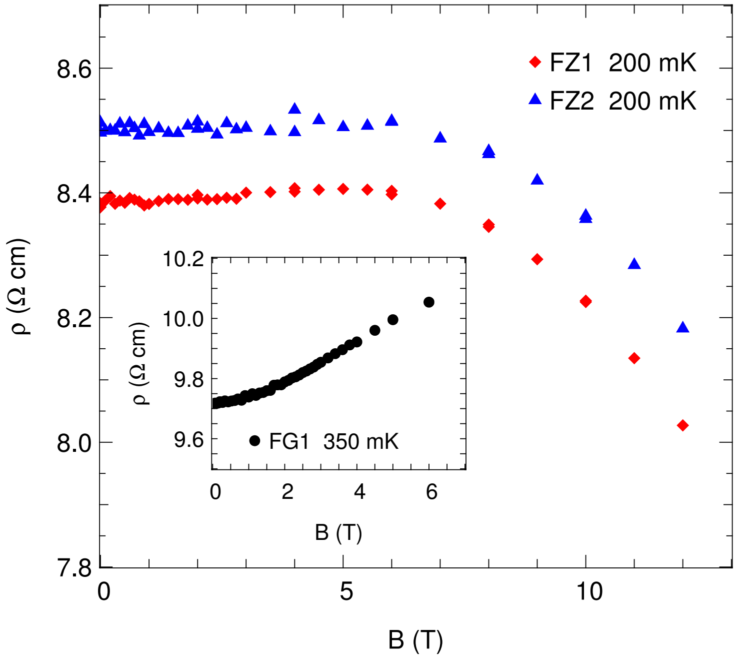

Figure 10.3: The field dependence of the resistivity for FZ1 and FZ2 at 200 mK. *Inset:* Field dependence of the resistivity of FG1.

shows the field dependence of the resistivity of FG1. Rather than decreasing with field, as in FZ1 and FZ2, FG1 displays a positive magnetoresistance up to 6 T. This behaviour is observed in SmB_6 samples which have been doped with magnetic ions [198]. Thus, both the field dependence and the zero field temperature dependence of FG1 are consistent with the presence of a small concentration of magnetic impurities.

10.3.2 Thermal conductivity: $T \leq 50$ K

The thermal conductivity at temperatures up to 50 K is seen in figure 10.4 for all three samples. Also featured in figure 10.4 is the thermal conductivity of SmB_6 measured by Popov *et al.* [200]. Samples FZ1, FZ2 and FG1 all display a peak in the conductivity at approximately 12 K. In general, insulating materials exhibit a peak in the thermal conductivity where the phonon mean free path transitions from being limited by the sample boundaries at low temperatures to being dominated by phonon-phonon scattering (Umklapp processes) at higher temperatures. The magnitude and shape of this peak is strongly dependent on lattice defects such as point defects, dislocations and stacking faults, which

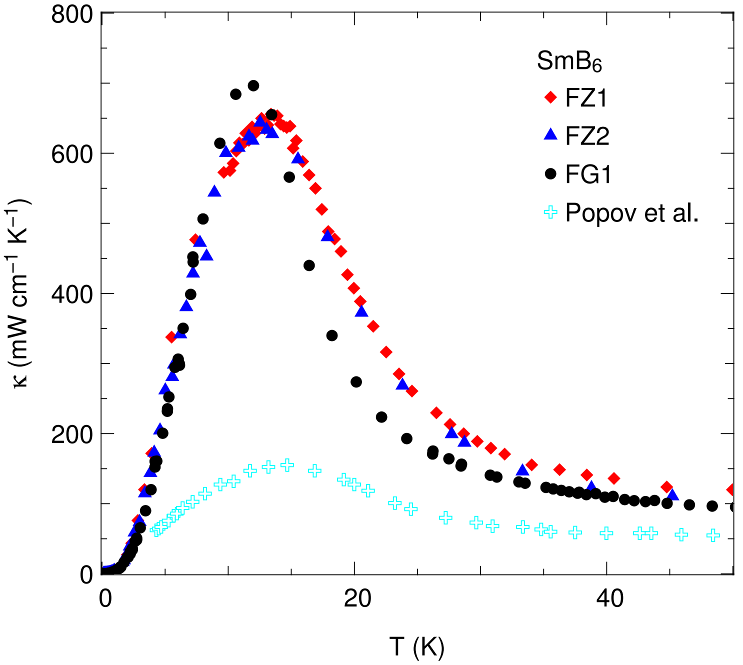

Figure 10.4: High temperature thermal conductivity data for FZ1 (red diamonds), FZ2 (blue triangles) and FG1 (black circles). The conductivity measured by Popov *et al.* is plotted on the same axes (cyan crosses) [200].

tend to suppress the conductivity. Hence, comparing the peak conductivity of each sample can provide information about the relative level of disorder between the samples. With this in mind, Fig 10.4 suggests that FG1 has the lowest level of disorder in the lattice. The peak conductivity is equivalent in both FZ1 and FZ2, indicating comparable levels of disorder in these samples. Although the magnitude of the conductivity peak between all three samples is equivalent to within 10%, the width of the peak in FG1 is visibly narrower than the floating zone grown samples which could be an indication of additional defect scattering of the phonons in this sample. This difference is quantified by fitting the conductivity using kinetic theory and Mattheissen's rule to extract the phonon scattering rates from the various scattering mechanisms. This analysis is found in section 10.4.1. Finally, the sample measured by Popov *et al.* has a peak conductivity approximately four times lower than the samples measured here indicating a much larger level of disorder [200]. This illustrates the high quality of the samples examined in this study.

It is important to note that this analysis pertains only to the phonon conductivity in insulators. Metallic systems will have a significant contribution to the conductivity from electrons which makes this analysis impossible. However, we can estimate an upper limit of the electronic contribution to the conductivity using the electrical resistivity via the Wiedemann-Franz law (WFL). In the case of SmB_6, the resistivity at 12 K (the peak location) is approximately 10 mΩcm in FZ1 or FZ2, and 1.2 mΩcm in FG1, corresponding to a thermal conductivity of approximately 0.03 mW $\mathrm{cm}^{-1}\mathrm{K}^{-1}$ and 0.22 mW $\mathrm{cm}^{-1}\mathrm{K}^{-1}$ respectively. Thus, the electronic contribution to the peak conductivity is less than 0.03% of the total conductivity, and we can safely assume that the conductivity is essentially entirely due to phonons.

10.3.3 Thermal conductivity: $T \leq 1$ K

Thermal transport measurements allow us to probe the delocalized quasiparticles in a system by separating the various contributions to the conductivity. In metallic systems, the low temperature conductivity is comprised of a linear electronic term AT, and a phonon term BT^{γ}. Thus, the low temperature thermal conductivity can be modelled using the functional form

$$\kappa/T = A + BT^{\gamma-1}. \tag{10.2}$$

As the temperature approaches absolute zero, the mean free path of the phonons become long and is eventually limited by the boundaries of the sample. In this case, the phonon conductivity can be expressed via kinetic theory such that $\kappa_{\mathrm{ph}} = \frac{1}{3}c_{\mathrm{ph}}v_{\mathrm{s}}d$ where $c_{\mathrm{ph}} = \beta T^3$ is the lattice specific heat, v_{s} is the sound velocity and d is the average sample width. So, this model predicts a cubic phonon conductivity in the boundary limited regime. In practice, γ is often observed to be slightly less than 3 due to specular scattering of phonons of the sample boundaries which can occur when the surface of the sample is smooth when compared to the phonon wavelength [201]. This introduces a frequency dependence into phonon mean free path which alters the temperature dependence of the conductivity. The presence of defects in the lattice also serve as phonon scattering mechanisms which cause the conductivity to deviate from the expected cubic temperature dependence. Note that a single power law may not accurately capture the phonon conductivity if there are multiple sources of scattering at play. However, plotting the data as κ/T versus T^2 and fitting to equation 10.2 leaving A, B and γ as fitting parameters provides a heuristic examination of both the electronic and phonon contributions to the conductivity. If γ differs significantly from 3, then it is possible that defects are scattering the phonons or that an additional, non-linear channel of conductivity is present. Thus, a more accurate model of the conductivity would be required to properly describe the data.

Figure 10.5 shows the thermal conductivity for all three samples, FZ1, FZ2 and FG1, is plotted as κ/T versus T^2 at zero field and in applied magnetic fields up to 12 T. The

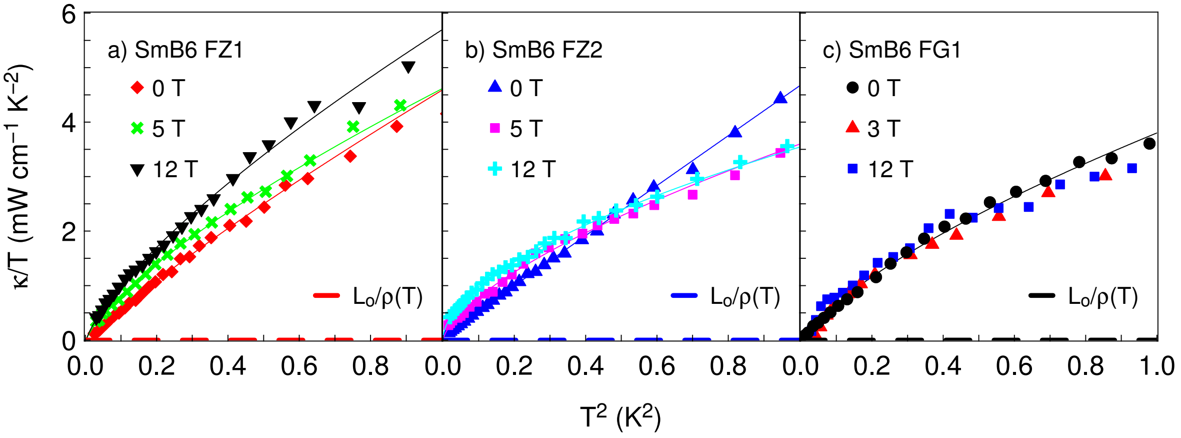

Figure 10.5: The zero field conductivity for FZ1 (a), FZ2 (b) and FG1 (c) plotted as κ/T versus T^2. The solid lines are fits to the data using equation 10.2.

Sample	Field	A	B	γ
FZ1	0 T	-0.13	4.66	2.69
	5 T	-0.06	4.67	2.45
	12 T	-0.07	5.76	2.47
FZ2	0 T	0.07	4.60	2.99
	5 T	-0.01	3.61	2.31
	12 T	0.03	3.51	2.14
FG1	0 T	-0.18	3.98	2.35

Table 10.3: The fit parameters obtained from fitting the low temperature conductivity of all three SmB_6 samples to equation 10.2.

solid lines are fits to equation 10.2 and the resulting fit parameters are found in table 10.3. First, notice that this analysis indicates that the linear term A is approximately zero for all thee samples at all field values measured. Hence, it appears that there is no residual electronic contribution to the conductivity as $T \to 0$ K. Next, we will focus on the conductivity of FZ1. The zero field data follows a $T^{2.7}$ temperature dependence which may be an indication of specular phonon scattering from the sample boundaries, or the presence of a small amount of disorder in the lattice. The data shows a clear enhancement with the application of a magnetic field over the zero field conductivity. This could be an indication of a reduction of phonon scattering, or the emergence of an additional channel for heat conduction. The former is unlikely since the exponent α is reduced from the zero field value suggesting that the enhancement in the conductivity is not due to a reduction of phonon scattering. Thus, it is possible that the field enhanced conductivity is due to emergent excitations. If we now consider the conductivity of FZ2, we see the the zero field data is very well described by a cubic temperature dependence, which is consistent with phonons in the boundary limited regime. Similar to FZ1, the low temperature conductivity is enhanced over the 0 T data in a magnetic field suggesting the presence of an additional, field induced channel of conductivity. However, the conductivity drops below the 0 T data above $\sim$ 700 mK, indicating the presence of an additional phonon scattering mechanism not present in the 0 T data. This is observed as a deviation in the temperature dependence from the T^3 boundary limited regime in an applied magnetic field. Turning now to the flux grown sample, FG1, we find that the zero field data roughly follows a $T^{2.35}$ temperature dependence, suggesting that there is some level of defect scattering of the phonons. Unlike the floating zone grown samples, the conductivity of FG1 does not exhibit an enhancement in an applied magnetic field to within the scatter of the data. The noise in the 3 T and 12 T data is caused by a small thermal gradient due to poor thermal contacts which is exacerbated by vibrations in the high magnetic field (see chapter 2 for more information on the issues that arise from poor thermal contact to the sample). Therefore, this data suggests that the behaviour of the low temperature conductivity is strongly dependent on the growth technique.

The dashed lines in figure 10.3 represent the electrical resistivity for each sample in zero field expressed in thermal units via the Wiedemann-Franz Law (WFL). We define the contribution to the thermal conductivity from the electronic surface states as $\kappa_e/T \equiv L_o/\rho$ where ρ is the value of the resistivity plateau at low temperatures and $L_o = 2.44$ WΩK^{-2} is the Lorenz number. For FZ1, the value of the resistivity plateau in zero field is approximately $\rho_{\text{FZ1}} = 8.4$ Ωcm, which corresponds to a thermal conductivity of $\kappa_e/T = L_o/\rho_{\text{FZ1}} = 2.9 \cdot 10^{-6}$ mW cm^{-1}K^{-2} via the WFL. Similarly for FZ2, the resistivity plateau has value of $\rho_{\text{FZ2}} = 8.5$ Ωcm, corresponding to a thermal conductivity of $L_o/\rho_{\text{FZ2}} = 2.9 \cdot 10^{-6}$ mW cm^{-1}K^{-2}. Recall from figure 10.2 that the resistivity does not saturate at low temperatures for FG1, but continues to increase reaching a value of 15.7 Ωcm at 100 mK. We approximate the electronic contribution to the conductivity in the same manner and find that $L_o/\rho_{\text{FG1}} = 1.5 \cdot 10^{-6}$ mW cm^{-1}K^{-2}. Thus, the contribution to the conductivity from the electrons is approximately five order of magnitude less than the measured thermal conductivity.

We can also consider the relative change in the electrical conductivity from 0 T to 12 T to see if the field enhancement in the thermal conductivity is due to the field dependence of the electrical conductivity. From figure 10.3 we see that the resistivity of FZ1 at 12 T is 8.02

Ωcm corresponding to a thermal conductivity of $3.04 \cdot 10^{-6}$ mW cm^{-1}K^{-2}, for an increase in the electronic contribution to the conductivity of $0.14 \cdot 10^{-6}$ mW cm^{-1}K^{-2}. Similarly, the resistivity of FZ2 at 12 T is 8.18 Ωcm, corresponding to a thermal conductivity of $2.98 \cdot 10^{-6}$ mW cm^{-1}K^{-2}, for an increase in the conductivity of $0.08 \cdot 10^{-6}$ mW cm^{-1}K^{-2}. For comparison, the measured thermal conductivity increase by 0.47 mW cm^{-1}K^{-2} in FZ1 and 0.41 mW cm^{-1}K^{-2} in FZ2 from 0 T to 12 T at 300 mK. Thus, the observed enhancement of the thermal conductivity in a magnetic field is six orders of magnitude larger than enhancement of the electronic contribution to the conductivity from the surface states.

10.3.4 Thermal conductivity: field dependence

The field dependence of the thermal conductivity of FZ1, FZ2 and FG1 at $T = 240$ mK 245 mK, and 350 mK respectively is seen in figure 10.6. The field sweeps were conducted at approximately 240 mK for the floating zone grown samples since the settling times increase dramatically at lower temperatures. The average sample temperature of the flux grown sample is 350 mK since additional power was required from the sample heater to achieve a significant thermal gradient across the sample due to the poor thermal contact to the sample. The floating zone grown samples show a large enhancement in their thermal conductivities in an applied magnetic field with FZ1 reaching a value 2 times larger than the zero field value $\kappa(0)$, and FZ2 reaching a value 1.6 times larger than $\kappa(0)$ at 12 T. Both floating zone grown samples shown similar step-like features in the conductivity which saturates at high field characteristic of excitation gaps closing, leading to enhanced conductivity from quasiparticle excitations. The flux grown sample shows a modest enhancement of approximately 10% of $\kappa(0)$ by 3 T, which then regresses to the zero field value by 5 T. This is consistent with the temperature dependence in field, where the conductivity can show either a small enhancement, or suppression depending on the temperature.

Error can be incurred in the field dependent data due to the magnetoresistance of the sample thermometers. Since the sample thermometers are temperature dependent semiconductors, their resistance is also dependent on the magnetic field. This is accounted for by recording the value of thermometers resistance at each field step with the sample heater turned off, yielding the magnetoresistance of the thermometer at the fridge temperature. The temperature of the fridge is measured in a field-compensated region. This is then used to correct the resistance values of the thermometers when the sample heater is turned on. The magnetoresistance correction can be sensitive to the interpolation method when applying it to the data. This is especially true if the thermal gradient is small since small changes in each sample thermometer translates to larger relative changes in the thermal

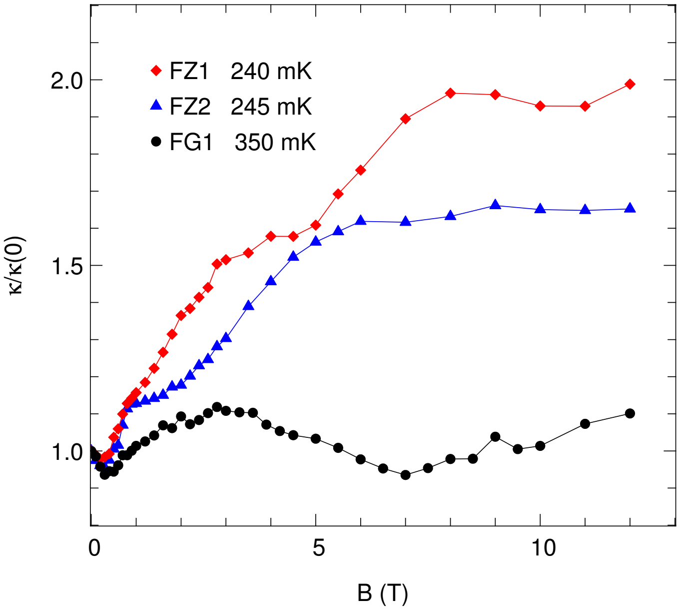

Figure 10.6: The thermal conductivity normalized by its zero field value, $\kappa(0)$, is plotted versus magnetic field for FZ1, FZ2 and FG1 at 240 mK, 245 mK and 350 mK respectively.

gradient. Thus, the magnetoresistance correction is determined for every field sweep *in situ* to ensure an accurate correction to the data.

10.4 Discussion

10.4.1 Phonon thermal conductivity

In order to properly examine any additional channels of conductivity, we must first have a very good understanding of the lattice contribution to the conductivity. To do this, we will examine the phonon specific heat which we can then relate to the thermal conductivity via kinetic theory. We need to be careful when modelling the specific heat to consider a specific temperature range since the active phonon modes can vary dramatically. The hexaboride family of materials in particular tend to have a complex phonon spectra. The main contribution to the specific heat above approximately 15 K comes from the Einstein modes of the boron atoms which behave as independent harmonic oscillators, rather than collective spin waves as in the Debye model [202, 31]. However, at low temperatures the long wavelength phonon modes dominate and the Debye term becomes the only relevant contribution [42].

Let us start by considering the specific heat of the isostructural material $\mathrm{LaB_6}$ as measured by Mandrus *et al.* and Anisimov *et al.* [202, 31]. They show that the specific heat above 15 K is well described by a combination of an Einstein term corresponding to the independent harmonic oscillations of the lanthanum ions with $\Theta_\mathrm{E} = 150$ K, and a Debye term from the rigid boron cages with $\Theta_\mathrm{D} = 1160$ K. Here, the Einstein and Debye temperatures have been determined from x-ray crystallography data for $T > 15$ K [202]. The phonon specific heat from Anisimov *et al.* is seen in figure 10.7 (b). The data above 15 K is well described by the total calculated specific heat from the Einstein and Debye modes (dashed line). Panel (a) shows the individual components of the specific heat illustrating that the Einstein component is effectively null below 6 K, meaning the specific heat should be well described by the Debye model below this temperature. However, examining the low temperature phonon specific heat in panel (c), it becomes apparent that the high temperature model fails to accurately describe the low temperature data. Rather, the low temperature data is much better described by the Debye model with $\Theta_\mathrm{D} = 404$ K, which was calculated from the elastic constant [187]. It is evident from this analysis that the Debye temperature is not a constant value at all temperatures, rather it is a characteristic temperature scale used to describe the lattice vibrations for a given temperature range. This effect has also been observed in other systems [203, 204]. The variation in the Debye temperature is a result of deviations from the Debye approximation which imposes a quadratic frequency dependence of the density of states. This tends to happen at higher temperatures where the high frequency longitudinal phonon modes become important and can be dependent on the coordination number of the lattice. However, at temperatures approaching absolute zero, low frequency transverse modes dominate and the Debye model is a good approximation to what is observed [42]. Futhermore, reference [203] shows that as T approaches absolute zero, the value of the Debye temperature from the specific heat is equivalent to the value calculated from the elastic constants since both probe the active phonon modes. This is consistent with what is observed in $\mathrm{LaB_6}$; the Debye temperature evolves from 1160 K at high temperatures to 404 K at low temperatures, matching the value extracted from the elastic constants.

Recall from chapter 9 that the low temperature specific heat of $\mathrm{SmB_6}$ has a low temperature nuclear contribution from the boron ions as well as a considerable linear electronic contribution [30, 29]. This makes it difficult to accurately determine the lattice specific heat, and subsequently the Debye temperature. Thus, the Debye temperature must be ascertained by other means. High temperature x-ray crystallography yields $\Theta_\mathrm{D} = 1180$ K [205] and $\Theta_\mathrm{E} = 120$ K [206, 207, 208]. However, low temperature measurements of the

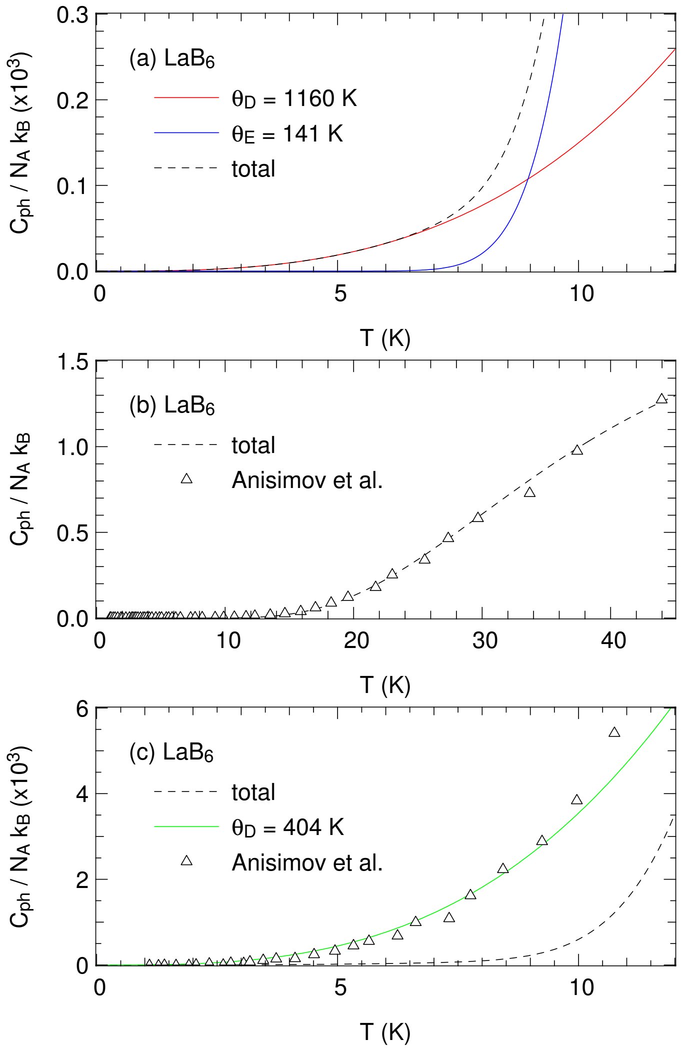

Figure 10.7: (a) The calculated Debye and Einstein contributions to the lattice specific heat of LaB_6. (b) Specific heat of LaB_6 measured by Anisimov *et al.* and the total calculated specific heat [31]. The data is well described by the total calculated specific heat up to 40 K. (c) The specific heat of LaB_6 below 10 K fits the Debye model with $\Theta_D = 404$ K rather than the total calculated specific heat from the high temperature data.

elastic constant yield a Debye temperature of $\Theta_D = 373$ K [186, 187, 209, 210]. Thus, applying the above analysis of the phonon specific heat of LaB_6 to SmB_6, the low temperature phonon specific heat will be best described by the Debye model using a Debye temperature of $\Theta_D = 373$ K.

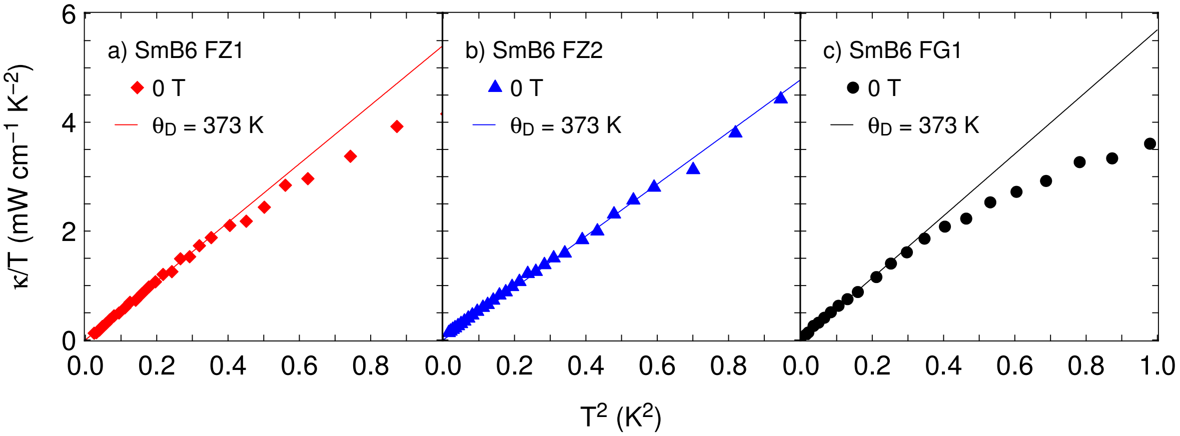

Figure 10.8: The zero field conductivity for FZ1 (a), FZ2 (b) and FG1 (c) plotted as κ/T versus T^2. The solid lines are the calculated phonon conductivities for each sample in the boundary limited regime.

Referring back to chapter 2 we have shown that the phonon thermal conductivity can be expressed using kinetic theory as $\kappa_{\text{ph}} = \frac{1}{3}c_{\text{ph}}v_{\text{s}}l$ where $c_{\text{ph}} = \beta T^3$ is the lattice specific heat, v_{s} is the sound velocity and l is the phonon mean free path. In the Debye model, the specific heat and sound velocity can be described using the Debye temperature, Θ_{D}, through the following formula:

$$\begin{gathered} c_{\text{ph}} = \frac{12\pi^4}{5}N_{\text{A}}k_{\text{B}}\left(\frac{T}{\Theta_{\text{D}}}\right)^3 \\ v_{\text{s}} = \frac{2k_{\text{B}}}{h}\Theta_{\text{D}}\left(\frac{\pi}{6n}\right)^{1/3} \end{gathered} \tag{10.3}$$

where $n = 1.42 \cdot 10^{22}$ cm^{-3} is the number density per unit volume of SmB$_6$. This yields $c_{\text{ph}} = 3.75 \cdot 10^{-2}$ mJ mol^{-1}K^{-4} and $v_{\text{s}} = 5.18 \cdot 10^5$ cm s^{-1}. As $T \to 0$ K, the phonon mean free path will be limited by the physical boundaries of the sample. In this case, the phonon mean free path, l, is temperature independent and equal to the average width of the sample given by $d \equiv \sqrt{4A/\pi}$, where A is the cross-sectional area. We can therefore estimate the phonon thermal conductivity using kinetic theory and $\Theta_{\text{D}} = 373$ K. The results are seen in figure 10.8 for FZ1 (a), FZ2 (b) and FG1 (c) revealing that the Debye model describes thermal conductivity very well as $T \to 0$ K, with no fitting parameters! Therefore, we can confidently attribute the zero field conductivity entirely to phonons in the boundary scattering limit as $T \rightarrow 0$ K. We then define the phonon conductivity as the zero field data such that $\kappa_{\mathrm{ph}} \equiv \kappa(0\ \mathrm{T})$. Note that the phonon contribution to the conductivity in the boundary limited regime is the maximum amount the lattice can contribute to the thermal transport. As a result of this, any enhancement in the conductivity must be from a separate additional channel of conductivity since the phonon mean free path cannot be increased further.

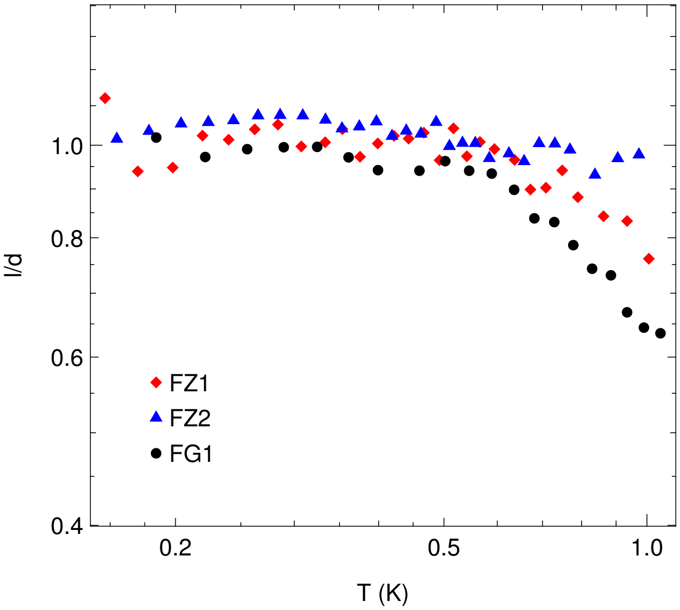

Figure 10.9: The ratio of the measured phonon mean free path to the average sample width for FZ1 (red diamonds), FZ2 (blue triangles) and FG1 (black circles).

As the temperature approaches 1 K, the thermal conductivity of FZ1 and FG1 (and FZ2 to a lesser extent) deviates from the T^3 temperature dependence of the calculated boundary limited phonon conductivity. An effective method of observing this is to examine the ratio of the measured phonon mean free path l to the average sample width d. This is seen in figure 10.9. We find that l/d for FZ2 is roughly temperature independent and equal to unity over the entire temperature range confirming that this sample is in the boundary limited phonon scattering regime below 1 K. On the other hand, the phonon mean free path for FZ1 and FG1 is temperature independent below approximately 600 mK and 400 mK respectively, above these temperatures l/d decreases from unity. In practice, the temperature dependence of the phonon conductivity in the boundary limited regime can be slightly less than cubic if the phonons are specularly reflected off the surface of the sample which occurs when the surface is very smooth when compared to the phonon wavelength [1, 201]. The presence of defects in the lattice can also cause the lattice thermal conductivity to be reduced from the predicted T^3 boundary scattering limit by scattering the phonon with a temperature dependent scattering rate. To systematically examine the effect of specular boundary scattering and defect scattering on the phonon thermal conductivity, we will fit the zero field thermal conductivity over a wider temperature range using kinetic theory and Mattheissen's rule as described in chapter 2. This allows us to determine the scattering rates of the various possible lattice defects.

Modelling the phonon conductivity

As previously stated, defect scattering of phonons will affect both the low temperature thermal conductivity by reducing the phonon conductivity from the T^3 boundary scattering limit, and the high temperature thermal conductivity by suppressing the magnitude and modifying the width of the conductivity peak. Modelling the thermal conductivity allows us to quantify the level of defects in the lattice by obtaining the phonon scattering rates from each type of lattice defect. To do this, the data is fit via kinetic theory and Mattheissen's rule such that

$$\kappa_{\mathrm{ph}} = \frac{1}{3}\frac{c_{\mathrm{ph}} v_{\mathrm{s}}^2}{\sum_i \Gamma_i} \tag{10.4}$$

where Γ_i are the various scattering rates. Recall from chapter 2 that the boundary scattering term is given by $\Gamma_{\mathrm{B}} = v_{\mathrm{s}}/d$ where v_{s} is the sound velocity and d is the aver sample width. In order to account for specular scattering of the phonons from the surface of the sample, the exponent of the boundary scattering term is allowed to deviate from the expected T^3 so that $\frac{c_{\mathrm{ph}} v_{\mathrm{s}}^2}{3\Gamma_{\mathrm{B}}} \sim T^{\gamma}$ where $\gamma \lesssim 3$. We will also consider defect scattering from dislocations ($\Gamma_{\mathrm{D}} \sim T$), stacking faults ($\Gamma_{\mathrm{SF}} \sim T^2$), and point defects ($\Gamma_{\mathrm{PD}} \sim T^4$) [48, 49]. To fit the high temperature conductivity peak, we need to include phonon-phonon scattering from Umklapp processes which has a functional form of $\Gamma_{\mathrm{U}} \sim T^3 e^{-\alpha\Theta_{\mathrm{D}}/T}$ in the modified Callaway model [149]. Since we are comparing three SmB_6 samples, the phonon spectra should be the same in each samples and hence the Umklapp scattering term should be equivalent in all three cases. The fit of the thermal conductivity up to 50 K is seen in figure 10.10 for all three samples, and the resulting fit parameters are listed in table 10.4.

The first thing to notice is that the boundary scattering term is the dominant scattering mechanism in all three samples indicating the samples measured here are very high quality with a low concentration of defects. This is consistent with the observation of a conductivity peak four times larger than previously measured SmB_6 samples [200], as well as the realization of the boundary limited phonon conductivity at low temperatures. Second, the

Sample	Γ_{B} (*const.*)	γ	Γ_{D} (T)	Γ_{SF} (T^2)	Γ_{PD} (T^4)	Γ_{U} $(T^3 e^{-\alpha\Theta_{\mathrm{D}}/T})$	α
FZ1	$1.46 \cdot 10^7$	2.95	/	$1.10 \cdot 10^6$	/	$2.6 \cdot 10^6$	0.16
FZ2	$1.69 \cdot 10^7$	3.0	/	$1.12 \cdot 10^6$	/	$2.6 \cdot 10^6$	0.16
FG1	$1.38 \cdot 10^7$	2.8	$5.53 \cdot 10^6$	/	$2.46 \cdot 10^3$	$2.6 \cdot 10^6$	0.14

Table 10.4: The fit parameters for phonon scattering from dislocations, stacking faults point defects and Umklapp processes obtained by fitting the high temperature data for all three samples to equation 10.4. The boundary scattering term is calculated, however, the exponent is allowed to deviate from the expected T^3 temperature dependence.

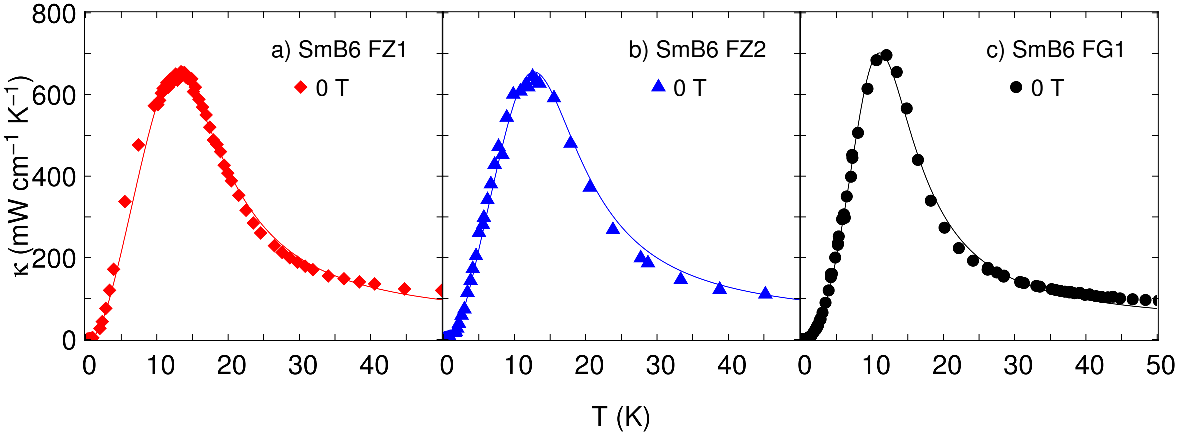

Figure 10.10: The zero field conductivity for FZ1 (a), FZ2 (b) and FG1 (c) is fitted up to 50 K using kinetic theory and Mattheissen's rule to account for multiple scattering mechanisms.

temperature dependence of the boundary scattering term is cubic for FZ2, however, FZ1 and FG1 have power law exponents slightly less than 3 due to specular scattering of the phonons from the surface of the sample. This partially explains the deviation from the T^3 behaviour of the calculated phonon conductivity in the boundary limited regime for these two samples as seen in figure 10.8. Third, the coefficient of the Umklapp term is equivalent across all three samples as expected. However, a small deviation in the α parameter for FG1 compared to the floating zone grown samples. Finally, fitting the floating zone grown samples yields a similar scattering rate for phonon scatting from stacking faults but are free of other defects. On the other hand, fitting FG1, indicates that the flux grown sample has a small concentration of dislocations and point defects. This suggests that the different growth techniques used for fabricating SmB_6 are predisposed to the inclusion of

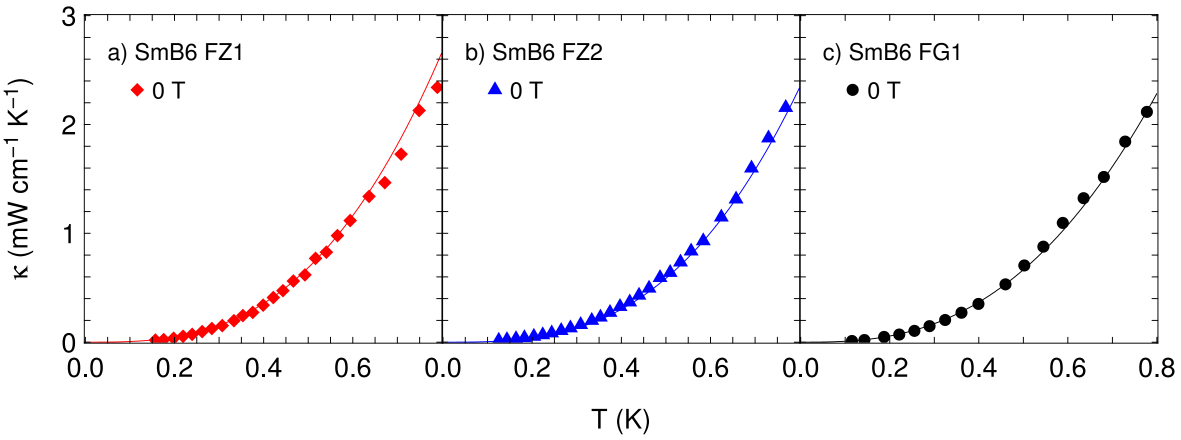

Figure 10.11: The zero field conductivity for FZ1 (a), FZ2 (b) and FG1 (c) below 1 K using the same fitparameters obtained from fitting the data up to 50 K.

different types of lattice defects. So, although all three samples studied here are all high quality, as indicated by the approximately equivalent magnitude of the conductivity peak, the differing types of defects in each sample affects the width of the conductivity peak. The observation of point defects in FG1 is consistent with the presence of magnetic impurities that suppress the electronic surface states, neither of which are seen in FZ1 or FZ2.

The parameters obtained from fitting the high temperature conductivity peak up to 50 K also accurately describe the thermal conductivity below 1 K as seen in figure 10.11. This confirms two aspects of the data. First, the zero field data is indeed purely due to phonons since the simple kinetic theory of phonons describes the data over two decades of temperature. Second, we can correlate the behaviour of the phonon conductivity peak at approximately 13 K to the level of disorder in the system which then explains the deviation from the T^3 temperature dependence expected for phonons in the boundary scattering limit as $T \to 0$ K.

10.4.2 Field induced conductivity channel

Now that the phonon conductivity is well characterized, we can separate the additional field induced conductivity by considering $\kappa - \kappa_{\mathrm{ph}}$. In the following section, the additional conductivity channel will be examined in the context of a collective spin wave excitation (magnons) and a spin excitation from a quantum spin liquid state (spinons).

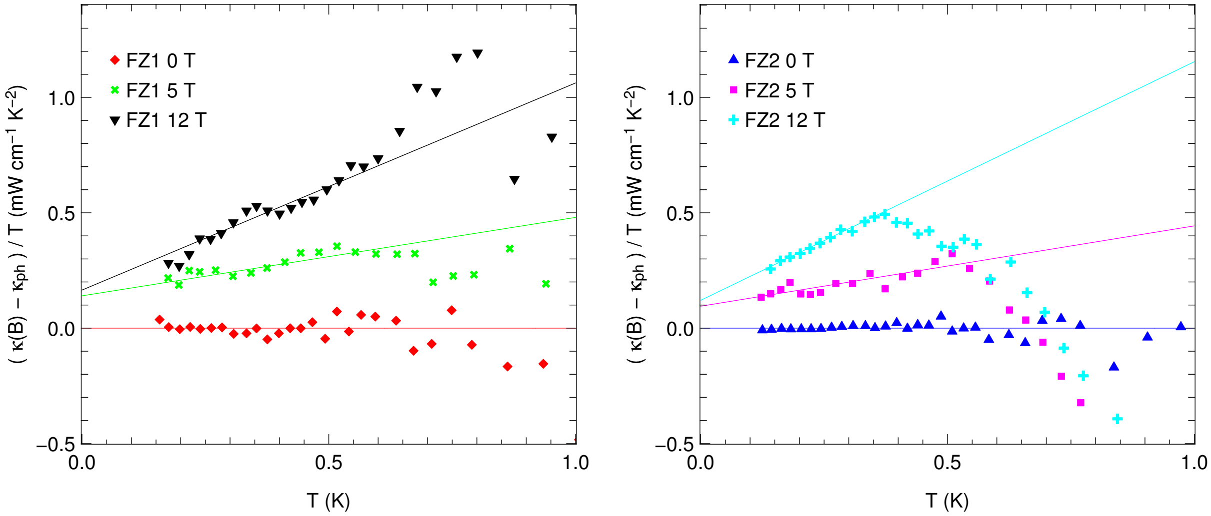

Figure 10.12: Thermal conductivity at 0 T and 12 T less the phonon conductivity for FZ1 (left) and FZ2 (right). The sold lines are linear fits to the data for $T < 600$ mK for FZ1 and $T < 400$ mK for FZ2.

Collective spin waves: magnons

A magnon is a quantized collective spin wave excitation originating from either an antiferromagnetically or a ferromagneticaly ordered state which can be described as a bosonic quasiparticle [42, 63, 211]. Antiferromagnetic magnons have a linear dispersion and hence the conductivity follows a cubic temperature dependence, similar to phonons in the boundary limited regime [211, 212]. Ferromagnetic magnons have a quadratic dispersion and the thermal conductivity has been shown to follow a quadratic temperature dependence [213, 214, 215, 211, 212]. Furthermore, the magnon conductivity is suppressed with the application of a magnetic field [213, 214, 215]. Figure 10.12 shows $(\kappa(B) - \kappa_{\mathrm{ph}})/T$ plotted versus T at 0 T, 5 T and 12 T for both FZ1 and FZ2. The flux grown sample is not considered here because no significant field enhancement was observed in the field dependence of FG1. We see that the low temperature conductivity of both FZ1 and FZ2 follows a quadratic temperature dependence up to approximately 600 mK and 400 mK respectively, as indicated by the solid lines in figure 10.12. The conductivity in a magnetic field continues to increase in FZ1 for $>$ 600 mK whereas the in field conductivity is suppressed in FZ2, falling below the zero field conductivity when $T \gtrsim 700$ mK. This might suggest more substantial magnetic scattering of the phonons in FZ2 than in FZ1 for $B > 0$ T. The origin of this difference is not understood. The additional low temperature conductivity in both samples is enhanced by a magnetic field, contrary to the expected behaviour for magnons. In addition to this, there is no sign of magnetic ordering in SmB_6 down to the lowest temperatures measured which is necessary for the existence of collective spin waves [162, 216]. Therefore, it is unlikely that the field induced conductivity is due to magnon excitations.

Quantum spin liquid: spinons

A quantum spin liquid (QSL) is an elusive and exotic phase of matter where magnetic moments avoid ordering down to the lowest temperatures. This can occur when competing interactions cause frustration between the spins. A fascinating property of the QSL state is that it can support fractionalized spin excitations known as spinons. We will see in this section that SmB_6 shares similar temperature and field dependences of known QSL candidate materials. This leads us to explore the possibility that the additional conductivity channel is due to spinon excitations. Before we examine the observed thermal conductivity in the context of a spinon contribution, we will first compare the temperature and field dependence of the conductivity of SmB_6 to other QSL candidates in order to see if it is appropriate to describe SmB_6 using QSL theory.

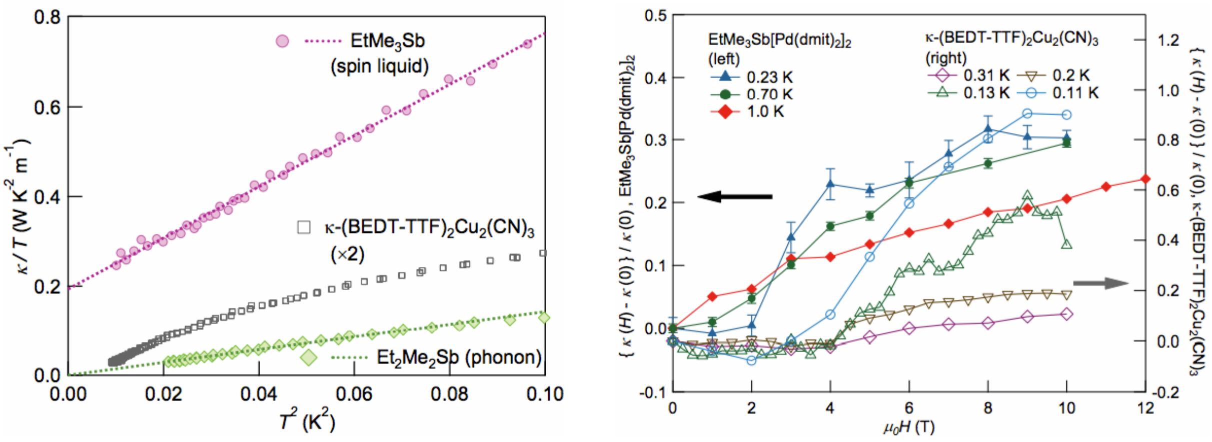

Figure 10.13: Temperature (left) and field (right) dependences of the thermal conductivity of proposed organic quantum spin liquid materials, $EtMe_3Sb[Pd(dmit)_2]_2$ and κ-(BEDT-TTF)$_2$Cu$_2$(CN)$_3$, measured by Yamashita *et al.* [217, 32, 218].

Yamashita *et al.* have measured two organic compounds which are candidate spin liquid materials: $EtMe_3Sb[Pd(dmit)_2]_2$ (dmit-131) [32] and κ-(BEDT-TTF)$_2$Cu$_2$(CN)$_3$ [217].

Their thermal conductivity data is seen in figure 10.13 revealing many similarities to SmB_6. When plotted as κ/T versus T^2, dmit-131 (pink circles) follows a linear temperature dependence with a clear non-zero intercept, indicating the presence of gapless fermionic excitations. The phonon contribution to dmit-131 is estimated by considering a related, nonmagnetic compound $Et_2Me_2Sb[Pd(dmit)_2]_2$ (dmit-221) (green diamonds). Thus, the phonons only contribute approximately 15% of the total conductivity at 300 mK indicating a considerable additional contribution to the conductivity. This system differs from SmB_6 since the magnetic excitations are observable in zero field, whereas the application of a field is required to observe the additional conductivity channel in SmB_6. On the other hand, the zero field data of κ-(BEDT-TTF)$_2$Cu$_2$(CN)$_3$ is more comparable to SmB_6 as it also has no linear term. In this system, Yamashita *et al.* utilize a two channel conductivity model to describe their data [217]. Their model consisted of a T^3 term to describe the phonon contribution and an exponential term to describe a contribution from gapped excitations. They found that the phonons only contribute approximately one quarter of the total conductivity at 100 mK. So, although the excitations are gapped in κ-(BEDT-TTF)$_2$Cu$_2$(CN)$_3$, they still contribute to the conductivity in zero field. This is unlike SmB_6, where the zero field conductivity is entirely due to phonons. Therefore, the QSL candidates dmit-131 and κ-(BEDT-TTF)$_2$Cu$_2$(CN)$_3$ appear to have gapless and gapped spinon excitations respectively at zero field. This is contrary to SmB_6 where a magnetic field is required to observe the additional magnetic channel of conductivity.

The field dependence of the conductivity of these organic QSL candidate materials is seen in the right panel of figure 10.13. The field dependence shares many qualitative and quantitative similarities to SmB_6 FZ1 and FZ2. The conductivity is enhanced in a magnetic field reaching values between 1.3 and 1.6 times the zero field conductivity value. Furthermore, step like features are also observed in both materials reminiscent of our FZ1 and FZ2 samples. Therefore, these results are consistent with the possibility that SmB_6 may also be a QSL candidate.

A first order approximation of the conductivity due to spinon excitations is $\kappa \propto T$ since the spinon specific heat is linear in temperature, and the spinon mean free path is assumed to be constant at low temperatures [219, 220]. The low temperature conductivity for all three samples is plotted as κ/T versus $T^{1.95}$ for FZ1, $T^{2.0}$ for FZ2 and $T^{1.8}$ for FG1 in figure 10.14. These exponents are less than 2 due to specular scattering of the phonons from the sample boundaries and were obtained from fitting the phonon conductivity in section 10.4.1. The dashed lines are the electrical conductivities of each sample in thermal units as in figure 10.5. The solid lines are linear fits to the data below 380 mK, where the phonons are in the boundary limited regime. This low temperature fit to the data reveals a small linear term in the 12 T data of 0.19 mW cm^{-1} K^{-2} for FZ1 and 0.33 mW cm^{-1}

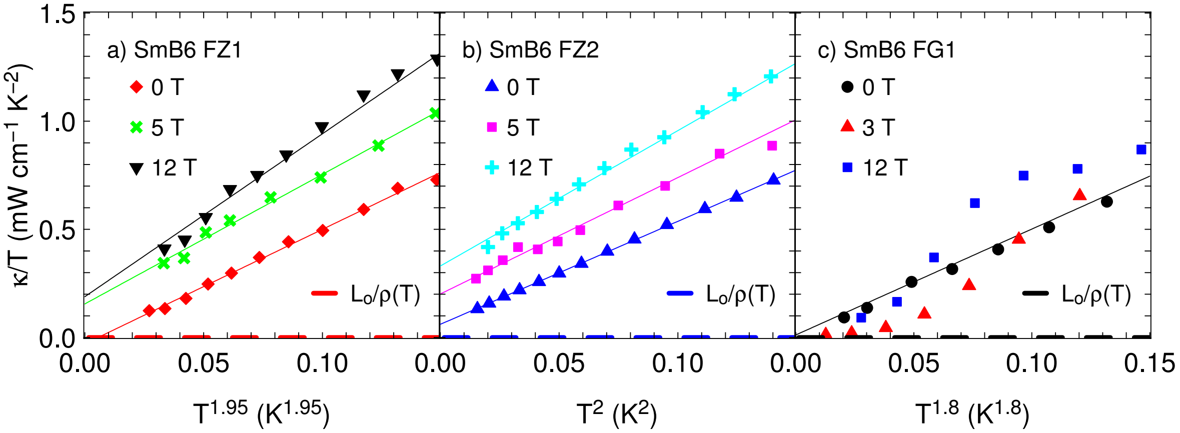

Figure 10.14: The zero field conductivity for all three SmB_6 samples plotted as κ/T versus $T^{\gamma-1}$ where $\gamma = 2.95$ for FZ1 (a), $\gamma = 3.0$ for FZ2 (b) and $\gamma = 2.8$ for FG1 (c) . The solid lines are linear fits to the data below 380 mK.

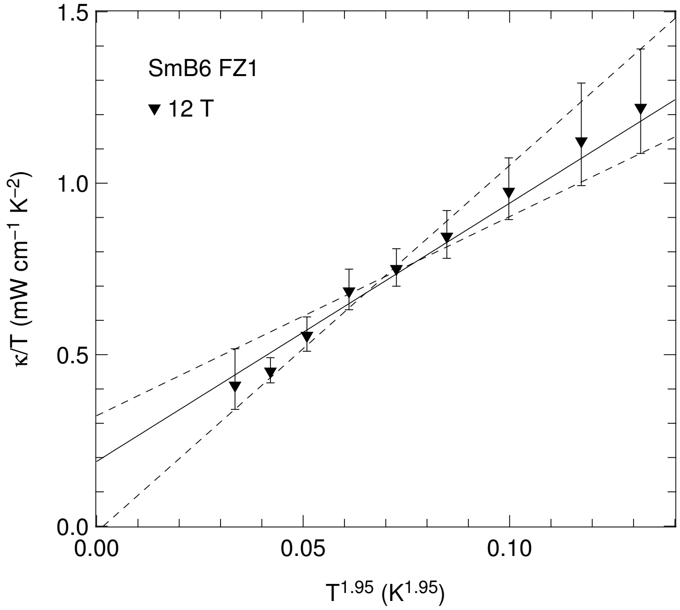

Figure 10.15: Low temperature thermal conductivity data for FZ1 at 12 T. Error is approximated by the standard deviation of the sample thermometer resistances.

K^{-2} for FZ2. No field-induced linear term is seen in FG1. We can estimate the mean free path l of the quasi-particles that would give rise to this linear term in the floating zone grown samples by considering the expression for the electronic contribution to the thermal conductivity given in chapter 2:

$$\kappa_e/T = \frac{1}{9}\frac{k_B^2 k_F^2 l}{\hbar}. \tag{10.5}$$

The Fermi wave-vector, k_F, is determined by the oscillation frequency F via $k_F = \sqrt{2eF/\hbar}$. So, at 1 K, in the field range of 35 T to 45 T, oscillations are observed to have frequencies between approximately 330 T to 11 kT [28, 29] which gives rise to $k_F \sim 1.0$ nm^{-1} and 5.8 nm^{-1} respectively. Thus, for FZ1, we find a mean free path of approximately 95 nm for the 330 T band and 3 nm for the 11 kT band. Similarly, for FZ2 we find a mean free path of approximately 160 nm for the 330 T band and 5 nm for the 11 kT band. The mean free path extracted from the dHvA oscillations yielded quasi-particle mean free paths between 27 nm and 52 nm [28], which is within a factor of 10 from the values estimated from the thermal transport. This suggests that the quasi-particles causing the quantum oscillations may also be responsible for the field-enhancement of the thermal conductivity. Furthermore, the fact that the non-zero linear term in the floating zone grown samples is many orders of magnitude larger than the electronic contribution from the surface states suggests that the field-induced conductivity may be due to spinons. However, as mentioned above, the data follows a quadratic temperature dependence as T is increased. Therefore, this conductivity channel is more complex than this basic model for spinon conductivity.

The error in the extrapolated linear term can be estimated for the 12 T data by approximating the error in the conductivity as the standard deviation of the sample thermometers. That is, the maximum (minimum) each conductivity point could be is estimated by increasing (decreasing) the hot thermometer by one standard deviation, and decreasing (increasing) the cold thermometer by one standard deviation from the time averaged value. Using the extrema of the error bars in this temperature range, we can estimate the error in the linear term extrapolation. We find that $A = 0.19^{+0.13}_{-0.20}$ mW cm^{-1} K^{-2}. Thus, the extrapolated linear term can be zero within the error bounds of the extrapolation and hence it is difficult to place much confidence in its existence. This is further evidence that the field induced excitations in SmB$_6$ are unlikely to be spinons with a linear temperature dependent conductivity.

A more rigorous examination of the conductivity due to spinon excitations is done by considering well studied example of a QSL which consists of quantum spins on a triangular lattice with antiferromagnetic interactions. Cody Nave and Patrick Lee used a Greens functions formalism within this model to calculate the transport properties arising from a spinon Fermi surface [221]. They found that to first order, the low temperature thermal conductivity is proportional to $\kappa \propto T^{1/3}$ [217]. More specifically, the conductivity per layer

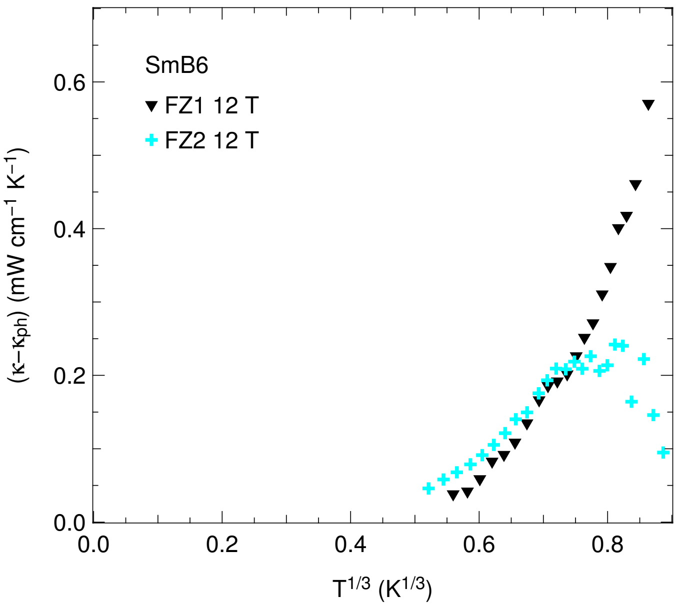

Figure 10.16: The 12 T conductivity data for FZ1 and FZ2 is plotted as $\kappa - \kappa_{\text{ph}}$ versus $T^{1/3}$ [221].

can be expressed as

$$\frac{\kappa}{T} = \frac{k_{\text{B}}^2}{\hbar}\left(\frac{\epsilon_{\text{F}}}{k_{\text{B}}T}\right)^{2/3}. \tag{10.6}$$

Although this is for the case of a two dimensional triangular system, it will provide a useful comparison to the three dimensional excitations in SmB$_6$. Thus, we will consider the functional form of $\kappa = aT^{1/3} + \kappa_{\text{ph}}$. The thermal conductivity is plotted as $\kappa - \kappa_{\text{ph}}$ versus $T^{1/3}$ in figure 10.16. The lack of linearity suggest that the conductivity is incompatible with the spinon conductivity proposed by Nave and Lee [221]. Therefore, a full microscopic theory of the excitations in SmB$_6$ would prove to be very useful in understanding the origin of the field enhancement of the thermal transport.

10.4.3 Floating zone versus flux grown samples

The results presented here suggest that the growth technique, whether grown via the floating zone technique or flux method, has strong implications on the behaviour of the conductivity, especially below 1 K. A similar dependence on sample growth technique has also been reported to occur in other measurement techniques [164, 222]. We have seen that the resistivity plateau is suppressed in FG1 which could be due to the presence of magnetic impurities preventing the formation of the electronic surface states. Fitting the thermal conductivity reveals that the floating zone grown samples have a small density of stacking fault defects in the lattice whereas the flux grown sample has dislocations and a low level of point defects as well. Therefore, it appears that the different growth techniques tend to be predisposed to different types of defects. In order to examine if impurities which cause the suppression of the resistivity plateau in FG1 are also responsible for the lack of a field enhanced conductivity we turn to previously reported conductivity and resistivity measurements of a flux grown SmB_6 sample by Xu *et al.* [33]. Their reported resistivity and conductivity are seen in figure 10.17 and figure 10.18 respectively. First note that their resistivity exhibits the expected saturation below 3 K, indicating that magnetic impurities are not present in their sample. That said, their IRRR = 5115, a factor 10 lower than the samples measured here. However, as stated above, the IRRR may not be the most reliable method of characterizing the level of disorder in SmB_6. The thermal transport data is qualitatively and quantitatively similar to our flux grown sample. Their zero field data is well described by phonons in the boundary scattering limit, which is approximately one fifth of the magnitude of our data because their sample's average width is five times smaller than FG1. Finally, no obvious enhancement of the thermal conductivity if field, similar to FG1. Therefore, the fact that the flux grown samples do not exhibit a field enhancement of the thermal conductivity regardless of the inclusion of magnetic impurities, indicates that the difference between flux grown and floating zone grown samples is likely not due to disorder in the sample.

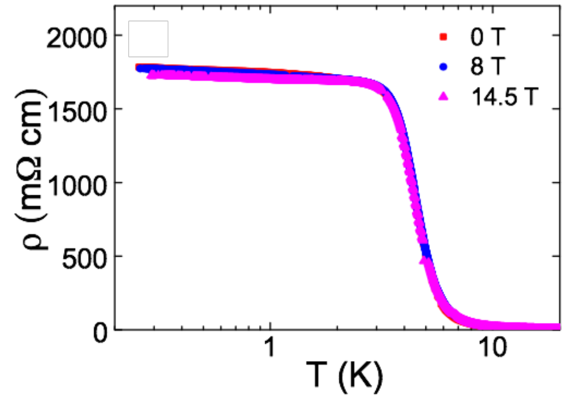

Figure 10.17: Resistivity of a flux grown sample of SmB_6 at 0 T, 8 T and 14.5 T measured by Xu *et al.* [33].

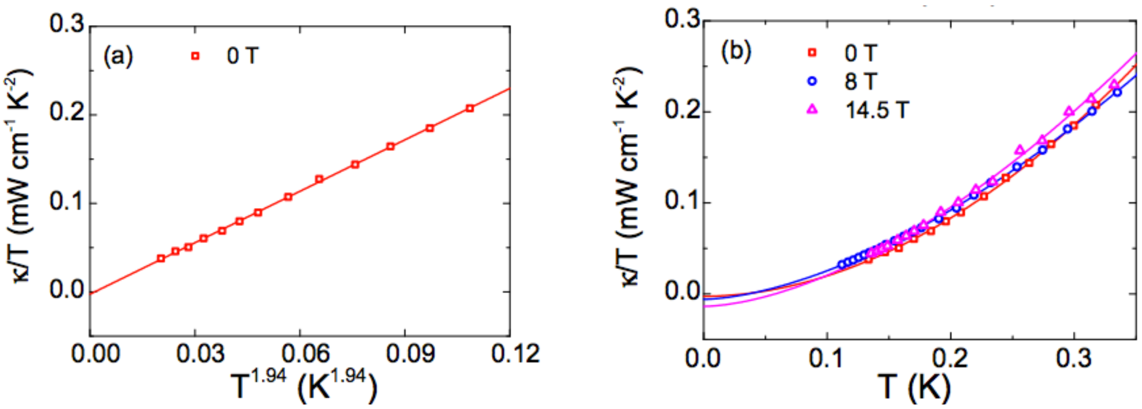

Figure 10.18: *Left:* Thermal conductivity of a flux grown sample of SmB_6 plotted as κ/T versus $T^{1.94}$ at zero field measured by Xu *et al.* [33]. *Right:* Thermal conductivity plotted as κ/T versus T for the same flux grown sample of SmB_6 at 0 T, 8 T and 14.5 T.

Another possible reason for this sensitivity could be from strain in the lattice induced by the different growth techniques which affect the Kondo exchange coupling. Monte Carlo simulations of a magnetic Kondo lattice reveal that as the Kondo exchange coupling increases, the system evolves from the staggered moment antiferromagnetic ordered phase to a magnetically disordered phase as schematically illustrated in figure 10.19 which has been adapted from reference [223]. Furthermore, they show the opening of a charge excitation gap while maintaining gapless neutral excitations. A gap opens for these neutral excitations at lower temperatures which is dependent on the Kondo exchange parameter [223]. Thus, the induced strain from the floating zone growth method may move SmB_6 towards the quantum critical point, where the neutral excitation gap is suppressed. Similar sample preparation dependent effects have been observed in the heavy fermion material $CeCu_2Si_2$ which is also in the vicinity of a magnetic quantum critical point [224].

10.5 Conclusion

Extensive thermal transport and electrical resistivity measurements have been conducted on three SmB_6 samples: two grown using the floating zone image furnace method, and one grown via the flux method. The zero field data for all three samples is well described by phonons in the boundary scattering limit for $T < 650$ mK. The two floating zone grown samples show a significant enhancement in the conductivity in an applied magnetic field.

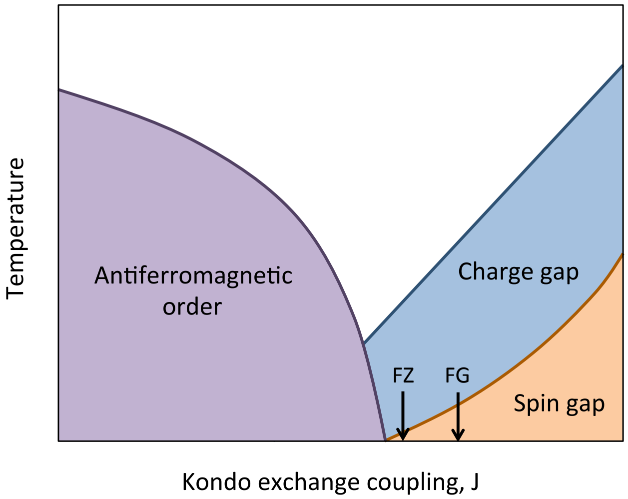

Figure 10.19: Kondo exchange parameter phase diagram determined by Monte Carlo simulations of the Kondo lattice model adapted from reference [223]. The arrows indicate approximately where the floating zone (FZ) and flux grown (FG) samples lay on the phase diagram.

The WFL expectation for the electronic thermal conductivity is approximately ten thousand times less than the observed enhancement in the conductivity indicating the field induced conductivity channel is not due to the electronic surface states. Furthermore, the enhancement with an applied field suggests a magnetic nature of the bulk excitations. The temperature dependence and field dependence share many similarities to the organic quantum spin liquid candidates. That said, the temperature dependence of the magnetic contribution to the conductivity is not well described by either magnons, or by spinon excitations proposed by Nave and Lee for a two dimensional QSL [221]. Thus, it is clear further theoretical work is required to properly describe these excitations. On the other hand, the flux grown sample does not exhibit the same field enhancement of the conductivity, suggesting both the charge and spin excitations are fully gapped in this sample. This suggests that the growth method may affect the Kondo exchange coupling, modifying the low energy excitation landscape.

Chapter 11

Conclusion

Thermal conductivity measurements were made on a variety of different systems in order to explore the nature of their ground states by probing the low energy, delocalized excitations. Thermal transport can provide information about quasiparticle excitations either by observing an auxiliary channel for conductivity, or an additional phonon scattering mechanism. Thus, we have conducted thermal conductivity measurements on the classical spin ice materials $Ho_2Ti_2O_7$ and $Dy_2Ti_2O_7$ in order to examine the effect an applied magnetic field, and the effect that disorder has on the magnetic monopole excitations. Transport measurements were also conducted on the quantum spin ice material $Yb_2Ti_2O_7$ to explore the controversial ground state as well as the difference between samples as grown and samples that were annealed in oxygen. Finally, thermal conductivity and electrical resistivity measurements were also conducted on the topological Kondo insulator, SmB_6, to investigate the Landau quasiparticles responsible for the large quantum oscillations at low temperature. A brief summary of the results follows.

11.1 Summary

The field dependence of the thermal conductivity of $Ho_2Ti_2O_7$ (HTO) and $Dy_2Ti_2O_7$ (DTO) reveals that both samples exhibit hysteresis at temperatures below 360 mK due to a first order phase transition from the Kagomé ice phase to a long range ordered phase at high field. It is shown that this low temperature hysteresis can be suppressed in DTO if the system is allowed to settle at each field step for extended periods of time, as expected for a first order phase transition [137]. Additionally, we show that the hysteresis previously reported at temperatures up to 600 mK [102, 14, 101, 104] can be induced by increasing the magnetic field ramp rate. This is in part due to the local heating of the sample caused by thermal runaway processes which are known to occur in the spin ice state when continually sweeping the magnetic field [16, 135]. We were thus able to construct a field versus temperature phase diagram with $B \parallel [111]$, accurately indicating the first order phase transition line which is consistent with the Clausius-Clapeyron equation. The high field data for HTO shows an increase in the conductivity which scales onto the Brillouin function, indicating a suppression of spin-phonon scattering. On the other hand, the high field data in DTO shows a modest decrease in the conductivity to a constant value, suggesting that spin-phonon scattering is not a dominant mechanism in DTO, consistent with the observed spin-lattice decoupling in DTO [7, 8]. This implies that the spin-lattice coupling is much stronger in HTO than in DTO. Therefore, the zero field lattice contribution to the conductivity can be approximated by the field independent conductivity for $B \gtrsim 4$ T for DTO. This approximation is invalid in HTO due to the strong spin-phonon scattering.

The effect of disorder on the magnetic conductivity is explored by measuring two DTO samples with differing levels of disorder. The level of disorder is initially characterized via x-ray diffraction measurements by directly probing the crystal structure and lattice parameter which has recently been shown to be an accurate indication of the level of magnetic ion stuffing in the rare-earth titanates [125]. The relative level of disorder in these two samples is further characterized via high temperature transport measurements which probes the defect scattering of phonons [48, 49]. Having established differing levels of disorder in the two samples, we are then able to examine the effect magnetic disorder has on the magnetic channel of conductivity. We have seen from the field dependent study that the high field data in DTO is an accurate approximation of the zero field phonon conductivity. This is confirmed by the observation of the T^3 temperature dependence of the conductivity at 8 T which is due to phonons in the boundary limited regime. Since the phonon conductivity is now well established, we are able to isolate the magnetic channel of conductivity. We find that the monopole conductivity in the sample with less disorder follows an exponential temperature dependence, as expected for an activated quasiparticle excitation [156]. On the other hand, the sample with a higher level of disorder follows a power law temperature dependence with a larger magnitude than the pure sample. This indicates that the disorder in the sample tends to enhance the density of monopoles either by acting as nucleation sites for monopole quasiparticles, or by pinning monopoles upon cooling from higher temperatures. Finally, an analogy is made to doped semiconductors.

The rare-earth pyrochlore material $Yb_2Ti_2O_7$ (YbTO) has been shown to be susceptible to the inclusion of lattice defects such as excess Yb^{3+} ions on the Ti^{4+} sub-lattice, and off-stoichiometric oxygen content originating from the floating zone growth technique [98]. This is in part responsible for the observation of a sample dependent peak in the specific heat [121, 18, 120]. Thus, thermal transport measurements have been conducted on two YbTO samples, one as grown, and one which has been annealed in oxygen after the growth procedure to replenish the depleted oxygen content. This was done in order to examine both the effect on the phase transition as well as the effect on the magnetic excitations. The annealed YbTO sample exhibits a step-like drop in the conductivity at approximately 180 mK corresponding to the sharp peak which has been observed in specific heat measurements. The step-like feature is smeared out in the as-grown sample of YbTO, consistent with the broadening of the peak observed in single crystal specific heat measurements at the transition temperature. The field dependence of the conductivity above the transition temperature indicating that the low field data has a sizeable contribution from monopole excitations consistent with previously reported thermal transport studies [13, 23]. The high field data exhibits an increase in the conductivity which scales onto the Brillouin function, similar to HTO, suggesting a considerable amount of spin-phonon scattering. This impedes our ability to accurately estimate the zero field phonon conductivity, and hence we are unable to reliably extract the magnetic contribution to the conductivity. Finally, there has been some controversy about whether the ground state orders or remains dynamic as in the case of a quantum spin liquid [19, 36, 37, 38, 39, 40, 41]. We observe that the suppression rate of the monopole excitations diverges as the temperature approaches the critical temperature, which is consistent with ferromagnetic fluctuations associated with the onset of a ferromagnetically ordered ground state. A field versus temperature phase diagram for $B \parallel [111]$ is then extracted from the field dependence of the conductivity.

The recent observation of large quantum oscillations in the Kondo insulator SmB_6 have been interpreted as being due to either the topologically protected electronic surface states, or charge neutral excitations in the bulk [28, 29]. Thermal and electrical transport measurements have thus been conducted on three SmB_6 samples, two which have been grown via the floating zone method, and one which was grown in Al flux. This was done in order to probe the delocalized quasiparticles in SmB_6. Our zero field thermal transport data for all three samples is well described by phonons in the boundary scattering limit with no additional electronic contribution. The conductivity of the floating zone grown samples is clearly enhanced with the application of a magnetic field, indicating the presence of an additional channel of heat conduction. The magnitude of this field induced conductivity channel far exceeds the expected contribution from the electronic surface states via the Wiedemann-Franz law, suggesting that the excess conductivity is due to charge neutral, magnetic excitations. We show that the temperature dependence of the magnetic conductivity is not well described by collective spin waves (magnons) [213, 214, 215] or by current theoretical models of spinon excitations in a quantum spin liquid state [221]. However, the field dependence of the conductivity exhibits many similarities with candidate quantum spin liquid materials [32]. On the other hand, the flux grown sample does not exhibit any field enhancement of the conductivity, consistent with previously reported conductivity data [33]. This is proposed to be due to a variation in the Kondo exchange coupling resulting from strain induced in the lattice from the different growth techniques.

References

[1] R. O. Pohl and B. Stritzer, Phys. Rev. B **25**, 6 (1982).

[2] I. A. Ryzhkin, Journal of Experimental and Theoretical Physics **101**, 481 (2005).

[3] S. T. Bramwell and M. Gingras, Science **294**, 1495 (2001).

[4] B. C. den Hertog and M. J. P. Gingras, Phys. Rev. Lett. **84**, 3430 (2000).

[5] R. Melko and M. Gingras, J. Phys. Cond. Mat. **16**, R1277 (2004).

[6] J. A. Quilliam, L. R. Yaraskavitch, H. A. Dabkowska, B. D. Gaulin, and J. B. Kycia, Phys. Rev. B **83**, 094424 (2011).

[7] L. R. Yaraskavitch, H. M. Revell, S. Meng, K. A. Ross, H. M. L. Noad, H. A. Dabkowska, B. D. Gaulin, and J. B. Kycia, Phys. Rev. B **85**, 020410(R) (2012).

[8] D. Pomaranski, L. R. Yaraskavitch, S. Meng, K. A. Ross, H. M. L. Noad, H. A. Dabkowska, B. D. Gaulin, and J. B. Kycia, Nat Phys **9**, 353 (2013).

[9] S. T. Bramwell, M. J. Harris, B. C. den Hertog, M. J. P. Gingras, J. S. Gardner, D. F. McMorrow, A. R. Wildes, A. L. Cornelius, J. D. M. Champion, R. G. Melko, and T. Fennell, Phys. Rev. Lett. **87**, 4 (2001).

[10] C. Castelnovo, R. Moessner, and S. Sondhi, Nature **451**, 06433 (2008).

[11] S. R. Dunsiger, A. A. Aczel, C. Arguello, H. A. Dabkowska, A. Dabkowski, M.-H. Du, T. Goko, B. Javanprast, T. Lin, F. L. Ning, H. M. L. Noad, D. J. Singh, T. J. Williams, Y. J. Uemura, M. J. P. Gingras, and G. M. Luke, Phys. Rev. Lett. **107**, 207207 (2011).

[12] L. Bovo, J. A. Bloxsom, D. Prabhakaran, G. Aeppli, and S. T. Bramwell, Nature Communications **4**, 1535 EP (2013).

[13] S. J. Li, Z. Y. Zhao, C. Fan, B. Tong, F. B. Zhang, J. Shi, J. C. Wu, X. G. Liu, H. D. Zhou, X. Zhao, and X. F. Sun, Phys. Rev. B **92**, 094408 (2015).

[14] G. Kolland, O. Breunig, M. Valldor, M. Hiertz, J. Frielingsdorf, and T. Lorenz, Phys. Rev. B **86**, 060402 (2012).

[15] H. Fukazawa, R. G. Melko, R. Higashinaka, Y. Maeno, and M. J. P. Gingras, Phys. Rev. B **65**, 054410 (2002).

[16] D. Slobinsky, C. Castelnovo, R. A. Borzi, A. S. Gibbs, A. P. Mackenzie, R. Moessner, and S. A. Grigera, Phys. Rev. Lett. **105**, 267205 (2010).

[17] L. Savary and L. Balents, Phys. Rev. Lett. **108**, 037202 (2012).

[18] K. A. Ross, L. Savary, B. D. Gaulin, and L. Balents, Phys. Rev. X **1**, 021002 (2011).

[19] J. A. Hodges, P. Bonville, A. Forget, A. Yaouanc, P. Dalmas de Réotier, G. André, M. Rams, K. Królas, C. Ritter, P. C. M. Gubbens, C. T. Kaiser, P. J. C. King, and C. Baines, Phys. Rev. Lett. **88**, 077204 (2002).

[20] E. Lhotel, S. R. Giblin, M. R. Lees, G. Balakrishnan, L. J. Chang, and Y. Yasui, Phys. Rev. B **89**, 224419 (2014).

[21] L.-J. Chang, M. R. Lees, I. Watanabe, A. D. Hillier, Y. Yasui, and S. Onoda, Phys. Rev. B **89**, 184416 (2014).

[22] J. Robert, E. Lhotel, G. Remenyi, S. Sahling, I. Mirebeau, C. Decorse, B. Canals, and S. Petit, Phys. Rev. B **92**, 064425 (2015).

[23] Y. Tokiwa, T. Yamashita, M. Udagawa, S. Kittaka, T. Sakakibara, D. Terazawa, Y. Shimoyama, T. Terashima, Y. Yasui, T. Shibauchi, and Y. Matsuda, Nature Communications **7**, 10807 EP (2016).

[24] P. Syers, D. Kim, M. S. Fuhrer, and J. Paglione, Phys. Rev. Lett. **114**, 096601 (2015).

[25] D. J. Kim, S. Thomas, T. Grant, J. Botimer, Z. Fisk, and J. Xia, Scientific Reports **3**, 3150 EP (2013).

[26] D. J. Kim, J. Xia, and Z. Fisk, Nat Mater **13**, 466 (2014).

[27] M. Neupane, N. Alidoust, S.-Y. Xu, T. Kondo, Y. Ishida, D. J. Kim, C. Liu, I. Belopolski, Y. J. Jo, T.-R. Chang, H.-T. Jeng, T. Durakiewicz, L. Balicas, H. Lin, A. Bansil, S. Shin, Z. Fisk, and M. Z. Hasan, Nature Communications **4**, 2991 EP (2013).

[28] G. Li, Z. Xiang, F. Yu, T. Asaba, B. Lawson, P. Cai, C. Tinsman, A. Berkley, S. Wolgast, Y. S. Eo, D.-J. Kim, C. Kurdak, J. W. Allen, K. Sun, X. H. Chen, Y. Y. Wang, Z. Fisk, and L. Li, Science **346**, 1208 (2014).

[29] B. S. Tan, Y.-T. Hsu, B. Zeng, M. C. Hatnean, N. Harrison, Z. Zhu, M. Hartstein, M. Kiourlappou, A. Srivastava, M. D. Johannes, T. P. Murphy, J.-H. Park, L. Balicas, G. G. Lonzarich, G. Balakrishnan, and S. E. Sebastian, Science **349**, 287 (2015).

[30] S. Gabáni, K. Flachbart, E. Konovalova, M. Orendáč, Y. Paderno, V. Pavlík, and J. Šebek, Solid State Communications **117**, 641 (2001).

[31] M. Anisimov, A. Bogach, V. Glushkov, S. Demishev, N. Samarin, S. Gavrilkin, K. Mitsen, N. Shitsevalova, A. Levchenko, V. Filippov, and et al., Acta Physica Polonica A **126**, 350351 (2014).

[32] M. Yamashita, N. Nakata, Y. Senshu, M. Nagata, H. M. Yamamoto, R. Kato, T. Shibauchi, and Y. Matsuda, Science **328**, 1246 (2010).

[33] Y. Xu, S. Cui, J. K. Dong, D. Zhao, T. Wu, X. H. Chen, K. Sun, H. Yao, and S. Y. Li, Phys. Rev. Lett. **116**, 246403 (2016).

[34] A. P. Ramirez, A. Hayashi, R. J. Cava, R. Siddharthan, and B. S. Shastry, Nature **399**, 333 (1999).

[35] M. J. Harris, S. T. Bramwell, D. F. McMorrow, T. Zeiske, and K. W. Godfrey, Phys. Rev. Lett. **79**, 2554 (1997).

[36] J. S. Gardner, G. Ehlers, N. Rosov, R. W. Erwin, and C. Petrovic, Phys. Rev. B **70**, 180404 (2004).

[37] P. Bonville, J. A. Hodges, E. Bertin, J.-P. Bouchaud, P. D. de Réotier, L.-P. Regnault, H. M. Rønnow, J.-P. Sanchez, S. Sosin, and A. Yaouanc, *Transitions and Spin Dynamics at Very Low Temperature in the Pyrochlores Yb2Ti2O7 and Gd2Sn2O7* (Springer Netherlands, Dordrecht, 2004), pp. 103–111.

[38] K. A. Ross, J. P. C. Ruff, C. P. Adams, J. S. Gardner, H. A. Dabkowska, Y. Qiu, J. R. D. Copley, and B. D. Gaulin, Phys. Rev. Lett. **103**, 227202 (2009).

[39] K. A. Ross, L. R. Yaraskavitch, M. Laver, J. S. Gardner, J. A. Quilliam, S. Meng, J. B. Kycia, D. K. Singh, T. Proffen, H. A. Dabkowska, and B. D. Gaulin, Phys. Rev. B **84**, 174442 (2011).

[40] Y. Yasui, M. Soda, S. Iikubo, M. Ito, M. Sato, N. Hamaguchi, T. Matsushita, N. Wada, T. Takeuchi, N. Aso, and K. Kakurai, Journal of the Physical Society of Japan **72**, 3014 (2003).

[41] L.-J. Chang, S. Onoda, Y. Su, Y.-J. Kao, K.-D. Tsuei, Y. Yasui, K. Kakurai, and M. R. Lees, Nature Communications **3**, 992 EP (2012).

[42] N. W. Ashcroft and N. D. Mermin, *Solid State Physics* (Brooks Cole, 1976).

[43] C. Kittel, *Solid State Physics - 8th ed.* (Wiley, 2004).

[44] H. Rosenberg, *Low Temperature Solid State Physics* (Oxford University Press, 1963).

[45] S. Y. Li, J.-B. Bonnemaison, A. Payeur, P. Fournier, C. . H. Wang, X. H. Chen, and L. Taillefer, Phys. Rev. B **77**, 134501 (2008).

[46] X. F. Sun and Y. Ando, Phys. Rev. B **79**, 176501 (2009).

[47] B. K. Singh, V. J. Menon, and K. C. Sood, Phys. Rev. B **74**, 184302 (2006).

[48] R. Berman, E. L. Foster, and J. M. Ziman, Proc. Roy. Soc. (London) **A231**, 130 (1955).

[49] P. Klemens, *Solid State Physics Volume 7* (Academic Press Inc., 1958).

[50] J. M. Ziman, *Electrons and Phonons: The Theory of Transport Phenomena in Solids* (Oxford University Press, 1963).

[51] W. H. Toews and R. W. Hill, RSI **85**, 043905 (2013).

[52] P. L. Kapitza, Phys. Rev. **60**, 354 (1941).

[53] E. T. Swartz and R. O. Pohl, Reviews of Modern Physics **61**, 605 (1989).

[54] K. Liu, A thermal expansion coefficient study of several magnetic spin materials via capacitive dilatometry, Master's thesis, Univeristy of Waterloo, Waterloo, ON, Canada, 2013.

[55] R. Pott and R. Schefzyk, Journal of Physics E: Scientific Instruments **16**, 444 (1983).

[56] F. Pobell, *Matter and Methods at Low Temperatures* (Springer, 1996).

[57] J. T. Tough, W. D. McCormick, and J. G. Dash, Phys. Rev. **132**, 2373 (1963).

[58] R. J. Donnelly and C. F. Barenghi, Journal of physical and chemical reference data **27**, 1217 (1998).

[59] D. S. Greywall, Phys. Rev. B **27**, 2747 (1983).

[60] D. S. Greywall, Phys. Rev. B **33**, 7520 (1986).

[61] A. C. Anderson, W. R. Roach, R. E. Sarwinski, and J. C. Wheatley, Phys. Rev. Lett. **16**, 263 (1966).

[62] E. Polturak and R. Rosenbaum, Journal of Low Temperature Physics **43**, 477 (1981).

[63] J. Coey, *Magnetism and Magnetic Materials*Magnetism and Magnetic Materials (Cambridge University Press, 2010).

[64] J. S. Gardner, M. J. P. Gingras, and J. E. Greedan, Physical Review **82**, 53 (2010).

[65] N. Majlis, *The Quantum Theory of Magnetism - 2nd ed.* (World Scientific Publishing Company, 2007).

[66] J. Mulak and Z. Gajek, *The Effective Crystal Field Potential* (Elsevier Science, 2000).

[67] G. H. Wannier, Physical Review **79**, 357 (1950).

[68] R. M. F. Houtappel, Physica **26**, 425 (1950).

[69] P. W. Anderson, Physical Review **102**, 4 (1956).

[70] J. D. Bernal and R. H. Fowler, J. Chem. Phys. **1**, 515 (1933).

[71] L. Pauling, Journal of the American Chemical Society **57**, 2680 (1935).

[72] J. S. Gardner, A. Keren, G. Ehlers, C. Stock, E. Segal, J. M. Roper, B. Fåk, M. B. Stone, P. R. Hammar, D. H. Reich, and B. D. Gaulin, Phys. Rev. B **68**, 180401 (2003).

[73] H. R. Molavian, M. J. P. Gingras, and B. Canals, Phys. Rev. Lett. **98**, 157204 (2007).

[74] S. Legl, C. Krey, S. R. Dunsiger, H. A. Dabkowska, J. A. Rodriguez, G. M. Luke, and C. Pfleiderer, Phys. Rev. Lett. **109**, 047201 (2012).

[75] L. Savary, K. A. Ross, B. D. Gaulin, J. P. C. Ruff, and L. Balents, Phys. Rev. Lett. **109**, 167201 (2012).

[76] K. A. Ross, Y. Qiu, J. R. D. Copley, H. A. Dabkowska, and B. D. Gaulin, Phys. Rev. Lett. **112**, 057201 (2014).

[77] Y. M. Jana and D. Ghosh, Phys. Rev. B **61**, 9657 (2000).

[78] S. Rosenkranz, A. P. Ramirez, A. Hayashi, R. J. Cava, R. Siddharthan, and B. S. Shastry, Journal of Applied Physics **87**, 9 (2000).

[79] T. Fennell, O. A. Petrenko, B. Fåk, S. T. Bramwell, M. Enjalran, T. Yavors'kii, M. J. P. Gingras, R. G. Melko, and G. Balakrishnan, Phys. Rev. B **70**, 134408 (2004).

[80] T. Fennell, S. T. Bramwell, D. F. McMorrow, P. Manuel, and A. R. Wildes, Nat Phys **3**, 566 (2007).

[81] J. Snyder, J. S. Slusky, R. J. Cava, and P. Schiffer, Nature **413**, 48 (2001).

[82] K. Matsuhira, Y. Hinatsu, and T. Sakakibara, J. Phys.: Condens. Matter **13**, L737 (2001).

[83] K. Matsuhira, Y. Hinatsu, K. Tenya, and T. Sakakibara, J. Phys.: Condens. Matter **12**, L649 (2000).

[84] J. Snyder, B. G. Ueland, J. S. Slusky, H. Karunadasa, R. J. Cava, and P. Schiffer, Phys. Rev. B **69**, 064414 (2004).

[85] M. Orendáč, J. Hanko, E. Čižmár, A. Orendáčová, M. Shirai, and S. T. Bramwell, Phys. Rev. B **75**, 104425 (2007).

[86] B. Klemke, M. Meissner, P. Strehlow, K. Kiefer, S. A. Grigera, and D. A. Tennant, J. Low Temp. Phys. **163**, 345 (2011).

[87] S. R. Giblin, S. T. Bramwell, P. C. Holdsworth, D. Prabhakaran, and I. Terry, Nature Physics **7**, 252 (2011).

[88] R. Higashinaka, H. Fukazawa, K. Deguchi, and Y. Maeno, J. Phys. Cond. Mat. **16**, S679 (2004).

[89] H. Kadowaki, N. Doi, Y. Aoki, Y. Tabata, T. J. Sato, J. W. Lynn, K. Matsuhira, and Z. Hiroi, J. Phys. Soc. Japan **78**, 103706 (2009).

[90] H. Blöte, R. Wielinga, and W. Huiskamp, Physica **43**, 549 (1969).

[91] P. A. M. Dirac, Proceedings of the Royal Society of London A: Mathematical, Physical and Engineering Sciences **133**, 60 (1931).

[92] CERN Press Office, *Restarting the LHC: Why 13 TeV?*, `http://cds.cern.ch/record/1998739`, (2014).

[93] C. Castelnovo, R. Moessner, and S. L. Sondhi, Phys. Rev. B **84**, 144435 (2011).

[94] D. J. P. Morris, D. A. Tennant, S. A. Grigera, B. Klemke, C. Castelnovo, R. Moessner, C. Czternasty, M. Meissner, K. C. Rule, J.-U. Hoffmann, K. Kiefer, S. Gerischer, D. Slobinsky, and R. S. Perry, Science **326**, 411 (2009).

[95] S. T. Bramwell, S. R. Giblin, S. Calder, R. Aldus, D. Prabhakaran, and T. Fennell, Nature **461**, 15 (2009).

[96] H. M. Revell, L. R. Yaraskavitch, J. D. Mason, K. A. Ross, H. M. L. Noad, H. A. Dabkowska, B. D. Gaulin, P. Henelius, and J. B. Kycia, Nat Phys **9**, 34 (2013).

[97] E. R. Kassner, A. B. Eyvazov, B. Pichler, T. J. S. Munsie, H. A. Dabkowska, G. M. Luke, and J. C. S. Davis, Proceedings of the National Academy of Sciences **112**, 8549 (2015).

[98] K. A. Ross, T. Proffen, H. A. Dabkowska, J. A. Quilliam, L. R. Yaraskavitch, J. B. Kycia, and B. D. Gaulin, Phys. Rev. B **86**, 174424 (2012).

[99] C. Jaccard, Physik der kondensierten Materie **3**, 99 (1964).

[100] L. D. C. Jaubert and P. C. W. Holdsworth, Nature Phys. **5**, 258 (2009).

[101] G. Kolland, M. Valldor, M. Hiertz, J. Frielingsdorf, and T. Lorenz, Phys. Rev. B **88**, 054406 (2013).

[102] C. Fan, Z. Y. Zhao, H. D. Zhou, X. M. Wang, Q. J. Li, F. B. Zhang, X. Zhao, and X. F. Sun, Phys. Rev. B **87**, 144404 (2013).

[103] W. H. Toews, S. S. Zhang, K. A. Ross, H. A. Dabkowska, B. D. Gaulin, and R. W. Hill, Phys. Rev. Lett. **110**, 217209 (2013).

[104] S. Scharffe, G. Kolland, M. Hiertz, M. Valldor, and T. Lorenz, JPS Conf. Proc. **3**, 014030 (2014).

[105] S. Scharffe, G. Kolland, M. Valldor, V. Cho, J. Welter, and T. Lorenz, Journal of Magnetism and Magnetic Materials **383**, 83 (2015).

[106] T. Fennell, O. A. Petrenko, B. Fåk, J. S. Gardner, S. T. Bramwell, and B. Ouladdiaf, Phys. Rev. B **72**, 224411 (2005).

[107] J. P. Clancy, J. P. C. Ruff, S. R. Dunsiger, Y. Zhao, H. A. Dabowska, J. S. Gardner, Y. Qiu, J. R. D. Copley, T. Jenkins, and B. D. Gaulin, Phys. Rev. B **79**, 014408 (2009).

[108] R. Moessner and S. L. Sondhi, Phys. Rev. B **68**, 064411 (2003).

[109] Y. Tabata, H. Kadowaki, K. Matsuhira, Z. Hiroi, N. Aso, E. Ressouche, and B. Fåk, Phys. Rev. Lett. **97**, 257205 (2006).

[110] T. Sakakibara, T. Tayama, Z. Hiroi, K. Matsuhira, and S. Takagi, Phys. Rev. Lett. **90**, 207205 (2003).

[111] Z. Hiroi, K. Matsuhira, S. Takagi, T. Tayama, and T. Sakakibara, J. Phys. Soc. Japan **72**, 2 (2003).

[112] L. D. C. Jaubert, SPIN **05**, 1540005 (2015).

[113] M. J. P. Gingras and P. A. McClarty, Reports on Progress in Physics **77**, 056501 (2014).

[114] L. Savary and L. Balents, Phys. Rev. B **87**, 205130 (2013).

[115] M. Hermele, M. P. A. Fisher, and L. Balents, Phys. Rev. B **69**, 064404 (2004).

[116] A. Banerjee, S. V. Isakov, K. Damle, and Y. B. Kim, Phys. Rev. Lett. **100**, 047208 (2008).

[117] J. A. Hodges, P. Bonville, A. Forget, M. Rams, K. Krlas, and G. Dhalenne, Journal of Physics: Condensed Matter **13**, 9301 (2001).

[118] B. Z. Malkin, A. R. Zakirov, M. N. Popova, S. A. Klimin, E. P. Chukalina, E. Antic-Fidancev, P. Goldner, P. Aschehoug, and G. Dhalenne, Phys. Rev. B **70**, 075112 (2004).

[119] N. R. Hayre, K. A. Ross, R. Applegate, T. Lin, R. R. P. Singh, B. D. Gaulin, and M. J. P. Gingras, Phys. Rev. B **87**, 184423 (2013).

[120] R. M. D'Ortenzio, H. A. Dabkowska, S. R. Dunsiger, B. D. Gaulin, M. J. P. Gingras, T. Goko, J. B. Kycia, L. Liu, T. Medina, T. J. Munsie, D. Pomaranski, K. A. Ross, Y. J. Uemura, T. J. Williams, and G. M. Luke, Phys. Rev. B **88**, 134428 (2013).

[121] A. Yaouanc, P. Dalmas de Réotier, C. Marin, and V. Glazkov, Phys. Rev. B **84**, 172408 (2011).

[122] S. Bhattacharjee, S. Erfanifam, E. L. Green, M. Naumann, Z. Wang, S. Granovsky, M. Doerr, J. Wosnitza, A. A. Zvyagin, R. Moessner, A. Maljuk, S. Wurmehl, B. Büchner, and S. Zherlitsyn, Phys. Rev. B **93**, 144412 (2016).

[123] P. D. de Rotier, V. Glazkov, C. Marin, A. Yaouanc, P. Gubbens, S. Sakarya, P. Bonville, A. Amato, C. Baines, and P. King, Physica B: Condensed Matter **374375**, 145 (2006).

[124] G. Will, *Powder Diffraction* (Springer-Verlag Berlin Heidelberg, 2006).

[125] K. Baroudi, B. D. Gaulin, S. H. Lapidus, J. Gaudet, and R. J. Cava, Phys. Rev. B **92**, 024110 (2015).

[126] K. E. Arpino, B. A. Trump, A. O. Scheie, T. M. McQueen, and S. M. Koohpayeh, ArXiv e-prints (2017), 1701.08821.

[127] L. D. C. Jaubert, O. Benton, J. G. Rau, J. Oitmaa, R. R. P. Singh, N. Shannon, and M. J. P. Gingras, Phys. Rev. Lett. **115**, 267208 (2015).

[128] O. A. Petrenko, M. R. Lees, and G. Balakrishnan, Phys. Rev. B **68**, 012406 (2003).

[129] H. Sato, K. Matsuhira, T. Tayama, Z. Hiroi, S. Takagi, and T. Sakakibara, Journal of Physics: Condensed Matter **18**, L297 (2006).

[130] C. Krey, S. Legl, S. R. Dunsiger, M. Meven, J. S. Gardner, J. M. Roper, and C. Pfleiderer, Phys. Rev. Lett. **108**, 257204 (2012).

[131] M. E. Brooks-Bartlett, S. T. Banks, L. D. C. Jaubert, A. Harman-Clarke, and P. C. W. Holdsworth, Phys. Rev. X **4**, 011007 (2014).

[132] T. Sakakibara, T. Tayama, K. Matsuhira, S. Takagi, and Z. Hiroi, Journal of Magnetism and Magnetic Materials **272276**, 1312 (2004).

[133] O. A. Petrenko, M. R. Lees, and G. Balakrishnan, J. Phys. Cond. Mat. **23**, 164218 (2011).

[134] M. J. Matthews, C. Castelnovo, R. Moessner, S. A. Grigera, D. Prabhakaran, and P. Schiffer, Phys. Rev. B **86**, 214419 (2012).

[135] S. Erfanifam, S. Zherlitsyn, J. Wosnitza, R. Moessner, O. A. Petrenko, G. Balakrishnan, and A. A. Zvyagin, Phys. Rev. B **84**, 220404 (2011).

[136] A. Aharoni, Journal of Applied Physics **83**, 3432 (1998).

[137] G. S. Agarwal and S. R. Shenoy, Phys. Rev. A **23**, 2719 (1981).

[138] C. Castelnovo, R. Moessner, and S. L. Sondhi, Phys. Rev. Lett. **104**, 107201 (2010).

[139] R. Higashinaka, H. Fukazawa, K. Deguchi, and Y. Maeno, J. Phys. Soc. Japan **73**, 10 (2004).

[140] S. Grigera, R. Borzi, D. Slobinsky, A. Gibbs, R. Higashinaka, Y. Maeno, and T. Grigera, Papers in Physics **7** (2015).

[141] R. A. Borzi, F. A. Gómez Albarracín, H. D. Rosales, G. L. Rossini, A. Steppke, D. Prabhakaran, A. P. Mackenzie, D. C. Cabra, and S. A. Grigera, Nature Communications **7**, 12592 EP (2016).

[142] M. Udagawa, M. Ogata, and Z. Hiroi, Journal of the Physical Society of Japan **71**, 2365 (2002).

[143] D. Prabhakaran and A. Boothroyd, Journal of Crystal Growth **318**, 1053 (2011).

[144] G. Balakrishnan, O. A. Petrenko, M. R. Lees, and D. M. Paul, Journal of Physics Condensed Matter **10**, L723 (1998).

[145] J. Kang, Z. Fang, X. Chen, W. Liu, F. Guo, S. Wu, Y. Zhang, and J. Chen, Journal of Alloys and Compounds **599**, 170 (2014).

[146] W. C. McCrone, L. B. McCrone, and J. G. Delly, *Polarized Light Microscopy* (Ann Arbor Science Publishers, 1978).

[147] E. Clementi, D. L. Raimondi, and W. P. Reinhardt, The Journal of Chemical Physics **47**, 1300 (1967).

[148] Y. Nakanishi, T. Kumagai, M. Yoshizawa, K. Matsuhira, S. Tagaki, and Z. Hiroi, Phys. Rev. B **83**, 184434 (2011).

[149] C. J. Glassbrenner and G. A. Slack, Phys. Rev. **134**, A1058 (1964).

[150] G. Sala, M. J. Gutmann, D. Prabhakaran, D. Pomaranski, C. Mitchelitis, J. B. Kycia, D. G. Porter, C. Castelnovo, and J. P. Goff, Nat Mater **13**, 488 (2014).

[151] R. Berman, *Thermal Conduction in Solids* (Oxford University Press, 1976).

[152] S. Erfanifam, *Ultrasound investigations of spin-ice materials*, PhD thesis, Technische Universität Dresden, 01069 Dresden, Germany, 2013.

[153] S. T. Bramwell and M. J. Harris, Journal of Physics: Condensed Matter **10**, L215 (1998).

[154] R. C. Silva, R. J. C. Lopes, L. A. S. Mól, W. A. Moura-Melo, G. M. Wysin, and A. R. Pereira, Phys. Rev. B **87**, 014414 (2013).

[155] A. León, Current Applied Physics **13**, 2014 (2013), 1208.6284.

[156] J. H. Moeser, F. Steglich, C. Leser, and E. Müller-Hartmann, Zeitschrift für Physik B Condensed Matter **25**, 339 (1976).

[157] L. Pan, N. J. Laurita, K. A. Ross, B. D. Gaulin, and N. P. Armitage, Nat Phys **12**, 361 (2016).

[158] A. Scheie, J. Kindervater, S. Säubert, C. Duvinage, C. Pfleiderer, H. J. Changlani, S. Zhang, L. Harriger, S. M. Koohpayeh, O. Tchernyshyov, and C. Broholm, ArXiv e-prints (2017), 1703.06904.

[159] X. F. Sun, I. Tsukada, T. Suzuki, S. Komiya, and Y. Ando, Phys. Rev. B **72**, 104501 (2005).

[160] X. F. Sun, A. A. Taskin, X. Zhao, A. N. Lavrov, and Y. Ando, Phys. Rev. B **77**, 054436 (2008).

[161] J. C. Nickerson, R. M. White, K. N. Lee, R. Bachmann, T. H. Geballe, and G. W. Hull, Phys. Rev. B **3**, 2030 (1971).

[162] A. Menth, E. Buehler, and T. H. Geballe, Phys. Rev. Lett. **22**, 295 (1969).

[163] G. Aeppli and Z. Fisk, Comments Condens Matter Phys **16**, 155 (1992).

[164] Z. Fisk, J. Sarrao, S. Cooper, P. Nyhus, G. Boebinger, A. Passner, and P. Canfield, Physica B: Condensed Matter **223**, 409 (1996).

[165] P. Coleman, *Heavy Fermions: Electrons at the Edge of Magnetism* (John Wiley & Sons, Ltd, 2007).

[166] N. E. Sluchanko, A. A. Volkov, V. V. Glushkov, B. P. Gorshunov, S. V. Demishev, M. V. Kondrin, A. A. Pronin, N. A. Samarin, Y. Bruynseraede, V. V. Moshchalkov, and S. Kunii, Journal of Experimental and Theoretical Physics **88**, 533 (1999).

[167] N. E. Sluchanko, V. V. Ġlushkov, B. P. Gorshunov, S. V. Demishev, M. V. Kondrin, A. A. Pronin, A. A. Volkov, A. K. Savchenko, G. Grüner, Y. Bruynseraede, V. V. Moshchalkov, and S. Kunii, Phys. Rev. B **61**, 9906 (2000).

[168] M. Dzero, K. Sun, V. Galitski, and P. Coleman, Phys. Rev. Lett. **104**, 106408 (2010).

[169] V. Alexandrov, P. Coleman, and O. Erten, Phys. Rev. Lett. **114**, 177202 (2015).

[170] O. Erten, P. Ghaemi, and P. Coleman, Phys. Rev. Lett. **116**, 046403 (2016).

[171] X. Zhang, N. P. Butch, P. Syers, S. Ziemak, R. L. Greene, and J. Paglione, Phys. Rev. X **3**, 011011 (2013).

[172] N. Xu, X. Shi, P. K. Biswas, C. E. Matt, R. S. Dhaka, Y. Huang, N. C. Plumb, M. Radović, J. H. Dil, E. Pomjakushina, K. Conder, A. Amato, Z. Salman, D. M. Paul, J. Mesot, H. Ding, and M. Shi, Phys. Rev. B **88**, 121102 (2013).

[173] J. Beille, M. B. Maple, J. Wittig, Z. Fisk, and L. E. DeLong, Phys. Rev. B **28**, 7397 (1983).

[174] S. Wolgast, c. Kurdak, K. Sun, J. W. Allen, D.-J. Kim, and Z. Fisk, Phys. Rev. B **88**, 180405 (2013).

[175] J. Jiang, S. Li, T. Zhang, Z. Sun, F. Chen, Z. R. Ye, M. Xu, Q. Q. Ge, S. Y. Tan, X. H. Niu, M. Xia, B. P. Xie, Y. F. Li, X. H. Chen, H. H. Wen, and D. L. Feng, Nature Communications **4**, 3010 EP (2013).

[176] E. Frantzeskakis, N. de Jong, B. Zwartsenberg, Y. K. Huang, Y. Pan, X. Zhang, J. X. Zhang, F. X. Zhang, L. H. Bao, O. Tegus, A. Varykhalov, A. de Visser, and M. S. Golden, Phys. Rev. X **3**, 041024 (2013).

[177] A. Yoichi, Journal of the Physical Society of Japan **82**, 102001 (2013).

[178] T. Zhang, P. Cheng, X. Chen, J.-F. Jia, X. Ma, K. He, L. Wang, H. Zhang, X. Dai, Z. Fang, X. Xie, and Q.-K. Xue, Phys. Rev. Lett. **103**, 266803 (2009).

[179] Y. Okada, C. Dhital, W. Zhou, E. D. Huemiller, H. Lin, S. Basak, A. Bansil, Y.-B. Huang, H. Ding, Z. Wang, S. D. Wilson, and V. Madhavan, Phys. Rev. Lett. **106**, 206805 (2011).

[180] D. Shoenberg, *Magnetic Oscillations in Metals* (Cambridge University Press, 1984).

[181] Y. Luo, H. Chen, J. Dai, Z.-a. Xu, and J. D. Thompson, Phys. Rev. B **91**, 075130 (2015).

[182] S. Wolgast, Y. S. Eo, T. Öztürk, G. Li, Z. Xiang, C. Tinsman, T. Asaba, B. Lawson, F. Yu, J. W. Allen, K. Sun, L. Li, i. m. c. Kurdak, D.-J. Kim, and Z. Fisk, Phys. Rev. B **92**, 115110 (2015).

[183] G. Baskaran, ArXiv e-prints (2015), 1507.03477.

[184] T. Kasuya, K. Takegahara, T. Fujita, T. Tanaka, and E. Bannai, J. Phys. Colloques (Paris) **40**, C5 (1979).

[185] S. Von Molnar, T. Theis, A. Benoit, A. Briggs, J. Flouquet, J. Ravex, Z. Fisk, P. Wachter, and H. Boppart, *Valence Instabilities* (North-Holland, Amsterdam, 1982).

[186] T. Kasuya, M. Kasaya, K. Takegahara, T. Fujita, T. Goto, A. Tamaki, M. Takigawa, and H. Yasuoka, Journal of Magnetism and Magnetic Materials **31**, 447 (1983).

[187] H. Smith, G. Dolling, S. Kunii, M. Kasaya, B. Liu, K. Takegahara, T. Kasuya, and T. Goto, Solid State Communications **53**, 15 (1985).

[188] L. Taillefer and G. G. Lonzarich, Phys. Rev. Lett. **60**, 1570 (1988).

[189] P. H. P. Reinders, M. Springford, P. T. Coleridge, R. Boulet, and D. Ravot, Phys. Rev. Lett. **57**, 1631 (1986).

[190] H. Shishido, R. Settai, H. Harima, and Y. Onuki, Journal of the Physical Society of Japan **74**, 1103 (2005).

[191] S. A. Hartnoll and D. M. Hofman, Phys. Rev. B **81**, 155125 (2010).

[192] P. Coleman, E. Miranda, and A. Tsvelik, Physica B: Condensed Matter **186**, 362 (1993).

[193] M. C. Hatnean, M. R. Lees, D. M. Paul, and G. Balakrishnan, Scientific Reports **3**, 3071 EP (2013).

[194] Z. Fisk, D. C. Johnston, B. Cornut, S. von Molnar, S. Oseroff, and R. Calvo, Journal of Applied Physics **50**, 1911 (1979).

[195] G. Balakrishnan, M. Lees, and D. Paul, Journal of Crystal Growth **256**, 206 (2003).

[196] M. L. Sutherland, E. C. T. O'Farrell, W. H. Toews, J. Dunn, K. Kuga, S. Nakatsuji, Y. Machida, K. Izawa, and R. W. Hill, Phys. Rev. B **92**, 041114 (2015).

[197] J. Morillo, C.-H. de Novion, and J. Jun, Solid State Communications **48**, 315 (1983).

[198] S. Gabáni, M. Orendáč, G. Pristáš, E. Gažo, P. Diko, S. Piovarči, V. Glushkov, N. Sluchanko, A. Levchenko, N. Shitsevalova, and K. Flachbart, Philosophical Magazine **96**, 3274 (2016).

[199] B. Y. Kang, C.-H. Min, S. S. Lee, M. S. Song, K. K. Cho, and B. K. Cho, Phys. Rev. B **94**, 165102 (2016).

[200] P. A. Popov, V. V. Novikov, A. A. Sidorov, and E. V. Maksimenko, Inorganic Materials **43**, 1187 (2007).

[201] S. Y. Li, J.-B. Bonnemaison, A. Payeur, P. Fournier, C. H. Wang, X. H. Chen, and L. Taillefer, Phys. Rev. B **77**, 134501 (2008).

[202] D. Mandrus, B. C. Sales, and R. Jin, Phys. Rev. B **64**, 012302 (2001).

[203] D. L. Martin, Phys. Rev. **141**, 576 (1966).

[204] D. L. Martin, Phys. Rev. **167**, 640 (1968).

[205] S. Funahashi, K. Tanaka, and F. Iga, Acta Crystallographica Section B **66**, 292 (2010).

[206] P. A. Alekseev, A. S. Ivanov, B. Dorner, H. Schober, K. A. Kikoin, A. S. Mishchenko, V. N. Lazukov, E. S. Konovalova, Y. B. Paderno, A. Y. Rumyantsev, and I. P. Sadikov, EPL (Europhysics Letters) **10**, 457 (1989).

[207] V. A. Trunov, A. L. Malyshev, D. Y. Chernyshov, A. I. Kurbakov, M. M. Korsukova, V. N. Gurin, L. A. Aslanov, and V. V. Chernyshev, Journal of Applied Crystallography **24**, 888 (1991).

[208] V. A. Trounov, A. L. Malyshev, D. Y. Chernyshov, M. M. Korsukova, V. N. Gurin, L. A. Aslanov, and V. V. Chernyshev, Journal of Physics: Condensed Matter **5**, 2479 (1993).

[209] K. Takegahara and T. Kasuya, Solid State Communications **53**, 21 (1985).

[210] S. Nakamura, T. Goto, M. Kasuya, and S. Kunii, Journal of the Physical Society of Japan **60**, 4311 (1991).

[211] U. Rössler, *Solid state theory: an introduction* (Springer Science & Business Media, 2009).

[212] B. Y. Pan, T. Y. Guan, X. C. Hong, S. Y. Zhou, X. Qiu, H. Zhang, and S. Y. Li, EPL (Europhysics Letters) **103**, 37005 (2013).

[213] J. Callaway, Phys. Rev. **132**, 2003 (1963).

[214] D. C. McCollum, R. L. Wild, and J. Callaway, Phys. Rev. **136**, A426 (1964).

[215] A. Kumar, Phys. Rev. B **25**, 3369 (1982).

[216] P. K. Biswas, Z. Salman, T. Neupert, E. Morenzoni, E. Pomjakushina, F. von Rohr, K. Conder, G. Balakrishnan, M. C. Hatnean, M. R. Lees, D. M. Paul, A. Schilling, C. Baines, H. Luetkens, R. Khasanov, and A. Amato, Phys. Rev. B **89**, 161107 (2014).

[217] M. Yamashita, N. Nakata, Y. Kasahara, T. Sasaki, N. Yoneyama, N. Kobayashi, S. Fujimoto, T. Shibauchi, and Y. Matsuda, Nat Phys **5**, 44 (2009).

[218] M. Yamashita, T. Shibauchi, and Y. Matsuda, ChemPhysChem **13**, 74 (2012).

[219] A. V. Sologubenko, E. Felder, K. Giannò, H. R. Ott, A. Vietkine, and A. Revcolevschi, Phys. Rev. B **62**, R6108 (2000).

[220] M. Yamashita, T. Shibauchi, and Y. Matsuda, ChemPhysChem **13**, 74 (2012).

[221] C. P. Nave and P. A. Lee, Phys. Rev. B **76**, 235124 (2007).

[222] W. A. Phelan, S. M. Koohpayeh, P. Cottingham, J. A. Tutmaher, J. C. Leiner, M. D. Lumsden, C. M. Lavelle, X. P. Wang, C. Hoffmann, M. A. Siegler, N. Haldolaarachchige, D. P. Young, and T. M. McQueen, Scientific Reports **6**, 20860 EP (2016).

[223] S. Capponi and F. F. Assaad, Phys. Rev. B **63**, 155114 (2001).

[224] F. Steglich, B. Buschinger, P. Gegenwart, M. Lohmann, R. Helfrich, C. Langhammer, P. Hellmann, L. Donnevert, S. Thomas, A. Link, C. Geibel, M. Lang, G. Sparn, and W. Assmus, Journal of Physics: Condensed Matter **8**, 9909 (1996).